ISSN:1305-130X e-ISSN:1305-1385

CELAL BAYAR UNIVERSITY JOURNAL OF SCIENCE

2024

VOLUME:20

ISSUE:3

Manisa Celal Bayar Üniversitesi
Fen Bilimleri Dergisi

Journal of Science

Volume: 20, Issue: 3, Year: 2024

Contact

Manisa Celal Bayar University

The Graduate School

Campus of Şehit Prof Dr İlhan Varank 45140 Yunusemre – MANİSA, TÜRKİYE

Tel: (00 90) 236 201 27 05

Fax: (00 90) 236 241 21 49

E-mail: lee.fendergi@cbu.edu.tr

Web: https://dergipark.org.tr/tr/pub/cbayarfbe

"CBU Journal of Science is indexed by ULAKBIM-TUBITAK TR-DIZIN"

ISSN 1305-130X E-ISSN 1305-1385

CBUJOS is published quarterly at The Graduate School of Manisa Celal Bayar University

"CBU Journal of Science is a refereed scientific journal"

Celal Bayar University Journal of Science
Volume 20, Issue 3, 2024, p 1-105

Celal Bayar University Journal of Science

Celal Bayar University Journal of Science
Volume 20, Issue 3, 2024, p 1-105

CBU Journal of Science

Celal Bayar University Journal of Science (CBUJOS) covers scientific studies in the fields of Engineering and Science and publishes accounts of original research articles concerned with all aspects of experimental and theoretical studies. CBU Journal of Science is a refereed scientific journal published four times annually (March, June, September and December) by The Graduate School of Manisa Celal Bayar University. CBU Journal of Science considers the original research articles written in English for evaluation.

CBU Journal of Science is indexed by TUBİTAK ULAKBIM TR-DIZIN, and also is included in DOAJ, Cite Factor, Journal TOCS, Advanced Science Index and OAJI databases. Digital Object Identifier (DOI) number will be assigned for all the articles being published in CBU Journal of Science.

Instructions for Authors and Article Template can be found on the page of Celal Bayar University Journal of Science DergiPark (https://dergipark.org.tr/tr/pub/cbayarfbe)

Celal Bayar University Journal of Science
Volume 20, Issue 3, 2024, p 1-105

Vol: 20, Issue: 3, Year: 2024

Contents

Celal Bayar University Journal of Science

Investigation the Role of miR-506 in Metformin-Induced Cell Death Mechanism in MCF-7 and MDA-MB-231 Breast Cancer Cells

Özge Rencüzoğulları[1*], Suraya Qayoumi[1]

[1] Department of Science and Letter, Istanbul Kultur University, 34158, Istanbul, Türkiye

*o.berrak@iku.edu.tr
* Orcid No: 0000-0002-2157-1289

Received: 15 March 2024
Accepted: 6 July 2024
DOI: 10.18466/cbayarfbe.1453535

Abstract

Micro RNAs (miRNA) play a role in basic cellular processes such as cell growth, development, cell cycle and apoptosis by affecting gene expression. Abnormal regulation or changes in expression of miRNAs can be observed in many diseases, especially cancer. Therefore, miRNAs are also being investigated as potential therapeutic targets. It has been suggested that miR-506 may be expressed at low levels in various types of cancer and this may contribute to cancer development. In this study, the effect of miR-506 on the sensitivity of breast cancer cells to metformin was evaluated in terms of its effect on cell survival and apoptotic mechanism. Metformin caused a dose-dependent decrease in cell viability and induced loss of mitochondrial membrane potential in MCF-7 cells while MDA-MB-231 cells were more resistant. The colony formation and migration potential of both cell lines with increased miR-506 expression were significantly suppressed after metformin treatment. Additionally, apoptotic cell death triggered by metformin was induced in both cell lines when miR-506 expression was increased. In conclusion, miR-506 acts as a tumor suppressor in MCF-7 and MDA-MB-231 cells and increases their sensitivity to metformin, indicating the potential of miR-506 to be an important therapeutic target in future studies.

Keywords: Apoptotic cell death, Breast cancer, Metformin, miR-506

1. Introduction

MicroRNAs (miRNAs) are non-translated RNAs of almost 22 nucleotides in length which are found in various organisms, including plants, animals, and some viruses [1]. MicroRNAs mostly bind to the 3' untranslated region (3' UTR) of the mRNA and in a minority can bind to the 5'-UTR, ORF (open reading frame) or promoter regions to carry out their transcription regulation functions [2]. Irregularities in miRNA expressions are related with various types of cancer initiation, progression and metastasis. Abnormally low expression of tumor suppressor miRNAs in cancer cells causes such abnormalities in cellular processes like as decrease in cell death mechanism, increased cell growth and metastasis. However, suppressing the functions of tumor suppressor miRNAs causes a decrease in sensitivity to treatment [3]. OncomiRs generally target genes involved in normal cell regulation, causing these genes to support uncontrolled cell growth, metastasis (spread of tumor cells to other regions) and other cancer features [4]. Studies have shown that miR-506 expressed at significantly low levels in various types of cancer and has tumor suppressor role by targeting oncogenes such as N-Ras, PIM3 and ROCK1 [5]. Many studies have investigated the role of miR-506 in breast cancer cases, which have the second highest incidence worldwide. Accordingly, it has been shown that increased miR-506 expression reduces c-Myc and E2F protein levels in breast cancer cells, resulting in suppression of cell viability and migration capacity [6]. The molecular mechanism of the tumor suppressor role of miR-506, which is found at low levels in breast cancer, continues to be investigated, and its role in combined treatments, which is one of the aims of our project, is a matter of curiosity.

Metformin, used in type 2 diabetes therapies, has an anti-proliferative effect on various cancer cells [7]. In fact, a meta-analysis conducted in 2014 showed that individuals using metformin had a lower incidence of breast cancer [8]. Metformin activates AMP-activated protein kinase (AMPK) by suppressing the mammalian target of rapamycin (mTOR), thus inhibiting cell survival [9]. The

effect of metformin on glucose metabolism in breast cancer cells are related to the duration of administration and has been shown to cause different effects on the uptake of 3H-deoxy-D-glucose (3H-DG) into the cell [10]. In studies conducted on different cancer cells such as pancreatic, gastric or osteosarcoma, metformin has been shown to induce apoptosis, which is programmed cell death [11-13]. Extrinsic and intrinsic molecular mechanisms can be triggered in apoptosis, which is determined by blebbing on the cell membrane, chromatin condensation and the formation of apoptotic bodies. The mitochondrial signaling mechanism, which is activated in the intrinsic pathway, is activated by increasing Bax/Bak protein expressions, which cause polarization in the mitochondrial membrane, and especially by triggering the loss of mitochondrial membrane potential (MMP). At this stage, cytochrome c, which is translocated to the cytosol, forms an apoptosome complex with APAF-1 in the cytosol, triggering caspase activation that takes part in the apoptotic process. Members of the caspase protease family are involved in the initiation and progression of apoptosis. The caspases have the ability to activate each other proteolytically. Caspase 9 known as the initiator caspase in the intrinsic pathway, stimulates PARP cleavage by activating caspase 3 and caspase 7 in the downstream signaling pathway [12]. There are studies showing that the effect of metformin on the intrinsic pathway is due to an increase in reactive oxygen species [7]. However, the effect of metformin on cellular death mechanisms may vary depending on both the application time and the cancer cell. For this reason, studies are continuing to increase the cell viability inhibitory effect of metformin with combined agents.

In the current study, the expression of miR-506, which has a tumor suppressor role, was increased in estrogen receptor positive (ER+) MCF-7 and triple negative breast cancer (ER-, PR-, HER2-) MDA-MB-231 breast cancer cells. Then, the effect of metformin on colony formation potential, migration and effect on cell death mechanism were examined in these cells. In the results obtained, it was observed that miR-506 expression was at a lower level in MDA-MB-231 cells compared to MCF-7 cells. Metformin treatment increased miR-506 expression in both cell lines. When miR-506 expression was increased in both cell lines by synthetic miRNA transfection, the effect of metformin in suppressing colony-forming potential was significantly increased. Additionally, in cells with increased miR-506 expression, metformin suppressed cell migration and triggered apoptotic cell death. As a result, our study revealed that miR-506 is an important target to increase the therapeutic effectiveness of metformin in both types of breast cancer cell lines.

2. Material and Methods

2.1. Cell Culture

MDA-MB-231 (HTB-26) and MCF-7 (HTB-22) cell lines were obtained from ATCC (American Type Culture Collection). Cells were incubated in DMEM (Dulbecco's modified Eagle serum) medium containing 10% FBS and 1% penicillin/streptomycin in an incubator at 5% CO_2 and 37 ℃. Passaging was performed when the cells reached a certain density. For the passaging process, the upper media was removed and the cells were washed with 1 X PBS, an isotonic solution. Then, 0.25% trypsin-EDTA was added to cover the surface of the flask and the cells were allowed to lift off the surface for 3-5 minutes at 37 ℃. The medium was added with trypsin at a ratio of 1:1, and after trypsin inactivation was achieved, the cells were centrifuged at 500 g for 4 minutes. After centrifugation, the cell pellet was homogenized with media and counting was performed using hemocytometry. miR-506 mimic (5 nM) miRCURY LNA miRNA Mimics, (Cat. No: 339173; Qiagen, Hilden, Germany) and mirVana™ miRNA Mimic Negative Control (Cat. No: 4464058; Thermo Scientific, Massachusetts, USA) were transfected by lipofectamine reagent at 1:3 (µg/ml) ratio for 24-48 hours [13].

2.2. Cell survival test

A cell survival test was performed using the 3-(4,5-Dimethylthiazol-2-yl (MTT) agent. In our study, cells were seeded in a 96-well/plate as 1 $X10^4$ cells/well and incubated overnight for adhesion. Following this, different concentrations of metformin (1.5-25 mM) were treated to the cells for 24 hours. Then, the supernatant was carefully removed from the cells to which 10 µL MTT agent was applied in an incubator of 5% CO_2 and 37 ℃ for 4 hours and then 100 µl DMSO was added. Absorbance measurement due to the color change was made in a plate reader at dual wavelengths (570 nm and 655 nm).

2.3. Fluorescence microscopy

DAPI staining: Cells were seeded in a 12-well/plate as $5x10^4$ cells/well. After adhesion, 2.5 mM and 5 mM metformin was treated to the cells for 24 hours. After a 15-minute waiting period with the medium containing DAPI (5 mg/ml), it was observed that the nuclei were stained blue in the fluorescence microscope with at 350/470 nm (Ext./ Em.). DiOC6 staining: Cells were treated as mentioned above. Then, cells treated with 4mM DiOC6 for 15 minutes. The cells with intact mitochondrial membrane structure was observed in green color under a fluorescence microscope at 488/525 nm (Ext./Em). Propidium iodide (PI) staining: Drug-treated/un-treated cells were incubated with 5 mg/ml PI for 30 minutes. Under a fluorescence microscope, dead cells were observed in red color at 536/617 nm (Ext./Em).

2.4. miRNA analysis

miR-506 level was analyzed by qRT-PCR after miR-506 mimic transfection into cells. At the same time, miR-506 level in metformin-treated cells was also examined. Purification of miRNA from cells was carried out with the mirnEasy miRNA isolation Kit with the protocol prescribed by the commercial kit (Qiagen, Cat No: 217004). miScript II RT Kit was used for cDNA synthesis (Qiagen, Cat No: 218161). Following the conversion to cDNA, RT-PCR for miR-506 and endogenous control RNU6B primer was performed on the CFX Connect (BioRad), using miScript SYBR Green PCR Kit (Qiagen, Cat No: 218073) following the steps of 15 s denaturation at 94 °C, 30 s binding at 55°C and 30 s extension at 70°C, 40 cycles were continued. Data analysis was normalized by the ΔCT values of miRNAs of each sample against the internal control RNU6B and was performed in at least 2 replicates.

2.5. Colony formation assay

It was conducted to determine the effect of metformin and miR-506 on colony formation potential of MDA-MB-231 and MCF-7 breast cancer cells. 2000 cells/well were seeded into a 6-well plate. Cells were transfected with synthetic miR-506 miRNA mimic for 24 hours. Then, 5mM metformin was treated for 24 hours. Then, fresh medium was replaced with fresh medium. For approximately two weeks, when the control group reached 80% colony density, the cells were fixed with methanol: acetic acid (3:1 ratio) for 10 minutes at room temperature and observed by staining with 0.5% crystal violet. Colony numbers were counted by ImageJ image processing program.

2.6. Wound healing assay

Wound healing test, also referred to as cell migration test, helps to analyze the effect of metformin and miR-506 on migration capacity of breast cancer cells. The cells were transfected with miR-506 mimic after seeding them in a 6-well petri dish at $6x10^5$ cells/well. At the end of 24 hours, a wound was created by scratching the petri dish with a 10 µl sterile pipette tip. After washing with 1 X PBS, fresh media was added to control groups and 5 mM metformin was treated for drug-treated groups. The change in wound width was measured with the help of a light microscope for 24, 48 and 72 hours. At the ends of the 72 hours, cells were stained with DiOC6 and observed with fluorescence microscope.

2.7. Flow cytometry-PI staining

$6x10^5$ (cells/well) cells were seeed and miR-506 transfection protocol was proceeded. Then, metformin was applied and after 24 hours, the cells were Trypsinized and fixed with ice-cold 70% ethanol at +4 °C for 2 days. Following fixation,cells were stained with 50µg/mL PI dye and 100mg/mL RNase. Finally analyzed by cell flow cytometry (BD AccuriTM C6 Flow Cytometer).

2.8. Immunoblotting

Following transfection and the treatment procedures, cells were harvested using 1 X PBS. Total protein was obtained with the cell extraction buffer (20 mM Tris-HCl (pH 7.5), 150 mM NaCl, NP-40 0.5%, (v/v), 1 mM EDTA, 0.5 mM PMSF, 1 mM DTT, protease inhibitor cocktail (Complete EDTA -free, Roche) and then centrifuged at 16000 g at 4 °C. Protein concentrations were determined by Bradford analysis. 30 µg total protein lysate were loaded and proceeded to 10-12% SDS-PAGE gel electrophoresis method. After being separated according to protein weight, the transfer process was carried out to transfer them to the PVDF membrane. AMPK, Bak, Puma, Bax, Caspase 9, Caspase 7 and PARP (CST; Danvers, MA) primer antibodies were incubated for 24 h in TBS-T containing %5 non-fat milk. Then, membranes were incubated with HRP-conjugated-anti-rabbit secondary antibody (CST; Danvers, MA) for 24 h at 4°C at 1:3000 ratio. β-actin was used as a loading control. After membranes were exposed to chemiluminescence reagent, results were detected by Chemidoc (Bio-Rad, California, USA).

2.9. Statistical analysis

All results obtained regarding the effect mechanism of metformin on cell viability and cell migration were examined with the Tukey's multiple comparisons test with Two-way ANOVA statistical method compatible with the number of data using the Graphpad program and presented as a graph/table.

3. Results and Discussion

3.1. Metformin treatment reduced cell viability in MCF-7 and MDA- MB-231 breast cancer cells

MTT analysis was performed in order to determine the effect of metformin on cell viability in MCF-7 and MDA-MB-231 breast cancer cells depending on the concentration (1.5, 2.5, 5, 10, 15, 20, 25 mM). The viability of each breast cancer cell line was decreased after metformin treatment for 24 hours depending on the increasing dose (Figure 1a-b). Treatment of 2.5 mM and 5 mM metformin to MCF-7 cells decreased cell viability by 20% and 40%, respectively. The same concentrations suppressed cell survival by 15% and 30%, respectively in MDA-MB-231 cells. Metformin exerted more potent cytotoxic effect against MCF-7 (IC_{50}, 10 mM) compared with MDA-MB-231 cells (IC_{50}, 25 mM).

The effect of metformin on cell death and MMP loss was detected by fluorescence staining (Figure 1c). Dead cells take PI into the cell with the deterioration of membrane

permeability. It was observed that the number of PI stained cells were increased after 2.5 mM and 5 mM metformin treatment. DiOC6 is a fluorescent dye that visualizes living cells as green at certain wavelengths, depending on the MMP maintained in living cells.

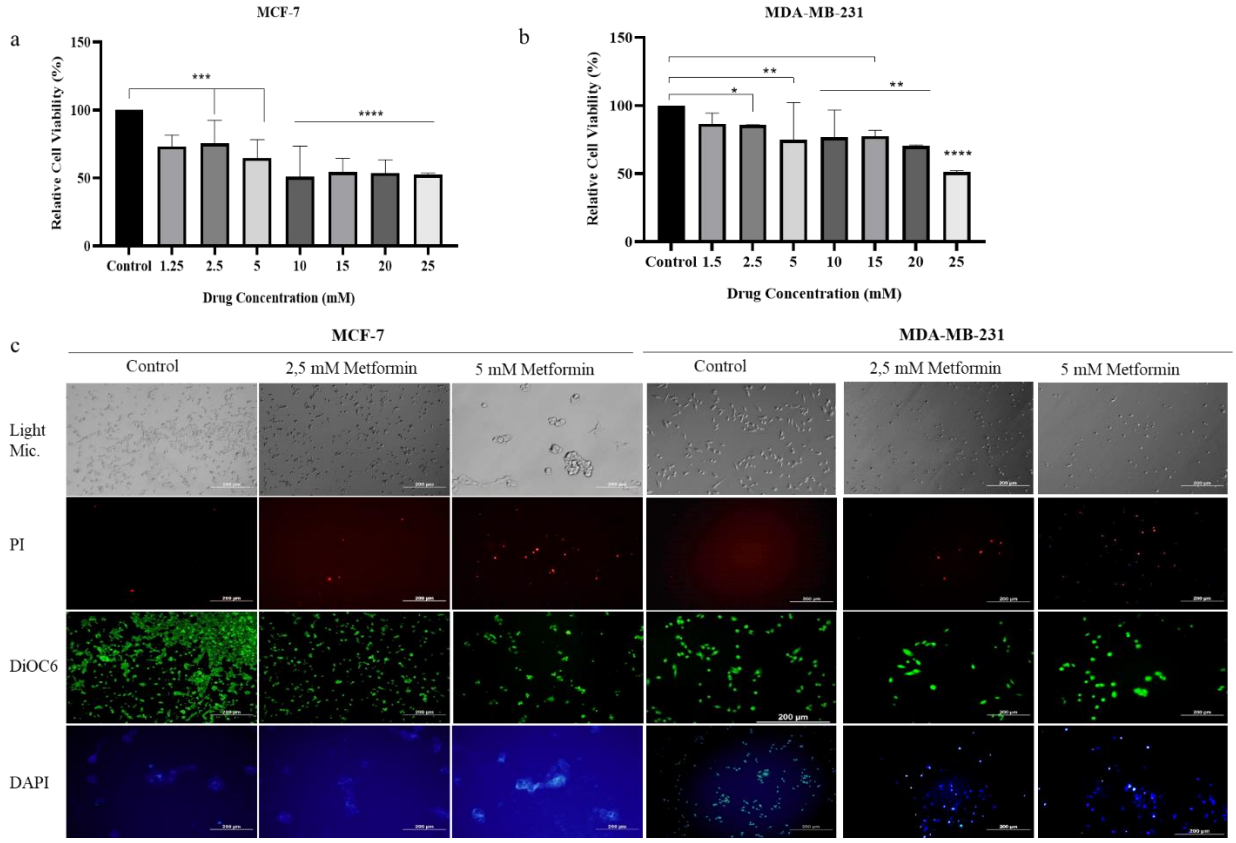

Figure 1. Metformin reduced cell viability in MCF-7 and MDA-MB-231 cells in a dose dependent manner. (a-b) MTT cell viability test was proceeded after metformin treatment in various concentration (1.5-25 mM) for 24 hours in MCF-7 and MDA-MB-231 cells.* p<0.05, **p<0.01 ***p<0.001, ****p<0.0001 (c) Cells were treated by metformin (2.5 and 5 mM) for 24 hours and then the ratio of cell death was examined by PI staining, the MMP loss was observed by DiOC6 staining and the DNA breaks was analyzed by DAPI staining with fluorescence microscopy.

Metformin treatment to each breast cancer cells caused a noticeable decrease in viable cells. DNA breaks in cells caused by metformin were analyzed by DAPI staining. Metformin caused an increase in DNA breaks in each breast cancer cells compared to the control groups. Similar to our study, a decrease in cell survival was shown with the treatment of metformin (2.5 and 5mM) for 24-hours [14]. The indicated concentrations induced MMP loss in both breast cancer cells and caused a decrease in cell survival.

3.2. Examination of miR-506 level in MCF-7 and MDA-MB-231 breast cancer cells

The expression of miR-506, a tumor suppressor, in both cell lines was examined by real-time PCR following miRNA isolation. Normalization were accomplished according to the RNU6 expression, an internal control. miR-506 expression was observed to be higher in MCF-7 cells. A concentration of 5 mM metformin was chosen for subsequent experiments to determine the molecular mechanism triggered in relation to metformin and miR-506. Treatment of 5 mM metformin for 24 hours increased miR-506 expression by 2.4 in MCF-7 and 2 fold MDA-MB-231 cells (Figure 2a-b). Synthetic miR-506 was transfected into both cell lines and then expression of miR-506 was examined by qRT-PCR. After transfection, miR-506 expression increased 4.3-fold in MCF-7 cells and 6-fold in MDA-MB-231 cells. These transfection rates were continued to be used in subsequent experiments (Figure 2a-b). It has been shown that the effect of metformin on cancer cells is due to its inhibition of mTOR by activating AMPK [7]. A significant increase in AMPK level was observed in both cell lines treated with metformin. When miR-506 expression was increased in both cell lines, AMPK levels increased. However, a significant increase in AMPK level was observed in metformin-treated miR-506+ cells compared to the metformin-only group (Figure 2c). Studies have shown that activation of AMPK, one of the

main targets of metformin treatment, triggers apoptosis by using the p53/p21 axis in the cell [17]. However, the exact molecular mechanisms of metformin are needed to be clarification in breast cancer. For this reason, in the current study, the effect of metformin on cell survival, migration and cell death was investigated through miR-506 expression**.**

3.3. High expression of miR-506 increased the effect of metformin on colony formation in MCF-7 and MDA-MB-231 breast cancer cells

After increasing miR-506 expression, the long-term effect of metformin treatment was investigated by colony formation assay (Figure 3a).

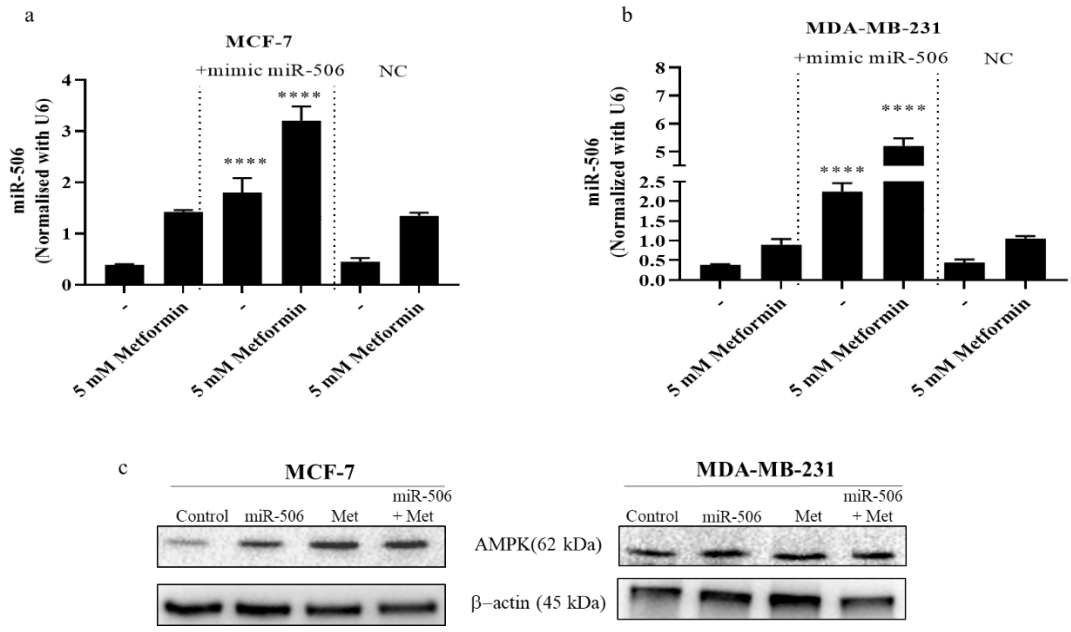

Figure 2. Metformin treatment increased the miR-506 levels in each cell line. (a) MCF-7 and (b) MDA-MB-231 cells were transfected with synthetic miR-506 and negative control (NC) miRNA for 48 hours then treated with 5 mM metformin for 24 hours. qRT-PCR was performed in non-transfected and transfected cells after metformin treatment. Results were normalized with RNU6 internal miRNA control. The results obtained are the average/st. deviation values of two replicate data of three different experiments **** $p<0.00001$. (c) After transfection of miR-506 and 5 mM metformin treatments total protein isolation was proceeded. AMPK levels were determined in each cell line by immunoblotting. β-actin was used as a loading control.

According to the results obtained, no significant difference was observed in the number of colonies of each cell with increased miR-506 expression compared to the untreated group. MCF-7 cells were observed to be more sensitive to metformin. When miR-506 expression was increased, both cell lines became more sensitive to metformin, and the number of colonies was significantly reduced compared to cells treated with metformin alone (Figure 3a). Similar to our study, overexpression of miR-506 has been reported as suppressor on the progression of various cancer types such as ovarian and cervical cancer [5]. However, Streicher and colleagues reported that high expression of miR-506 acts as an oncogene in melanomas [18]. Therefore, it can be concluded that the role of miR-506 might be vary in specific cell types. It has been uncovered that miR-506 suppressed cell proliferation and invasion of breast cancer cells through the ERK pathway by suppressing the expression of IQGAP1 [19]. However, the molecular mechanism of process of miR-506 on different breast cancer cells is still the focus of research.

Following metformin treatment to normal and miR-506+ breast cancer cells, the effect of cell migration was examined (Figure 3b-c). It was observed that increasing miR-506 expression, which had no effect on colony formation, suppressed cell migration in each cell. When metformin was treated to breast cancer cells with high miR-506 expression, it was observed that migration was significantly reduced in both cell lines. In addition, miR-506 led to an increase of the effect of metformin on cell migration compared to the metformin-only group. In the study on hepatocellular carcinoma cells (HCC), overexpression of miR-506 was shown to significantly inhibit the migration and invasiveness of HCC cells *in vitro* and *in vivo* [20]. In the same study, it was showed that the ectopic expression of miR-506 led to significant decrease in the expression of vimentin and an increase of E-cadherin level in HCC cells, suggesting that miR-506 inhibits HCC metastasis by suppressing EMT. In another study in MDA-MB-231 cells that examined the effects of miR-506 on invasion and migration, miR-506 played a suppressor role in the EMT mechanism by directly targeting CD151, VIM and SNAI2 [21]. In this context,

it has been shown in our study that the migration inhibitory effect of metformin is increased in miR-506 + breast cancer cells.

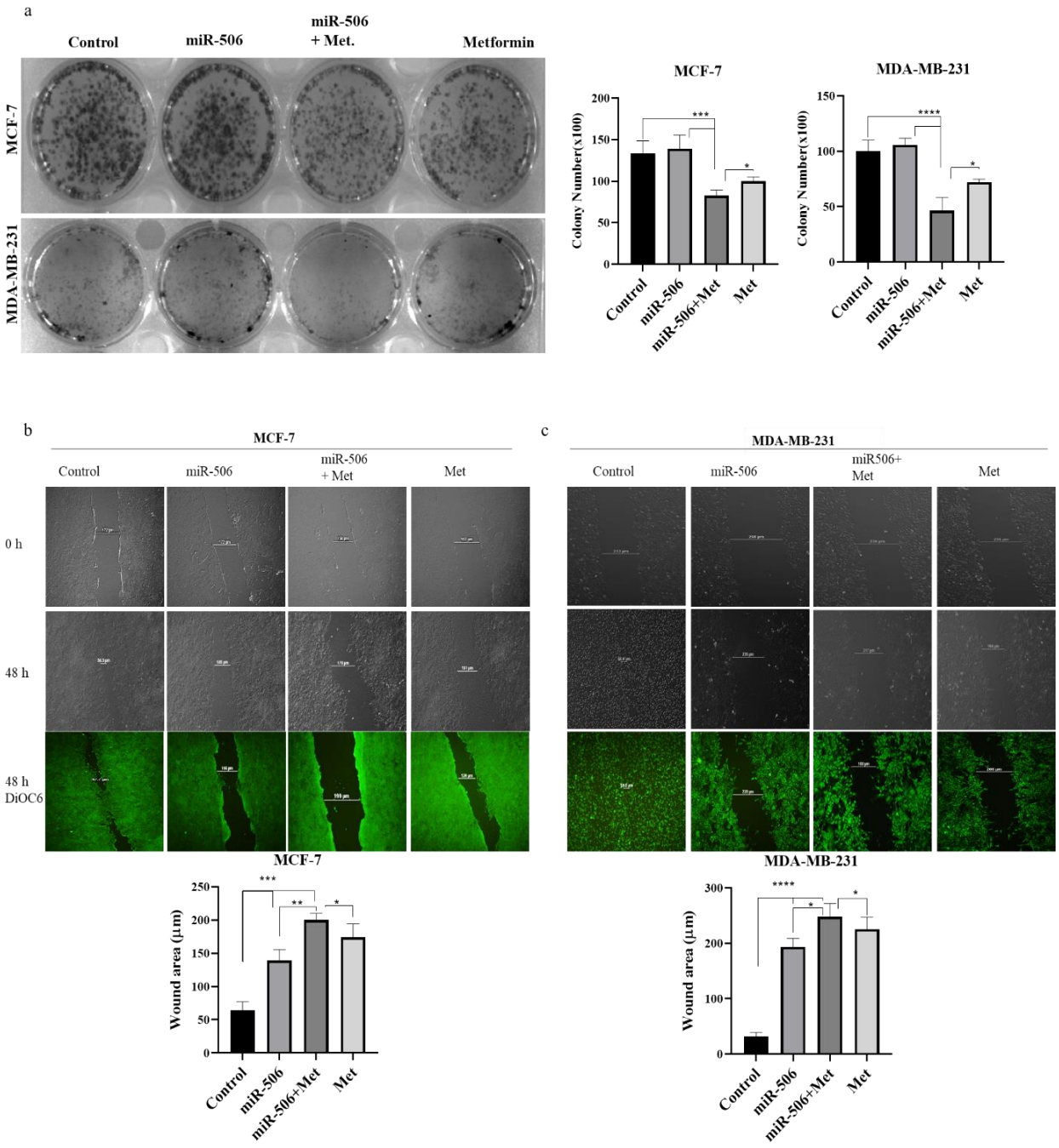

Figure 3. Metformin was more effective in the reduction of colony formation and cell migration capacity of the cell while miR-506 levels were increased in MCF-7 and MDA-MB-231 cells. (a) Colony formation test was performed in miR-506+ and normal breast cancer cells after 5 mM metformin treatment. (b-c) Cell migration assay was proceeded to observe the effect of increased level of miR-506 after metformin treatment in MCF-7 (b) and MDA-MB-231 (c) cells. Wound area was calculated and analyzed then presented as bar graphics for each cell line. * $p<0.05$, ** $p<0.02$, *** $p<0.001$, **** $p<0.0001$

3.4. Examining the effect of miR-506 and metformin treatment on cell cycle and apoptotic cell death

The effects of miR-506 and metformin treatments on cell cycle phases were examined by cell flow cytometry following PI staining (Figure 4a). Increasing miR-506 expression had different effects on cell cycle phases in both cell lines. When miR-506 expression was increased in MCF-7 cells, there was suppression in G1 phase.

Metformin alone treatment caused suppression of S phase in MCF-7 cells. When metformin was treated to MCF-7 miR-506+ cells, the arrest of S phase was observed compared to the control group and the metformin alone group. There were no similar results in MDA-MB-231 cells. Although the effect of miR-506 on protein expressions involved in the cell cycle is still a subject of research, studies have shown that miR-506-3p led to a significant decrease in E2F and cMyc levels, an increase in RB protein levels. Which is known that the potent proto-oncogene Myc is highly expressed in breast cancer [22]. There are studies showing that miR-506 suppresses breast cancer cell viability and migration capacity, but there are still many points of its molecular mechanism that need to be elucidated.

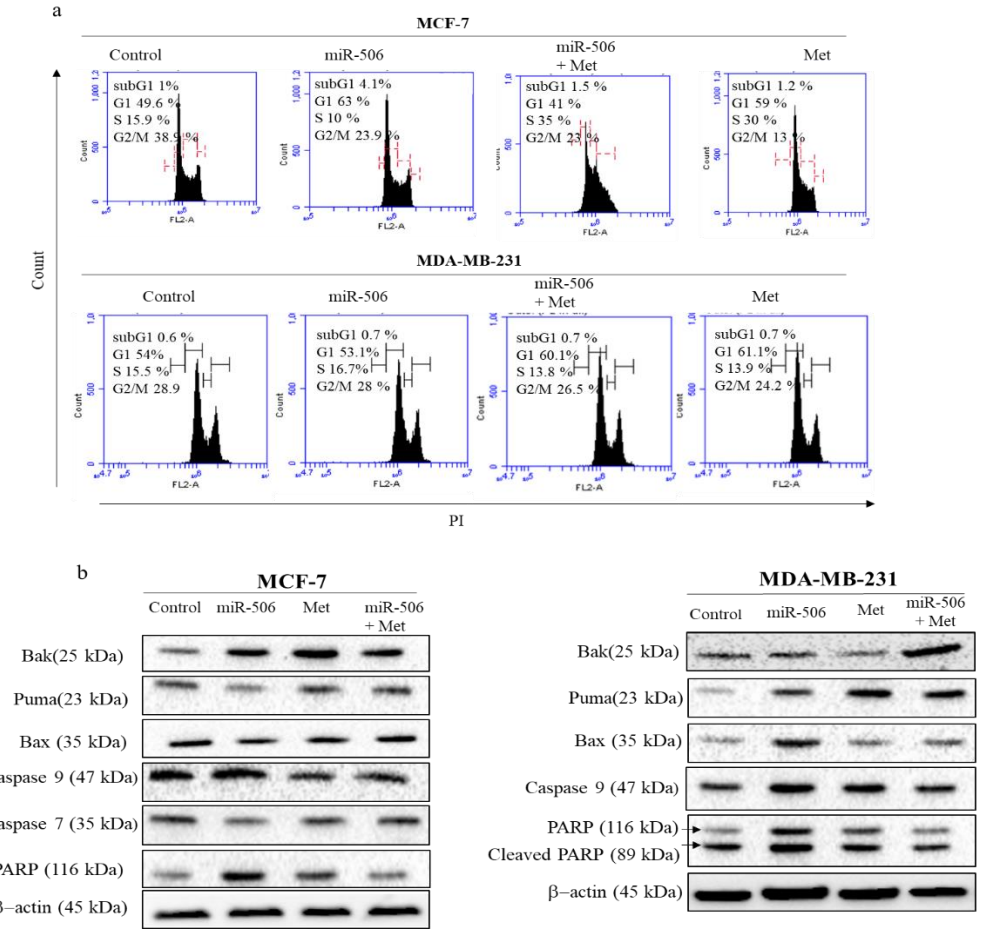

Figure 4. miR-506 and metformin combine treatment increased apoptotic cell death in MCF-7 and MDA-MB-231 cells. (a) The effect of miR-506 and metformin on cell cycle phases, the flow cytometry analysis was performed after PI staining. (b) The expression level of Bak, Puma, Bax, Caspase 9, Caspase 7 and PARP were determined by immunoblotting in MCF-7 and MDA-MB-231 cells. β-actin was used as a loading control.

To observe the effect of metformin on apoptotic cell death, total protein isolation was performed on normal cells and miR-506+ cells after 5 mM metformin treatment. Changes in the pro-apoptotic protein expressions (Bak, Bax, puma, caspase 9, PARP) were examined in each breast cancer cells by immunoblotting (Figure 4b).

When miR-506 expression was increased, an increase in Bak expression was observed in both cell lines. While metformin further increased Bak expression in MCF-7 cells, there was no similar result in MDA-MB-231 cells. However, metformin significantly increased Bak expression in miR-506+ MDA-MB-231 cells. Puma and Bax expression were higher in miR-506+ MDA-MB-231 cells compared to miR-506+ MCF-7 cells. Puma expression increased further in MDA-MB-231 cells when metformin was treated to these cells. However, Bax expression is higher in metformin-treated miR-506+ MCF-7 cells than in MDA-MB-231 cells. Studies was conducted that metformin increased the Bax expression in prostate cancer cells [23]. However, a study in breast cancer cells showed that metformin had no significant effect on Bax expression but, decreased the anti-apoptotic Bcl-2, c-Myc and Akt expression levels.

Therefore, metformin showed anti-tumorigenic effect on breast cancer cells [24].

Metformin treatment resulted in a higher reduction of the inactive caspase 9 form in miR-506+ cells. Metformin led to decrease of inactive caspase 7 expression in miR-506+ MCF-7 cells compared to the control group. The numerous DNA strand breaks that are likely to be present in the cell undergoing apoptosis lead to PARP activation which is a DNA repair protein. A decrease in full PARP (116 kDa), inactive PARP, expression was observed after metformin treatment in both cells. Moreover, increased miR-506 expression further increased the cleavage of PARP in both cell lines. Similar to the current study, miR-506 showed a pro-apoptotic effect by increasing cytochrome c, Bax and cleaved caspase 9 expression levels while by decreasing the anti-apoptotic Bcl-2 and Bcl-xL expression levels in lung cancer cells [25]. Moreover, overexpression of miR-506 has a significant potential to prevent pancreatic cancer progression and chemoresistance *via* Akt/NF-κB signaling [26]. Therefore, in the current study the tumorsuppressor role of miR-506 was used to increase the effect of anti-proliferative capacity of metformin in different breast cancer cells.

4. Conclusions

In conclusion, metformin treatment induced cell viability loss and induced MMP loss in MCF-7 and MDA-MB-231 cells. However, the MDA-MB-231 cells were more resistant to metformin treatment than MCF-7 cells. The expression level of miR-506 which has a tumor suppressor role, was lower in MDA-MB-231 cells. Therefore, elevated expression level of miR-506 increased the effect of metformin on the reduction of cell migration capacity and induction of cell death mechanism in each cell line. However, the signaling pathways through which metformin and miR-506 activate the cell death mechanism need to be further investigated. In our study, miR-506, which has the potential to be used as a combined therapy model in the future, has been shown for the first time to have a synergistic effect with metformin.

Acknowledgement

The authors wish to thank Scientific Research Projects Unit of Istanbul Kultur University for their constant interest in this project.

Author's Contributions

Özge Rencüzoğulları: Conceptualization, Validation, Writing- original draft, Supervision, Writing- review and editing.
Suraya Qayoumi: Methodology, Data curation, Software, Visualization, Investigation.

Ethics

There are no ethical issues after the publication of this manuscript.

References

[1]. Otmani K., Lewalle P. 2021. Tumor Suppressor miRNA in Cancer Cells and the Tumor Microenvironment: Mechanism of Deregulation and Clinical Implications. *Front. Oncol*.; 11: 708-765.

[2]. Michlewski G., Cáceres J. F. 2019. Post-transcriptional control of miRNA biogenesis. *RNA*; 25(1): 1–16.

[3]. Muñoz J. P., Pérez-Moreno P., Pérez Y., Calaf G. M. 2023. The Role of MicroRNAs in Breast Cancer and the Challenges of Their Clinical Application., *Diagnostics (Basel, Switzerland)*; 13(19): 3072.

[4]. Annese T., Tamma R., De Giorgis M., Ribatti D. 2020. microRNAs Biogenesis, Functions and Role in Tumor Angiogenesis., *Front. Oncol*.; 10(1): 581007-58127.

[5]. Wen S.Y., Lin Y., Yu YQ., Cao S.J., Zhang R., Yang X.M., Li J., Zhang Y.L., Wang Y.H., Ma M.Z., Sun W.W., Lou X.L., Wang J.H., Teng Y.C., Zhang Z.G. 2015. miR-506 acts as a tumor suppressor by directly targeting the hedgehog pathway transcription factor Gli3 in human cervical cancer. *Oncogene*; 34(6): 717–725.

[6]. Saad El Din G., Youness R. A., Assal R. A., Gad M. Z. 2018. Mir-506-3p synergistically represses breast cancer progression through altering cell cycle regulators. *Ann. Oncol;* 29: 28-34.

[7]. Lu C.C., Chiang J.H., Tsai F.J., Hsu Y.M., Juan Y.N., Yang J.S., Chiu H.Y. 2019. Metformin triggers the intrinsic apoptotic response in human AGS gastric adenocarcinoma cells by activating AMPK and suppressing mTOR/AKT signaling, Metformin triggers the intrinsic apoptotic response in human AGS gastric adenocarcinoma cells by activating AMPK and suppressing mTOR/AKT signaling. *Int. J. Oncol*; 54(4): 1271–1281.

[8]. Balkan B., Demir G., Balkan F., Çetingök H., Atiç E. 2020. Metformin İlişkili Laktik Asidoz; Bir Olgu Nedeni ile Literatürün Gözden Geçirilmesi, *Tıp Fakültesi Klinikleri Dergisi*; 3(1): 49-53.

[9]. Samuel S. M., Varghese E., Koklesová L., Líšková A., Kubatka P., Büsselberg D. 2020. Counteracting Chemoresistance with Metformin in Breast Cancers: Targeting Cancer Stem Cells., *Cancers (Basel)*; 12 (9): 2482-2490.

[10]. Amaral I., Silva C., Correia-Branco A., and Martel F. 2017. Metformin interferes with glucose cellular uptake by both estrogen and progesterone receptor-positive (MCF-7) and triple-negative (MDA-MB-231) breast cancer cell lines: PS156. *Porto Biomed. J*.; 2(5): 218-226.

[11]. Li B., Zhou P., Xu K., Chen T., Jiao J., Wei H., Yang X., Xu W., Wan W., Xiao J. 2020. Metformin induces cell cycle arrest, apoptosis and autophagy through ROS/JNK signaling pathway in human osteosarcoma. *Int. J. Biol. Sci*.; 16 (1): 74–84.

[12]. Szymczak-Pajor I., Drzewoski J., Świderska E., Strycharz J., Gabryanczyk A., Kasznicki J., Bogdańska M., Śliwińska A. 2023. Metformin Induces Apoptosis in Human Pancreatic Cancer (PC) Cells Accompanied by Changes in the Levels of Histone Acetyltransferases (Particularly, p300/CBP-Associated Factor (PCAF) Protein Levels). *Pharmaceuticals*; 16(1): 115-123.

[13]. Zhu M., Wang J., and Zhou R. 2022. Combination of metformin and oxaliplatin inhibits gastric cancer cell proliferation and induces apoptosis. *Acta Biochim. Pol*.; 69(2): 321–326.

[14]. Elmore S. 2007. Apoptosis: a review of programmed cell death. *Toxicol. Pathol*.; 35 (4) (2007) 495–516.

[15]. Rencüzoğullari Ö., Arisan E. D. 2022. Palbociclib suppresses the cancer stem cell properties and cell proliferation through increased levels of miR-506 or miR-150 in Panc-1 and MiaPaCa-2 cells. *Turkish J. Biol*., 46(5): 342–360.

[16]. Gao Z.Y., Liu Z., Bi M.H., Zhang J.J., Han Z.Q., Han X., Wang H.Y., Sun G.P., Liu H., Metformin induces apoptosis via a mitochondria-mediated pathway in human breast cancer cells in vitro. *Exp. Ther. Med*.; 11(5): 1700–1706.

[17]. Chen Y.H., Yang S.F., Yang C.K., Tsai H.D., Chen T.H., Chou M.C., Hsiao Y.H. 2021. Metformin induces apoptosis and inhibits migration by activating the AMPK/p53 axis and suppressing PI3K/AKT signaling in human cervical cancer cells. *Mol. Med. Rep*.; 23(1): 88-97.

[18]. Streicher K.L., Zhu W., Lehmann K.P., Georgantas R.W., Morehouse C.A., Brohawn P., Carrasco R.A., Xiao Z., Tice D.A., Higgs B.W., Richman L., Jallal B., Ranade K., Yao Y. 2012. A novel oncogenic role for the miRNA-506-514 cluster in initiating melanocyte transformation and promoting melanoma growth. *Oncogene*; 31(12): 1558–1570.

[19]. Sun G., Liu Y., Wang K., Xu Z. 2015. miR-506 regulates breast cancer cell metastasis by targeting IQGAP1. *Int. J. Oncol.;* 47(5): 1963–1970.

[20]. Wang Z., Si M., Yang N., Zhang H., Fu Y., Yan K., Zong Y., Zhu N., Wei Y. 2018. MicroRNA-506 suppresses invasiveness and metastasis of human hepatocellular carcinoma cells by targeting IL8. *Am. J. Cancer Res*.; 8(8): 1586–1594.

[21]. Arora H., Qureshi R., Park W.Y. 2013. miR-506 regulates epithelial mesenchymal transition in breast cancer cell lines. *PLoS One*, 8(5): e64273.

[22]. García-Gutiérrez L., Delgado M. D., León J. 2019. MYC Oncogene Contributions to Release of Cell Cycle Brakes. *Genes (Basel)*; 10(3): 244-254.

[23]. Budiani D., Mahanani M., Wibowo Y., Probandari A., Prasetyo D., Mudigdo A. 2017. Molecular Therapeutic Potency of Metformin by Targeting p53-Related Molecules in Mutant p53 Colon Cancer Cell Line. *Indonesian Journal of Cancer Chemoprevention*; 7(1): 17-24.

[24]. Zhang, J., Li, G., Chen, Y., Fang, L., Guan, C., Bai, F., Ma, M., Lyu, J., Meng, Q. H. 2017. Metformin Inhibits Tumorigenesis and Tumor Growth of Breast Cancer Cells by Upregulating miR-200c but Downregulating AKT2 Expression. *Journal of Cancer*; 8(10: 1849–1864.

[25]. Li, Z. H., Zhou, J. H., Chen, S. N., Pan, L., Feng, Y., Luo, M. Q., Li, R. X., Sun, G. L. 2021. MicroRNA-506 has a suppressive effect on the tumorigenesis of nonsmall-cell lung cancer by regulating tubby-like protein 3. *Bioengineered*; 12(2): 10176–10186.

[26]. Li, J., Wu, H., Li, W. Yin, L., Guo, S., Xu, X., Ouyang, Y., Zhao, Z., Liu, S., Tian, Y., Tian, Z. Ju, J., Ni, B., Wang, H. 2016. Downregulated miR-506 expression facilitates pancreatic cancer progression and chemoresistance via SPHK1/Akt/NF-κB signaling. *Oncogene* ;35(1): 5501–5514.

Celal Bayar University Journal of Science

Propolis: as an Additive in Bacterial Cellulose Production

Nermin Hande Avcıoğlu[1]*

[1] Department of Biology, Hacettepe University, Ankara, Türkiye

* hurkmez@hacettepe.edu.tr
* Orcid No: 0000-0003-2243-5817

Received: 27 May 2024
Accepted: 17 July 2024
DOI: 10.18466/cbayarfbe.1490668

Abstract

This study investigates the effect of propolis supplementation on bacterial cellulose (BC) production efficiency with *Komagataeibacter* species. Compared to production in Hestrin-Schramm medium, the addition of propolis increased BC production with *K. intermedius*, *K. maltaceti*, and *K. nataicola* by 1.31-fold, 2.09-fold, and 1.43-fold, and optimal propolis concentration were determined to be 25%, 20%, and 30%, yielding 7.15 g/L BC, 5.4 g/L BC, and 4.15 g/L BC, respectively. *K. intermedius* - *K. maltaceti* consortia, increased production by 1.57-fold compared to *K. intermedius* and 2.07-fold compared to *K. maltaceti* monocultures. Increasing the volume of the cultivation vessel also increased BC production by 1.08-1.59-fold. Agitation induced production efficiency by 1.01-1.18-fold; however, obtained BC exhibited irregular shapes. BC obtained from *K. maltaceti* exhibited the highest Water Holding Capacity (WHC) and Moisture Content Retention (MCR) as 97.63% and 33.22 g/g. Characteristic BC bands and nanofibrillar structure of BC were observed with Focused Ion Beam Scanning Electron Microscopy (FIB-SEM) and Fouirer Transform Infrared (FT-IR) Spectrometer.

Keywords: Bacterial cellulose, Bacterial consortia, Propolis, *Komagataeibacter* sp.

1. Introduction

Propolis is a traditional therapeutic agent collected by bees from plant secretions, containing active compounds such as soluble polyphenols and flavonoids in its structure. Besides exhibiting antimicrobial properties, showing protective effects against bacteria and fungi in bee hives, it is also known to possess antiviral and antiparasitic effects [1-4]. Propolis also contains various amino acids, minerals, sugars, and many other valuable components and can be used as an *ex situ* and *in situ* agent in the modification of polymers due to its unique properties [4-8].

Bacterial cellulose (BC) is a carbohydrate-based biopolymer synthesized extracellularly by microorganisms, forming a hydrogel membrane on the culture surface [5, 8]. With its ultrapure structure, high water retention capacity, biocompatibility, porosity, mechanical strength, high crystallinity, large surface area, and biodegradability, BC is increasingly being used in industrial areas, including food, biomedicine, cosmetics, textiles, and acoustics [5,9-11]. The fibrous structure of BC, formed by hydrogen bonds, creates a dense polymer matrix that is insoluble in water and organic solvents, making it a preferred material [12]. The easily controllable structure and being obtained in a pure form from the cultivation media makes this biomaterial a significant advantage for its preference in industrial applications [13].

The high cost of the cultivation medium used in BC production and the low production yield limit its industrial use. Therefore, it is crucial to use low-cost substrates and additives in Hestrin Schramm (HS) broth or replace the ingredients in HS medium to obtain BC with a high yield [13-16]. Increasing industrial production, reducing costs, and improving the mechanical properties of BC are crucial for enhancing product yield [10]. Additionally, the properties and morphology of the BC obtained during production are directly influenced by the nutrients comprising the culture medium and cultivation conditions such as pH, oxygen, and temperature. Therefore, modifying structural and physiological properties can be achieved by using additives during BC fermentation [17]. Through *in situ* modifications, it becomes possible to alter the

properties of BC fibrils such as size, surface area, crystallinity, electrical conductivity, and mechanical characteristics [13,18]. Despite lacking antimicrobial properties, due to its easily moldable structure and the ability to integrate with various substances and release the integrated material, this biopolymer is commonly modified with the use of additives during the fermentation process or combined with additives to create composites through *ex situ* modification [5, 16, 19, 20]. Accordingly, carboxymethylcellulose (CMC) [21], gellan gum [13], silicone polyether surfactant (SPS) [16], pullulan [10], ethanol and lactic acid [22], and polyethylene terephthalate ammonia hydrolysate (PETAH) [23] used as additives in BC production and resulting as to highly form product yield in the literature.

Indeed, in addition to *in situ* and *ex situ* modifications, it is possible to modify BC with co-cultivation by using multiple microorganisms in the fermentation media [20]. Co-cultivation is noted to be a method that reduces production costs in biotechnological applications and alleviates metabolic burdens among microorganisms through factors such as cross-feeding of nutrients when microbial consortia are used together [19, 24]. In recent years, an increasing trend in co-cultivation has been observed in BC production with the use of *Komagataeibacter* sp. and *Lactocaseibacillus* [20], *K. sucrofermentans*, *Leuconostoc mesenteroides* and *Xanthomonas campestris* [25], *Saccharomyces cerevisiae* and *K. rhaeticus* [11], and *Enterobacter* sp. and *Lactobacillus lactis* [19].

In this study, propolis was used as an additive in HS broth to determine the effect of propolis on BC production with *Komagataeibacter* species (*K. intermedius, K. maltaceti* and *K. nataicola*) and their consortia (*K. nataicola - K. intermedius, K. maltaceti - K. nataicola, K. intermedius - K. maltaceti*). Additionally, inoculum ratios of binary consortia of *Komagataeibacter* species and the impact of culture volume (2 mL, 10 mL, and 20 mL with the vessel dimensions of 15mm, 45mm and 85mm, respectively) on BC production was investigated. The effect of agitation on BC yield was also evaluated. Furthermore, obtained BC membranes were characterized using Focused Ion Beam Scanning Electron Microscopy (FIB-SEM) and Fourier Transform Infrared (FT-IR) Spectrometer, and Water Holding Capacity (WHC) and Moisture Content Ratio (MCR) were also calculated, which are crucial data for the industrial use of this valuable biomateral.

2. Materials and Methods

2.1. *Komagataeibacter* strains and pre-cultivation conditions

K. intermedius, K. maltaceti and K. nataicola strains obtained from Avcioglu's research [14, 15, 26] were used as BC producers in this study. Pre-cultivation was performed in HS broth (containing in g/L: 20 glucose, 5 peptone, 5 yeast extract, 2.7 Na_2HPO_4 and 1.15 citric acid) at 30˚ C for 3 days statically (MCI 120, Mipro, Ankara, Turkey). Cultures with fibril formation were used as pre-culture in the rest of the study [26].

2.2. Propolis effect on BC production

Propolis, obtained from a local manufacturer (Ankara, Turkey), was used as an additive in HS broth to investigate the effect on BC yield by using *K. intermedius, K. maltaceti* and *K. nataicola* species. Accordingly, 5-40% concentrations of propolis were added in HS broth and 10% (v/v) of each bacterial culture (OD_{600nm} = 0.20-0.25) were inoculated, separately. Optimal propolis concentration for each *Komagataeibacter* species was evaluated after an incubation period at 30˚ C for 7 days in a static incubator (MCI 120, Mipro, Ankara, Turkey). HS broth without propolis addition was used as a negative control for demonstrating the difference between production yield incubated in propolis included media [26].

2.2.1. Effect of incubation period on BC production

To compare BC production, pH and bacterial growth (OD_{600nm}) during the incubation period (1-7 days) with *Komagataeibacter* species, incubation was performed at 30˚ C in a static incubator (MCI 120, Mipro, Ankara, Turkey) and all parameters were evaluated for each day from 1 to 7.

2.2.2. BC production with *Komagataeibacter* consortia

To investigate the effect of propolis supplementation to HS broth on BC production with binary consortia of *Komagataeibacter* species (*K. intermedius-K. nataicola, K. maltaceti-K. intermedius* and *K. nataicola-K. maltaceti*), 1:1, 1:2, 1:4 and 1:8 inoculum ratio of *Komagataeibacter* species were inoculated in propolis including HS broth, separately. Incubation was performed at 30˚ C for 7 days in a static incubator (MCI 120, Mipro, Ankara, Turkey).

2.2.3. Effect of cultivation volume/dimension and agitation on BC formation

Komagataeibacter species were inoculated in propolis including HS broth with a production volume of 2 mL, 10 mL and 20 mL (and vessel dimensions of 15mm, 45mm and 85mm, respectively). Incubation was performed at 30˚ C for 7 days in a static incubator (MCI 120, Mipro, Ankara, Turkey). Cultures also incubated in agitated condition at 150 rpm, 30˚ C for 7 days (MCI 120, Mipro, Ankara, Turkey). Obtained BC membranes were compared using BC yield and membrane form.

2.3. BC purification

Harvested BC membranes from the surface of the cultivation media were treated with 0.1 M NaOH

solution at 80 °C for 30 min and entrapped cells were removed by washing distilled water until reaching neutral pH. Purified membranes were dried at 30 °C and the dry weight of BC was calculated [14, 15].

2.4. Moisture content ratio (MCR) and Water holding capacity (WHC) of BC membranes

The weight of the wet and dried BC membranes was used to calculate the moisture content ratio (MCR) of the membranes as follows;

$$\text{MCR (\%)} = \frac{\text{Wwet}-\text{Wdry}}{\text{Wwet}} \text{ x } 100 \quad (\mathbf{2.1}) \qquad [27]$$

$$\text{WHC (g/g)} = \frac{\text{Wwet}-\text{W dry}}{\text{Wdry}} \qquad (\mathbf{2.2}) \qquad [14]$$

2.5. Characterization of BC membranes

Morphological and dimensional characteristics of purified BC membranes obtained from propolis including media were analyzed with FIB-SEM GAIA3, Tescan, operating at 3 kV with a magnification of 60 kx [15, 26]. Additionally, FT-IR spectra of BC membranes were collected on the Vertex FT-IR (Bruker, Germany) over the range of 4000 to 400 cm^{-1} with a resolution of 1 cm^{-1} and 20 scans in the region.

2.6. Statistical analysis

SPSS (The Statistical Package for the Social Sciences) 23 program (Chicago, IL, USA) was used to evaluate the obtained data. The mean, standard deviation and median are given, and the results of BC production with propolis supplementation were compared using the Kruskal-Wallis H test with a 5% significance level.

3. Results and Discussion

3.1. Propolis effect on BC production

Due to its nanofibrillar structure and the unique properties such as high water-holding capacity, mechanical strength, porosity, and ease of modification, BC has gained significant interest from researchers in recent years. For this reason, studies to improve its production and structural properties are actively continuing [28, 29]. The presence of free hydroxyl groups on the membrane surface allows BC to be modified with other polymers or additives [30]. Therefore, increasing the production efficiency of this valuable biopolymer and improving its existing mechanical properties is only possible by supplementing it with additives to the cultivation media or modifying it with various agents following the production process [8, 15].

Accordingly, current methods to improve the production yield of BC include the supplementation of additives to commercial media or the substitution of these media with low-cost substrates. In this study, the effect of propolis supplementation, which has rich nutritional content, at different concentrations (5-40%) to HS medium on BC production with *Komagataeibacte*r species was investigated. The optimal propolis concentrations for *K. intermedius*, *K. maltaceti*, and *K. nataicola* were determined to be 25%, 20%, and 30%, respectively, yielding 7.15 g/L BC (20.09 g/g WHC, 96.31% MCR) ($p=0.002$, Table S1a), 5.4 g/L BC (31.01 g/g WHC, 96.87% MCR) ($p=0.002$, Table S1b), and 4.15 g/L BC (21.67 g/g WHC, 95.59% MCR) ($p=0.002$, Table S1c). It was observed that the effect of the propolis concentration on BC yield varied depending on the species, and there was a decrease in BC production at concentrations above the optimal value (**Figures 1a, 1b and 1c**). Compared to the propolis-free medium (HS broth) used as a negative control, *K. intermedius*, *K. maltaceti*, and *K. nataicola* strains were found to cause an increase in production efficiency as 1.31-fold (5.47g/L), 2.09-fold (2.58g/L), and 1.43-fold (2.91), respectively (data not shown). Therefore, in addition to the use of the nutritional elements contained in HS, it was observed that the propolis content was also used as carbon and nitrogen sources and contributed to the production of BC up to a certain concentration. However, it was concluded that as the amount of propolis, which contains essential oils, resins, polyenes, and various organic and inorganic chemicals, as well as flavonoids and phenolics, increases in the medium, it also acts as an antimicrobial agent in the cultivation media [31-33]. Thus, Avcioglu 2024 [15] found that the total phenolics in the plant content contributed to BC production at optimal plant concentrations. Therefore, the inclusion of propolis content, in addition to the HS medium, contributes to BC production. Amorim et al. 2022, [5] was found that propolis supplementation to the production medium of *G. hansenii* prevented reproduction and suppressed BC production even in the medium containing 25% propolis [5]. However, the data obtained from this study show that the addition of propolis, which has a rich content, has a positive effect on BC production efficiency up to certain concentrations, and that increasing the amount of propolis reduces BC production as stated by Amorim et al. 2022 [5]. Propolis, which has antimicrobial properties, was interpreted as a decrease in BC production by inhibiting bacterial growth. Therefore, by taking advantage of the antimicrobial effect of propolis, red propolis is used for wound healing in diabetic patients with bacterial cellulose membrane [34], propolis included chitosan-based films used for food packaging [35].

In the literature, many additives other than propolis have been used in BC production and have been found to significantly contribute to BC yield. Accordingly, the use of carboxymethylcellulose (CMC) in the cultivation media increases BC production from 1.3 g/L to 8.2 g/L [21], and that gellan gum used as an additive in BC production increases the production efficiency by 47-59% [13]. In a different study, it was stated that the

addition of konjac glucomannan and xanthan gum increased the BC production efficiency resulting in 6.97 g/L and 6.52g/L, respectively [31]. The effect of ethanol and lactic acid on BC production by *Gluconacetobacter kombuchae* was determined that these supplements had an increasing effect on BC production efficiency compared to HS. Also, it was found that the use of 0.6% lactic acid caused as 4.89 g/L BC, and the use of 1% ethanol caused as 3.7 g/L BC production [22]. HS broth enriched with 1% polyethylene terephthalate ammonia hydrolysate (PETAH) caused a 215% increase in production efficiency in BC production with *Taonella mepensis*, a Gram-negative bacterium [23]. Accordingly, this study concluded that the use of propolis as an additive in BC production caused an increase in BC production efficiency, but increased concentrations caused a decrease in BC efficiency as it suppressed its nutritional quality and made its antimicrobial properties dominant.

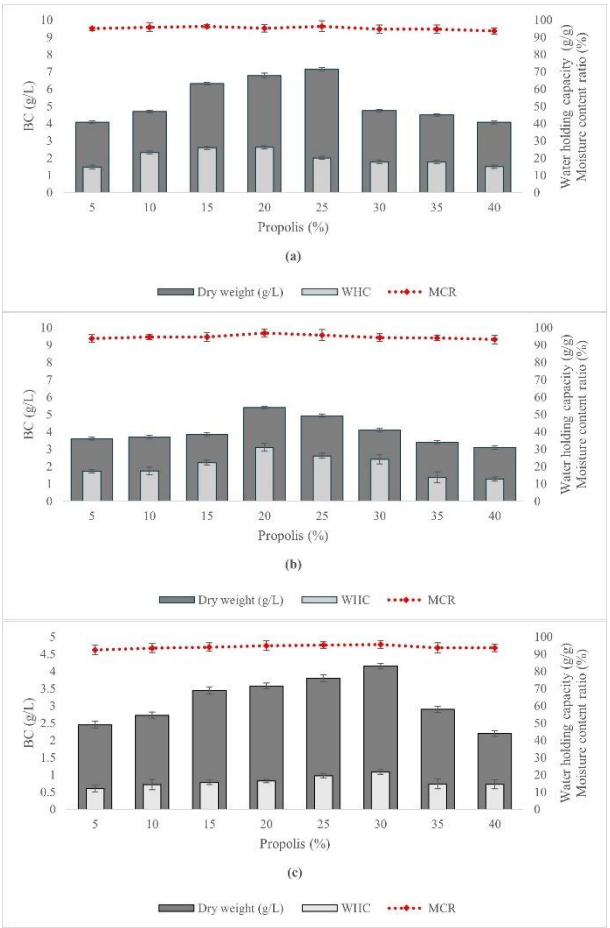

Figure 1. Effect of propolis supplementation on BC production with (a) *K. intermedius*, (b) *K. maltaceti*, (c) *K. nataicola.*

3.2. Effect of incubation period on BC production

BC formation increases with the growth of bacteria inoculated into the fermentation medium and the increase in C-H bonds between the BC fibrils formed. However, as pellicle formation slows down and all bacteria in the culture medium are trapped in the formed pellicle, BC synthesis reaches the production threshold [36]. Additionally, where time-dependent production continues and nutrients are not added regularly to the medium, it is inevitable that reproduction and biopolymer synthesis will stop because of the consumption of nutrients by the growing microorganisms. In this study, it was determined that pellicle formation in all three *Komagataeibacter* species started from the 3rd day and there was a decrease in the pH of the culture liquid due to bacterial growth resulting as formation of acidic products (**Figure 2a, 2b and 2c**). It is known that the rapid decrease in pH is mainly due to the presence of organic acids, especially gluconic acid, formed in the culture medium with the growth of acetic acid bacteria [37]. This is a result of the glucose contained in the medium being rapidly used by bacteria in the reproductive stage, causing gluconic acid accumulation [38]. In this study, as a result of bacterial growth, the culture pH of *K. intermedius*, *K. maltaceti* and *K. nataicola* decreased from 6.0 to 2.93 (p=0.003, Table S2a), 3.11 (p=0.003, Table S2b) to 3.36 (p= 0.004, Table S2c), respectively. In addition, the pH of the culture media, bacterial growth and the amount of BC production during the BC production process varied species-specifically (**Figure 2**).

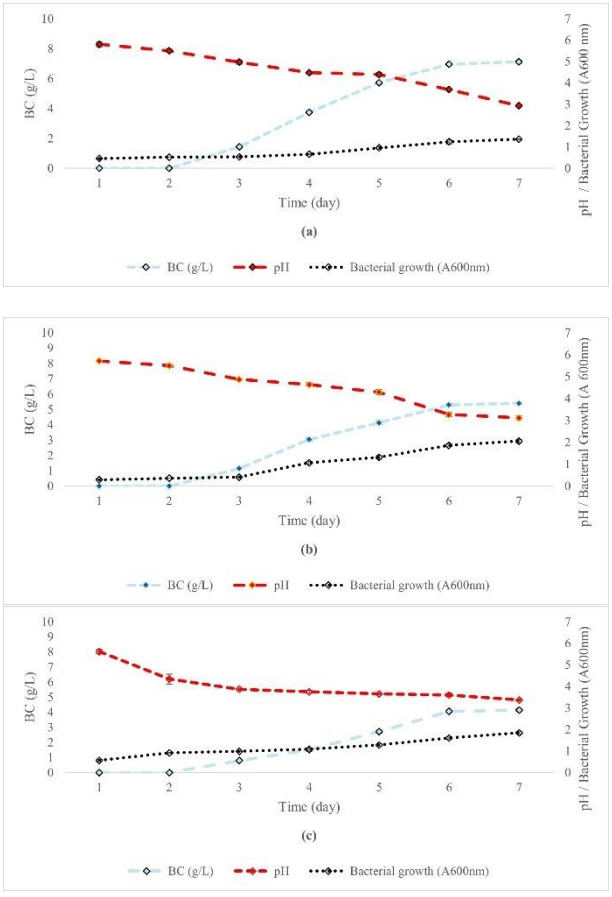

Figure 2. The change in the bacterial growth, pH and BC production during incubation period of **(a)** *K. intermedius*, **(b)** *K. maltaceti*, **(c)** *K. nataicola*.

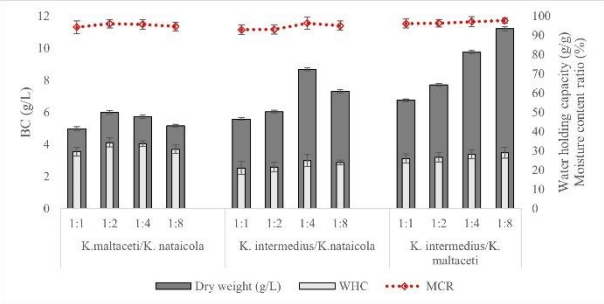

Figure 3. Effect of co-cultivation of *Komagataeibacter* species on BC production

3.3. BC production with *Komagataeibacter* consortia

Studies have shown that the co-cultivation of microorganisms causes an increase in biopolymer production and supports the development of the physicochemical properties of the resulting biopolymers [11, 19, 20]. In the literature, the co-culture of acetic acid and lactic acid bacteria causes the formation of BC-Hyaluronic Acid composites that can be used in biomedical and cosmetic fields [20]. In a different study, nisin-containing BC production was determined by *Enterobacter* sp. FY-07 and *Lactococcus lactis* N8 bacteria resulted in the synthesis of BC film with antimicrobial properties [19] and BC production was carried out using a co-culture of *Saccharomyces cerevisiae* yeast and *Komagataeibacter rhaeticus* bacteria [11]. Also, BC production efficiency increased from 2.64 to 5.99 g/L with the co-culture of *Komagataeibacter sucrofermentans* and *Leuconostoc mesenteroides* [25]. Accordingly, it was found that 5.99 g/L BC was produced (34.25 g/g WHC, 95.98% MCR) with 1:2 co-culture of *K. maltaceti-K. nataicola* (p=0.019, Table S3a), 8.67 g/L BC was obtained (24.92 g/g WHC, 96.27% MCR) (p=0.016, Table S3b) with 1:4 co-culture of *K. intermedius-K. nataicola*, and 11.20 g/L BC was produced (28.19 g/g WHC, 96.27% MCR) (p=0.016, Table S3c) with 1:8 co-culture of *K. intermedius-K. maltaceti* in this study (**Figure 3**). Additionally, *K. intermedius-K. maltaceti* consortium, which achieved the highest yield, increased production by 1.57-fold compared to *K. intermedius* and 2.07-fold compared to *K. maltaceti* monocultures. Therefore, the contribution of co-cultivation to biopolymer yield was supported across all consortia investigated in this research.

3.4. Effect of cultivation volume/dimension and agitation on BC formation

BC is a unique biopolymer that takes the shape of the fermentation vessel where it occurs, thus allowing it to be obtained in the desired size and shape [30,39]. When the effect of changing production volume and container diameter on production efficiency was examined, it was found that increasing the production volume of *K. intermedius* by 5-fold resulted in a 1.24-fold increase in BC yield (8.86 g/L), and a 10-fold increase in production volume (20 mL with a vessel dimension of 85 mm) led to a 1.30-fold increase in production efficiency (9.73 g/L) (p=0.016, Table S4a). Similarly, a 5-fold increase in volume resulted in a 1.08-fold increase in BC yield (5.86 g/L), and a 10-fold increase in volume led to a 1.27-fold increase in production efficiency (6.82 g/L) (p=0.022, Table S4b) with *K. maltaceti*. The respective increases were 1.38-fold (5.72 g/L) and 1.59-fold (6.57 g/L) with a 5-fold and 10-fold increase in volume (p=0.016, Table S4c) with *K. nataicola* (**Figures 4a, 4b, 4c and Figure 5**). Therefore, it was found that production volume had an inducing effect on BC production efficiency, depending on the increase in the amount of nutrients in the culture media. Similarly, it has been found in the literature that the increase in fermentation volume increases the formation of BC pellicle and thus BC production efficiency, as it provides high amounts of nutrients for bacterial growth [39].

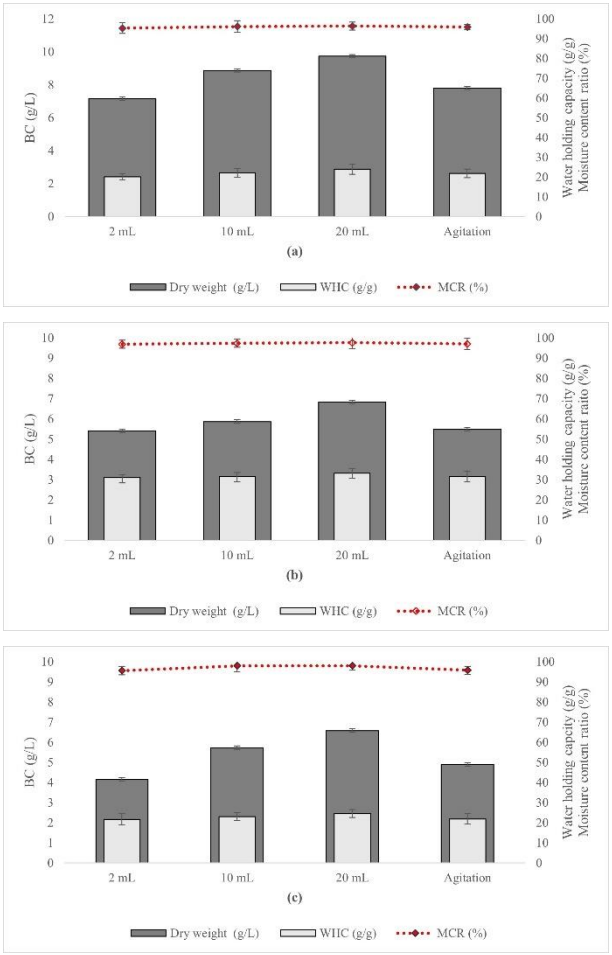

Figure 4. Effect of cultivation volume/dimension and agitation on BC production with (a) *K. intermedius*, (b) *K. maltaceti* and (c) *K. nataicola*.

Static cultivation requires a long cultivation time and extensive steps for BC production, resulting in a

gelatinous BC pellicle on the air surface of the culture medium [40]. However, it is seen that BC formation with agitation occurs in a short time and is widely used in commercial fermentative production [41]. While a layer-shaped BC membrane is obtained with static cultivation, irregular pellets, irregular masses or fibrous granules are formed in agitated conditions [41-43]. In this study, agitated production caused an increase in BC production of 1.08-fold (p=0.016, Table S4a), 1.01-fold (p=0.022, Table S4b) and 1.18-fold (p=0.016, Table S4c) compared to the static production of *K. intermedius*, *K. maltaceti* and *K. nataicola*, respectively. However, similar to the literature, it was observed that BC produced as a membrane under static production lost its layer form under agitated conditions and irregular BC formation was observed. Although it is very important to obtain products in a short time in biotechnological production processes, the importance of static culture is obvious since the materials whose surface properties need to be used are biopolymers produced in membrane form and are more suitable for modification for industrial use.

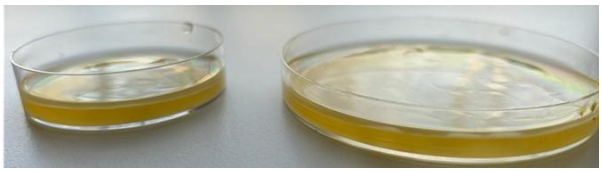

Figure 5. Images of BC membranes produced in different cultivation volumes/dimensions.

3.6. Characterization of BC membranes
3.6.1. FIB-SEM

When FIB-SEM images of obtained BCs were examined, it was determined that BC membranes exhibited 3-D, porous and nanofibrillar structure similar to the literature [14, 15, 26]. *K. intermedius*, *K. maltaceti* and *K. nataicola* species show fibrillar structure with widths of 51-59 nm, 49-85 nm and 70-87 nm, and lengths of 1502-2668 nm, 1180-1356 nm and 435-2085 nm, respectively (**Figure 6**).

BC membranes are known to have a water-holding capacity (WHC) of approximately 100 times their own weight [24]. It was found that *K. maltaceti* exhibited the highest WHC and Moisture Content Retention (MCR) values, ranging from 96.87% to 97.63% and 30.01 g/g to 33.22 g/g, respectively. This high capacity was correlated with its fibril size, which measured around 45 nm (**Figure 4 and Figure 6**). Therefore, in this study where propolis was used as an additive, it was observed that BCs with high WHC and MCR ratios were obtained.

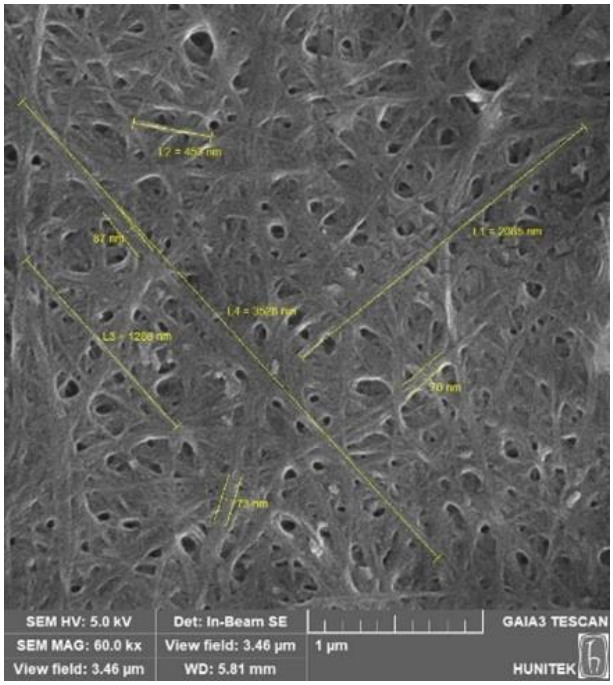

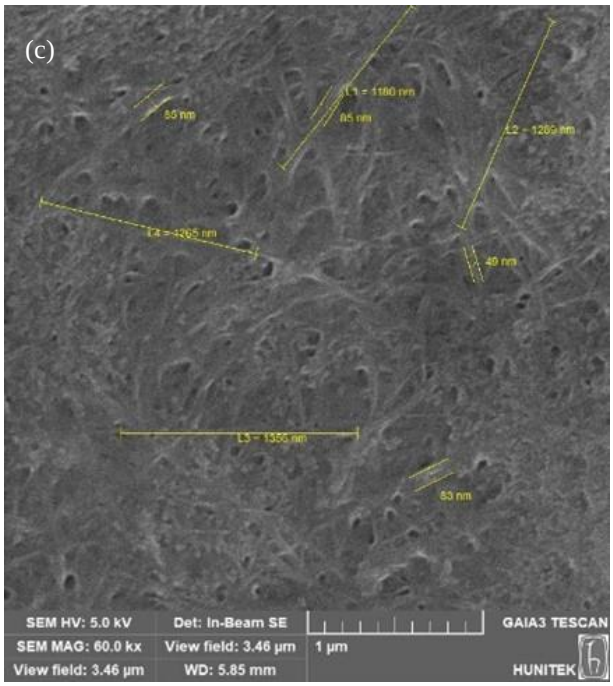

Celal Bayar University Journal of Science
Volume 20, Issue 3, 2024, p 10-18
Doi: 10.18466/cbayarfbe.1490668

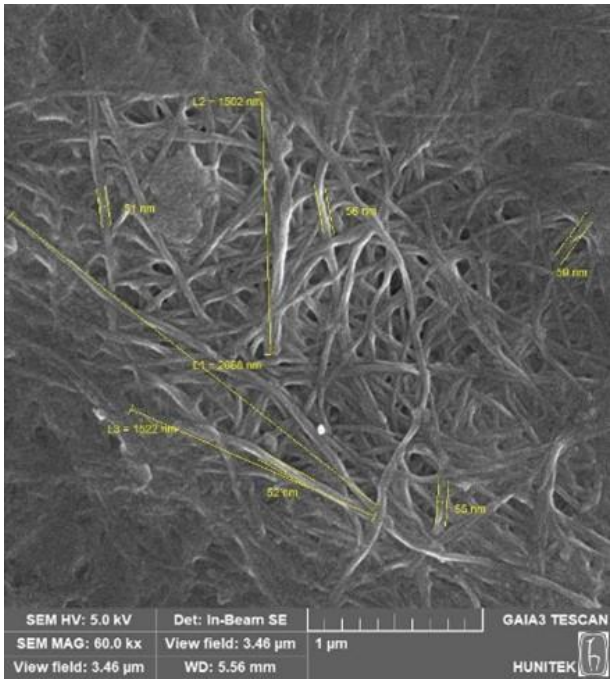

Figure 6. FIB-SEM image of BC fibrils obtained from **(a)** *K. intermedius*, **(b)** *K. maltaceti* and **(c)** *K. nataicola*.

3.6.2. FTIR analyzes

As a result of FTIR obtained from *K. intermedius*, *K. maltaceti* and *K. nataicola* species, it was determined that the membranes of each species showed characteristic vibration peaks. Accordingly, 3000-3600 cm^{-1} shows the hydrogen-bonding region and mainly corresponds to -OH stretching vibration, 2800-3000 cm^{-1} refers to C-H stretching vibration, the bands at ~1600 cm^{-1} corresponds to O-H bonds in adsorbed H_2O molecules, the bands at ~1300-1400 cm^{-1} refers to C-H and CH_2 bending and 900 ~1200 cm^{-1} refers to the stretching vibrations of carbohydrate molecules mainly corresponds to C–O–C, C–OH, C–H stretching vibration [15, 28, 44-46] (**Figure 7**).

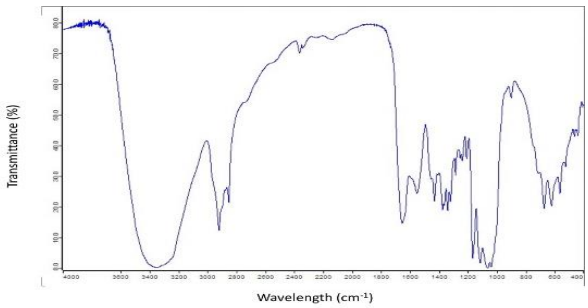

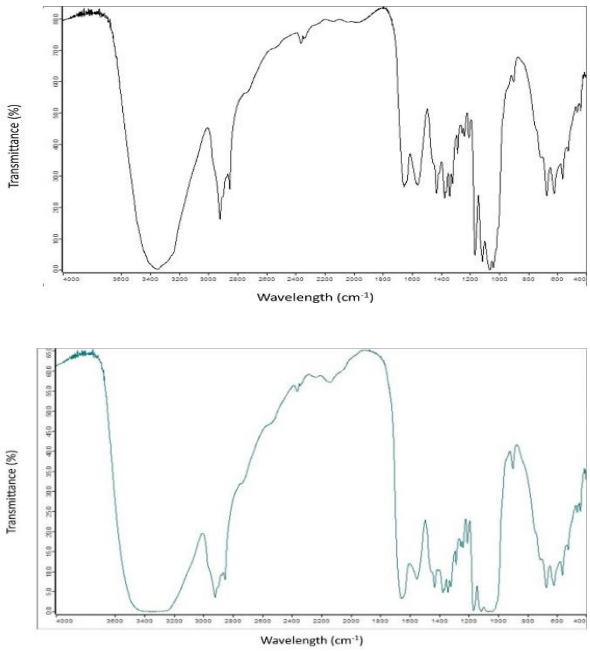

Figure 7. FTIR spectroscopy of **(a)** *K. intermedius*, **(b)** *K. maltaceti* and **(c)** *K. nataicola*.

4. Conclusion

The data obtained from this study indicate that propolis, at optimally determined concentrations for each *Komagataeibacter* species, contributed to BC production. However, higher concentrations of propolis inhibited BC production due to its antimicrobial properties. Additionally, bacterial consortia were found to enhance biopolymer production compared to the monocultures of the individual bacterial species and *K. intermedius* - *K. maltaceti* consortia is the most effective one. The increase in the volume of the production vessel was observed to enhance BC production due to the corresponding increase in nutritional content and surface area. Under static conditions, cellulose production was observed in membrane form, whereas under agitated conditions, irregularly shaped cellulose was formed. BC produced in HS broth containing propolis was found to have a high water-holding capacity (WHC) and moisture content ratio (MCR). The produced BC membranes were observed to have a three-dimensional nanofibrillar structure. As a result, it was concluded that the addition of propolis contributes to an increase in BC production efficiency.

Author's Contributions

Nermin Hande AVCIOGLU: Drafted and wrote the manuscript, performed the experiment and result analysis.

Ethics

There are no ethical issues after the publication of this manuscript.

References

[1]. Katiyar, D. 2023. Propolis: A natural biomaterial. *Materials Today: Proceedings* (In press).

[2]. Eslami, M, Zaretabar, A, Dawood, MA, Mohammadzadeh, S, Shahali, Y, Ahmadifar, E, Sheikhzadeh, N, Moghadam, MS, Hoseinifar, SH, Van Doan, H. 2022. Can dietary ethanolic extract of propolis alter growth performance, digestive enzyme activity, antioxidant, and immune indices in juvenile beluga sturgeon (Huso huso)?. *Aquaculture*; 552: 737939.

[3]. Sharaf, SM, Al-Mofty, SED, El-Sayed, ESM, Omar, A, Dena, ASA, El-Sherbiny, IM. 2021. Deacetylated cellulose acetate nanofibrous dressing loaded with chitosan/propolis nanoparticles for the effective treatment of burn wounds. *International Journal of Biological Macromolecules*; 193: 2029-2037.

[4]. Farag, MR, Abdelnour, SA, Patra, AK, Dhama, K, Dawood, MA, Elnesr, SS, Alagawany, M. 2021. Propolis: Properties and composition, health benefits and applications in fish nutrition. *Fish & Shellfish Immunology*; 115: 179-188.

[5]. Amorim, JD, Nascimento, HA, Silva Junior, CJG, Medeiros, AD, Silva, IDL, Costa, AFS, Vnhas, GM, Sarubbo, LA. 2022. Obtainment of bacterial cellulose with added propolis extract for cosmetic applications. *Polymer Engineering & Science*; 62 (2): 565-575.

[6]. Ceylan, O, Karakus, H, Cicek, H. 2021. Design and in vitro antibiofilm activity of propolis diffusion-controlled biopolymers. *Biotechnology and Applied Biochemistry*; 68 (4): 789-800.

[7]. Salama, A, El-Sakhawy, M. 2024. Polysaccharides/propolis composite as promising materials with biomedical and packaging applications: A review. *Biomass Conversion and Biorefinery*; 14 (4): 4555-4565.

[8]. Blanco Parte, FG, Santoso, SP, Chou, CC, Verma, V, Wang, HT, Ismadji, S, Cheng, KC 2020. Current progress on the production, modification, and applications of bacterial cellulose. *Critical reviews in biotechnology*; 40 (3): 397-414.

[9]. Lin, SP, Singajaya, S, Lo, TY, Santoso, SP, Hsu, HY, Cheng, KC 2023. Evaluation of porous bacterial cellulose produced from foam templating with different additives and its application in 3D cell culture. *International Journal of Biological Macromolecules*; 234: 123680.

[10]. Hu, H, Catchmark, JM, Demirci, A. 2022. Effects of pullulan additive and co-culture of *Aureobasidium pullulans* on bacterial cellulose produced by *Komagataeibacter hansenii*. *Bioprocess and biosystems engineering*; 45 (3): 573-587.

[11]. Gilbert, C, Tang, TC, Ott, W, Dorr, BA, Shaw, WM, Sun, GL, Lu, TK, Ellis, T. 2021. Living materials with programmable functionalities grown from engineered microbial co-cultures. *Nature materials*; 20 (5): 691-700.

[12]. Nascimento, HA, Amorim, JD, M. Filho, LED, Costa, AFS, Sarubbo, LA, Napoleão, DC, Maria Vinhas, G. 2022. Production of bacterial cellulose with antioxidant additive from grape residue with promising cosmetic applications. *Polymer Engineering & Science*; 62 (9): 2826-2839.

[13]. Wu Y, Huang, TY, Li, ZX, Huang, ZY, Lu, YQ, Gao, J, Hu, Y, Huang, C. 2021. In-situ fermentation with gellan gum adding to produce bacterial cellulose from traditional Chinese medicinal herb residues hydrolysate. *Carbohydrate Polymers*; 270: 118350.

[14]. Avcioglu, NH, Birben, M, Bilkay, IS. 2021. Optimization and physicochemical characterization of enhanced microbial cellulose production with a new Kombucha consortium. *Process Biochemistry*; 108: 60-68.

[15]. Avcioglu, NH. 2024. Eco-friendly Production of Bacterial Cellulose with *Komagataeibacter intermedius* Strain by Using *Jasminum sambac* and *Camellia sinensis* Plants. *Journal of Polymers and the Environment*; 32 (1): 460-477.

[16]. Szymańska, M, Hoppe, J, Dutkiewicz, M, Sobolewski, P, Palacz, M, Janus, E, Zielińska, B, Drozd, R. 2022. Silicone polyether surfactant enhances bacterial cellulose synthesis and water holding capacity. *International Journal of Biological Macromolecules*; 208: 642-653.

[17]. Campano, C, Balea, A, Blanco, A, Negro, C. 2016. Enhancement of the fermentation process and properties of bacterial cellulose: a review. *Cellulose*; 23: 57-91.

[18]. Andriani, D, Apriyana, AY, Karina, M.2020). The optimization of bacterial cellulose production and its applications: a review. *Cellulose*; 27 (12): 6747-6766.

[19]. Gao, G, Fan, H, Zhang, Y, Cao, Y, Li, T, Qiao, W, Wu, M, Ma, T, Li, G. 2021. Production of nisin-containing bacterial cellulose nanomaterials with antimicrobial properties through co-culturing *Enterobacter* sp. FY-07 and *Lactococcus lactis* N8. *Carbohydrate Polymers*; 251: 117131.

[20]. Brugnoli, M, Mazzini, I, La China, S, De Vero, L, Gullo, M. 2023. A Microbial Co-Culturing System for Producing Cellulose-Hyaluronic Acid Composites. *Microorganisms*; 11 (6): 1504.

[21]. Cheng, KC, Catchmark, JM, Demirci, A. 2009. Enhanced production of bacterial cellulose by using a biofilm reactor and its material property analysis. *Journal of biological engineering*; 3: 1-10.

[22]. Sharma, P, Sharma, R, Ahuja, S, Yadav, A, Arora, S, Aggarwal, NK. 2023. Enhancement of bacterial cellulose production by ethanol and lactic acid by using *Gluconacetobacter kombuchae*. *Preparative Biochemistry & Biotechnology*; 1-9.

[23]. Zhou, J, Sun, J, Ullah, M, Wang, Q, Zhang, Y, Cao, G, Chen, L, Ullah, MW, Sun, S. 2023. Polyethylene terephthalate hydrolysate increased bacterial cellulose production. *Carbohydrate Polymers*; 300: 120301.

[24]. Brown, JL, Perisin, MA, Swift, CL, Benyamin, M, Liu, S, Singan, V, Zhang, Y, Savage, E, Pennacchioc, C, Grigoriev, IV, O'Malley, MA. 2022. Co-cultivation of anaerobic fungi with *Clostridium acetobutylicum* bolsters butyrate and butanol production from cellulose and lignocellulose. *Journal of Industrial Microbiology and Biotechnology*; 49 (6): kuac024.

[25]. Nazarova, NB, Liyaskina, EV, Revin, VV. 2023. Production of Bacterial Cellulose by Cocultivation of *Komagataeibacter sucrofermentans* with Producers of Dextran *Leuconostoc mesenteroides* and Xanthan Xanthomonas campestris. *Biochemistry (Moscow), Supplement Series B: Biomedical Chemistry*; 17 (2): 101-109.

[26]. Avcioglu, NH, Sevim, C, Alver, E., Donmez, Seyis Bilkay, I. 2021. Comparison of bacterial cellulose production by *Komagataeibacter intermedius* strain using *Lavandula angustifolia*, *Rosa canina* and *Tilia cordata* plants as low-cost media. *Cellulose Chemistry and Technology*; 55 (9-10): 1029-1041.

[27]. Szymańska, M, Hoppe, J, Dutkiewicz, M, Sobolewski, P, Palacz, M, Janus, E, Zielińska, B, Drozd, R. 2022. Silicone polyether surfactant enhances bacterial cellulose synthesis and water holding

capacity, International Journal of Biological Macromolecules; 208: 642-653.

[28]. Gorgieva, S, Trček, J. 2019. Bacterial cellulose: Production, modification and perspectives in biomedical applications. *Nanomaterials*; 9 (10): 1352.

[29]. Moniri, M, Boroumand Moghaddam, A, Azizi, S, Abdul Rahim, R, Bin Ariff, A, Zuhainis Saad, W, Navaderi, M, Mohamad, R. 2017. Production and status of bacterial cellulose in biomedical engineering. *Nanomaterials*; 7 (9): 257.

[30]. Urbina, L, Corcuera, MÁ, Gabilondo, N, Eceiza, A, Retegi, A. 2021. A review of bacterial cellulose: sustainable production from agricultural waste and applications in various fields. *Cellulose*; 28 (13): 8229-8253.

[31]. Nguyen, QD, Nguyen, NN. 2022. Effects of different hydrocolloids on the production of bacterial cellulose by *Acetobacter xylinum* using Hestrin–Schramm medium under anaerobic condition. *Bioresource Technology Reports*; 17: 100878.

[32]. Sapie, SR, Kamari, A, Jumadi, J. (2023, March). A brief review of propolis as an additive in biopolymer matrix films for food packaging. In *AIP Conference Proceedings* (Vol. 2556, No. 1). AIP Publishing.

[33]. Boisard, S, Le Ray, AM, Gatto, J, Aumond, MC, Blanchard, P, Derbre, S, Flurin, C, Richomme, P. 2014. Chemical Composition, Antioxidant and Anti-AGEs Activities of a French Poplar Type Propolis. *J Agric Food Chem*; 62:1344−1351.

[34]. Picolotto, A, Pergher, D, Pereira, GP, Machado, KG, da Silva Barud, H, Roesch-Ely, M, Gonzalez, MH, Tasso, L, Figueiredo, JG, Moura, S. 2019. Bacterial cellulose membrane associated with red propolis as phytomodulator: Improved healing effects in experimental models of diabetes mellitus. *Biomedicine & Pharmacotherapy*; 112: 108640.

[35]. De Carli, C, Aylanc, V, Mouffok, KM, Santamaria-Echart, A, Barreiro, F, Tomás, A, Pereira, C, Rodrigues, P, Vilas-Boas, M, Falcão, SI. 2022. Production of chitosan-based biodegradable active films using bio-waste enriched with polyphenol propolis extract envisaging food packaging applications. *International Journal of Biological Macromolecules*; 213: 486-497.

[36]. Lahiri, D, Nag, M, Dutta, B, Dey, A, Sarkar, T, Pati, S, Edinur, HA, Kari, ZA, Noor, NHM, Ray, RR. 2021. Bacterial cellulose: Production, characterization, and application as antimicrobial agent. *International journal of molecular sciences*; 22 (23): 12984.

[37]. Singhania, RR, Patel, AK, Tseng, YS, Kumar, V, Chen, CW, Haldar, D, Saini, JK, Dong, CD. 2022. Developments in bioprocess for bacterial cellulose production. *Bioresource Technology*; 344: 126343.

[38]. Abdelraof M, El Saied H, Hasanin MS. 2022. Green Immobilization of *Glucanobacter xylinum* onto natural polymers to sustainable bacterial cellulose production. *Waste Biomass Valor*; 13 (4): 2053–69.

[39]. Azmi, SNNS, Fabli, SNNFM, Aris, FAF, Samsu, ZA, Asnawi, ASFM, Yusof, YM, Ariffin, H, Abdullah, SSS. 2021. Fresh oil palm frond juice as a novel and alternative fermentation medium for bacterial cellulose production. *Materials Today: Proceed*; 42: 101-106.

[40]. Hsieh, JT, Wang, MJ, Lai, JT, Liu, HS. 2016. A novel static cultivation of bacterial cellulose production by intermittent feeding strategy. *Journal of the Taiwan Institute of Chemical Engineers*; 63: 46–51.

[41]. Fernandes, IDAA, Pedro, AC, Ribeiro, VR, Bortolini, DG, Ozaki, MSC, Maciel, GM, Haminiuk, CWI. 2020. Bacterial cellulose: From production optimization to new applications. *International Journal of Biological Macromolecules*; 164: 2598-2611.

[42]. Sperotto, G, Stasiak, LG, Godoi, JPMG, Gabiatti, NC, De Souza, SS. 2021. A review of culture media for bacterial cellulose production: complex, chemically defined and minimal media modulations. *Cellulose*; 28: 2649-2673.

[43]. Andriani, D, Apriyana, AY, Karina, M. 2020. The optimization of bacterial cellulose production and its applications: a review. *Cellulose*; 27 (12): 6747-6766.

[44]. Jiang, H, Song, Z, Hao, Y, Hu, X, Lin, X, Liu, S, Li, C. 2023. Effect of co-culture of *Komagataeibacter nataicola* and selected *Lactobacillus fermentum* on the production and characterization of bacterial cellulose. *LWT*; 173: 114224.

[45]. Li, W, Huang, X, Liu, H, Lian, H, Xu, B, Zhang, W, Sun, X, Wang, W, Jia, S, Zhong, C. 2023. Improvement in bacterial cellulose production by co-culturing *Bacillus cereus* and *Komagataeibacter xylinus*. *Carbohydrate Polymers*; 313: 120892.

[46]. Tapias, YAR, Di Monte, MV, Peltzer, MA, Salvay, AG. 2022. Bacterial cellulose films production by Kombucha symbiotic community cultured on different herbal infusions. *Food Chemistry*; 372: 131346.

Celal Bayar University Journal of Science

Investigation of Thickness Effect on Structural and Magnetic Properties of Ni Thin Films for Some Applications

Perihan AKSU[1,2]*

[1] Institute of Nanotechnology, Gebze Technical University, Gebze, 41400 Kocaeli, Türkiye.
[2]Nanotechnology Application and Research Center, Gebze Technical University, Gebze, 41400 Kocaeli, Türkiye.

* paksu@gtu.edu.tr
* Orcid No: 0000-0002-4175-9190

Received: 22 May 2024
Accepted: 14 August 2024
DOI: 10.18466/cbayarfbe.1488101

Abstract

In this study, it was investigated the effect on the structural, and magnetic properties dependent on the thickness of the Nickel films grown on MgO (100) substrates by the molecular beam epitaxy at a high vacuum. The structural and magnetic properties were examined by using X-ray diffraction and ferromagnetic resonance techniques. The X-ray diffraction and X-ray reflectivity measurements showed that Ni films grew in (200) orientation with tiny surface roughness. Experimental ferromagnetic resonance data showed that all samples had in-plane easy axis from out-of-plane measurements and fourfold anisotropy from in-plane measurements. Additionally, conditions under which Ni/MgO (100) films grew epitaxially were also observed. In this study, where the minimum thickness required for some applications to exhibit both magnetic properties and form the crystal structure of Ni thin films is determined, the importance of film thickness in terms of applications is emphasized and the minimum thickness condition is determined in terms of some applications.

Keywords: Ferromagnetic Resonance, Magnetic Anisotropy, Ni Thin Films, Spintronics, Thin Film Applications.

1. Introduction

Recently, significant developments in mechanical, biomedical, and spintronic technologies have attracted attention [1–5]. Studies in this field have gained great importance, and this situation has increased the need for new technologies and materials for use in various biomedical applications. Nickel (Ni) thin films, which have an important place among these materials because of their wide range of uses in various technological and scientific applications, attract the attention of researchers due to their properties such as electrical and magnetic properties, corrosion resistance, chemical stability, and mechanical durability.

Ni-based thin films are widely used in microelectromechanical systems (MEMS) due to their high hardness and good mechanical strength properties [6]. Such films are frequently used to coat moving parts in MEMS devices and the production of micro-scale actuators. They are also ideal materials for applications requiring friction and corrosion control due to their high corrosion resistance and surface hardness [7].

On the other hand, Ni-based thin films are also indispensable materials for spintronic applications, which are a field that aims to develop information processing and storage technologies using the spin property of electrons [8- 10]. In studies of this field, it is seen that Ni-based thin films are frequently used as key materials in spintronic devices such as magnetic tunnel junctions (MTJs) and spin valves [11]. These films are also quite useful in optimizing the performance of spintronic devices due to their magnetic anisotropy and low magnetic damping properties [12,13]. In addition, Ni is a magnetic material with a high Curie temperature (T_C) and is preferred in spintronic device development because this feature allows the devices to operate in a wide temperature range [14].

Furthermore, thin films have a wide range of biomedical applications such as biomedical devices, surgical instruments, sensors (such as glucose sensors), magnetic

resonance imaging (MRI), biocompatible coatings, human implants, and drug delivery systems [15–19]. On the other hand, it is important also to examine the behavior of these materials in biological environments since the possible interaction of Ni thin films with biological systems may cause a potential negative effect on health, such as Ni allergies and toxicity [20]. In addition, it can be accepted that the structure and thickness of the films are the determining parameters in the interaction of Ni thin films with biological systems.

In this context, Ni thin films of different thicknesses were prepared in the current study. It was aimed to investigate the magnetic and structural properties of Ni thin films of different thicknesses to increase their potential in some application fields such as magnetic storage devices, sensors, MEMS, biomedical devices, etc., and to create a background for these studies.

2. Materials and Methods

The Ni thin films were grown on magnesium oxide [MgO-(100)] substrates. The molecular beam epitaxy (MBE) thin film growth system was used and its base pressure was 7×10^{-10} mbar. Before growth, all MgO substrates were cleaned in acetone, methanol, and isopropanol using an ultrasonicator for 15 minutes. Additionally, all substrates were kept under thermal treatment for 1 hour at 475°C to remove the rest chemicals on the surface of the substrates and cooled down to room temperature (RT). The films were fabricated in different thicknesses (5.0 nm, 15 nm, and 30 nm) at a 2.022 nm/min deposition rate. After the growth procession, all Ni thin films were cooled down to the RT.

While the crystal structure and film thickness of the Ni thin films were examined by X-ray diffractometry (XRD), the magnetic properties were investigated by using an X-band JEOL series electron spin resonance (ESR) spectrometer with a microwave frequency of 9.8 GHz (JESFA 300) at the RT. The ferromagnetic resonance (FMR) measurements were carried out in both out-of-plane geometry (OPG) and in-plane geometry (IPG). During the measurement, the sample was rotated in the magnetic field, which was scanned between 0-2 Tesla.

The FMR technique is a very successful method used to analyze magnetic thin films' anisotropic behaviors [25]. This method can provide high precision, such as magnetic anisotropy and the size of magnetism [25–27]. This technique is based on magnetic resonance and is used to investigate the magnetic properties of samples that have one or more unpaired electrons. That is, the interaction of the magnetic moments of the electrons within the atom is examined. The magnetic moments behave like magnets when samples with unpaired electrons are placed in an external magnetic field. The spin values of unpaired electrons are split according to the allowed energy levels in this external field, and the Larmor frequency is directly proportional to the difference between these energy levels. Then, a microwave frequency is applied perpendicular to the field, and resonance occurs when this frequency is equal to the difference between the energy levels. While the frequency at which the resonance emerges corresponds to the resonance frequency, the magnetic field at which the resonance emerges corresponds to the resonance field. FMR experiments are performed using the ESR spectrometer. It is possible to determine the easy axis of magnetization since these experiments provide the opportunity to carry out a magnetic field to the sample at different angles. During the measurement, the interaction of the magnetic moments of the electrons in the sample is examined by using a microwave source in the wavelength range of 300 MHz-300 GHz.

3. Results and Discussion

Structural analysis of Ni/MgO (100) thin films was examined by XRD and X-ray reflectivity (XRR) measurements at the RT. Figure 1(a-c) shows the XRR oscillations of each sample and the simulation results obtained from the GlobalFit program used to analyze the XRR data [28]. The XRR fitting was made using the bulk density values of Ni while using the GlobalFit program. Perfect compatibility of the obtained fitting lines (red line) with experimental data (black empty circles) is important for the reliability of the results. The fact that the surface roughness obtained as a result of the fitting is below 1 nm is an important indicator of the growth of high-quality films (Table 1). Figure 1(d-f) shows the XRD patterns of all Ni/MgO (100) films. It is observed that only the thickest sample exhibits a distinct Ni (200) film peak [29]. Especially the fact that the thickest sample gives a distinct Ni (200) peak is an important indicator that the film thickness is effective in the formation of the crystal structure. Normally, Ni thin films are expected to oxidize when they come into contact with air from the moment they are removed from the system after preparation, and this oxide structure is detected by the oxide peak obtained in XRD measurements. However, no oxide peaks were found in the XRD patterns since XRD measurements were made immediately after the Ni film was prepared. Oxidation will continue as a slow and natural process once Ni is exposed to air, and it is known that this oxide layer that may form does not exceed 10 Å.

Table 1. The properties of Ni thin films.

Sample Name	Ni Thickness (nm)	Roughness (nm)
S1	5.0	0.420
S2	15	0.460
S3	30	0.152

The FMR measurements were performed at RT to examine the magnetic properties of Ni thin films, (Figure 2). The measurements were made at both the IPG (by applying a magnetic field parallel to the sample plane) and the OPG (by applying a magnetic field perpendicular to the sample plane) for each sample. During the measurement, the sample is placed in the cavity between two magnets and rotated in one direction at determined angles, and the resonance fields occurring at each angle are read. As a result of the measurement, the angular change of the resonance fields of the samples is obtained at both OPG (Figure 2(a-c) and IPG (Figure 2(d-f)). As a result of the FMR measurements, the easy and hard axis of magnetization of these magnetic thin films can be determined, as well as information about the type of magnetization is obtained. The easy axis is defined as the direction in which the magnetic moments of magnetic thin films are easily aligned in the direction of the magnetic field in the presence of a magnetic field [25]. It can be seen that the OPG is a hard axis and the easy axis is in the IPG for each sample looking at out-of-plane (OOP) measurements. Therefore, it can be said that Ni thin films have an in-plane (IP) easy axis for this sample structure. In the easy axis direction, interfacial tensions between the substrate and the film and crystal structure properties affecting magnetic anisotropy are the determining factors in the magnetic properties of thin films [25, 30-32].

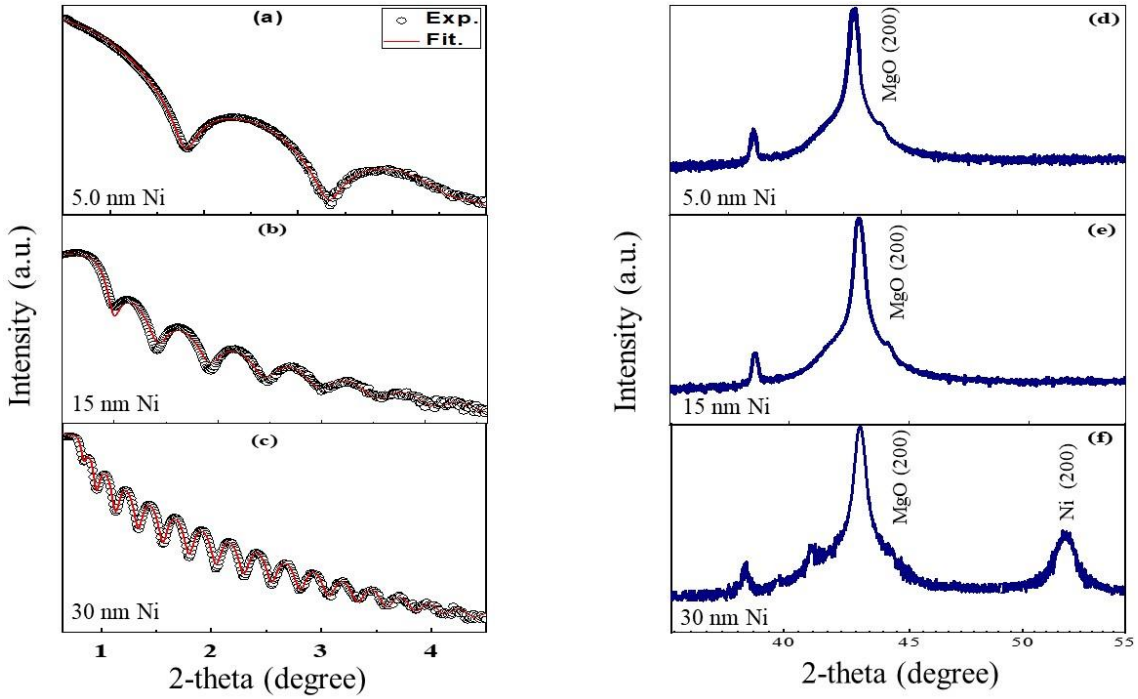

Figure 1. X-ray reflectivity (XRR) results of samples. The roughness of each film is 0.42 **(a)** for 5.0 nm Ni, 0.46 **(b)** for 15 nm Ni, and 0. 152 nm **(c)** for 30 nm Ni. The red line and the black empty circle represent fitting and experimental data, respectively. X-ray diffraction (XRD) measurement results of **(d)** 5.0 nm Ni, **(e)** 15 nm Ni, and **(f)** 30 nm Ni.

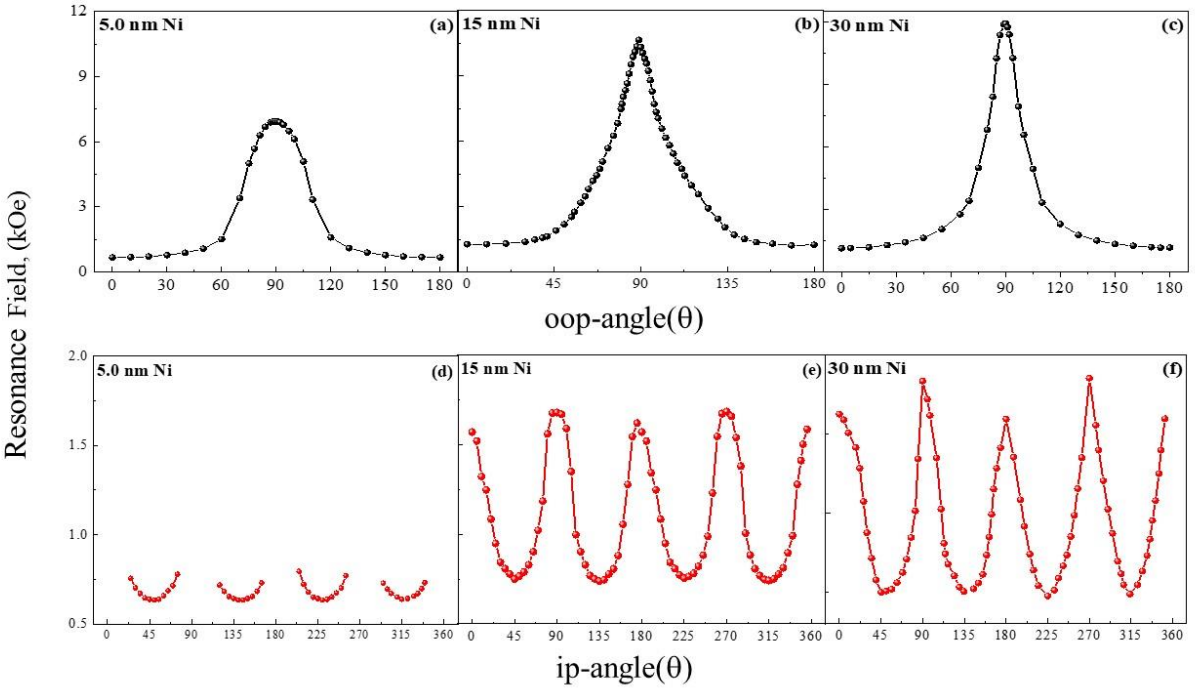

Figure 2. Ferromagnetic resonance fields of Ni thin films **(a)** for 5.0 nm Ni, **(b)** for 15 nm Ni, **(c)** for 30 nm Ni at the OPG. Ferromagnetic resonance fields of Ni thin films **(d)** for 5.0 nm Ni at the IPG, **(e)** for 15 nm Ni at the IPG, and **(f)** for 30 nm Ni at the IPG.

The measurements made in IPG are exhibited in Figure 2(d-f). The existence of fourfold anisotropy [33, 34] is seen for the S2 and S3 samples although the presence of a four-fold anisotropy is not evident for the thinnest Ni thin film. The substrates used in thin films are parameters that directly affect the physical properties of the films [35, 36]. The MgO substrates are among the substrates frequently used when preparing metallic thin films. The MgO (100) substrate used in this study has a cubic crystal structure. Ni has a face-centered cubic (fcc) crystal structure and is a suitable element to grow onto the surface of the MgO (100) substrate [37]. During the growth process, Ni atoms align in harmony with the crystal structure of the MgO substrate and enable the growth of an epitaxial film. Therefore, the MgO substrate, which has a certain crystallography, enables Ni films to grow in a certain crystallographic structure. The fourfold anisotropy observed from FMR measurements made in in-plane geometry in this study is a situation related to MgO substrate with four different growth orientations such as [100], [110], [111], and [001] [38]. As a result, the fact that Ni thin films have an IP easy axis according to OOP measurements and that they exhibit fourfold anisotropy according to IP measurements indicates that the samples grow in harmony with the crystallographic structure of the substrate and exhibit epitaxial growth [39, 40].

4. Conclusion

The effects of film thickness on Ni films' magnetic and structural properties have been investigated in this study. Ni thin films with different thicknesses have been deposited directly on the MgO (100) using the MBE system. The structural and magnetic properties have been examined using the XRD and the FMR techniques at RT. The cubic crystalline Ni films preferred growth orientation along the (200) plane and the roughness of each of the Ni films have been determined from the XRD and XRR measurements, respectively. Additionally, the easy axis direction and magnetic anisotropy behavior of Ni films have been identified from the IP and OOP-FMR measurements. As a result, it was observed that the crystal structure was formed more clearly for Ni films of over 15 nm, and higher quality epitaxial films were formed by following the crystal structure of the substrate.

Since the formation of the crystal structure after a certain thickness will provide high hardness and good mechanical strength properties, it will increase efficiency in MEMS applications. Because the thickness of the thin films prepared in spintronic applications has a significant effect on all properties, it is important in which thickness the thin film prepared exhibits both structural and magnetic properties. Otherwise, as the effects from that material will be lost in the presence of

interlayers or other elements if the thickness remains below this limit, it is important to determine the lower thickness limit. Because the growth of the Ni layer below this thickness will not make any contribution to the structure and will not be effective in any of its magnetic properties. Lastly, for biological applications, in applications where mechanical strength is required such as surgical instruments and human implants, the formation of the crystal structure is necessary and it has been shown that this structure is formed after a certain thickness. In addition, in biological sensor applications, starting from the minimum thickness where the magnetic behavior of Ni is evident will provide results. For all these reasons, the preparation and use of Ni films in thicknesses where both crystal and magnetic structures are formed together stably are essential for some applications. Therefore, in application fields such as mechanical, biomedical, and spintronic technologies, it would be more appropriate to use Ni film thicknesses of min above 15 nm in terms of both efficiency and physical properties. The background created by this result obtained in this study in terms of Ni film applications is important in terms of preventing waste of time and labor.

Acknowledgment

This work has not been supported by any funding. Device fabrication and measurements were done using Nanomagnetism and Spintronic Laboratory (NASAM) Facilities at the Institute of Nanotechnology, Gebze Technical University (GTU).

Author's Contributions

Perihan AKSU: Conceptualization, Methodology, Formal analysis and investigation, Validation, Writing-Reviewing and Editing, Writing- Original draft preparation.

Ethics

There are no ethical issues after the publication of this manuscript.

References

[1]. L. Lhotská and T. Welzer. 2015. Assistive technologies in biomedical engineering education. *World Congress on Medical Physics and Biomedical Engineering:* 1656-1659 (Springer International Publishing Toronto, Canada).

[2]. Y. Qiu, Z. Wu, J. Wang, C. Zhang, and H. Zhang, 2023. Introduction of materials genome technology and its applications in the field of biomedical materials. *Materials;* 16: 1906.

[3]. A. J. Kronemeijer, B. Peeters, G. de Haas, R. Verbeek, T. Bel, R. van de Laar, L. A. Ugalde Lopez, L. C. Peters, and G. H. Gelinck, 2021. Active-matrix mesh electronics thin-film-transistor arrays for biometrics-under-display and biomedical applications. *Journal of the Society for Information Display*; 29: 390–404.

[4]. T. Kalayci, 2024. Investigation of the Magnetic, Structural, and Electronic Properties of Pt/[Pt/Co]4/Pt Thin Film by Experimental and Theoretical Methods. *Moscow Univ. Phys;* 78: 839–845.

[5]. A. Behera, P. Parida, A. Kumar,2020. Advanced Manufacturing and Processing Technology. 1st Edition, ImprintCRC Press; 22.

[6]. J.-Y. Kim, A. Rehman, H. Ryu, I. Oh, G-D.Sim, 2024. Sputter deposited Ni-rich NiTi thin films: Mechanical behavior and composition sensitivity. *Materials Science and Engi*neering: A; 912: 146960.

[7]. Z.-X. Wang, F. Liang, G.-P. Zhang, B. Zhang, 2022. Enhancing high-temperature tensile properties of Ni/Ni-W laminated composites for MEMS devices. J*ournal of Materials Science & Tech*nology; 138: 129-137.

[8]. S.D. Bader, and S.S.P. Parkin, 2010. Spintronics. *Annual Review of Condensed Matter Physics*; 1: 71-88.

[9]. I. Žutić, J. Fabian, and S. D. Sarma, 2004. Spintronics: Fundamentals and applications. *Reviews of Modern Physics*; 76: 323.

[10]. J. Singh, S. K. Gupta, A. K. Singh, P. Kothari, R.K. Kotnala, J. Akhtar, 2012. Investigation of structural and magnetic properties of Ni, NiFe, and $NiFe_2O_4$ thin films. *Journal of Magnetism and Magnetic Materials*; 324: 999–1005.

[11]. N. Teichert, A. Boehnke, A. Behler, B. Weise, A. Waske, and A. Hütten, 2015. Exchange bias effect in martensitic epitaxial Ni-Mn-Sn thin films applied to pin CoFeB/MgO/CoFeB magnetic tunnel junctions. *Applied Physics Letters*; 106: 19.

[12]. K. Dev, A. Kadian, V. R. Reddy, Rohit Medwal, and S. Annapoorni, 2024. Magnetization Switching Dynamics of Electrodeposited Fe–Ni Thin Films. *Journal of Superconductivity and Novel Magnetism*; 37:1243–1255.

[13]. A. Ghita, T.-G. Mocioi, A. M. Lomonosov, J. Kim, O. Kovalenko, P. Vavassori, and Vasily V. Temnov, 2023. Anatomy of ultrafast quantitative magnetoacoustics in freestanding nickel thin films. *Phys. Rev. B*; 107: 134419.

[14]. P. Srivastava, F. Wilhelm, A. Ney, M. Farle, H. Wende, N. Haack, G. Ceballos, and K. Baberschke, 1998. Magnetic moments and Curie temperatures of Ni and Co thin films and coupled trilayers. *Phys. Rev. B*; 58: 5701.

[15]. A. Banigo, T. Azeez, K. Ejeta, A. Lateef, and E. Ajuogu, 2020. Nanobiosensors: applications in biomedical technology. *IOP Conference Series: Materials Science and Engineering*; 805: 012028 (IOP Publishing).

[16]. L. Vannozzi, V. Iacovacci, A. Menciassi, and L. Ricotti, 2018. Nanocomposite thin films for triggerable drug delivery. *Expert opinion on drug delivery*; 15: 509–522.

[17]. S. Miyazaki, Y. Q. Fu, and W. M. Huang, 2009. Thin film shape memory alloys: fundamentals and device applications *Cambridge University Press.*

[18]. M. C. RAO and M. S. SHEKHAWAT, 2013. A brief survey on basic properties of thin films for device application, *International Journal of Modern Physics: Conference Series*; 22: 576–582.

[19]. A. P. Piedade, F. Romeu, R. Branco, and P. V. Morais, 2018. Thin films for medical and environmental applications, *Methods for Film Synthesis and Coating Procedures, edited by L. Nánai, A. Samantara, L. Fábián, and S. Ratha (IntechOpen, Rijeka, Chap.* 8).

[20]. R. Said, W. Ahmed, J. Uhomoibhi, and M. Jackson, 2009. Engineering studies of thin films for biomedical applications: Structural and compositional analysis of NiAl and Ni-Al-N films, *Proceedings of the International Conference on Engineering Education and Research, ICEE-iCEER*.

[21]. E. Yang, V. M. Sokalski, M. T. Moneck, D. M. Bromberg, and J.G. Zhu, 2013. Annealing effect and under/capping layer study on Co/Ni multilayer thin films for domain wall motion. *Journal of Applied Physics*; 113: 17C116.

[22]. T. KALAYCI, 2023. Investigation of cap and buffer layer effect in Co/Ni thin films by ferromagnetic resonance technique. *Karadeniz Fen Bilimleri Dergisi*; 13: 724–733.

[23]. P. Salunkhe, M. A. AV, and D. Kekuda, 2020. Investigation on tailoring physical properties of nickel oxide thin films grown by dc magnetron sputtering. *Materials Research Express*; 7: 016427.

[24]. P. Aksu, 2024. Strong perpendicular magnetic anisotropy and interlayer coupling in CoRh/Rh/Fe multilayers tailored by Rh spacer layer thickness. *Physica B: Condensed Matter*; 676: 415662.

[25]. M. Farle, 1998. Ferromagnetic resonance of ultrathin metallic layers. *Reports on progress in physics*; 61: 755.

[26]. O. Udalov, A. Fraerman, and E. Demidov, 2019. Definition of the interlayer interaction type in magnetic multilayers analyzing the shape of the ferromagnetic resonance peaks. *Journal of Applied Physics;* 125: 103902.

[27]. L. Figueiredo, F. Pelegrini, A. Biondo, M. Pessoa, V. Nascimento, and E. Baggio-Saitovitch, 2020. Uncovering magnetic properties of NiFe/WTi multilayers by FMR and SWR analyses. *Journal of Magnetism and Magnetic Materials*; 498: 166183.

[28]. M. Yasaka et al., 2010. X-ray thin-film measurement techniques. *The Rigaku Journal*; 26: 1–9.

[29]. J. Potocnik, M. Nenadovi, N. Bundaleskia, B. Joki, M. Mitri, M. Popovi, Z. Rakocev, 2016. The influence of thickness on magnetic properties of nanostructured nickel thin films obtained by GLAD technique. *Materials Research Bulletin*; 84: 455-46.

[30]. C. Kittel, and P. McEuen, 2018. Introduction to solid state physics. *John Wiley & Sons.*

[31]. C. Yan *et al*, 2023. Thickness-dependent magnetic properties in Pt/[Co/Ni]*n* multilayers with perpendicular magnetic anisotropy. *Chinese Phys. B*; 32: 017503.

[32]. P. Gambardella, and Stefan Blügel, 2020. Magnetic Surfaces, Thin Films and Nanostructures. *Springer Handbook of Surface Science*; ISBN: 978-3-030-46904-7.

[33]. Klaus Baberschke, 2001. Anisotropy in Magnetism. Band-Ferromagnetism; 580. ISBN: 978-3-540-42389-8.

[34]. J. G. Monsalve, J. E. Abrão, E. Santos, A. Ricalde, A. Azevedo, and O. Arnache, 2022. Twofold and fourfold anisotropies in zinc ferrite thin films investigated by ferromagnetic resonance. *PHYSICAL REVIEW B*; 105: 014420.

[35]. S.A. Haque, A. Matsuo, Y. Seino, Y. Yamamoto, S. Yamada, H. Hori, 2001. Effect of GaAs substrate on the magnetic properties of Ni film. *Physica B*; 305:121–126.

[36]. D. Kaya, H. S. Aydınoglu, E. S. Tüzemen, A. Ekicibil, 2021. Investigation of optical, electronic, and magnetic properties of p-type NiO thin film on different substrates. *Thin Solid Films*; 732: 138800.

[37]. Z. Mao, W. Zhao, Z. A. Al-Mualem, and C.T. Campbell, 2020. Energetics and Structure of Nickel Atoms and Nanoparticles on MgO (100). *The Journal of Physical Chemistry C*; 124: 14685−14695.

[38]. L. Trupina, L.Nedelcu, M. G. Banciu, A. Crunteanu, L. Huitema, C. Constantinescu, and Alexandre Boulle, 2020. Texture and interface characterization of iridium thin films grown on MgO substrates with different orientations. *J Mater Sci*; 55:1753–1764.

[39]. T Tanaka, T Nishiyama, K Shikada, M. Ohtake, F. Kirino, and M. Futamoto, 2010. Epitaxial growth of Ni thin films on MgO single-crystal substrates. *Journal of the Magnetics Society of Japan*; *34*: 21-29.

[40]. C. Deger, P. Aksu, and F. Yildiz, 2010. Effect of Interdot Distance on Magnetic Behavior of 2-D Ni Dot Arrays. *IEEE Transactions on Magnetics*; 52: 12.

Celal Bayar University Journal of Science

Central Composite and Factorial Design of Experiments for Textile Dye Removal from Solution by Pumice, KOH-Pumice, HCl-Pumice, Kaolinite, KOH-Kaolinite, HCl-Kaolinite Clays

Mustafa Korkmaz[1*]

[1] Department of Environmental Engineering, Balıkesir University, 10145, Balıkesir, Türkiye

* korkmazm@balikesir.edu.tr
* Orcid No: 0000-0001-8424-6339

Received: 16 May 2024
Accepted: 22 August 2024
DOI: 10.18466/cbayarfbe.1485528

Abstract

The pollution of surface waters by the textile dye-containing wastewaters causes to an increasing concern throughout the world. Methyl violet is a toxic, mutagenic and harmful textile dye against humans. Clays are cheap and vast adsorbents in the nature. Methyl violet dye removal from solution was studied by raw pumice and raw kaolinite using the central composite experimental design method. Firstly, raw kaolinite and raw pumice were tested for the dye adsorption and then capacities of raw kaolinite and raw pumice were aimed to increase by KOH and HCl modification. The experimental parameters studied for the central composite design were initial pHs (2-10), adsorbent amounts (0.2-1 g/50 mL) and initial concentrations (100-500 mg/L). In central composite experimental design of raw kaolinite and raw pumice, the all parameters were found as statistically unimportant for kaolinite and pH, pH-pH, concentration-concentration parameters were found statistically important and other parameters were unimportant for raw pumice. Maximum capacities for raw pumice and raw kaolinite were calculated as 7.15 and 18.31 mg/g, respectively. The dye removal of KOH-pumice and KOH-kaolinite were not high from raw pumice and raw kaolinite. HCl modified kaolinite and pumice were ineffective for dye removal. Kinetics of dye removal by raw kaolinite fitted to the pseudo second order model. pHpzc values of raw pumice and raw kaolinite were found as 6, respectively. Dye removal was obtained as 90% for 50 mg/L dye concentration by kaolinite. Raw kaolinite was determined as the most effective adsorbent for dye concentrations especially below 100 mg/L.

Keywords: Kaolinite, modified-kaolinite, methyl violete removal, modified-pumice, pumice, Optimization

1. Introduction

The raising population of humans necessitates to growing industrialization in food and textile industries which produce a huge amount of dye containing wastewater. Some dyes are toxic for humans, animals, soil microorganisms and plants according to their chemical ingredients. Worldwide, it is estimated that 700,000 tons of dyes are generated annually, and 12.5 % of them are inappropriately disposal into aquatic resources [1]. Textile industry wastewaters contain high dye residue, dense color, high BOI and COD [2]. Biological processes like activated sludge, trickling filter, anaerobic digestion are not effective to most of dyes due to dye toxicity for microorganisms. But, physicochemical methods such as adsorption, coagulation, electrocoagulation, electrooxidation, fenton oxidation-coagulation, biosorption generally have gave good results for dye removal [2,3-7]. Among the mentioned methods, adsorption method in which vast and cheap adsorbents are used has come forward in the last fifty years. Dye removal by adsorption can be realized by clay minerals [8]. Kaolinite and pumice clay minerals are present in vast amounts as pure in their pits and they may be used widely in adsorption investigations for heavy metal and dye treatment from wastewaters. Pumice is highly porous igneous rock, usually containing 67–75% SiO_2 and 10–20% Al_2O_3, with a glassy texture [9]. The pumice is used as abrasive material in cleaning and polishing and as light construction material [9]. The total amount of world pumice deposits is sixteen billion tons and the reserves

are hosting in ABD, Turkey, Italy, Greece, Spain, France, Yugoslavia and Germany [9]. Kaolinite is a phyllosilicate clay mineral with the formula of $Al_2Si_2O_5(OH)_4$ [10]. It is a layered silicate mineral, forming one tetrahedral layer of silica bounded to octahedral layer of alumina by oxygen atoms [10]. The chain like connection of these layers occurs by hydrogen bonds [10]. The adsorption of dyes on clay minerals occurs by interaction on positive surface Si and Al cations and further interaction with Si≡OH and Al=OH functional groups [10]. Dye binding realizes at surface of clay and if the clay pores are enough for dye molecule entrance, also dye binding occurs at interior of pores of clay. Textile dye types are reactive dyes, direct dyes, acid dyes, all-purpose dyes, natural dyes, VAT dyes, disperse dyes and azoic dyes. The surface of clay minerals shows different affinity properties for adsorption of different dyes. For instance, while cationic molecules of a cationic dye are adsorbed on negative surface, anionic molecules of an anionic dye are adsorbed on positive surface. Thus, modification of clay surface sometimes becomes necessary. In this study, methyl violet, a cationic dye, adsorption was aimed to increase on kaolinite and pumice surface by modification by KOH and HCl solution. Since methyl violete is cationic dye and requires to negative surface, but sometimes hydrogen bonds at pHs (3-6) may increase the cationic dye adsorption as has been in present study results. Full factorial experimental design by the Minitab 16.0 programme uses surface, counter and optimization graphs. It requires low experimental run.

Optimization study for experiments of adsorption can be done by various computer programmes. Minitab 16.0 computer program is one of the choices for optimization of adsorption data. Central composite experimental design is a tool of Minitab 16.0 programme. This optimization method uses a wide experimental matrix for optimization. This method enables a regression model and Anova analysis. Regression model is used for data estimation of operation of adsorption reactors and Anova analysis gives the confidence factor to understand the statistically important parameters. Also, central composite design method uses surface, counter and optimization graphs for data and parameter analysis [11]. Factorial design requires the low experimental runs and gives linear relationship between parameter levels changing from low value to high value.

In this study, methyl violet, a cationic dye, removal from solution was studied by using kaolinite and pumice clay minerals. Optimization by central composite experimental design was done using Minitab 16.0 programme. After determination of capacities of these mineral, their surfaces were modified by KOH and HCl solutions and it was expected to increase of capacities. The reason of selection of this dye and minerals was wide usage of dye in textile and wide presence of adsorbents in open pits in Turkey. Modified adsorbents were studied using factorial experimental design except acid modified clays. From the preliminary experiments, the acid modified clays were found as ineffective; therefore their results were not given completely.

2. Materials and Method

2.1 Adsorption Experiments for Central Composite Design in Dye Removal by Raw Kaolinite and Raw Pumice Clays

Methyl violet dye is a cationic dye. The open formula of methyl violet is given in Figure 1. The stock dye solution was prepared as 1,000 mg/L and the studied solutions were prepared from this stock solution. Adsorption experiments were carried out according to experimental matrix obtained from Minitab 16.0 programme. Firstly, 15 solutions for raw kaolinite and raw pumice clay minerals in central composite design were prepared at different concentrations, pHs and adsorbent amounts for 50 mL solutions. Then, prepared solutions were located to temperature controlled incubator shaker. Adsorption reactions of kaolinite and pumice clay minerals were conducted at 3 hours, 100 rpm and 20 °C. After reaction, 5 mL solution samples were taken and centrifugated at 3,000 rpm during 3 minutes. The supernatant samples of 1 mL were diluted and measured by using UV-visible spectrophotometer at 584 nm wave length. pH of solutions was adjusted using diluted HCl and KOH solutions. Automatic pipettes were used for adjustment and taking of solutions. A pH meter was used for pH measurements and a magnetic stirrer was used for dye solution preparation. Experiments were conducted with kaolinite and pumice at <850 µm particle size. A time span of 3 hours was found as enough for equilibrium between dye and raw pumice and raw kaolinite. The point of zero charge (pHpzc) values of both raw clays were measured for pHs of 2, 4, 6, 8, 10, 12. The pHpzc experiments were carried out for 50 mL solution, 1.5 g raw clay, 20 °C and 3 hours interaction by temperature controlled incubator shaker. The used pumice was from Tatvan and kaolinite from Balıkesir cities in Turkey. Adsorbent capacity and removal percentages were calculated using following equations.

$$\eta = \frac{(C_0 - C)\times 100}{C_0} \qquad \text{(Eq.1)}$$

Here, η is removal percentage (%). C_0 and C are initial and treated solution dye concentrations (mg/L).

Celal Bayar University Journal of Science
Volume 20, Issue 3, 2024, p 25-34
Doi: 10.18466/cbayarfbe.1485528

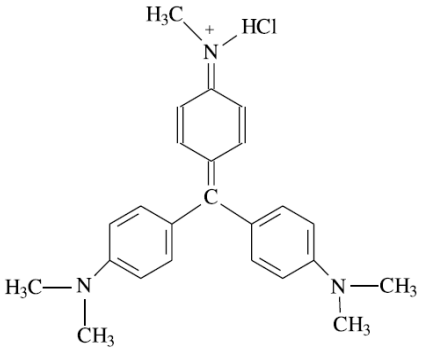

Figure 1. Chemical structure of methyl violete (MV) dye.

$$Qe = (\frac{C_0 - C) \times 50}{1,000 \times W})$$

(Eq.2)

Here, Qe is adsorption capacity (mg/g). C_0 and C are initial and treated solution dye concentrations (mg/L). W is adsorbent amount (g) in 50 mL.

2.2 Modification Experiments of Clay Minerals by KOH and HCl

For modification of kaolinite and pumice clay minerals, 200 g clay with <850 µm particle size was treated with 10 g KOH/1,000 mL pure water solution during 20 minutes. The equilibrium pHs of this clay-base solution mixtures were 13.34 for kaolinite and 13.37 for pumice. The modified clay minerals were filtered with filter paper and dried during 23 hours at 103 °C and sieved to <850 µm particle size. The theoretical pHs of base solution was calculated as 13.25, therefore, the modification by base was low or never happened. For HCl modification of pumice and kaolinite, 25 g of clays were modified with 10 mL concentrated HCl (37%) in total 250 mL pure water mixture during one hour while content was being stirred. After modification, solutions were filtered with Whatman filter paper and dried in an oven during 5 hours at 103 °C.

2.3 Factorial Design Experiments for Dye Removal by KOH and HCl Modified Clays

2^2 factorial experimental design was applied to KOH-pumice, KOH-kaolinite, HCl-pumice and HCl-kaolinite. The experimental parameters were 20 °C, 1.5 g adsorbent amount, 3 hours, 100 rpm, 50 mL solutions. The intervals of parameters were pH (4, 8) and concentration (200, 400 mg/L). Experiments were carried out by temperature controlled incubator shaker. The experimental procedure was the same of raw pumice and raw kaolinite. The HCl modified kaolinite and pumice gave the low adsorption capacities and therefore their results were not given.

3. Results and Discussion

3.1 Central Composite Design of Dye Removal by Raw Kaolinite and Raw Pumice

The low and high levels of parameters are given in Table 1. Fifteen different experimental runs were realized for raw kaolinite and raw pumice minerals by using central composite design. For this purpose, the experimental parameters were initial pHs (2-10), concentrations (100-500 mg/L), and adsorbent amounts (0.2-1 g/50 mL). Central composite design is a widely used approach for data optimization for maximum output. Central composite design uses face centered or face centered plus axial and center points for analysis cage matrix. Also, minumum two and maximum ten factors can be used for statistical analysis in central composite design. Central composite design uses counter graphs and surface graphs for data analysis. Central composite design analysis gives regression model coefficients for model formation and Anova analysis gives confidence constants for determination of statistically meaningful parameters. The regression model equation can be adjusted in the program (Minitab 16.0) as lineer, lineer plus squares, lineer plus interactions or full quadratic [12]. The regression models for kaolinite and pumice can be given as follows in full quadratic form:

Kaolinite (mg/g) = -20.3363 + 0.6469*pH + 33.9572*AA + 0.0951*C + 0.1680*pH*pH - 18.9759*AA*AA + 0.000*C*C + 0.1381*pH*AA – 0.0088*pH*C – 0.0627*AA*C (Eq.3)

Pumice (mg/g) = 11.5716 – 3.5036*pH + 15.6403*AA - 0.0568*C + 0.2910*pH*pH + 2.2724*AA*AA + 0.0001*C*C – 1.2429*pH*AA + 0.0042*pH*C – 0.0343*AA*C (Eq.4)

Here, pH is solution pH, AA is adsorbent amount (g/50 mL) and C is concentration (mg/L).
The all parameters were found as statistically unimportant for raw kaolinite. pH, pH*pH, C*C parameters were found statistically important and other parameters were unimportant for raw pumice. Uncodded factors (i.e. real values of factors) were used in analysis of data. The selection of full quadratic equation for model was due to high correlation coefficient. Experimental matrix was given in Table 2. Anova analysis was given in Table 3.

Table 1. The low and high values of parameters in central composite design for raw kaolinite and pumice.

Parameters	**-2**	**-1**	**0**	**1**	**2**
Kaolinite					
pHs	2	4	6	8	10
Adsorbent (g/50 mL)	0.2	0.4	0.6	0.8	1
Concentration (mg/L)	100	200	300	400	500

Pumice					
pHs	2	4	6	8	10
Adsorbent (g/50 mL)	0.2	0.4	0.6	0.8	1
Concentrations (mg/L)	100	200	300	400	500

3.2 Adsorbent Amount-pH Effect for Kaolinite

According to results given in Figure 2 (Surface plots), dye removal by kaolinite increased at both minumum pH and maximum pH for middle adsorbent amount. At high pH values, adsorbent surface gained more negative charge and cationic dye easily adsorbed but at low pH values, adsorbent surface gained positive charge and cationic dye molecules attached to surface by hydrogen bound [2]. Pollutant adsorption on adsorbent is related by solid-to-ion equilibrium. While sometimes capacities increase at low adsorbent amounts, the capacities sometimes remain constant from low adsorbent amount to high adsorbent amount. For instance, boron adsorption remained constant by increasing resin and alunite amount [13,14]. The reason of high adsorption capacity of middle adsorbent amount was probably due to solid-to-dye equilibrium [13,14]. This also may be related kaolinite surface zeta potential. Further, this was probably due to adsorbent amount-pH interaction. Dye dissociation or aggregation at low pHs might caused to easily or aggregation adsorption, respectively [15,16]. Sodium ions in methyl violete dye molecules exchanged with probably hydrogen atoms at low pHs by dissociation and dye molecules might aggregated with hydrogen atoms. Thus, aggregated dye molecules adsorbed on clay surface a bit high at low pHs.

Table 2. Experimental matrix in central composite design for dye removal by raw kaolinite and pumice (20 °C, 100 rpm, 50 mL, 3 hours, <850 µm particle size).

	Parameters			**Responses**			
Run	**pH**	**AA**	**C (mg/L)**	**Kaolinite (mg/g)**	**Kaolinite Estimation (mg/g)**	**Pumice (mg/g)**	**Pumice Estimation (mg/g)**
1	4	0.4	200	3.66	2.67	0.00	0.10
2	8	0.4	200	10.10	6.50	0.88	1.43
3	4	0.8	200	3.47	2.35	3.22	2.71
4	8	0.8	200	4.17	6.40	1.64	2.05
5	4	0.4	400	18.31	9.63	0.00	1.36
6	8	0.4	400	11.74	6.43	3.79	6.04
7	4	0.8	400	7.13	4.30	0.00	1.23
8	8	0.8	400	6.76	1.31	2.27	3.92
9	2	0.6	300	9.09	7.30	1.68	2.75
10	10	0.6	300	10.69	8.15	7.15	6.77
11	6	0.2	300	4.04	4.72	0.25	0.22
12	6	1	300	4.29	-0.72	0.00	0.71
13	6	0.6	100	5.30	4.10	2.02	2.54
14	6	0.6	500	11.36	5.97	4.97	5.66
15	6	0.6	300	6.82	5.04	0.00	0.10

pH is solution pH, AA is adsorbent Amount (g/50 mL), C is concentration (mg/L)

Table 3. Anova analysis of dye removal by raw kaolinite and pumice in central composite design.

Parameters	Kaolinite		Pumice	
	R-Sq=74.70%		R-Sq= 91.36%	
	R-Sq(pred)=0.00%		R-Sq(pred)=18.46%	
	R-Sq(adj)=29.16%		R-Sq(adj)=75.30%	
	Constant	p	Constant	p
Constant	-20.3363	0.519	11.5716	0.251
pH	0.6469	0.881	-3.5036	0.037
AA	33.9572	0.445	15.6403	0.264
C	0.0951	0.298	-0.0568	0.071
pH*pH	0.1680	0.548	0.2910	0.014
AA*AA	-18.9759	0.499	2.2724	0.786
C*C	0.000	0.797	0.0001	0.032
pH*AA	0.1381	0.966	-1.2429	0.240
pH*C	-0.0088	0.211	0.0042	0.073
AA*C	-0.0627	0.354	-0.0343	0.125

pH is solution pH, AA is adsorbent amount (mg/50 mL), C is concentration (mg/L)

Celal Bayar University Journal of Science
Volume 20, Issue 3, 2024, p 25-34
Doi: 10.18466/cbayarfbe.1485528

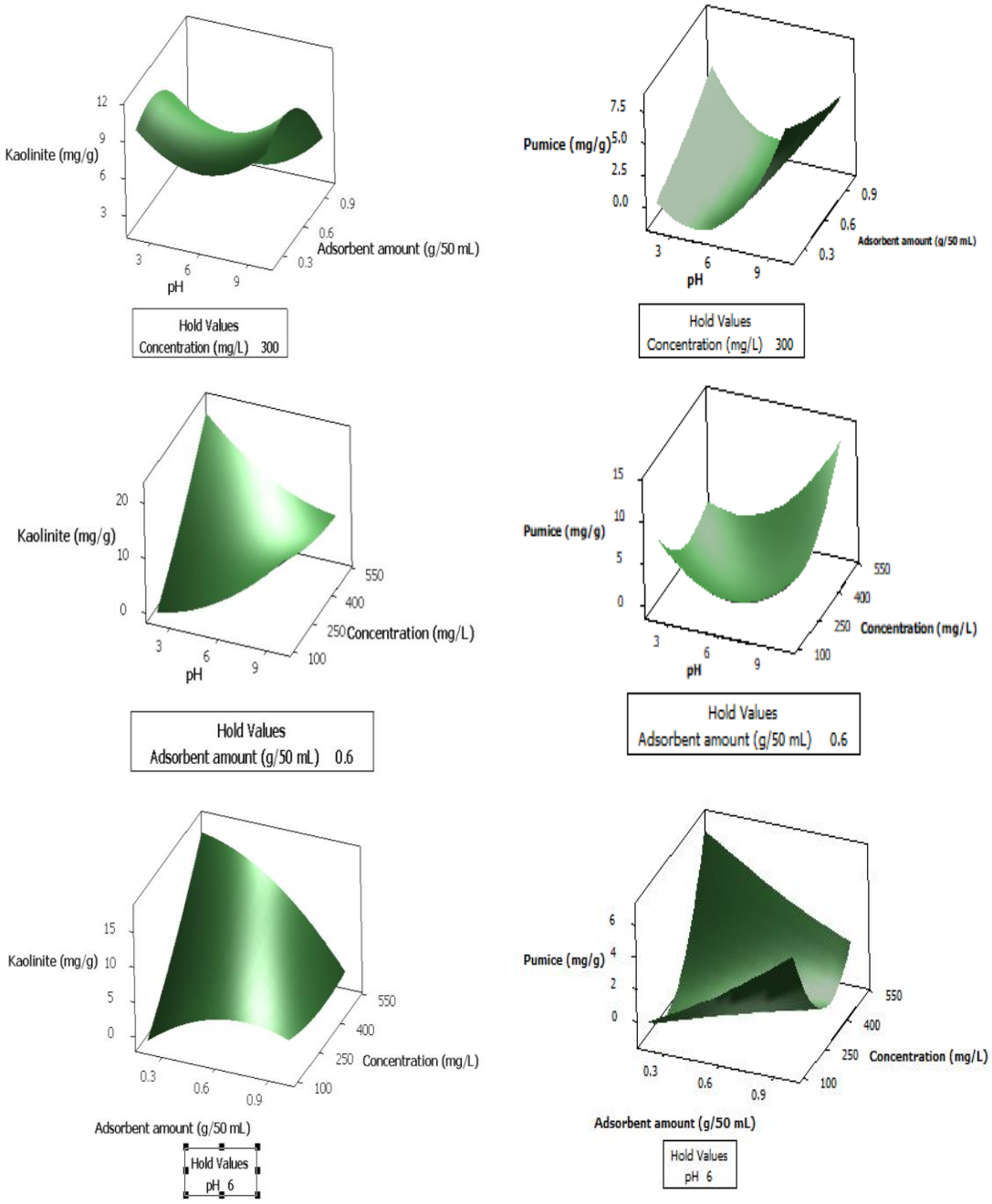

Figure 2: Surface plots of dye adsorption on kaolinite and pumice clays.

3.3 Concentration-pH Effect for Kaolinite

According to results given in Figure 2 (Surface plots), dye removal increased with low pH and high concentration for kaolinite mineral. At low pHs, kaolinite surface gained positive charge and probably cationic methyl violet dye molecules attached to kaolinite surface by hydrogen bounds. At high concentrations, kaolinite surface was loaded by dye molecules as a result of driving force of high dye concentration. Similar result for high concentration was reported in methyl violete dye adsorption on clinoptilolite and boron adsorption on alunite [2,14].

3.4 Concentration-Adsorbent Amount Effect for Kaolinite

According to results given in Figure 2 (Surface plots), kaolinite mineral showed high capacity for methyl violet dye at low adsorbent amounts and high concentrations. At low adsorbent amounts, dye concentration gradient on low adsorbent amount was high and therefore, more dye molecules adsorbed on kaolinite mineral. At high concentrations, the driving force of dye molecules caused to more dye adsorption on kaolinite mineral [2,14].

3.5 pH-Adsorbent Amount Effect for Pumice

According to results given in Figure 2 (Surface plots), methyl violet dye adsorption on pumice mineral increased at low and high pHs. Also, dye removal remained constant for adsorbent amount from low value to high value. At high pHs, pumice surface gained more negative charge and more dye adsorbed on pumice. The reason of constant patter of adsorption capacity for all adsorbent amounts was thought that the dye adsorption on pumice was related with dye-to-solid equilibrium [13,14,17]. Low pHs probably increased the surface hydrogen bonds that increasing dye adsorption. Because methyl violet dye adsorption increased at low pH. This is also be related with pH-adsorbent amount interaction. While dye adsorption increased at low pHs with increasing adsorbent amount, at high pHs, adsorbent amount was ineffective.

3.6 Concentration-pH Effect for Pumice

According to results given in Figure 2 (Surface plots), methyl violete dye adsorption capacities increased at high pHs and high concentrations. At high pHs, surface of pumice mineral was more negative for dye adsorption and at high concentrations, dye was adsorbed at high amount on pumice as a result of high concentration driving force [2,14]. Again, low pHs increased the capacity due to hydrogen bonds.

3.7 Concentration-Adsorbent Amount Effect for Pumice

According to results given in Figure 2 (Surface plots), methyl violet dye adsorption increased at low adsorbent amount and high concentration. At low adsorbent amounts and high concentrations more dye molecules penetrate to pumice surface due to high driving force [2,14].

3.8 Factorial Design of Experiments for Methyl Violet Dye Removal by KOH-Kaolinite and KOH-Pumice

Generally clay surfaces gain negative charge by base modification and they show high affinity against cationic dye like methyl violet. Thus, in this study, kaolinite and pumice clay minerals were modified by KOH solution. Modification experiments were carried out 200 g clay/10 g/L KOH solutions. After treatment of dye solutions with raw kaolinite and raw pumice by central composite design, the conducting of experiments by factorial experimental design for KOH-kaolinite and KOH-pumice would be practical in respect to time, cost and experimental number. Central composite design has required 15 experimental runs, but factorial design has required total 4 experimental runs for two factors and two levels. In the factorial design, concentrations (200 and 400 mg/L) and pHs (4 and 8) were applied. Factorial design is quite advantageous when compared with central composite, taguchi or classical single parameter experiments in respect to cost, time, experiment number and effort. On the other hand, central composite design is superior than factorial design in respect to wide experimental matrix. Factorial design and central composite design give statistically importance of main and interaction effect of parameters using Anova analysis. Both of the approaches use confidence factor (p) and regression model constants for Anova analysis. Also, Student-t test can be obtained from these statistically optimization methods. Generally, when the p values are low and Student-t test results are high, the importance of parameters is high [14]. The experimental matrix and response for factorial design is given in Table 4. The model constants are given in Table 5. According to Anova analysis, the all parameters are insignificant for KOH-kaolinite and KOH-pumice (coded factors and was not given). The surface plots of factorial analysis for KOH-kaolinite and KOH-pumice showed that high initial solution pHs and concentrations increased the capacities for modified kaolinite and pumice. The regression model are given in follows:

$$\text{Kaolinite (mg/g)} = -0.7375+0.458750*pH+ 0.006675*C \quad \text{(Eq.5)}$$

$$\text{Pumice (mg/g)} = -1.0875+0.15625*pH+0.007825*C \quad \text{(Eq.6)}$$

Here, pH is solution pH. C is concentration (mg/L). Models were developed according to uncoded factor values.The modification of raw pumice and raw kaolinite with HCl solution did not remove methyl violete dye. Therefore their removal results were not given in this study. Surface plots for factorial design were given in Figure 3 and 4.

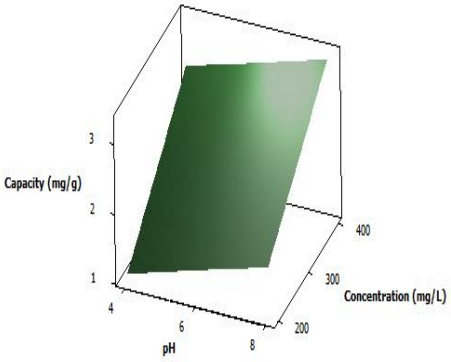

Figure 3: Surface plots of dye adsorption on KOH-kaolinite.

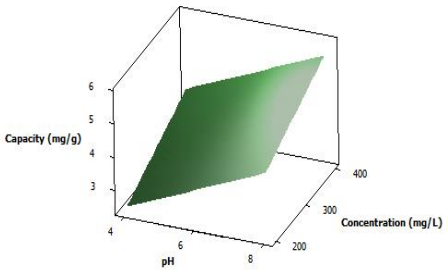

Figure 4: Surface plots of dye adsorption on KOH-pumice clay.

Table 4. Experimental matrix in factorial design for optimization and responses (20 °C, 100 rpm, particle size<850 µm, adsorbent 1.5 g/50 mL, 3 hours).

	Experimental Parameters			Dye Removal	
Adsorbent	**Run**	**C**	**pH**	**Adsorption Capacity (mg/g)**	**Estimation Adsorption Capacity (mg/g)**
Kaolinite	1	200	4	2.02	2.43
	2	200	8	4.68	4.27
	3	400	4	4.18	3.77
	4	400	8	5.19	5.60
Pumice	1	200	4	1.45	1.10
	2	200	8	1.38	1.73
	3	400	4	2.32	2.67
	4	400	8	3.64	3.29
pH is solution pH, C is concentration (mg/L).					

Table 5: Factorial fitness to dye removal from water (Uncoded).

	Parameters	**Regression Model Constants**
Kaolinite	Model Constant	-0.7375
	pH	0.458750
	Concentration	0.006675
Pumice	Model Constant	-1.0875
	pH	0.15625
	Concentration	0.007825

Table 6: Fitness of kinetic data to models for raw kaolinite (Natural pH, 25.7 °C, 1,000 rpm, 100 mg/L, 500 mL, 5 g kaolinite).

Kinetic Models	Coefficient of determination values (R^2)
Zero-order	0.339
First-order	0.344
Second-order	0.351
Pseudo-second-order	1

3.9 Kinetics of dye removal by kaolinite using linear analysis

The determination of kinetics of (ad)sorption is an important way of operation and modeling of batch and column reactors because optimum operation time and reaction degree are determined by kinetic analysis [18]. While the reaction is free from the concentration, the reaction degree is zero order and for dependence of reaction to concentration, reaction degree can be first order or second order. Also, generally adsorption kinetic data are described by pseudo-first-order and pseudo-second-order models. The model equations are as follows [19]:

Celal Bayar University Journal of Science
Volume 20, Issue 3, 2024, p 25-34
Doi: 10.18466/cbayarfbe.1485528

$$\left(\frac{dC}{dt} = -kC^n\right)$$ (Eq.7)

The zero-order kinetic model is as follows.

$$C = C_0 - kt$$ (Eq.8)

The first-order kinetic model is as follows.

$$\ln(C) = \ln(C_0) - kt$$ (Eq. 9)

The second-order kinetic model is as follows.

$$\frac{1}{C} = \frac{1}{C_0} - kt$$ (Eq.10)

Here, C_0 is the initial dye concentration (mg/L), C (mg/L) is the dye concentration at time t (min) and k is the rate constant (min^{-1}).
The Ho's pseudo second order kinetic model is given as follow [20].

$$\frac{t}{qt} = \left(\frac{1}{k_2 qe^2}\right) + \left(\frac{t}{qe}\right)$$ (Eq.11)

Where, k_2 is the rate constant of the pseudo-second-order equation (g/mg min). *q*e is the theoretically sorbed amount at equilibrium (mg/g). *qt* is the sorbed amount at any time *t* (mg/g). Fitness of the equations is determined from coefficient of determination values. Fitness of kinetic data to the pseudo-second-order model was given in Table 6. Comparison of adsorbents and kinetic data were given in Figure 5 and 6, respectively.

Adsorption capacities of raw and modified kaolinite clays are about near each other, therefore optimum adsorbent was determined as raw kaolinite. Also, raw kaolinite had high capacity from raw pumice and modified pumice. Acid modified pumice and kaolinite did not adsorb methyl violet dye at important amount. The reason of adsorption capacity decrease of KOH-kaolinite from raw kaolinite might be due to calcination of KOH-kaolinite at 103 °C. Thus, probably surface hydroxyl groups were deteriorated for dye adsorption. Also, acid modification probably deteriorated structure of pumice and kaolinite and dye adsorption did not occur. That is, surface functional groups of kaolinite and pumice by acid modification were shredded. On the other hand, raw pumice and raw kaolinite surface gained to high positive charge for cationic dye by acid modification and adsorption did not realize. On the other hand, base modification of raw kaolinite was poor for strong dye adsorption.

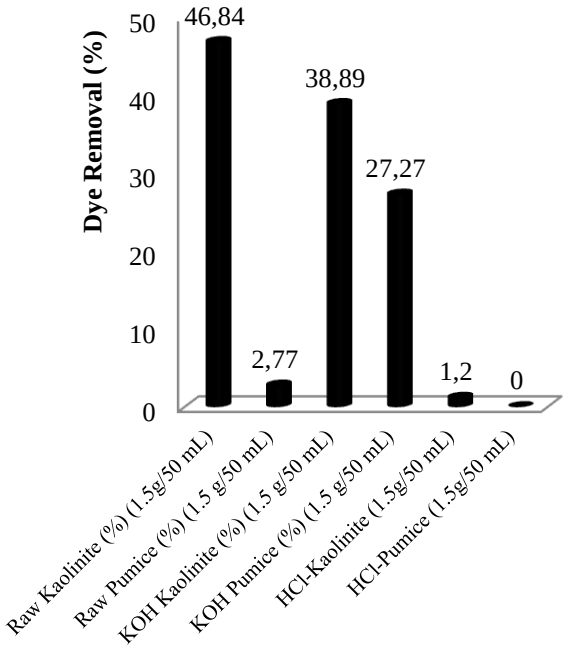

Figure 5. Comparison of adsorbents (Eq.9

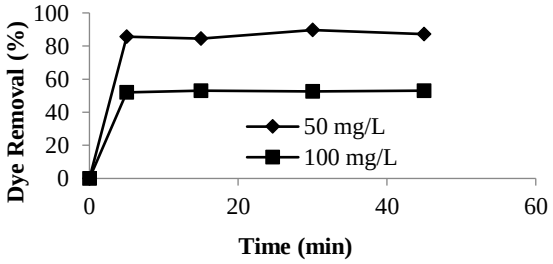

Figure 6: Kinetic data for raw kaolinite (Natural pH, 25. 7 °C, 1,000 rpm, 50 and 100 mg/L dye, 500 mL, 5 g kaolinite)

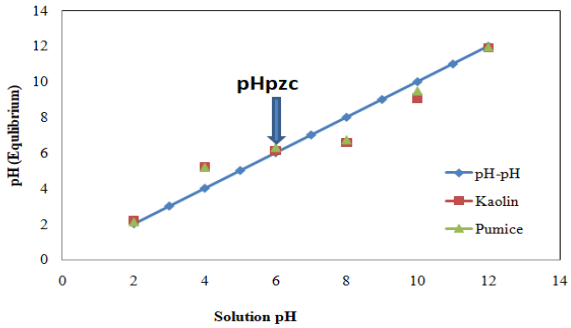

Figure 7. pHpzc values for raw kaolinite and pumice.

3.10 XRD and pHpzc (point of zero charge) Analysis of Adsorbents

pHpzc values for raw kaolinite and pumice were determined as about 6 and given in Figure 7. About below pH (6), raw pumice and kaolinite surface gained positive charge and above pH (6), raw pumice and kaolinite surface gained negative charge in aqueous medium. XRD pattern of raw pumice and kaolinite are given in Figure 8-9. As can be seen in Figure 8-9, the pics are belonging to typical pumice and kaolinite.

4. Conclusion

In this study, methyl violet dye removal by raw kaolinite and raw pumice was aimed from solutions by applying optimization technique. The results can be summarized as follow.

Kaolinite clay showed highest performance than pumice but its capacity was thought to increase with base (KOH) modification. Modification did not so increase the capacity for pumice and kaolinite.

Maximum capacity for raw pumice and raw kaolinite was calculated as 7.15 and 18.31 mg/g, respectively.

Optimization for raw pumice and raw kaolinite showed that the all parameters were found as statistically unimportant for kaolinite. pH, pH*pH, C*C parameters were found statistically important and other parameters were unimportant for pumice.

It was seen that low and high pH-middle adsorbent amount, low pH-high concentration and low adsorbent amount-high concentration interactions increased the capacity of kaolinite. High pH-low adsorbent amount, high pH-high concentration and low adsorbent amount-high concentration increased the capacity of pumice.

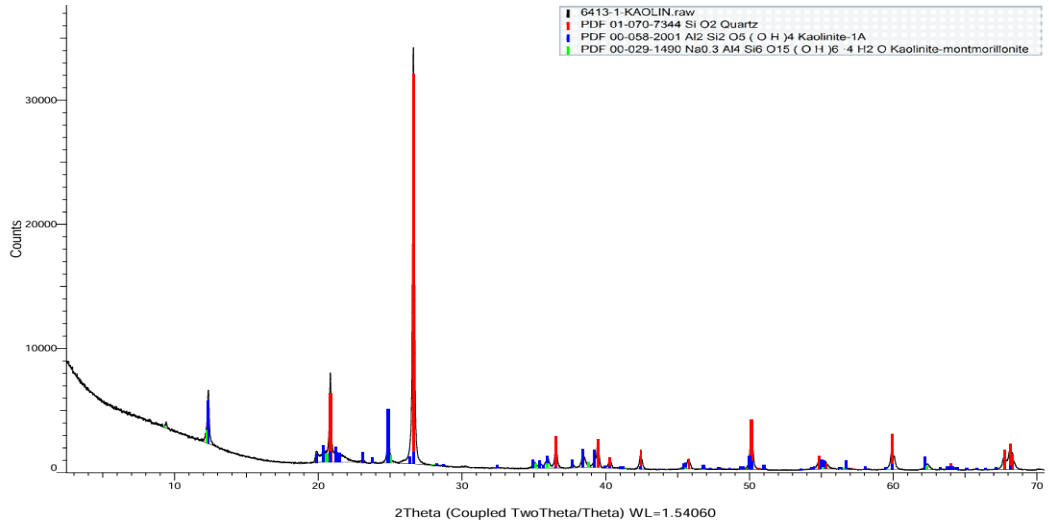

Figure 8. XRD pattern of kaolinite

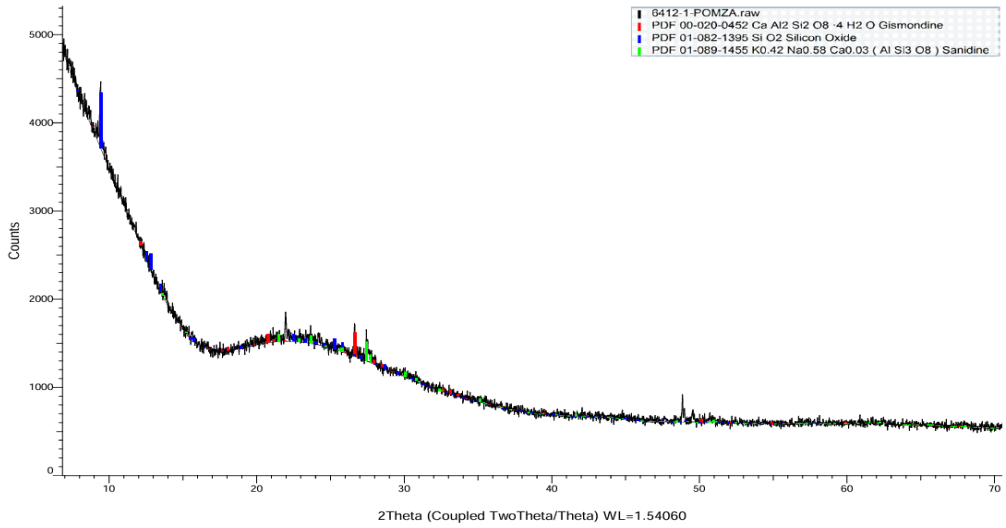

Figure 9. XRD pattern of pumice

Factorial design of dye removal by KOH-pumice and KOH-kaolinite showed that high concentration and pH increased the capacity. The kinetics of dye removal by raw kaolinite fitted to the pseudo second order model.Dye removal was achieved effectively by raw and modified kaolinite mineral.pHpzc values for raw kaolinite and raw pumice were determined as about 6. Acid modification was not effective for dye removal. Raw kaolinite removed methyl violete dye at 90% extent for 50 mg/L concentration.

References

[1]. Artifon, W, Cesca, K, Andrade, C.J, Souza, A.A.U, Oliveira, D. (2021). Dyestuffs from textile industry wastewaters: Trends and gaps in the use of bioflocculants. Process Biochemistry, 111:181-190.

[2]. Korkmaz, M, Özmetin, C, Fil, B.A, Özmetin, E, and Yaşar, Y. (2013). Methyl violet dye adsorption onto clinoptilolite (natural zeolite): isotherm and kinetic study. *Fresenius Environmental Bulletin*; 22(5): 1524-1533.

[3]. Shi, B, Li, G, Wang, D, Feng, C, Tang, H. (2007). Removal of direct dyes by coagulation: The performance of preformed polymeric aluminum species. *Journal of Hazardous Materials*; 143(1–2): 567-574.

[4]. Wei, M.C, Wang, K.S, Huang, C.L, Chiang, C.W, Chang, T.J, Lee, S.S, Chang, S.H. (2012). Improvement of textile dye removal by electrocoagulation with low-cost steel wool cathode reactor. *Chemical Engineering Journal*; 192: 37-44.

[5]. Nandhini, M, Suchithra, B, and Prakash, D.G, Saravanathamizhan, R. (2014). Optimization of parameters for dye removal by electro-oxidation using Taguchi Design. *Journal of Electrochemical Science and Engineering*; 4(4): 227-234.

[6]. Fernandes, N.C, Brito, L.B, Costa, G.G, Taveira, S. F, Cunha–Filho, M.S.S, Oliveira, G.A.R, Marreto, R.N. (2018). Removal of azo dye using Fenton and Fenton-like processes: Evaluation of process factors by Box–Behnken design and ecotoxicity tests. *Chemico-Biological Interactions*; 291: 47-54.

[7]. Crini, G, Torri, G, Lichtfouse, E, Kyzas, G.Z., Wilson, L.D., Morin-Crini , N. (2019). Dye removal by biosorption using cross-linked chitosan-based hydrogels. *Environmental Chemistry Letters*; 17:1645–1666.

[8]. Tahir, S.S., Rauf, N. (2006). Removal of a cationic dye from aqueous solutions by adsorption onto bentonite clay. *Chemosphere*; 63:1842-1848.

[9] Korkmaz, M, Özmetin, C, Özmetin, E, Çalgan, E, Süzen, Y. (2021). Boron Removal by Aluminum Modified Pumice and Aluminum Hydroxide from Boron Mine Wastewater-Full Factorial Experimental Design. *Nevşehir Bilim ve Teknoloji Dergisi*; 10(1): 1-13.

[10]. Karaoğlu, M.H, Doğan, M, Alkan, M. (2009). Removal of cationic dyes by kaoliniteite. *Microporous and Mesoporous Materials*; 122: 20–27.

[11]. Korkmaz, M, Özmetin, C, Süzen, Y, Mutlu, A. (2022). Boron Adsorption on Lime Soil and Phytoremediation of Lime Soil by Potato Plant (Solanum Tuberosum L.). *Celal Bayar University Journal of Science*; 18: 239-247.

[12]. Minitab 16.0 programme help tool

[13]. Öztürk, N, Köse, T.E. (2008). Boron removal from aqueous solutions by ion-exchange resin: Batch studies. *Desalination*; 227: 233–240.

[14]. Kavak, D. (2009). Removal of boron from aqueous solutions by batch adsorption on calcined alunite using experimental design. *Journal of Hazardous Materials*; 163: 308–314.

[15]. Özdemir, Y, Doğan, M, and Alkan, M. (2006). Adsorption of cationic dyes from aqueous solutions by Sepiolite. *Microporous Mesoporous Materials*; 96: 419–427.

[16]. Kerzabi, Y, Benomara, A, and Merghache, S. (2022). Removal of methyl violet 2B dye from aqueous solution by adsorption onto raw and modified carobs (Ceratonia siliqua L.). *Global NEST Journal*; 24(4): 706-719.

[17]. Korkmaz, M, Özmetin, C, Özmetin, E, Çalgan, E, Ziyanak, Ö. (2022). Boron Removal from Colemanite Mine Wastewater by Coagulation using Zinc Hydroxide—A Factorial Optimization Study. *Celal Bayar University Journal of Science*; 18(1), 77-83.

[18]. Özmetin,C, Aydın, Ö, Kocakerim, M.M, Korkmaz, M, Özmetin, E. (2009). An empirical kinetic model for calcium removal from calcium impurity-containing saturated boric acid solution by ion exchange technology using Amberlite IR–120 resin. *Chemical Engineering Journal*; 148: 420–424.

[19]. Yılmaz, A.E, (2009). Endüstriyel atıksulardan elektrokoagülasyon yöntemi ile bor giderimi. Doktora tezi Çevre Mühendisliği Anabilim Dalı, Erzurum, Türkiye.

[20]. Ho, Y. S., McKay, G. (1998). Sorption of dye from aqueous Solution by Peat. *Chemical Engineering Journal*; 70(2): 115–124.

Celal Bayar University Journal of Science

One-Step Enzymatic Surface Modification of Graphene Oxide

Merve Danisman[1]*, Ayhan Oral[2]

[1] Çanakkale Onsekiz Mart Üniversitesi, Bayramiç Meslek Yüksekokulu , Kimya ve Kimyasal Teknolojiler Bölümü, Çanakkale, Türkiye
[2] Çanakkale Onsekiz Mart Üniversitesi, Fen Fakültesi, Kimya Bölümü, Çanakkale, Türkiye

* mervedanisman@comu.edu.tr
* Orcid No: 0000-0001-7295-6341

Received: 3 June 2024
Accepted: 22 August 2024
DOI: 10.18466/cbayarfbe.1491450

Abstract

Graphene oxide (GO) is a material that possesses extremely particular chemical and physical properties. Graphene-based nanomaterials have spurred the advancement of flexible nanocomposites for innovative applications that demand exceptional mechanical, thermal, electrical, optical and chemical properties. These structures have the potential to be applied in various domains due to their multifunctionality. Nevertheless, GO employed have a tendency to create robust aggregate when mixed with organic components. Hence, it is necessary to alter the surfaces of polymer matrices and GO to enhance dispersion stability and compatibility. Chemical functionalization of GO allows for extensive structural change, offering a wide range of alternatives. However, chemical modifcation can lead to the utilization of ecologically harmful chemicals and substantial expenditures of energy, time and costs. Biocompatible, non-cytotoxic, target-selective biotechnological methods are being investigated for surface modification of nanoparticles to address these concerns. This work explored a new approach to modify the GO surface utilizing natural biocatalysts, specifically enzymes. The method used a one-step process where the lipase enzyme was used to modify the GO surface with the methacrylic acid. This method is conducive to mild reaction conditions, free from the generation of chemical waste, and devoid of solvent utilization, addressing the concerns associated with chemical modification methods.

Keywords: Graphene oxide, lipase, surface modification

1. Introduction

Graphene is a two-dimensional material made up of carbon atoms organized in a hexagonal pattern [1]. Because of its distinctive thermal, chemical, mechanical, optical, and electrical characteristics, it is the thinnest material currently known [2]. Because of its exceptional qualities, it has been a critical material for the twenty-first century [3]. Graphene oxide is a form of graphene that experienced chemical modification through the introduction of functional groups containing oxygen; including hydroxyl, epoxide, and carboxyl groups. [4, 5]. While GO is recognized as an oxidized layer of graphite, there is yet no precise model for its chemical structure [6, 7]. Various structural models have been suggested, such as the Lerf-Klinowski, Scholz-Boehm, Dekany, Nakajima-Matsuo, Hofmann and Ruess models. Among these models, the Lerf-Klinowski model is widely accepted configuration, with a regular lattice model containing discrete repeated units. Lerf's proposed structural model of GO consisted of sections that had unoxidized aromatic and six-membered aliphatic ring types, which contained epoxide and hydroxyl groups, as well as isolated C=C bonds. The edges of the model were terminated by COOH and OH chemical groups [6, 7, 8].

Celal Bayar University Journal of Science
Volume 20, Issue 3, 2024, p 35-39
Doi: 10.18466/cbayarfbe.1491450

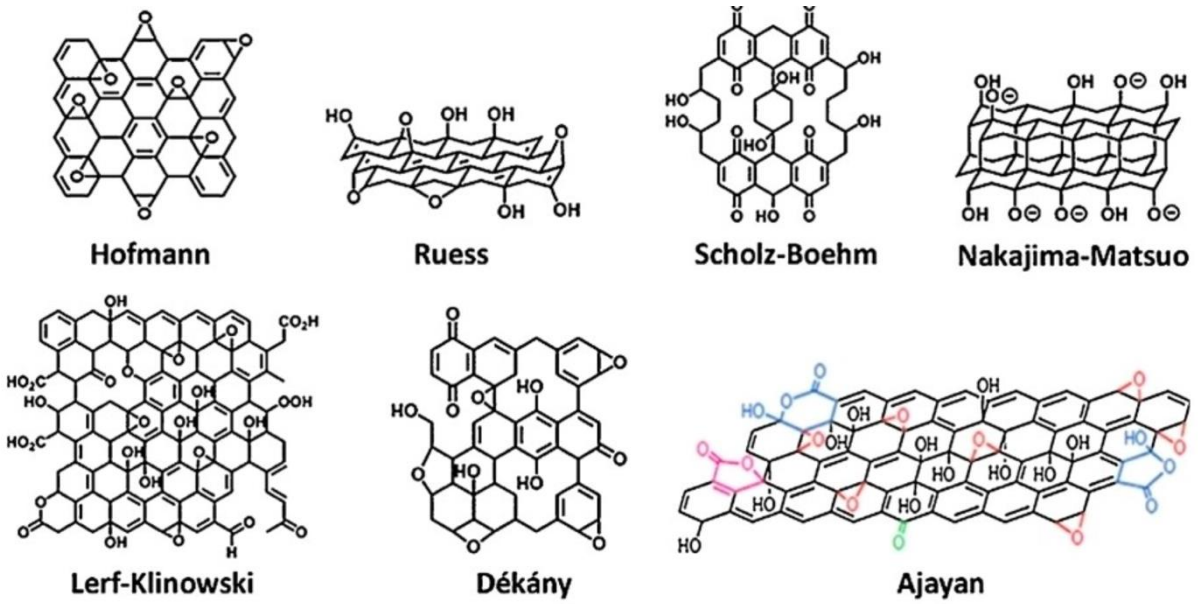

Figure 1. Structural models of GO [7]

Functionalization GO with different chemical moieties (organic, inorganic, and nanocomposites) allows for the exploration of unique and undiscovered nanoarchitectures due to its variable surface chemistry [9]. Many benefits come with surface-modified graphene oxide (GO), including exceptional optical, physico-chemical, electrical, and biocompatibility qualities [10]. Surface modification of GO is crucial for its wide applications [11, 12]. Modification of GO allows it to be processed using solvent-assisted processes, including layer-by-layer bonding and filtering methods. Additionally, it inhibits the agglomeration of graphene and preserves its intrinsic characteristics [13, 14]. Chemical functionalization of GO allows for extensive structural change, offering a wide range of alternatives for adjusting its composition. Various chemical and physical methods have been investigated to improve the stability and modification of graphene [11, 15, 16].

GO has been increasingly utilized to enhance the strength, heat resistance, and functionality of many polymers, including polymethyl methacrylate, polyvinyl alcohol, polystyrene, epoxy, and rubber. Graphene has a tendency to irreversibly accumulate together in the polymer matrix due to its extensive surface area and the strength of the van der Waals bonds between its particles [11, 17, 18]. In this instance, the process of chemically modifying graphene, along with other methods, becomes a crucial step in addressing the challenge and achieving graphene nanocomposites that possess a robust interface and a consistent dispersion of graphene sheets throughout the polymer matrix [13, 17].

Chemical procedures frequently necessitate the use of strong chemicals and rigorous reaction conditions. The use of these techniques leads to the utilization of ecologically hazardous chemicals and substantial expenditures of energy, time, and work. Also of concern is the impact of chemical wastes generated after the reaction and for their disposal [19]. Specifically, the materials used in the surface modification of biomaterials should not contain physiological toxicity and should be biocompatible [20]. Because the most important feature of biomaterials is biocompatibility and biomaterials should be materials that do not interfere with the normal changes of the surrounding tissues and do not cause unwanted reactions (inflammation, clots, etc.) in the tissue [18]. In the development of particles to be used in these areas, non-toxicity, biocompatibility, no accumulation in the human body, and no chemical pollution are the most important factors. For these reasons, biocompatible, non-cytotoxic, target-selective biotechnological methods are being investigated for the surface modification of nanoparticles [21].

Regarding the problems mentioned above, it is necessary to implement more robust procedures that apply covalent bonding, similar to chemical ways. However, it is also crucial to adopt a clean approach that avoids chemical pollution, such as physical methods. At this point, it was anticipated that these issues could be mostly prevented by utilizing enzymes, which are biocatalysts capable of facilitating chemical reactions.

This study developed an improved surface modification method that is suitable for mild reaction conditions, avoids chemical waste formation, and does not require solvents. The method leveraged natural biocatalysts, specifically enzymes, to modify the surface of GO with the methacrylic acid (MAA) through the use of a lipase enzyme.

Celal Bayar University Journal of Science
Volume 20, Issue 3, 2024, p 35-39
Doi: 10.18466/cbayarfbe.1491450

2. Materials and Methods

2.1. Materials

The graphene oxide supplied from Nanography Nanotechnology Inc. was utilized. The biocatalyst used in this study was lipase enzyme (Amano Lipase PS) sourced from Burkholderiacepacia. The specific activity of the enzyme, as indicated by the supplier, was 30,000 unit.g^{-1}. The lipase enzyme was purchased from Sigma-Aldrich. Methacrylic acid obtained from Sigma-Aldrich was used. The solvents, such as ethanol, acetone, hexane, and toluene were purchased from Merck and used for washing and purification of the synthesized products. Deionized water was used in all processes.

2.2. Method

As an experimental method, the method previously used by our team in hydroxyapatite surface modification was taken as a reference [22]. Figure 2 displays the experimental reaction. Since the lipase enzyme is stable and active in anhydrous medium, firstly, 0.1 g GO was pre-dried in an inert environment by vacuuming at regular intervals, and the moisture was removed. Then, the temperature was brought to 50 ˚C and 0.1 mg of lipase enzyme was added to the reaction medium and finally 0.1 mL of MAA was added to bind to the surface and the reaction was performed at 50 ˚C for 24 hours. The products obtained at the end of the reaction were washed and purified with appropriate solvents.

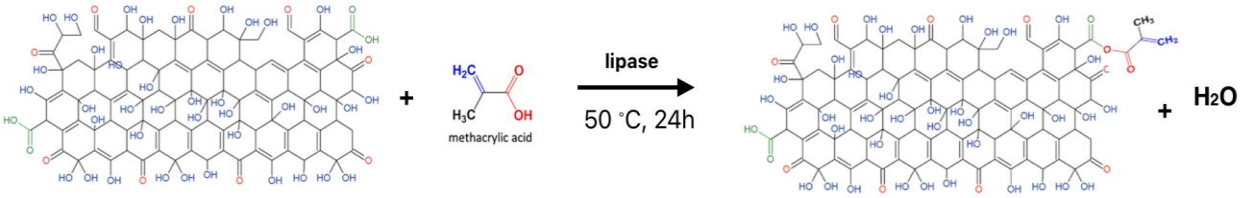

Figure 2. Schematic representation of the reaction of GO surface with MAA

2.3. Analysis

After the purified GO was dried in a vacuum oven for 24 hours, FT-IR (PerkinElmer) measurements were performed. The spectra were measured over a wavenumber range from 400 to 4000 cm^{-1}. From the spectra obtained, peaks belonging to the functional groups of the synthesized products were determined, and structural characterization was carried out in comparison with the starting materials. TG-dTG measurements of the materials were carried out in dry air between 30 °C and 700°C, with an increase of 10 ˚C per minute, and mass losses and thermal properties were determined from the thermograms obtained. SEM images (Carl Zeiss 300 VP) of the obtained particles were taken and their surface morphologies were analyzed.

GO dispersion stability in water is a critical aspect for its various applications, ranging from electronics to biomedical engineering [23]. GO exhibits hydrophilic properties because of the presence of oxygen-containing functional groups on its surface, including carboxyl (-COOH), hydroxyl (-OH) and epoxide (-O-) groups. The dispersibility of GO is influenced by the presence and density of functional groups on its surface [24]. For this reason, the agglomeration/dispersion behavior of GO in water was followed. For this, aqueous solutions of unmodified and modified GO at a concentration of 0.5 mg.mL^{-1} were prepared and dispersed in water for 1 min. in an ultrasonic bath. Then it was allowed to hang on for 30 minutes and the stability of agglomeration or dispersion in water was observed at regular intervals.

3. Results and Discussion

3.1. FT-IR Analysis

The FT-IR spectra of pure GO, surface modified GO (mGO) and MAA obtained after the reaction are given in Figure 3. The FT-IR spectra of the GO sample reveal the presence of hydroxyl bond (-OH) at 3080 cm^{-1}, carbonyl bond (C=O) at 1710 cm^{-1}, aromatic bond (C=C) at 1648 cm^{-1}, C-OH bond at 1440 cm^{-1}, and C-O bonds at approximately 1200 cm^{-1} and 1040 cm^{-1} in accordance with the literature [25, 26]. The MAA spectrum has peaks belonging to C=O and C=C bonds in the structure of MAA at 1562.8 cm-^{1} and 1601.7 cm^{-1} bands and peaks belonging to aliphatic -CHs at 2900 cm^{-1} [27]. The existence of carbonyl (C=O) and double bond (C=C) groups after the modification process does not help to clearly determine if major alterations have happened as they are already present in the GO structure. However, the increase in the intensity of the C=O band and the presence of aliphatic -CH bands at 2800 and 2950 cm^{-1} in the spectra of mGO samples are important indicators that modification has occurred [25].

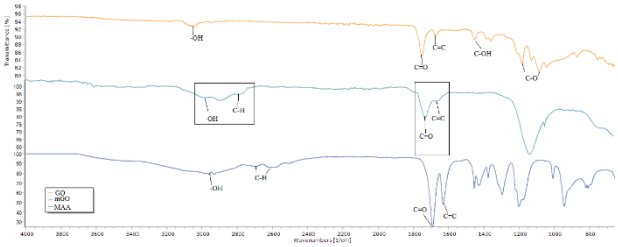

Figure 3. FT-IR spectra of GO, mGO and MAA

Celal Bayar University Journal of Science
Volume 20, Issue 3, 2024, p 35-39
Doi: 10.18466/cbayarfbe.1491450

3.2. TGA Analysis

TG-dTG spectra of pure GO and mGO particles are given in Figure 4. According to the TG-dTG thermograms, a mass loss of 0.946% occurred in pure GO around 42˚C. This loss is thought to belong to the water adsorbed on GO. In the thermograms of mGO obtained at the end of the reaction, the peak seen approximately at 100 ˚C is indicative of the presence of adsorbed water and the mass loss seen around 306 ˚C is thought to belong to the degradation of MAA bound to the GO surface. The total mass loss is 8.6%.

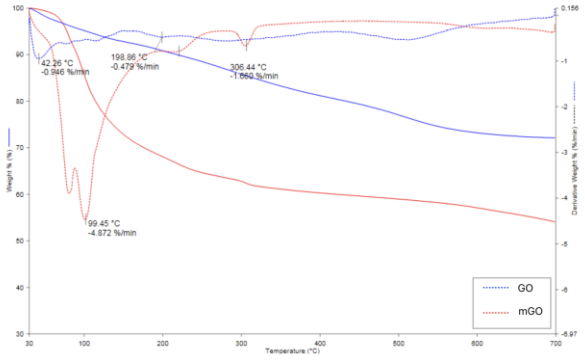

Figure 4. TG-dTG thermograms of GO and mGO

3.3. SEM Analysis

As shown in Figure 5, GO particles showed a flake-like structure in accordance with the literature [34]. When the SEM images of pure GO and mGO particles are compared, it is clearly seen that some bright regions are added between the GO layers and on the surface in the mGO images. It can be said that these regions indicate the binding of MAA to the surface as a result of surface modification. In addition, the fact that the roughness seen on the pure GO surface is reduced after modification with MAA supports that the surface is modified with MAA [28, 29, 30].

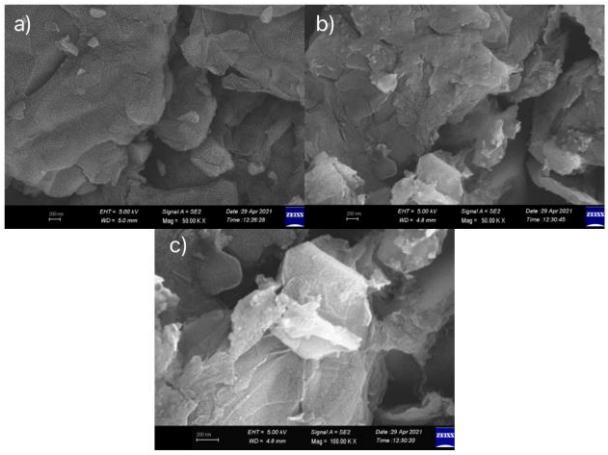

Figure 5. SEM images of (a)pure GO at mag: 50.00 kx, (b) mGO at mag: 50.00 kx , (c) mGO at mag: 100.00 **kx**

3.4. Dispersion Stability in Water

Images of the GO and mGO aqueous solutions at 1, 5, 15, 30 minutes are given in Figure 6. In the photographs, it is clearly seen that unmodified GO particles reach the bottom in a short time, whereas GO whose surface has been modified with MAA maintains its dispersion stability in water for a long time. This confirms the modification of GO and also shows that the dispersion stability of GO in water is significantly improved.

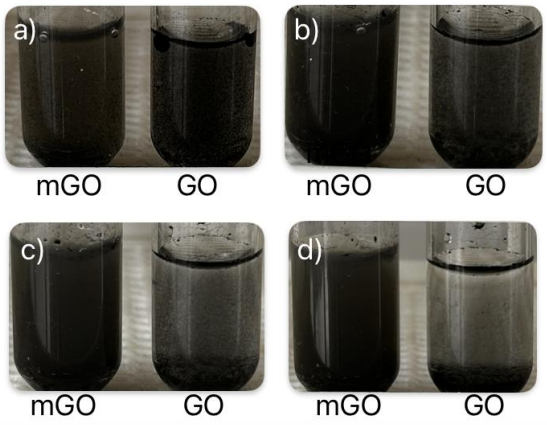

Figure 6. Images of the GO and mGO aqueous solutions at 1min. (a), 5 min. (b), 15 min. (c) and 30 min. (d)

4. Conclusion

The results obtained in this study demonstrate the feasibility of using enzymatic techniques to modify the surface of GO. In this way, by developing the enzymatic surface modification method, a reliable and ecological alternative process for surface modification has been proposed. Therefore, it is possible to readily create alternative materials that possess excellent biocompatibility and do not produce hazardous consequences; the properties of these materials can be improved and their current usage areas, especially in the field of biotechnology, can be increased. Surface modification of graphene oxide is an important area in nanomaterial research and could open the door to many more innovative applications in the future.

Acknowledgment

Canakkale Onsekiz Mart University's Scientific Research Projects Coordination Unit provided funding for this work (Grant Number: FDK-2020-3297).

Author's Contributions

Merve Danışman: Drafted and wrote the manuscript, performed the experiment and result analysis.

Ayhan Oral: Supervised the experiment's progress, result interpretation and helped in manuscript preparation.

Ethics

There are no ethical issues after the publication of this manuscript.

References

[1]. Allen M. J., Tung V. C., Kaner, R. B. Honeycomb carbon: a review of graphene. Chemical reviews. 2010;110(1), 132-145.

[2]. Wei W., Qu X. Extraordinary physical properties of functionalized graphene. Small. 2012;8(14), 2138-2151.

[3]. Lonkar S. P., Deshmukh Y. S., Abdala A. A. Recent Advances in Chemical Modifications of Graphene Recent Advances in Chemical Modifications of Graphene. Nano Research. 2015;8(4), 1039-1074.

[4]. Adetayo A., Runsewe D. Synthesis and fabrication of graphene and graphene oxide: A review. Open journal of composite materials, 2019;9(02), 207.

[5]. Khine Y. Y., Wen X., Jin X., Foller T., Joshi R. Functional groups in graphene oxide. Physical Chemistry Chemical Physics, 2022;24(43), 26337-26355.

[6]. Farjadian F., Abbaspour S., Sadatlu M. A. A., Mirkiani S., Ghasemi A., Hoseini-Ghahfarokhi M., Hamblin M. R. et al. Recent developments in graphene and graphene oxide: Properties, synthesis, and modifications: A review. ChemistrySelect. 2020;5(33), 10200-10219.

[7]. Yang Y., Han C., Jiang B., Iocozzia J., He C., Shi D., et al. Graphene-based materials with tailored nanostructures for energy conversion and storage. Materials Science and Engineering: R: Reports. 2016;102, 1-72.

[8]. AshokKumar S. S., Bashir S., Ramesh K., Ramesh S. A review on graphene and its derivatives as the forerunner of the two-dimensional material family for the future. Journal of Materials Science. 2022;57(26), 12236-12278.

[9]. Wei X., Meng Z., Ruiz L., Xia W., Lee C., Kysar J. W., et al. Recoverable slippage mechanism in multilayer graphene leads to repeatable energy dissipation. ACS nano. 2016;10(2), 1820-1828.

[10]. Dramou P., Dahn S. L., Wang F., Sun Y., Song Z., Liu H., et al. Current review about design's impact on analytical achievements of magnetic graphene oxide nanocomposites. TrAC Trends in Analytical Chemistry. 2021;137, 116211.

[11]. Yu W., Sisi L., Haiyan Y., Jie L. Progress in the functional modification of graphene/graphene oxide: A review. RSC advances. 2020;10(26), 15328-15345.

[12]. Liu J., Chen S., Liu Y., Zhao B. Progress in preparation, characterization, surface functional modification of graphene oxide: A review. Journal of Saudi Chemical Society. 2022;26(6), 101560.

[13]. Kuila T., Bose S., Mishra A. K., Khanra P., Kim N. H., Lee J. H. Chemical functionalization of graphene and its applications. Progress in Materials Science. 2012;57(7), 1061-1105.

[14]. Chhabra V. A., Deep A., Kaur R., Kumar R. Functionalization of graphene using carboxylation process. Int. j. adv. sci. eng. Technol. 2012;4, 13-19.

[15]. Joshi D. J., Koduru J. R., Malek N. I., Hussain C. M., Kailasa S. K. Surface modifications and analytical applications of graphene oxide: A review. TrAC Trends in Analytical Chemistry. 2021;144, 116448.

[16]. Huang G., Chen Z., Li M., Yang B., Xin M., Li S., et al. Surface functional modification of graphene and graphene oxide. Acta Chimica Sinica. 2016;74(10), 789.

[17]. Jin Y., Zheng Y., Podkolzin S. G., Lee W. Band gap of reduced graphene oxide tuned by controlling functional groups. Journal of Materials Chemistry C. 2020;8(14), 4885-4894.

[18]. Silva M., Alves N. M., Paiva M. C. Graphene-polymer nanocomposites for biomedical applications. Polymers for Advanced Technologies. 2018;29(2), 687-700.

[19]. Wang J., Liang G., Zhao W., Zhang Z. Enzymatic surface modification of PBO fibres. Surface and Coatings Technology. 2007;201(8), 4800–4804.

[20]. Qiu X., Hong Z., Hu J., Chen L., Chen X., Jing X. Hydroxyapatite Surface Modified by L -Lactic Acid and Its Subsequent Grafting Polymerization of L -Lactide. Biomacromolecules. 2005;1193–1199.

[21]. Battistel E., Morra M., Marinetti M. Enzymatic surface modification of acrylonitrile fibers. Applied Surface Science. 2001;177(1–2), 32–41.

[22]. Danisman M., Berisha A., Dagdag O., Oral, A. Surface modification of hydroxyapatite with enzyme-catalyzed reaction: Computation-supported experimental studies. *Materials* Chemistry and Physics. 2022;289, 126448.

[23]. Chen J., Dai F., Zhang L., Xu J., Liu W., Zeng S., et al. Molecular insights into the dispersion stability of graphene oxide in mixed solvents: Theoretical simulations and experimental verification. Journal of colloid and interface science. 2020;571, 109-117.

[24]. Rana K., Kaur H., Singh N., Sithole T., Siwal S. S. Graphene-based materials: Unravelling its impact in wastewater treatment for sustainable environments. Next Materials. 2024;3, 100107.

[25]. Goncalves G., Marques P. A. A. P., Granadeiro C. M., Nogueira H. I. S., Singh M. K., Gr J. Surface Modification of Graphene Nanosheets with Gold Nanoparticles : The Role of Oxygen Moieties at Graphene Surface on Gold Nucleation and Growth. Chem. Mater. 2009; 21, 20, 4796–4802.

[26]. Salihi E. Ç., Wang J., Coleman D.L., Siller L. Enhanced removal of nickel (II) ions from aqueous solutions by SDS-functionalized grapheme oxide. Journal of Seperation Sicence and Technology. 2016;51(8), 1317-1327.

[27]. Gao J., Huang B., Lei J., Zheng Z. Photografting of Methacrylic Acid Onto Hydroxyapatite Particles Surfaces. Journal of Applied Polymer Science. 2010; 115, 2156–2161.

[28]. Peng S., Liu C., Fan X. Surface Modification of Graphene Oxide by Carboxyl-Group : Preparation, Characterization, and Application for Proteins Immobilization, Integrated Ferroelectrics. 2015;163:42–53.

[29]. Sahoo S., Karthikeyan G., Nayak G. C., Das C. K. Modified graphene/polyaniline nanocomposites for supercapacitor application. Macromolecular Research. 2012;20(4), 415–421.

[30]. Sharma R., Chisti Y., Benarjae Chand U. Production, purification, characterization, and applications of lipases, Biotechnology Advances. 2019;19, 627–662.

Celal Bayar University Journal of Science

Synthesis and Catalytic Properties of Palladium Complex with Histamine Scaffold

Sinem Çakır[1], Hayati Türkmen[1]*

[1] Department of Chemistry, Faculty of Science, Ege University, Bornova, 35100 Izmir, Türkiye

* hayatiturkmen@hotmail.com
* Orcid No: 0000-0001-7411-2652

Received: 9 July 2024
Accepted: 29 August 2024
DOI: 10.18466/cbayarfbe.1513027

Abstract

In catalytic transformations, electronic s-donor properties are signifcantly affected by the presence of the heterocyclic skeleton Among heterocyclic skeletons, imidazole is among the most preferred in catalyst chemistry. In addition, the application of palladium complexes in sp2-sp2 carbon-carbon bond formation reactions has been successful. For this purpose, in the study, palladium complex carrying histamine moiety was systematically prepared to catalyze the Suzuki-Miyaura cross coupling reaction of bromobenzene with arylboronic acids to form biaryls in the presence of NaOH as base. All synthesized compound and palladium complex were fully characterized by Fourier Transform Infrared (FTIR) and ^{1}H- and ^{13}C-NMR spectroscopies. As a result of the investigation of the optimum conditions for the Suzuki-Miyaura cross coupling reaction, was determined that it was 30 minute, 82°C, NaOH as the base, and IPA-H_2O as the solvent. The presence of the bulky ditertbutyldicarbonate group, which is connected via the N atoms of the histamine skeleton in the structure, and the binding of Pd metal were determined by blanck test experiments to show that it affects the catalytic activity. As a result of the catalytic experiments, it was determined that the synthesized palladium complex was moderately effective in the Suzuki-Miyaura cross-coupling reaction.

Keywords: Palladium, Ionic liquid, Catalysis

1. Introduction

Carbon-carbon bond formation reactions with the help of palladium catalysis have become a frequently used method in organic synthesis [1-3]. In fact, the use of organopalladium complex as a catalyst won the Nobel Prize in Chemistry in 2010. Today, palladium complexes are widely used as catalysts [4,5]. Especially in recent years, many synthetic methods have been developed due to the numerous applications of palladium catalysts in various natural products, agrochemicals and pharmaceutical products, as well as in the preparation of advanced materials on both laboratory and industrial scales [6-10].

The interaction of organoboron reagents with aryl halides to form biaryl derivatives, the palladium-catalyzed traditional Suzuki-Miyaura cross-coupling reaction, has emerged as a powerful tool in organic synthesis in the last few years. The main purpose here is to ensure the formation of sp^2-sp^2 carbon-carbon bonds. However, considering most of the Suzuki Miyaura cross coupling reactions, it cannot effectively convert aryl chlorides, which are among the cheapest and easily available aryl halides [11,14].

Although phosphine-based ligands have been used to improve the catalytic conversion in cross-coupling reactions, N-heterocyclic carbene (NHC) ligands have recently attracted attention in light of many positive properties such as relatively high thermal stability and moisture. The electronic σ-donor properties of NHCs are significantly affected by the presence of the heterocyclic skeleton [15-21].

Although N-aryl classification comparison has been extensively studied in the studies conducted to date, studies on modification of the NHC-derived backbone are quite limited [22]. It is thought that the steric effects in the structure positively affect the catalytic transformations because such a modification will greatly

increase the steric and electronic capabilities of the palladium center [23,24]. In 2012, Zhou and co-workers synthesized acenaphthoimidazolylidene palladium complexes. They reported that they synthesized highly effective and general catalysts for sterically hindered Suzuki-Miyaura cross-coupling reactions in excellent yields using low catalyst loadings under mild reaction conditions. The high catalytic activity of these Pd complexes they synthesized emphasized that in addition to the concept of "flexible steric bulk", the σ-donor properties of the NHC ligands are also important for accelerating the transformations [25]. Glorius et. al. introduced a unique family of N-heterocyclic carbenes derived from bioxazolines (IBiox) for application in transition metal catalysis. The ligands in the scaffold are electron-rich, sterically demanding and have limited flexibility. Their activity was investigated in Suzuki-Miyaura cross-coupling of sterically hindered aryl chlorides and boronic acids. For the first time, tetraortho-substituted biaryls with methyl and larger ortho-substituents were synthesized from aryl chlorides using the Suzuki-Miyaura method [26]. Organ et. al. summarized recent advances with the PEPPSI style of Pd–NHC catalysts in aryl aminations and aryl sulfinations from both applications and mechanistic standpoints [27]. Lough et al synthesized a series of N-heterocyclic carbene catalysts in large volumes and evaluated their catalytic transformations in the Suzuki-Miyaura reaction. They concluded that the cyclopentyl-substituted catalyst was nearly inactive, suggesting that “flexible bulk” was required to support these transformations [28]. In a study by our group in 2018, a series of piperidoimidazolinium salts with different chain lengths (butyl, octyl, dodeacyl, octadeacyl) and their Pd–N-heterocyclic carbene complexes with pyridine were synthesized and characterized using elemental analysis and spectroscopic methods. The effects of these ligands on catalyst activation and the performance of the complexes were investigated in Suzuki–Miyaura reactions of arylboric acid with aryl chlorides. The complex with the ligand with the longest chain length was found to be the most active. The results showed that the alkyl chain length of piperidoimidazolin-2-ylidene controls the distribution and composition of the nanoparticles and affects the catalytic activity [29]. In a study conducted in 2021, a series of azolium salts containing benzothiazolium, benzimidazolium and imidazolium bearing CN-substituted benzyl moiety and their palladium complexes were synthesized. The synthesized palladium complexes were systematically prepared to catalyze the acylative Suzuki–Miyaura coupling reaction of acyl chlorides with arylboronic acids to form benzophenone derivatives in the presence of potassium carbonate as a base and to catalyze the conventional Suzuki–Miyaura coupling reaction of bromobenzene with arylboronic acids [30].

In this context, we prepared the NHC precursor and its palladium complex, which has histamine as its main scaffold, to investigate whether it would be useful for the Suzuki-Miyaura cross-coupling reaction. The reaction of interest was carried out under mild conditions and moderate catalytic conversions were obtained.

2. Materials and Methods

2.1. Chemicals

Reagents used in the synthesis are dichloromethane (Sigma Aldrich), dioxane (Sigma Aldrich), tetrahydrofuran (Sigma Aldrich), dimethyl sulfoxide (Riedel-de Haen), Boc_2O (Merck); Histamine (Precious Metals Online), $PdCl_2$ (Sigma Aldrich) were commercially purchased.

2.2. Instrumentations

^1H NMR and ^{13}C NMR spectra were recorded on a Varian AS 400 Mercury instrument. $CDCl_3$ were used as solvents. Chemical shifts are given in ppm relative to TMS; linkage constants (*J*) in Hz. FTIR spectra were recorded on a Perkin Elmer Spectrum 100 series. Analyses were performed with a gas chromatograph from Agilent Model 7820A Series, equipped with HP ECD detector systems. The analytical column used was a DB-5-MS column (30 m × 250 μm I.D. and film thickness 0.25 μm). Helium and nitrogen (99.99%) were used as carrier and make-up gas, respectively. The GC split valve was closed for 5 min., and helium was used as carrier gas with a flow rate of 15.0 mL min^{-1}. The flow rate of carrier gas was adjusted at 1.0 mL min^{-1}. The oven temperature program will be 50 °C for 5 minutes, increasing to 150 °C at 25 °C min^{-1}, increasing to 220 °C at 10 °C min^{-1}, and increasing to 280 °C at 5 °C min^{-1} will be released, the total running time is set to be 33 min. At the end of the analysis the fiber was cleaned by inserting it into the GC injection port for 15 min at 250 °C. The SPME holder for manual sampling was obtained from Supelco (Bellefonte, PA, USA).

General procedure for Suzuki cross-coupling reaction

A two-necked 25.0 ml flask fitted with a reflux condenser and septum was charged with aryl bromide (1.0 mmol), phenylboronic acid (1.0 mmol), NaOH (0.5 mmol) and the catalyst (0.5 mol%) in IPA–H_2O mixture (2 ml, 1:1). The mixture was heated to 82 °C at 30 min. under an air. For catalytic conversion monitoring, a small amount of sample was periodically withdrawn by syringe and conversion was analyzed by GC chromatography.

2.3. Synthesis of Ligand and its Palladium Complex

2.3.1. Synthesis and characterization of compound 1

Histamine dihydrochloride and Boc_2O (ditertbutyldicarbonate) were mixed in a mixture of dioxane and water in a balloon at room temperature for

24 hours. The amino group in its structure is protected by the Boc_2O (ditertbutyldicarbonate) structure. At the end of the reaction, dioxane and water were removed from the medium by simple distillation, and the remaining white solid was dried under vacuum. ^{1}H NMR (400 MHz, $CDCl_3$): δ 8.00 (s, 1 H, NC*H*N), 7.13 (s, 1 H, N-C*H*), 3.41 (d, J = 8 Hz, 2 H, CH_2) 2.72 (t, J = 8 Hz, 2 H, CH_2), 1.60 (s, 9 H, C-(CH_3)$_3$), 1.43 (s, 9 H, C-(CH_3)$_3$). ^{13}C NMR (100 MHz, $CDCl_3$): δ 156.2, 134.9, 79.3, 40.3, 28.4, 27.5. FT-IR (KBr disk, cm^{-1}): 3084, 2923, 2849, 2477, 1624, 1525, 1473, 1436, 1236, 1148, 1110, 1088, 1029, 956, 905, 852, 805, 730, 517.

2.3.2. Synthesis and characterization of complex Pd1

1 and bisacetonitrile palladium dichloride were refluxed in dichloromethane at 39 °C under gas for 24 hours. At the end of the reaction, the solvent was removed by simple distillation. Then, a yellow solid was obtained. The complex **Pd1** was isolated by column chromatography. ^{1}H NMR (400 MHz, $CDCl_3$): δ 8.35 (s, 2 H, NC*H*N), 7.19 (s, 2 H, N-C*H*), 7.40 (s, 2 H, N-C*H*), 5.00 (s, 2 H, N*H*), 3.93 (d, J = 8 Hz, 4 H, CH_2) 3.35 (t, J = 8 Hz, 4 H, CH_2), 1.61 (s, 18 H, C-(CH_3)$_3$), 1.44 (s, 18 H, C-(CH_3)$_3$). ^{13}C NMR (100 MHz, $CDCl_3$): δ 156.0, 144.9, 140.2, 138.2, 115.1, 87.7, 79.3, 39.1, 28.4, 27.7, 15.2. FT-IR (CsI disk, cm^{-1}): 3393, 3151, 2975, 2932, 1774, 1706, 1595, 1495, 1371, 1323, 1304, 1276, 1245, 1147, 1060, 1041, 1009, 952, 868, 841, 800, 789, 679, 606, 538, 492, 464, 428.

3. Results and Discussion

3.1. Synthesis of the azolium salt (1) and Pd(II) complex

Compound **1** was prepared by a one-pot reaction by histamine dihydrochloride with Boc_2O (ditertbutyldicarbonate) in a dioxane-water mixture at room temperature for 24 hours. The general synthesis route of the ligand is given in scheme 1. The compound was obtained as a white solid in 79% yield and exhibited good solubility in polar solvents. It was characterized by ^{1}H-NMR, ^{13}C-NMR and Fourier transform infrared (FT-IR) spectroscopies. The C_2–H resonance, NC*H*N peak of the imidazolium salt, was observed at δ = 8.00 ppm as a sharp singlet in the ^{1}H NMR spectrum. Additionally, there are C-(CH_3)$_3$ signals corresponding to a total of 18 protons at 1.60 and 1.43 ppm as evidence of the binding of the Boc_2 group to histamine. In the ^{13}C NMR spectrum (**1**) the chemical shift of NC*N* sp^2 carbon atoms appears at 156.2 ppm. In the high frequency region of the IR spectrum, a symmetric band of moderate intensity was observed at 3084 cm^{-1} due to the overlap of N-H group vibrations with hydrogen-bonded vibrations, and at 2923 cm^{-1} for C-H group vibrations. As for the vibrations of C=O and C-O groups, a strong band was observed at 1423 cm^{-1} and 1148 cm^{-1}, respectively.

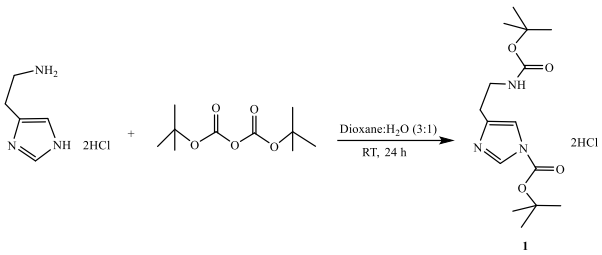

Scheme 1 Synthesis route to the compound **1**.

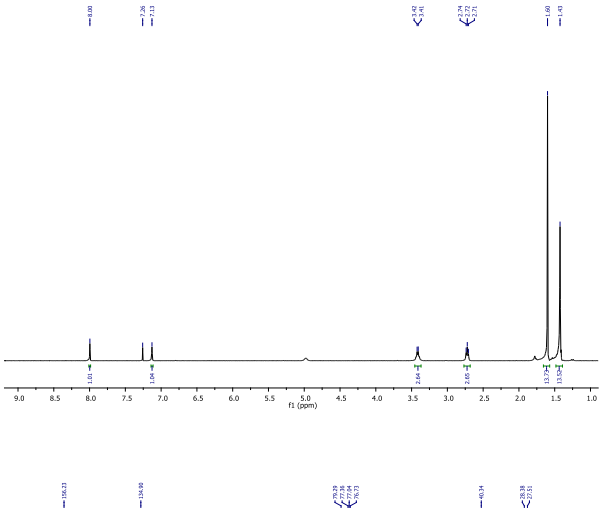

Figure S1. ^{1}H and ^{13}C NMR spectrums of compound **1** ($CDCl_3$).

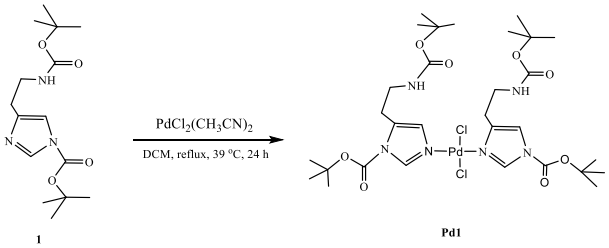

Scheme 2 Synthesis route to the complex **Pd1**.

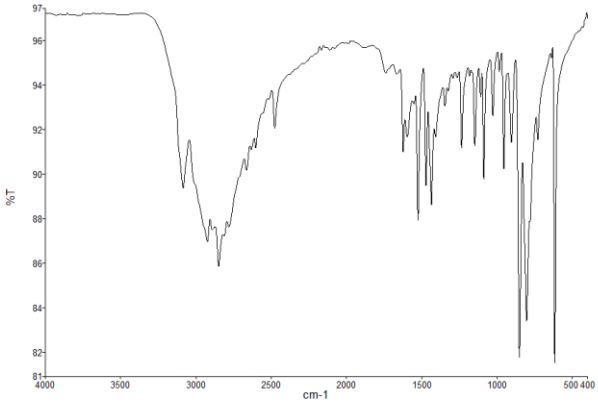

Figure S2. FT-IR spectrums of compound **1**.

The new palladium complex (**Pd1**) was obtained by refluxing in dichloromethane in the presence of bis(acetonitrile)palladium dichloride overnight (Scheme 2). The synthesized palladium complex was obtained in 66% yield as a yellow solid with good solubility in polar solvents and resistant to air and moisture. It was characterized by ^{1}H-NMR, ^{13}C-NMR and Fourier transform infrared (FT-IR) spectroscopies. After binding to palladium metal, the C_2-H resonance, the NC*H*N peak of the imidazolium salt, was observed at δ = 8.35 ppm as a sharp singlet in the ^{1}H NMR spectrum. The reason for the shift to the high ppm low area observed here is due to the change in electron density and the shielding effect due to the bonding of palladium metal. This shift is evidence of the bonding of palladium to us. Unlike compound **1**, medium intensity peaks were observed between 468 cm^{-1} and 424 cm^{-1}, which are defined as the fingerprint region of Pd-Cl bonds in the **Pd1** complex.

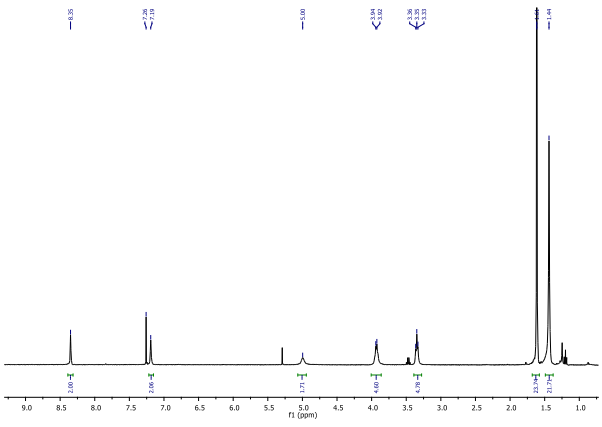

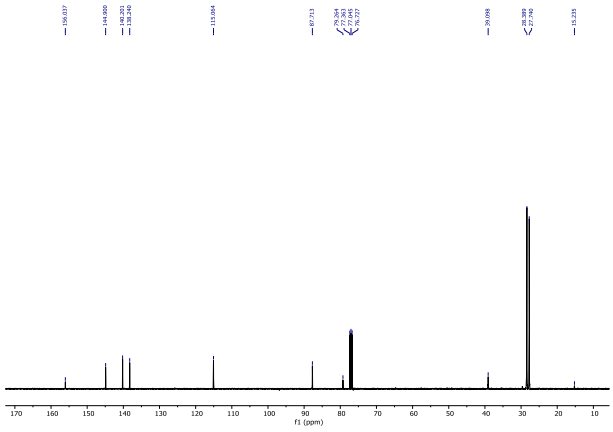

Figure S3. ^{1}H and ^{13}C NMR spectrums of compound **Pd1** ($CDCl_3$).

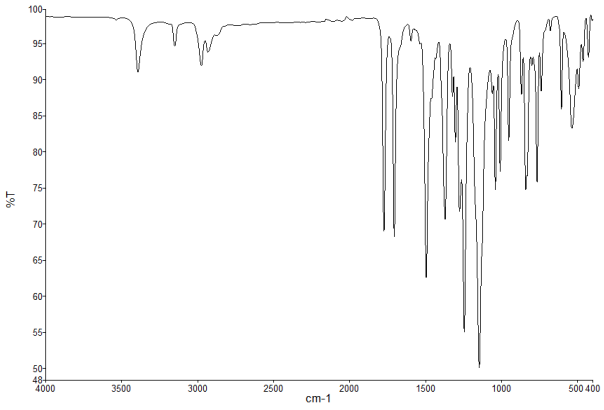

Figure S4. FT-IR spectrums of complex **Pd1**.

To look into the effect of the palladium complex on the Suzuki–Miyaura cross-coupling reaction, a model reaction was produced using 4-bromoacetophenone (1 mmol), phenyl boronic acid (1.5 mmol), and KOH (0.5 mmol). Conversions were determined by the GC. In optimization studies, the appropriate solvent system was determined as 2 mL (1:1, IPA-H_2O). In this catalytic cycle, the role of IPA was to dissolve aryl bromides and the role of water was to activate phenyl boronic acid and the base. Although weak bases such as $NaHCO_3$ and K_2CO_3 were used, the reaction was carried out efficiently (Table 1, entries 9, 6). Although KO^{t}Bu was a strong base, the reaction did not produce effective results (Table 1, entry 10). The best efficiency was achieved in Cs_2CO_3 and NaOH (Table 1, entries 7, 5). However, due to the price of Cs_2CO_3, substrate experiments were conducted with NaOH. Using only 2-propanol as the solvent negatively affected the catalytic conversion (Table 1, entry 1). A blank test was performed to investigate the effect of the presence of the catalyst. No product formation was observed in the reaction medium without addition of catalyst (Table 1, entry 4). Reducing the

catalyst loading into the catalytic cycle negatively affected the efficiency (Table 1, entry 2).

Evaluation of the substrate scope of the reaction of various phenylboronic acids with various bromoacetophenone derivatives under optimized reaction conditions was carried out (Table 2). Bearing electron-withdrawing or electron-donating substituents in the para and ortho positions, such as 4-CH_3, 4-tert-butyl, 4-Br, 4-F, 4-CF_3, 2-CF_3, 2-CH_3 and 4-F-3-COH converted into a large number of arylboronic acid-related target products (Table 2, entries 1-13). Results in the range of 47-88% were found in the obtained catalytic conversions. Aryl bromides formed from 4-CH_3, 4-OCH_3, 4-NO_2 and 4-CHO in the para position gave 4-methyl-biphenyl, 4-methoxybiphenyl 4-nitrobiphenyl and 4-carbaldehydebiphenyl products in yields of 64%, 65%, 63% and 59%, respectively (Table 2, entries 1-4). Also, different aryl phenyl boronic acids were studied. Phenyl boronic acids formed from these substituents 4-CH_3, 4-Br and 4-*t*-Bu in the para position gave the products 1-(4'-methyl-[1,1'-biphenyl]-4-yl)ethan-1-one, 1-(4'-bromo-[1,1'-biphenyl]-4-yl)ethan-1-one and 1-(4'-tertbutoxy-[1,1'-biphenyl]-4-yl)ethan-1-one in good yields of 69%, 59% and 65%, respectively (Table 4, entries 5, 6, 13). The effect of CH_3 group in the ortho and meta positions of aryl phenyl boronic acid was investigated. As a result of the catalytic cycle, phenyl boronic acids formed from 2-CH_3 and 3-CH_3 gave 1-(2'-methyl-[1,1'-biphenyl]-4-yl)ethan-1-one and 1-(3'-methyl-[1,1'-biphenyl]-4-yl)ethan-1-one products with good yields of 57% and 60%, respectively (Table 4, entries 7, 8). The effect of CF_3 group in para and ortho positions of aryl phenyl boronic acid was investigated. As a result of the catalytic cycle, phenyl boronic acids formed from 4-CF_3 and 2-CF_3 gave 1-(4'-(trifluoromethyl)-[1,1'-biphenyl]-4-yl)ethan-1-one and 1-(2'-(trifluoromethyl)-[1,1'-biphenyl]-4-yl)ethan-1-one products with good yields of 77% and 71%, respectively (Table 4, entries 9, 10). In addition, the increase of the CH_3 group in phenyl boronic acid was observed with a yield of 73% to 1-(2',5'-dimethyl-[1,1'-biphenyl]-4-yl)ethan-1-one (Table 4, entry 11).

Table 1. Screening of reaction conditions in the Suzuki-Miyaura cross-coupling reaction.

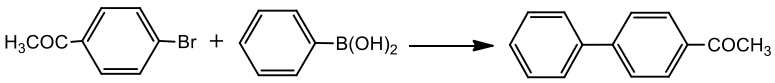

Entry	Cat. (%mol)	Solvent	Base	Yield (%)
1	0.5	IPA	NaOH	76
2	0.2	IPA	NaOH	54
3	0.5	IPA–H_2O	NaOH	88
4	-	IPA–H_2O	NaOH	trace
5	0.5	IPA–H_2O	KOH	66
6	0.5	IPA–H_2O	K_2CO_3	75
7	0.5	IPA–H_2O	Cs_2CO_3	95
8	0.5	IPA–H_2O	Na_2CO_3	35
9	0.5	IPA–H_2O	$NaHCO_3$	67
10	0.5	IPA–H_2O	KO^{t}Bu	55
11[b]	0.5	IPA–H_2O	NaOH	37
12[c]	0.5	IPA–H_2O	NaOH	52

[a] Reaction conditions: 4-bromoacetophenone (1.0 mmol), phenyl boronic acid (1.0 mmol), base (0.5 mmol), IPA-H_2O = 1:1 (2.0 ml), 82°C, 30 min. [b] $PdCl_2(NCCH_3)_2$ (0.5 mol %). [c] **1** (0.5 mol %).

Table 2. Effects of substrate for Suzuki-Miyaura Cross-Coupling reaction

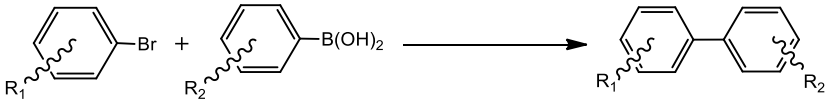

Entry	R_1	R_2	Yield (%)	TON/TOF
1	4-CH_3	H	64	128/256
2	4-$COCH_3$	H	65	130/260
3	4-NO_2	H	63	126/252
4	4-CHO	H	59	118/236
5	4-$COCH_3$	4-CH_3	69	138/276
6	4-$COCH_3$	4-Br	59	118/236
7	4-$COCH_3$	2-CH_3	57	114/228
8	4-$COCH_3$	3-CH_3	60	120/240
9	4-$COCH_3$	4-CF_3	77	154/308
10	4-$COCH_3$	2-CF_3	71	142/284
11	4-$COCH_3$	2,5-Me	73	146/292
12	4-$COCH_3$	4-F,3-COH	47	94/188
13	4-$COCH_3$	4-t-Bu	65	130/260

Reaction conditions: Aryl bromide (1.0 mmol), phenyl boronic acid (1.0 mmol), cat. **Pd1** (0.5 mol %), NaOH (0.5 mmol), IPA-H_2O=1:1 (2.0 ml), 82 ^oC, 30 min., TON = [yield]/[cat.], TOF = [TOF]/[h].

4. Conclusion

As a result, a series of studies were conducted to systematically examine the effect of the palladium complex bearing the histamine group on the Suzuki-Miyaura cross-coupling reaction. The structure of the synthesized complex and compound was elucidated with ^1H-^{13}C NMR and fourier transform infrared (FTIR) spectroscopies. Different base, solvent and catalyst loadings were investigated to reach optimum conditions in the reaction. Blanck test experiments were conducted to investigate the effect of the catalyst on the catalytic transformation. In these experiments, it was determined that the transformation remained at 37% when only $PdCl_2(NCCH_3)_2$ was added to the reaction medium as a catalyst. In addition, the addition of ligand to the reaction medium gave the transformation only as 52%. These experiments clearly demonstrated the effect of the **Pd1** catalyst we synthesized. At the end of the experiments, the optimum conditions were determined as 30 minutes, 82 °C, NaOH as base and 0.5 catalyst loading. As a result of the derivatization, efficiencies between 47-88% were obtained. It was observed that the groups in the para-position gave the desired final products with better yields compared to the groups in the meta- and ortho- positions. These obtained catalytic transformations provide a good basis for further studies.

Acknowledgement

Financial support from Ege University (Project 22224) is gratefully acknowledged.

Author's Contributions

Hayati Türkmen: Determination of the topic, interpretation of the results and preparation of the draft were carried out.

Sinem Çakır: Performed the experiment and wrote the publication

Ethics

There are no ethical issues regarding the publication of this study.

References

[1]. Alonso, F, Beletskaya, IP, Yus, M. 2008. Non-conventional methodologies for transition-metal catalysed carbon–carbon coupling: a critical overview. Part 2: The Suzuki reaction. *Tetrahedron*; 64: 3047.

[2]. Knappke, CEI, Jacobi von Wangelin, A. 2011. 35 years of palladium-catalyzed cross-coupling with Grignard reagents: how far have we come?. *Chemical Society Reviews*; 40: 4948.

[3]. Jana, R, Pathak, TP, Sigman, MS. 2011. Advances in Transition Metal (Pd,Ni,Fe)-Catalyzed Cross-Coupling Reactions Using Alkyl-organometallics as Reaction Partners. *Chemical Rev*iews; 111: 1417.

[4]. Nicolaou, KC, Bulger, PG, Sarlah, D. 2005. Palladium-Catalyzed Cross-Coupling Reactions in Total Synthesis. *Angewandte Chemie International Edition*; 44: 4442–4489.

[5]. Corbet, JP, Mignani, G. 2006. Selected Patented Cross-Coupling Reaction Technologies. *Chemical Rev*iews; 106: 26512710.

[6]. Levin, E, Ivry, E, Diesendruck, CE, Lemcoff, NG. 2015. Water in N-Heterocyclic Carbene-Assisted Catalysis. *Chemical Rev*iews; 115: 4607.

[7]. Yin, L, Liebscher, J. 2007. Carbon−Carbon Coupling Reactions Catalyzed by Heterogeneous Palladium Catalysts. *Chemical Rev*iews; 107: 133–137.

[8]. Beletskaya, IP, Alonso, F, Tyurin, V. 2019. The Suzuki-Miyaura reaction after the Nobel prize. *Coordination Chemistry Reviews*; 385: 137–173.

[9]. Torborg, C, Beller, M. 2009. Recent Applications of Palladium-Catalyzed Coupling Reactions in the Pharmaceutical, Agrochemical, and Fine Chemical Industries. *Advanced Synthesis Catalysis*; 351: 3027–3043.

[10]. So, CM, Kwong, FY. 2011. Palladium-catalyzed cross-coupling reactions of aryl mesylates. *Chemical Society Reviews*; 40: 4963.

[11]. Grushin, VV, Alper, H. 1994. Transformations of Chioroarenes, Catalyzed by Transition-Metal Complexes. *Chemical Reviews*; 94: 1047-1062.

[12]. Diederich, F, Stang, PJ. uzuki, A. In Metal-Catalyzed Cross-Coupling Reactions, Eds.; Wiley-VCH: Weinheim, Germany, 1998, Chapter 2.

[13]. Shen, W. 1997. Palladium catalyzed coupling of aryl chlorides with arylboronic acids. *Tetrahedron Letter*; 38: 5575-5578.

[14]. Miyaura, N, Yanagi, T, Suzuki, A. 2006. The Palladium-Catalyzed Cross-Coupling Reaction of Phenylboronic Acid with Haloarenes in the Presence of Bases. *Synthesis Communation*; 11: 513-519.

[15]. Grasa, GA, Viciu, MS, Huang, J, Zhange, C, Trudell, ML, Nolan, SP. 2002. Suzuki−Miyaura Cross-Coupling Reactions Mediated by Palladium/Imidazolium Salt Systems. *Organometallics*; 21: 2866.

[16]. Nelson, DJ, Nolan, SP. 2013. Quantifying and understanding the electronic properties of N-heterocyclic carbenes. *Chemical Society Reviews*; 42: 6723.

[17]. Mitchell, MB, Wallbank, PJ. 1991. Coupling of heteroaryl chlorides with arylboronic acids in the presence of [1,4-bis-(diphenylphosphine)butane]palladium(II) dichloride. *Tetrahedron Letter*; 32: 2273-2276.

[18]. Firooznia, F, Gude, C, Chan, K, Satoh, Y. 1998. Synthesis of 4-substituted phenylalanines by cross-coupling reactions: Extension of the methodology to aryl chlorides. *Tetrahedron Letter*; 39: 3985-3988.

[19]. Bumagin, NA, Bykov. VV. 1997. Ligandless palladium catalyzed reactions of arylboronic acids and sodium tetraphenylborate with aryl halides in aqueous media. *Tetrahedron*; 53: 14437-14450.

[20]. Beller, M, Fischer, H, Herrmann, WA, Öfele, K, Brossmer, C. 1995. *Angewandte Chemie International Edition*; 34: 1848-1849.

[21]. Movassagh, B, Hajizadeh, F, Mohammadi, E. 2018. Polystyrene-supported Pd(II)–N-heterocyclic carbene complex as a heterogeneous and recyclable precatalyst for cross-coupling of acyl chlorides with arylboronic acids. *Applied Organometalic Chemistry*; 32: e3982.

[22]. Benhamou, L, Chardon, E, Lavigne, G, Bellemin-Laponnaz, S, César, V. 2011. Synthetic routes to N-heterocyclic carbene precursors. *Chemical Review*; 111: 2705-2733.

[23]. He, X-X, Li, Y, Ma, B-B, Ke, Z, Liu, F-S. 2016. Sterically encumbered tetraarylimidazolium carbene Pd-PEPPSI complexes: highly efficient direct arylation of imidazoles with aryl bromides under aerobic conditions. *Organometallics;* 35: 2655-2663.

[24]. Winkler, A, Brandhorst, K, Freytag, M, Jones, PG, Tamm, M. 2016. Palladium (II) complexes with anionic N-heterocyclic carbene–borate ligands as catalysts for the amination of aryl halides. *Organometallics;* 35: 1160-1169.

[25]. Tu, T, Sun, Z, Fang, W, Xu, M, Zhou, Y. 2012. Robust acenaphthoimidazolylidene palladium complexes: highly efficient catalysts for suzuki–miyaura couplings with sterically hindered substrates. *Organic letters;* 14: 4250-4253.

[26]. Altenhoff, G, Goddard, R, Lehmann, CW, Glorius, F. 2004. Sterically demanding, bioxazoline-derived N-heterocyclic carbene ligands with restricted flexibility for catalysis. *American Chemical Society;* 126: 15195-15201.

[27]. Valente, C, Pompeo, M, Sayah, M, Organ, MG. 2014. Carbon–heteroatom coupling using Pd-PEPPSI complexes. *Organic Process Research & Development;* 18: 180-190.

[28]. Organ, MG, Çalimsiz, S, Sayah, M, Hoi, KH, Lough, AJ. 2009. Pd-PEPPSI-IPent: an active, sterically demanding cross-coupling catalyst and its application in the synthesis of tetra-ortho-substituted biaryls. *Angewandte Chemie International Edition;* 48: 2383-2387.

[29]. Çakır, S, Türkmen, G, Türkmen, H. 2018. Palladium(II) complexes bearing Nalkylpiperidoimidazolin-2-ylidene derivatives: Effect of alkyl chain length of ligands on catalytic activity. *Applied Organometallic Chemistry;* 32: e3969.

[30]. Çakır, S, Kavukcu, SB, Karabıyık, H, Rethinam, S, Türkmen, H. 2021. C(acyl)–C(sp2) and C(sp2)–C(sp2) Suzuki–Miyaura cross-coupling reactions using nitrilefunctionalized NHC palladium complexes. *RSC advances;* 11: 37684-37699.

Celal Bayar University Journal of Science

Empirical Advancements in Field Oriented Control for Enhanced Induction Motor Performance in Electric Vehicle

Mussaab Alshbib[1], Sohayb Abdulkerim[2]*

[1]Sham University, Ezaz, Syria
[2] Department of Aerospace Engineering, Gaziantep University, 27310, Gaziantep, Türkiye

*karim@gantep.edu.tr,
*Orcid No: 0000-0002-3448-9129

Received: 15 March 2024
Accepted: 31 August 2024
DOI: 10.18466/cbayarfbe.1453798

Abstract

This paper introduces an advanced Field Oriented Control (FOC) strategy, specifically tailored for electric vehicle drivetrains, that streamlines the tuning process of PI controllers within the α and β coordinates of the synchronous reference frame. The innovative approach mitigates torque and stator current fluctuations while maintaining a constant switching frequency and improves inverter voltage use through third harmonic injection. Crucially, the theoretical underpinnings and simulation outcomes, obtained via MATLAB/Simulink, are substantiated by rigorous experimental verification. A dedicated DS1103-controlled testbed replicates real-world electric vehicle conditions, demonstrating the practical efficacy of the FOC method. The experimental results underscore the robustness of the control strategy across a broad range of operating scenarios, establishing a significant leap forward in electric vehicle control technology.

Keywords: Voltage Source Inverter; Induction Motor, Electric Vehicles, Control Nonlinearities, Control System Synthesis

1. Introduction:

Several types of electric motors are widely used for EVs, including DC-brushed motors, DC brushless motors, permanent magnet synchronous motors (PMSMs), induction motors (IMs), and switch-reluctant motors (SRMs). The induction motors are the most commonly used in industry and traction applications since they are of good construction, lower cost, ease of fault detection, and lower power to weight ratio when compared with the permanent magnet synchronous motors [1]. In various industrial applications, such as robotics, heavy industry, ships, and renewable energy systems, there are two methods known to researchers: Field Oriented control (FOC) [2]-[3], and direct torque and stator flux control (DTC) [4]-[5].

Although the requirements for implementing the FOC strategy are more complex than the DTC strategy, especially the need to estimate or measure speed, it is more widespread and reliable, especially in electric vehicle applications.[6]. Therefore, the efforts of researchers focused on developing this strategy by introducing modern technologies that achieve high reliability while maintaining strong performance at the same time. The implementation of the FOC strategy using PID regulators has been widespread in many applications of FOC, such as driving a BLDC Motor enhanced by parallel optimized technique [7]. In the research [8], a PI regulator was used in the speed control loop of an induction motor with the use of a genetic algorithm to estimate the regulator values. However, this research lacked practical implementation that supported theoretical analysis. DSP based-Fuzzy FOC control method of permanent magnet synchronous motor was performed in [9]. The authors tried to simplify the design of the algorithm by using the toolbox in Matlab. However, they set manual values for parameters in addition to not testing the designed system on a wide range of operating conditions. A similar work to Research [9] was proposed in the paper [10] where the FOC strategy was applied to an induction motor with PI parameter values adjusted with the help of the Fuzzy controller. The speed signal was also obtained from Lunberger's estimator. However, this research was limited to theoretical simulation without practical application.

A modified research proposed by the researchers in [11] by applying the strategy to brushless DC motor with enhanced fuzzy controller. The authors tested their approch in cases of no load and load with variable speed. As it is known, the windup phenomenon is a negative one caused by PI controllers. This phenomenon has been analyzed in [12], which presented a study of solutions of antiwindup techniques to reduce problem of saturation suffered by these controllers in PMSM engines. The most advanced techniques have been introduced into the algorithm such as the use of neural networks as in [13].

The rest of this article is arranged as follows. Section 2 presents a detailed background for the FOC strategy. Section 3 presentes formulation FOC strategy of IM. Simulation and experimental results are outlined in Section 3 and Section 4 to verify the feasibility and effectiveness of the proposed strategy. Finally, the conclusion is performed in Section 5.

2. Theoritcal Background of FOC Algortihm

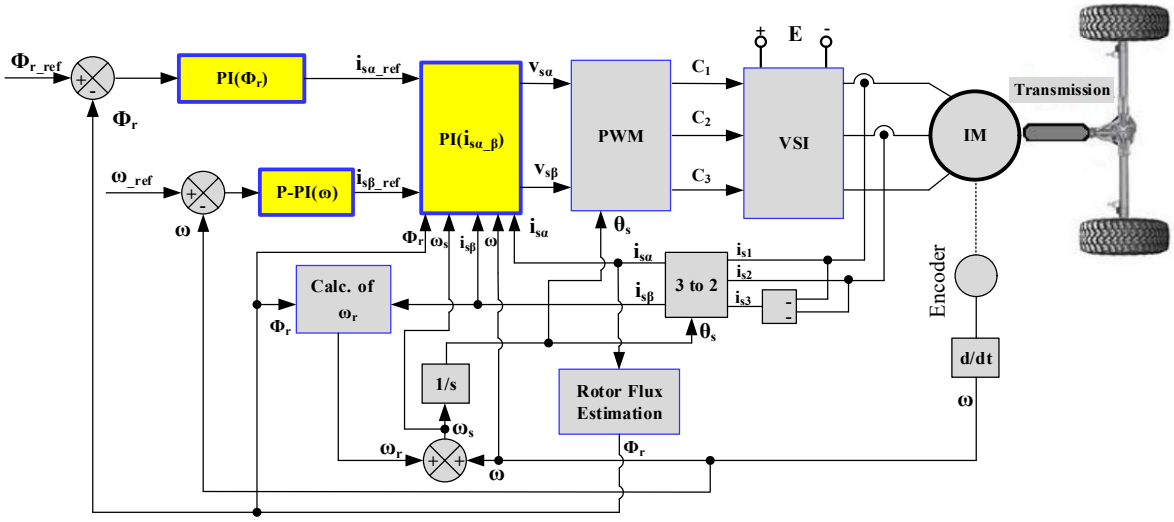

Figure 1. The block diagram of FOC of IM

where the researchers replaced the PID controller in the current loop with a neural network while maintaining the PID regulators in the speed loop. The work is especially noteworthy since it was tested in the field weakining region of PMSM motor, yet it was not without difficulty in tuning and training the network.

Model Predictive Contorl (MPC) principles based PID-FOC techniques to improve the performance in propulsion systems [14], MPC based FOC of the induction motors in electric vehicles [15], or MPC based FOC of five phase PMSM are are some of the research published within this context. In [16], The inverter investment in FOC algorithm was enhanced sliding mode and the injection of the third harmonic component. This proposed method was applied in an [16]- asynchronous generator of single-rotor wind turbine. These techniques have been used in other research in order to suppress the current harmonics [17], and to reduce the oscillations of both torque and magnetic flux [18].

This paper proposes an effective and simple method of field oriented control FOC which is suitable electric vehicles applications. The proposed scheme ensures the low chattering of the torque and the stator currents with fixed frequency. In addition, It is enhanced by using the third harmonic injection technique which improves the utiliy of the inverter voltage.

In fact, the orientation of the field control algorithm varies according to the method of obtaining the orientation angle. The name of direct field orientation (DFOC) control algorithm is given to that algorithm in which the value of the orientation angle is obtained from the direct measurement of the magnetic flux. This method is limited in use due to the difficulty of measuring the magnetic flux (for the stator or the rotor) directly, and it is also costly due to the need for a magnetic flux sensor. In contrast, the Indirect Field Orientation Control (IFOC) algorithm is defined as the algorithm that uses a slip relationship, that is, by adding the speed of the rotor ω with the slip speed ω_r [19]. Due to its dependence on the sliding relationship, it is influenced by machine parameters, yet it is considered the primary method used to flux orientation control of induction motors. Note that in both methods (direct and indirect flux orientation control), the presence of the current control loop stage is preferred. Therefore, Hystereis regulators can be used at this stage or any type of traditional or smart regulator [20].

The detailed block scheme of the direct FOC strategy is shown in Figure (1). It has two loops of control, the first loop is to control the modulus of the rotor flux, while the second one is to control the rotor speed [21]. The three phase currents of the motor are captured, which are used to obtain two phases currents in synchronous reference

Celal Bayar University Journal of Science
Volume 20, Issue 3, 2024, p 47-57
Doi: 10.18466/cbayarfbe.1453798

frame. The orientation angle is calculated depending on the rotor speed calculated from the position of the motor shaft, and load-dependent slip speed. The two phases voltages are introduced within the PWM stage in order to obtain the suitable pulses to be applied to the electronic switches of the mold driving the motor [22].

3. FOC strategy formulation

In the FOC strategy, control is achieved through two separate loops: the rotor flux control loop along the α-axis and the speed control loop along the β-axis. Figure (2) illustrates the block diagram for this structure, detailing the rotor flux control for the α-axis Figure (2a) and the speed control for the β-axis Figure (2b).

The mathematical model in terms of the stator currents of the rotor flux is given as follows [23] [24]:

$$\begin{bmatrix} \frac{d\underline{i}_s^k}{dt} \\ \frac{d\underline{\Phi}_r^k}{dt} \end{bmatrix} = \begin{bmatrix} \frac{1}{\sigma L_s} \\ 0 \end{bmatrix} \underline{V}_s^k + \begin{bmatrix} -\frac{1}{\sigma\tau_s} - \frac{L_m^2}{\sigma\tau_r L_s L_r} - j\omega_k & \frac{L_m}{\sigma L_s L_r}\left(\frac{1}{\tau_r} - j\omega\right) \\ \frac{L_m}{\tau_r} & -\frac{1}{\tau_r} - j(\omega_k - \omega) \end{bmatrix} \begin{bmatrix} \underline{i}_s^k \\ \underline{\Phi}_r^k \end{bmatrix} \quad (1)$$

Where, $\underline{V}_s^k$ is the stator voltage vector; L_s, L_r, and L_m are the stator, rotor, and mutual self inductances respectively; $(\sigma = 1 - \frac{L_m^2}{L_S L_r})$ is the leakage constant; τ_s, τ_r refer to the time constant of the stotor rotor respectively,

$$\frac{d\Phi_{s\alpha}^s}{dt} = V_{s\alpha}^s - R_s i_{s\alpha}^s \quad (2)$$

$$\frac{d\Phi_{s\beta}^s}{dt} = V_{s\beta}^s - R_s i_{s\beta}^s \quad (3)$$

$$\Phi_{r\alpha} = \frac{a_2}{s + a_1} i_{s\alpha} \quad (4)$$

where, R_s is the stator resistance for one phase.

The real rotor flux component, taking into account the the rotor flux vector orientation, can be written as [25]:

The slip frequency ω_r is calculated by one of the two equations [26]:

$$\omega_r = \frac{a_2 i_{s\beta}}{|\Phi_r|} \quad (5)$$

$$\omega_r = \frac{a_2}{\Phi_r}\frac{L_r}{pL_m}\frac{T_{em}}{\Phi_r} = \frac{a_2 L_r}{pL_m \Phi_r^2} T_{em} \quad (6)$$

the motor torque can be written as follows, via substituting the formula (5) into the formula (6),

$$T_{em} = \frac{pL_m}{L_r}(\Phi_r i_{s\beta}) \quad (7)$$

The angle of orientation can be estimated using the equation [27]:

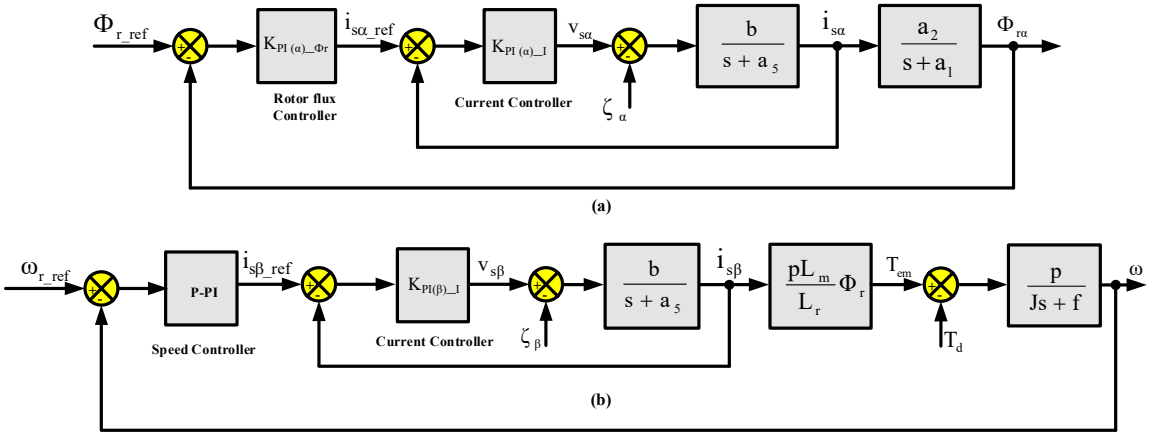

Figure 2. Clarifies the block diagram of both the rotor flux control and the speed control of FOC strategy of α-axis, and β-axis, respectively, (a) Rotor flux control for α-axis, (b) Speed control for β-axis.

ω is the rotational speed; p is the pole pairs number

the components of the stator flux vector are given as follows,

$$\omega_s = \omega_r + \omega \quad (8)$$

In order to accomplish the control process, PI regulators will be used for thoughtful control loops. This choice is due to the simplicity of these controllers compared to

Celal Bayar University Journal of Science
Volume 20, Issue 3, 2024, p 47-57
Doi: 10.18466/cbayarfbe.1453798

other controllers, and their ability to cancel the steady state error [28]. However, They suffer from instability due to the fact that they contain the integrator. Therefor, this problem will be solved by using antiwindup technique that eliminates the malfunction condition of the regulator's operation [29]. Due to its simplicity as well as its ability in maintaining the system order, the technique of zero-pole cancellation will be used for calculating the gains of the controllers [30].
The controller rotor flux as well as the speed regulator gains are calculated after calculating the current controller gains in the inner loop.The detailed calculations is performed in the Appendix A.

4. Simulation Results

The tested motor was an induction motor of squirrel cage type. Its nominal speed at *282.7 [rad/sec]*, The nominal torque and the rotor flux are *0.945[Wb]*, *1.76 [Nm]*, respectively. Its nominal power was *0.25[Kw]*. In order to investigate the the FOC performance, important parameteres should be set as follows. The inverter switching frequency and the sampling period were set as f_{PWM}=10[KHZ] and T_s=50[µs], respectively. The technique of the third harmonic injection was used in order to enhance the reference voltages with PWM stage (That means an increasing of 15.47% of ($\frac{E}{\sqrt{2}}$) is gained) [31].

In order to test the performance of the proposed method over a wide speed range, the simulation results are conducted in Figure (3). Consecutive jumps in the reference speed signal with different values made at specific times. At the moment 0.3 seconds, a reference speed of 100 [rad/sec] was requested. At the moment 3, a reference speed of 150 [rad/sec] was requested. At moment 5 seconds, A negative reference speed of -50 [rad/sec] was requested until the moment 7.5 seconds a positive reference speed requested again. It is observed that the measured speed of the motor was well tracked the reference speed without any disturbances in transient states. The developed torque of the motor followed the changes of the speed with low chattering and high dynamics. The rotor flux was maintained controlled around its nominal value (0.945 [Wb]). The motor three currents remained sinusoidal without spikes during transitions changes.

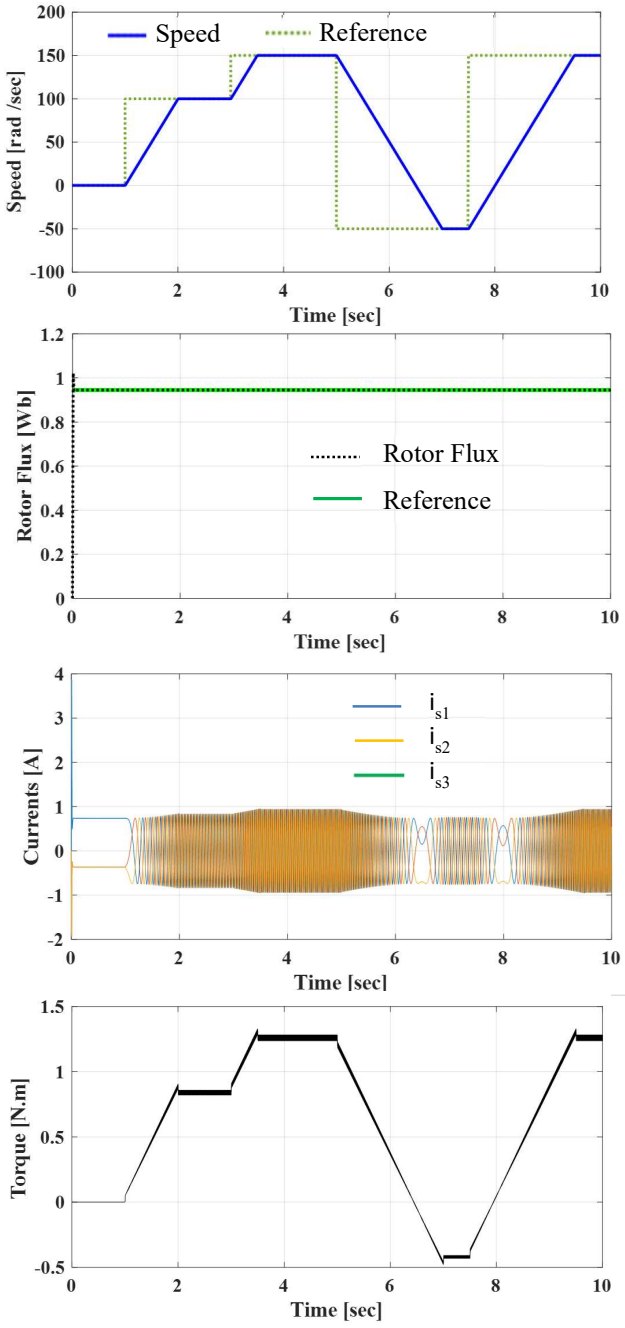

Figure 3. Behaviour of FOC strategy for wide speed range.

To verify the correct α-axis orientation in terms of the rotor flux vector since it is the core of FOC strategy, the two components of Φ_r vector were plotted, for the the frame (α, β), in Figure (4). it is indeed observed that the imaginary component is approximately equalled zero, and the real component is approximately equalled the value of the nominal rotor flux magnitude as it reached the value 0.951[wb].

Celal Bayar University Journal of Science
Volume 20, Issue 3, 2024, p 47-57
Doi: 10.18466/cbayarfbe.1453798

00000000

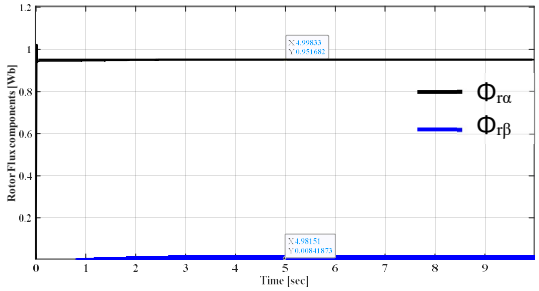

Figure 4. Components responses of the rotor flux vector

Similarly, Figure (5) shows the components of the stator current vector for the synchronous frame. It is noted that the current of α- axis reached 4.75A during the startup, while it stabilized in the steady state at 0.89A. On the other hand, the imaginary current increased gradually due to the graded reference speed and stabilized at a value of 1.32A.

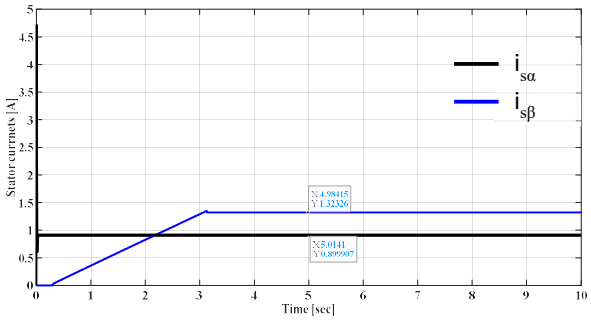

Figure 5. The two components of the stator current vector

Figure (6) clarifies the three-phase voltage signals before being injected with the third harmonic signal divided by the parameter (E) with the third harmonic signal. With this case, an extra reference voltages could be secured by an increase of (15.47%), or the DC-link could be reduced by 15.47%.

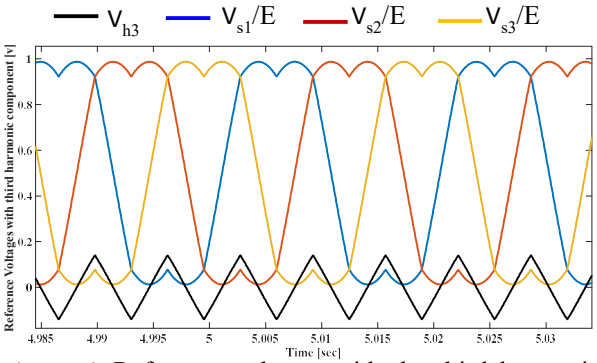

Figure 6. Reference voltages with the third harmonic injection technique

Figure (7) shows the voltage vector amplitude developed from the FOC algorithm. The nominal voltage of the tested motor is 230V, that is, the maximum value of the nominal voltage is 325V. Since the two phases voltages amplitude is greater than the three phases voltages by 1.224, the maximum value of the Vs in the synchronous frame is 400V. However, there is an increase in this value of 24[V]. This increase is due to the optional gains. These values can be changed to obtain less voltage, but this change may cause worse performance of the system, so a slight overrun of the applied voltage to the motor can be accepted.

Figure (8) shows the slip speed with the orientation angle in the synchronous reference frame.

The slip speed has a similar response to the torque response according to equation (6) for a constant rotor flux value.

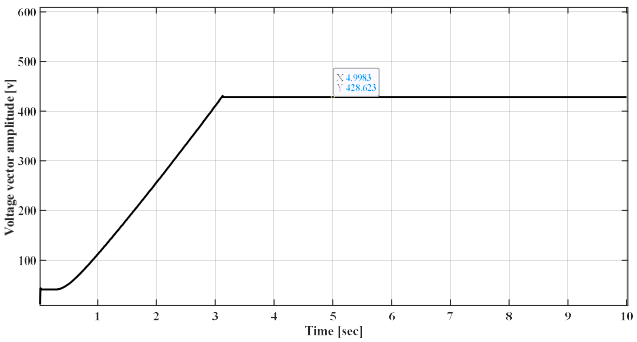

Figure 7. Voltage vector amplitude response

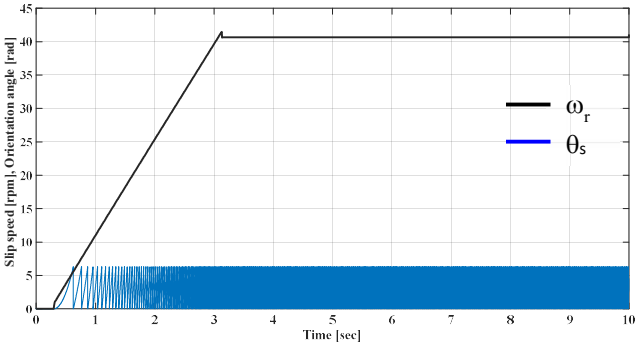

Figure 8. Slip speed and orientation angle responses

5. Experimental results

In order to test the performance of the approach over a wide range of speed and verify the the simulation results, experiments were carried out on a test rig within the laboratory equipped for electric drive systems. The platform has been invested in some of our literature research [32]. The experiments were conducted on a 50Hz, 230/400V squirrel cage three-phase induction motor with a power of 0.25 kW, a rated speed of 1350 rpm, and a rated torque of 1.76 Nm. Full details of the motor's parameters are provided in Appendix B. The motor was powered by a 22.8 kVA three-phase Semikron inverter, with the DC-link voltage set at 550V.

The core component of the platform is the DS1103 digital processing card which is supported by dSPACE company. The card is supported by a graphical environment (called ControlDesk) that helps the designer to build a control interface that is used for the control commands and monitoring measured and calculated signals in real time. As for the sensors in the platform, they are two current-sensors, a differential sensor to measure the inverter dc-link. The interface circuit for the current sensors outputs ±0.5V for each ±1A of input. The currents were fed into three channels of the 4-channel Analog-Digital Converter (DS1103ADC_Cx). This ADC divides its input by 10, so an input range of [-10, +10] yields an output range of [-1, +1]. To get the actual current value, the output signal of the ADC must be multiplied by a gain factor of 20 (2 × 10). In addition, An incremental encoder with 1024 pulses per revolution was used to measure speed. The conversion between mechanical speed and electrical speed is achieved by multiplying by the number of pole pairs. To calculate the position differential, the current position is subtracted from the previous position, and then the result is multiplied by the conversion factor to obtain the electric speed. First-order intermediate filters were used to minimize noise during position signal acquisition from the encoder.

The interface circuit for the measured DC-link outputs ±0.5V for every ±100V of input. This ADC_20 divides its input by 10. To get the actual DC-link voltage, the output signal from the ADC_20 must be multiplied by a gain of 2000 (200 × 10).
As for the inverter, it is a three-phase of Semikron type that has the capabilities of adding dead time to the driving transistors in addition to its capabilities in protecting the motor and dSPACE at any sudden error or failure. The block diagram of the platform and the experimental setup is shown in Figure (9) and Figure (10), resecitvely.

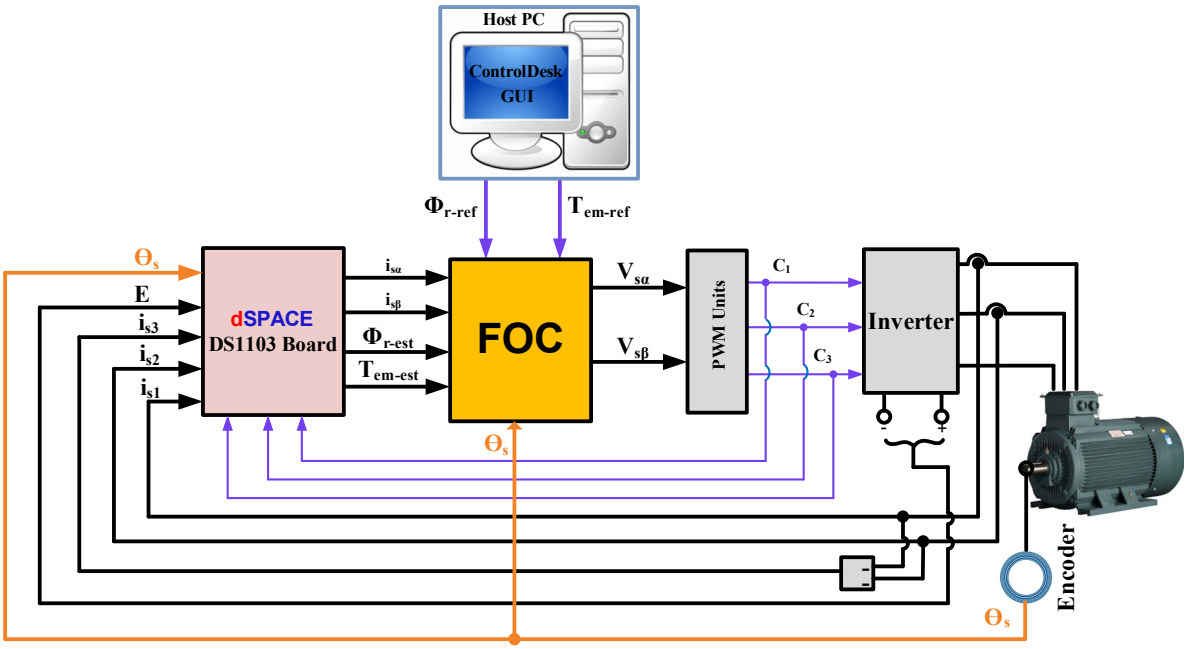

Figure 9. Block diagram of the test rig for experimental test of FOC method

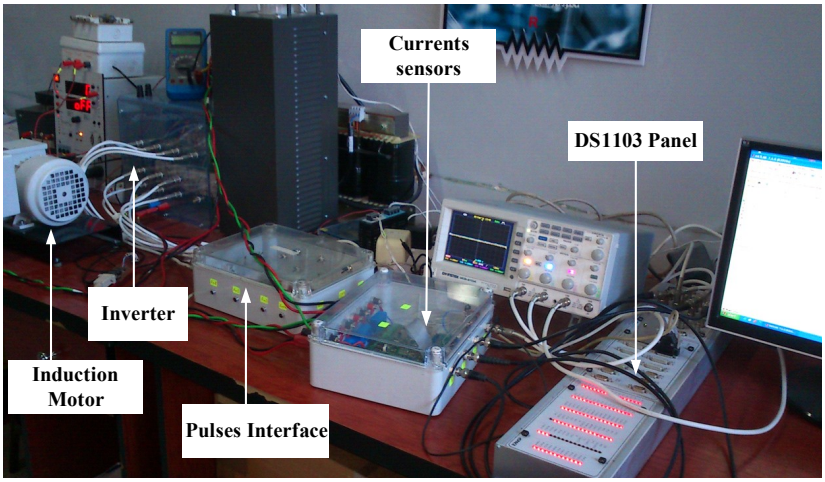

Figure 10. Experimental setup of FOC method

Celal Bayar University Journal of Science
Volume 20, Issue 3, 2024, p 47-57
Doi: 10.18466/cbayarfbe.1453798

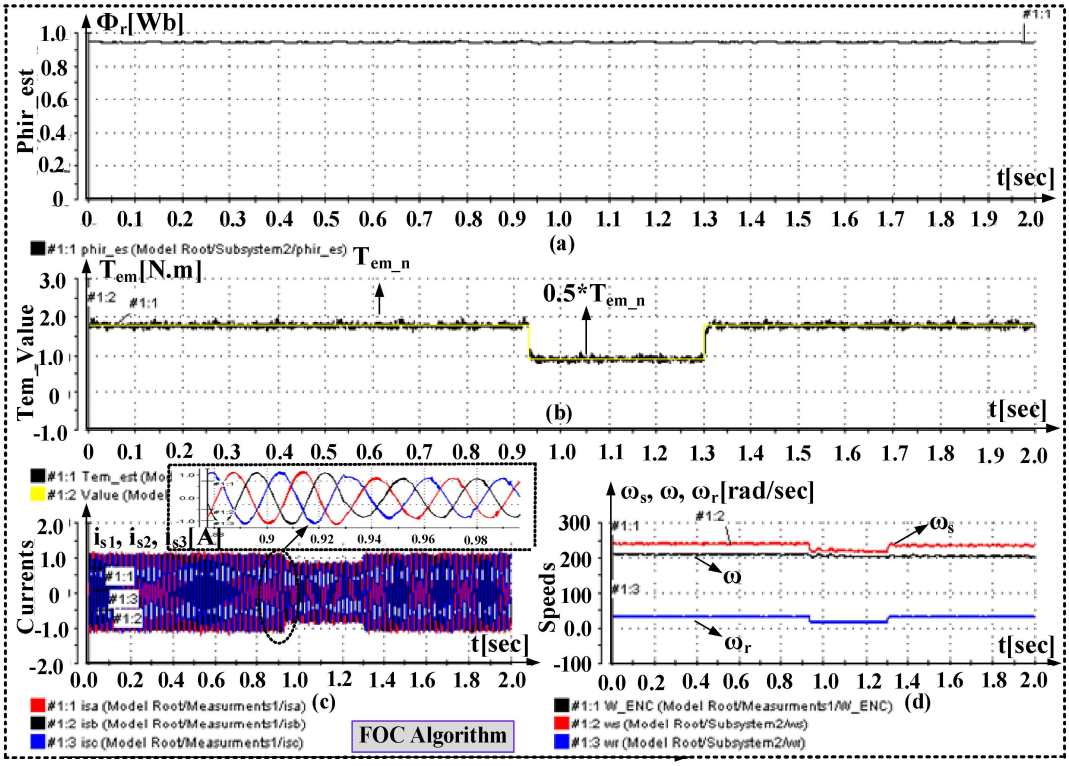

Figure 11. Experimental test of FOC strategy

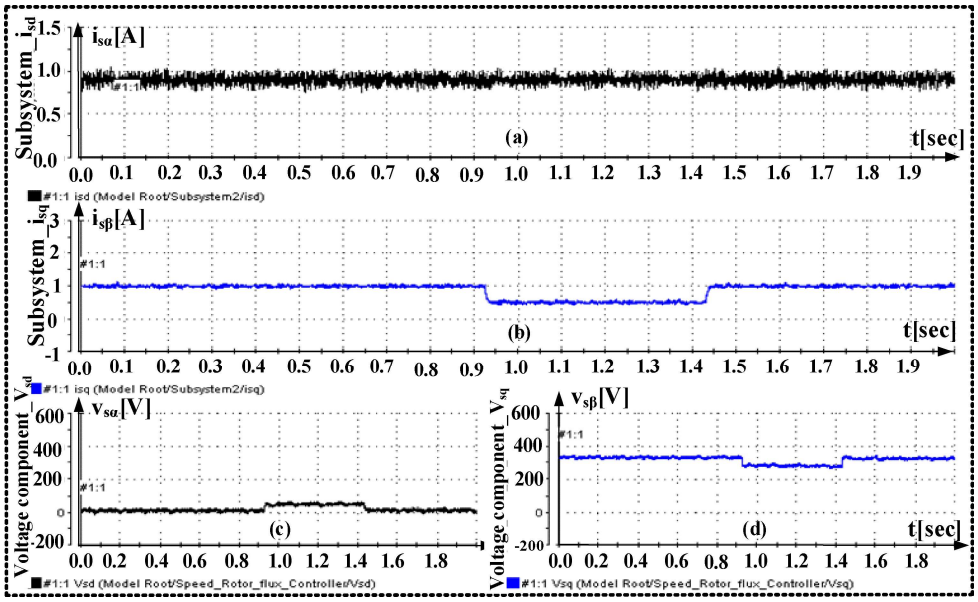

Figure 12. Experimental results of FOC: (a, b):The two components currents, (c,d): The two components voltatges

Celal Bayar University Journal of Science
Volume 20, Issue 3, 2024, p 47-57
Doi: 10.18466/cbayarfbe.1453798

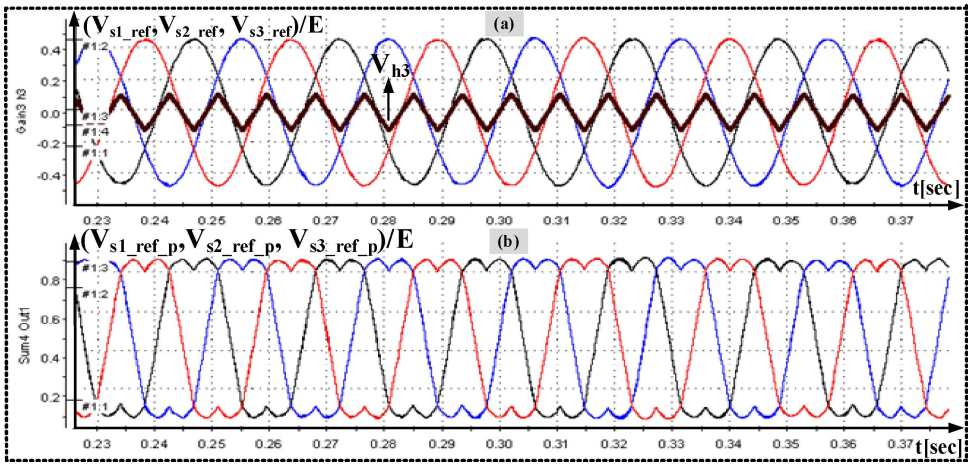

Figure 13. Reference voltages with the component of the third harmonic

The experiments were conducted so that they are largely compatible with the conditions of work at the simulation stage. The inverter frequency was set at 10 [KHz] and the sampling time was 50 [μs]. As shown in Figure (11), the nominal value of the rotor flux equalled 0.945[wb] was requested. Different torque reference values have been requested so that the performance of the algorithm with transient situations is ascertained. At the moment 0.9[sec], the nominal reference value of 1.76[N.m] was moved to half the nominal value. At the moment 1.3[sec] the nominal reference value of the torque was redialed again**.** It is noted that the rotor flux remained organized around the required reference value without any noticeable disturbances, and the generated torque well pursued the reference torque with high dynamics. The motor currents were sinusoidal ones without any jumps or turbulence, which confirmed that the performance has been quiet. It should be noted that the operation speed was about 210 [rad/sec], and the slip speed was variable between the nominal value and half the nominal value according to the torque value generated by the motor.

Figure (12) enhances the performance of the strategy, showing the components of stator current and voltage vectors in the synchronous reference frame. The value of the α-axis current component was 0.9[A], while the value of the β-axis component was changed between 1[A] and 0.5[A] depending on the torque range**.**

Figure (13) shows the reference three-phase voltage signals before being injected with the third harmonic signal divided by the DC-link (E) with the third grader signal. As mentioned above, an increase in the amplitude of the reference voltages can be secured by an increase of (15.47%), or reducing the DC-link by (15.47%).

6. Comparison with recent related papers

To verify the feasibility and effectiveness of the proposed algorithm, its performance is compared with previous and more recent approaches from the literature, specifically those in works referenced as [6, 9, 16]. As shown in Table (1), which presents seven works considered appropriate for comparison with the proposed control scheme, the algorithm's performance metrics are benchmarked against these established methods.

Table 1. Comparison with literature.

Used Method	**Proposed Method**	**Ref [6]**	**Ref [9]**	**Ref [16]**
Sample Time Type	Variable Step	Fixed Step	Fixed Step	Fixed Step
Antiwindup Technique	Yes	No	No	No
Third Harmonic Injection Technique	Yes	No	No	No
Optional Gains	4	4	6	6

Based on the table above, the benefits resulting from the proposed design, according to the characteristics outlined in the table, can be summarized as follows:

- **Variable Sampling Time**: The proposed algorithm offers high dynamics and accuracy when calculating state variables, unlike fixed-step-based methods, which may lack this accuracy.
- **Antiwindup Technique**: The proposed algorithm prevents PID regulators from exceeding permissible values. Without this feature, there's no guarantee that the regulator's outputs will stay within the allowed range.
- **Third Harmonic Injection Technique**: The proposed algorithm optimizes the DC-link voltage of the inverter, achieving a value that is 15.47% less than an algorithm without this property.
- **Optional Gains**: The small number of optional gains ensures simplicity in practical

implementation. Increased complexity occurs with a greater number of parameters. Therefore, the proposed strategy balances simplicity and effectiveness compared to other similar strategies..

7. Conclusions

In conclusion, the extensive laboratory testing of the proposed FOC algorithm on a well-equipped electric drive system test rig has empirically confirmed the robustness and effectiveness of the approach across a broad speed spectrum. The DS1103 digital processing card, central to the experimental platform, facilitated real-time control and monitoring, demonstrating the practical viability of transitioning from simulation to real-world application.

The experimental results have corroborated the simulated performance, with the inverter operating efficiently at a fixed frequency of 10 kHz and a precise sampling time of 50 µs. Notably, the system maintained the rotor flux at the nominal value of 0.945 wb without disturbances, even when faced with transient torque conditions. This stability is a testament to the algorithm's dynamic response capabilities, as the torque swiftly and accurately tracked the reference values.

Furthermore, the motor currents displayed an ideal sinusoidal waveform, indicative of the system's tranquility and absence of electrical noise. Operating at a speed of approximately 210 rad/sec, the system adeptly managed variations in slip speed, aligning with changes in the torque produced by the motor.

The strategic integration of stator current and voltage vectors, as illustrated in Figure (11), showcases the fine-tuned control achieved over the α and β components, further validating the precision of the system under variable torque demands.

Enhancements to the strategy are visually evident in Figure (12), where the implementation of third harmonic injection was found to notably increase the amplitude of reference voltages by 15.47%, concurrently allowing for a reduction in DC-link voltage requirements by the same margin.

These results not only validate the proposed FOC algorithm but also suggest potential for improvements in electric drive systems. With such clear demonstrations of enhanced performance and dynamic control, this research lays a strong foundation for future advancements, including potential integration with intelligent control systems, to further optimize performance and energy efficiency in varied and demanding industrial applications.

Acknowledgement

The authors declare that no acknowledgments are applicable for this study.

Author's Contributions

Mussaab Alshbib: was instrumental in conceptualizing the advanced FOC strategy, drafting and writing the manuscript, and performing the analytical analysis. contributed to enhancing the manuscript by providing insights into the practical applications of the FOC strategy, supervising the setup of the DS1103-controlled testbed, and ensuring the experimental verification aligned with real-world electric vehicle conditions. Both authors collaborated closely on all sections of the manuscript, ensuring a cohesive presentation of both the theoretical framework and experimental validation of the FOC strategy

Sohayb Abdulkerim: helped in performing the analytical analysis, performed the simulation work in MATLAB/Simulink, and result interpretation for the theoretical aspects of the study.S.A also played a key role in designing the experiment and analyzing experimental data to validate the simulation results.

Ethics

This study, which developed an advanced Field Oriented Control strategy for electric vehicle drivetrains, did not involve human or animal subjects and therefore did not require ethical approval. The work was purely analytical and simulation-based, adhering to relevant ethical standards for technical research. There are no ethical issues after the publication of this manuscript.

Conflict of Interest Statement:

The authors declare no potential conflicts of interest with respect to the research, authorship, and/or publication of this article. This includes, but is not limited to, financial, personal, or professional relationships that could be perceived to influence the work described in this manuscript.

References

[1]. M. Ganchev, "Control unit for a laboratory motor test bench for monitoring and controlling PMSM and induction motors," 2007 European Conference on Power Electronics and Applications, 2007, doi: 10.1109/epe.2007.4417431.

[2]. J. C. Nustes, D. P. Pau, and G. Gruosso, "Modelling the Field Oriented Control applied to a 3-phase Permanent Magnet Synchronous Motor," Software Impacts, vol. 15, p. 100479, Mar. 2023, doi: 10.1016/j.simpa.2023.100479.

[3]. R. Ghassani, Z. Kader, M. Fadel, P. Combes, and M. Koteich, "Comparison Study of Rotor Field-Oriented Control and Stator Field-Oriented Control in Permanent Magnet Synchronous Motors," 2023 IEEE International Electric Machines & Drives Conference (IEMDC), May 2023, doi: 10.1109/iemdc55163.2023.10239079.

[4]. Gudey, S.K.; Malla, M.; Jasthi, K.; Gampa, S.R. Direct Torque Control of an Induction Motor Using Fractional-Order Sliding Mode Control Technique for Quick Response and Reduced Torque Ripple. World Electr. Veh. J. 2023, 14, 137. https://doi.org/10.3390/wevj14060137

[5]. Alshbib, Mussaab M., Ibrahim Mohd Alsofyani, and Mohamed Mussa Elgbaily. 2023. "Enhancement and Performance Analysis for Modified 12 Sector-Based Direct Torque Control of AC Motors: Experimental Validation" Electronics 12, no. 3: 549. https://doi.org/10.3390/electronics12030549

[6]. B. Boomiraja and R. Kanagaraj, "DQ-axis Modelling and Field Oriented Control of Hybrid Flux Motor," Sep. 2022, doi: 10.21203/rs.3.rs-2008400/v1.

[7]. N. T. Dat, C. V. Kien, and H. P. H. Anh, "Optimal FOC-PID Parameters of BLDC Motor System Control Using Parallel PM-PSO Optimization Technique," International Journal of Computational Intelligence Systems, vol. 14, no. 1, p. 1142, 2021, doi: 10.2991/ijcis.d.210319.001.

[8]. Manepalli, Jaya Raju, and C. V. N. Raja. "Speed control of induction motor by ZN method and genetic algorithm optimization with PI and PID controller." Int J Innov Res Electr Electron Instrum Control Eng 3.3 (2015): 15-20.

[9]. S. -C. Chen and H. -K. Hoai, "Studying an Adaptive Fuzzy PID Controller for PMSM with FOC based on MATLAB Embedded Coder," 2019 IEEE International Conference on Consumer Electronics - Taiwan (ICCE-TW), Yilan, Taiwan, 2019, pp. 1-2, doi: 10.1109/ICCE-TW46550.2019.8991743.

[10]. V. S. Virkar and S. S. Karvekar, "Luenberger observer based sensorless speed control of induction motor with Fuzzy tuned PID controller," 2019 International Conference on Communication and Electronics Systems (ICCES), Coimbatore, India, 2019, pp. 503-508, doi: 10.1109/ICCES45898.2019.9002268.

[11]. A Mohammed Eltoum, M., Hussein, A. & Abido, M.A. Hybrid Fuzzy Fractional-Order PID-Based Speed Control for Brushless DC Motor. Arab J Sci Eng 46, 9423–9435 (2021). https://doi.org/10.1007/s13369-020-05262-3

[12]. J. Espina, A. Arias, J. Balcells and C. Ortega, "Speed Anti-Windup PI strategies review for Field Oriented Control of Permanent Magnet Synchronous Machines," 2009 Compatibility and Power Electronics, Badajoz, Spain, 2009, pp. 279-285, doi: 10.1109/CPE.2009.5156047.

[13]. H. P. H. Anh, C. V. Kien, T. T. Huan and P. Q. Khanh, "Advanced Speed Control of PMSM Motor Using Neural FOC Method," 2018 4th International Conference on Green Technology and Sustainable Development (GTSD), Ho Chi Minh City, Vietnam, 2018, pp. 696-701, doi: 10.1109/GTSD.2018.8595688.

[14]. A. A. Abdelrauf, W. W. Saad, A. Hebala and M. Galea, "Model Predictive Control Based PID Controller for PMSM for Propulsion Systems," 2018 IEEE International Conference on Electrical Systems for Aircraft, Railway, Ship Propulsion and Road Vehicles & International Transportation Electrification Conference (ESARS-ITEC), Nottingham, UK, 2018, pp. 1-7, doi: 10.1109/ESARS-ITEC.2018.8607585.

[15]. Uralde, J.; Barambones, O.; Artetxe, E.; Calvo, I.; del Rio, A. Model Predictive Control Design and Hardware in the Loop Validation for an Electric Vehicle Powertrain Based on Induction Motors. Electronics 2023, 12, 4516. https://doi.org/10.3390/electronics12214516.

[16]. Benbouhenni, H.; Bizon, N. Improved Rotor Flux and Torque Control Based on the Third-Order Sliding Mode Scheme Applied to the Asynchronous Generator for the Single-Rotor Wind Turbine. Mathematics 2021, 9, 2297. https://doi.org/10.3390/math9182297

[17]. L. Guo, D. Wang, Z. Peng, and L. Diao, "Improved super-twisting sliding mode control of a stand-alone DFIG-DC system with harmonic current suppression," IET Power Electronics, vol. 13, no. 7, pp. 1311–1320, May 2020, doi: 10.1049/iet-pel.2019.0691.

[18]. D. Zellouma, H. Benbouhenni, and Y. Bekakra, "Backstepping Control Based on a Third-order Sliding Mode Controller to Regulate the Torque and Flux of Asynchronous Motor Drive," Periodica Polytechnica Electrical Engineering and Computer Science, vol. 67, no. 1, pp. 10–20, Jan. 2023, doi: 10.3311/ppee.20333.

[**19].** R. S. Hiware and J. G. Chaudhari, "Indirect Field Oriented Control for Induction Motor," 2011 Fourth International Conference on Emerging Trends in Engineering & Technology, 2011, pp. 191-194, doi: 10.1109/ICETET.2011.56.

[20]. Kabache, Nadir.; Moulahoum, S.; Houassine, H" FPGA Implementation of direct Rotor Field Oriented Control for Induction Motor.

[21]. B. Bahrani, S. Kenzelmann and A. Rufer, "Multivariable-PI-Based dq Current Control of Voltage Source Converters With Superior Axis Decoupling Capability," in IEEE Transactions on Industrial Electronics, vol. 58, no. 7, pp. 3016-3026, July 2011, doi: 10.1109/TIE.2010.2070776.

[22]. G. Acevedo, Hernando, N. Vargas, G. M. Hernando, C. Torres and J. Jairo, "Design of Rotor Flux Oriented Vector Control Systems for Induction Motor," Proceedings of The 7th International Power Electronics and Motion Control Conference, 2012, pp. 1384-1388, doi: 10.1109/IPEMC.2012.6259010.

[23]. A. M. Trzynadlowski, "Dynamic model of the induction motor," Control of Induction Motors, pp. 107–117, 2001, doi: 10.1016/b978-012701510-1/50006-4.

[24]. G. Zhang, Z. Du, Yu. Ni, and C. Li, "Nonlinear model reduction-based induction motor aggregation," International Transactions on Electrical Energy Systems, vol. 26, no. 2, pp. 398–411, May 2015, doi: 10.1002/etep.2089.

[25]. H. Grotstollen and A. Bunte, "Control of induction motor with orientation on rotor flux or on stator flux in a very wide field weakening region-experimental results," Proceedings of IEEE International Symposium on Industrial Electronics, doi: 10.1109/isie.1996.551065.

[26]. H. Seo, G. Choe, J. Lim, and J. Jeong, "Slip frequency control of linear induction motor considering normal force in semi-high speed MAGLEV train," 2017 IEEE International Magnetics Conference (INTERMAG), Apr. 2017, doi: 10.1109/intmag.2017.8007999.

[27]. C. Zhou, Z. Cai, and F. Xie, "Research on speed regulation system of induction motor based on slip frequency control," 2018 13th IEEE Conference on Industrial Electronics and Applications (ICIEA), May 2018, doi: 10.1109/iciea.2018.8397926.

[28]. B. Singh, S. Pandey, A. Junghare and M. V. Aware, "Design of an anti-windup fractional order PI controller based on integral state predictor within stability bound," 2016 IEEE 1st International Conference on Power Electronics, Intelligent Control and Energy Systems (ICPEICES), Delhi, India, 2016, pp. 1-6, doi: 10.1109/ICPEICES.2016.7853493.

[29]. M. O. Ajangnay, "Optimal PID controller parameters for vector control of induction motors.," SPEEDAM 2010, Jun. 2010, doi: 10.1109/speedam.2010.5545043.

[30]. T. Singh, "Pole-Zero, Zero-Pole Canceling Input Shapers," Journal of Dynamic Systems, Measurement, and Control, vol. 134, no. 1, Dec. 2011, doi: 10.1115/1.4004576.

[31]. M. Ziyuan and Z. Xiaoqin, "Torque Calculation for A Nine-phase Induction Motor with Third-harmonic Current Injection," 2021 24th International Conference on Electrical Machines and Systems (ICEMS), Oct. 2021, doi: 10.23919/icems52562.2021.9634376.

[32]. M. Alshbib and S. Abdulkerim, "An Experimental and Analytical Investigation of the Direct Torque Control Method of a Three-Phase Induction Motor," Journal of Electrical Engineering & Technology, vol. 18, no. 6, pp. 4367–4379, Apr. 2023, doi: 10.1007/s42835-023-01483-2.

APPENDIX A

Calculation of the gains controllers for α and β loops:

The transfer function of the current control loop is as follows:

$$\frac{i_{s\alpha}}{i_{s\alpha\_ref}} = \frac{K_{P(\alpha)\_I}.b}{s + K_{P(\alpha)\_I}.b} \quad (1A)$$

The following equation is supposed:

$$a_5 = \frac{K_{I(\alpha)\_I}}{K_{P(\alpha)\_I}} \Rightarrow K_{I(\alpha)\_I} = a_5.K_{P(\alpha)\_I} \quad (2A)$$

The gain $K_{P(\alpha)\_I}$ is optional and can be set during the design.

The transfer function of the rotor flux is written as:

$$\frac{\Phi_r}{\Phi_{r\_ref}} = \frac{K_{P(\alpha)\_\Phi_r}.K_{P(\alpha)\_I}.b.a_2}{S^2 + K_{P(\alpha)\_I}.b.S + K_{P(\alpha)\_\Phi_r}.K_{P(\alpha)\_I}.b.a_2} \quad (3A)$$

The following equation is supposed:

$$a_1 = \frac{K_{I(\alpha)\_\Phi_r}}{K_{P(\alpha)\_\Phi_r}} \quad (4A)$$

One can suppose that $\xi = \frac{1}{\sqrt{2}}$),

$$\left.\begin{aligned} 2\zeta\omega_n = K_{P(\alpha)\_I}.b \Rightarrow \omega_n = \frac{K_{P(\alpha)\_I}.b}{2.\frac{1}{\sqrt{2}}} \\ \omega_n{}^2 = K_{P(\alpha)\_\Phi_r}.K_{P(\alpha)\_I}.b.\ a_2 \end{aligned}\right\} \Rightarrow K_{P(\alpha)\_\Phi_r} = \frac{\omega_n{}^2}{K_{P(\alpha)\_I} b\, a_2} \quad (5A)$$

$$K_{I(\alpha)\_\Phi_r} = a_1.K_{P(\alpha)\_\Phi_r} \quad (6A)$$

$$\frac{i_{s\beta}}{i_{s\beta\_ref}} = \frac{K_{P(\beta)\_I}.b}{S + K_{P(\beta)\_I}.b} \quad (7A)$$

Where the following equation was supposed:

$$a_5 = \frac{K_{I(\beta)\_I}}{K_{P(\beta)\_I}} \Rightarrow K_{I(\beta)\_I} = a_5.K_{P(\beta)\_I} \quad (8A)$$

The value of $K_{P(\beta)\_I}$ is optional and can be set during the design.

For the Speed loop gains, they can be obtained through the following equations:

$$\frac{\omega}{\omega_i} = \frac{\frac{K_p K_{P\_I} b P^2 L_m \Phi_{r\alpha}}{JL_r}}{S^2 + K_{P\_I} bS + \frac{K_p K_{P\_I} b P^2 L_m \Phi_{r\alpha}}{JL_r}} \quad (9A)$$

The propotional gain K_v can be calculated (suppose that $\xi = 1$) as follows,

$$K_V = \frac{JL_r \omega_{n1}^2}{K_{P\_I} b P^2 L_m \Phi_{r\alpha}} \quad (10A)$$

Where:

$$\omega_{n1}^2 = \frac{K_{P\_I} b}{2} \quad (11A)$$

The final transfer function can be written as

$$\frac{\omega}{\omega_{ref}} = \frac{\frac{K_{p\_\omega} K_p K_{P\_I} b P^2 L_m \Phi_{r\alpha}}{JL_r}}{S^2 + \omega_{n1} S + \frac{K_{p\_\omega} K_p K_{P\_I} b P^2 L_m \Phi_{r\alpha}}{JL_r}} \quad (12A)$$

So one can get

$$K_{p\_\omega} = \frac{\omega_n{}^2 JL_r}{K_p K_{P\_I} b P^2 L_m \Phi_{r\alpha}} \quad (13A)$$

APPENDIX B: The used motor parameters

Nominal voltage	230/400[V]
Phase resestance stator	R_s=45.83[Ω]
Phase resestance rotor	R_r=31[Ω]
Phase inductance stator	L_s=1.24[H]
Phase inductance rotor	L_r=1.11[H]
Mutual inductance	L_m=1.05[H]
Inertia	$J = 0.006$ [kg.m^2]
Friction factor	f=0.001[N.m.sec/rad]
Number of poles pairs	p=2
Nominal stator flux	Φ_s=1.14[H]
Nominal power	P_n=0.25[kW]
Nominal frequency	F=50[Hz]
Nominal speed	N=1350[rpm]
Nominal torque	T_{em}=1.76[N.m]
Slip speed	ω_r=29.5[r/s]

Celal Bayar University Journal of Science

The Effect of Contrast Material in Three Dimensional Conformal and Helical Treatment Plans in Rectal Radiotherapy

Hikmettin Demir[1]*, Gül Kanyılmaz[2], Osman Vefa Gül[3]

[1]Department of Radiation Oncology, Faculty of Medicine, Van Yuzuncu Yıl University, Van, Türkiye
[2]Department of Radiation Oncology, Faculty of Medicine, Necmettin Erbakan University, Konya, Türkiye
[3]Department of Radiation Oncology, Faculty of Medicine, Selcuk University, Konya, Türkiye

* hikmettindemir@yyu.edu.tr
* Orcid No: 0000-0002-1171-4821

Received: 31 May 2024
Accepted: 2 September 2024
DOI: 10.18466/cbayarfbe.1493473

Abstract

The aim of this study to investigate the impact of contrast agent used for imaging purposes in the treatment of neoadjuvant rectal cancer patients. In rectal radiotherapy, contrast agent is used during the treatment simulation but the patient treated without contrast. In our study, we will examine whether CTs taken with contrast agent are sufficient for clinical application. A total of eighteen patients who had undergone neoadjuvant treatment with rectal cancer randomly selected. Two different CT scans were performed for each patient. The contours were delineated on a non-contrast CT images with the help of image fusion with contrast CT images. Then, the contours drawn on the non-contrast CT were copied to the contrast-enhanced CT with the help of fusion to be used in contrast CT plans for our retrospective study. Subsequently, all plans were generated in Eclipse TPS and Accuray Precision TPS. Finally the plans with contrast agent and non-constrat agent were compared. 3DCRT plans were compared for contrast and non-contrast images, no significant differences were observed in either the PTV or the maximum and mean values of critical organs. It was observed that the average post-contrast doses increased significantly for small bowel only in helical therapy ($p = 0.019$). As a result, no significant difference was observed in terms of PTV and critical organs in the comparison of 3DCRT plans. In the comparison of helical plans, there was only a significant difference in the bladder. Based on these results, we suggest that planning can be done with a single contrast CT for 3DCRT treatments, both to avoid further discomfort for the patient and to prevent additional tomography doses. On the other hand, for helical therapy, we believe that it can be clinically evaluated whether the treatment will be performed with contrast CT depending on the patient's condition.

Keywords: Contrast, conformal radiotherapy, helical therapy, rectum.

1. Introduction

Rectal cancer is a disease that significantly affects the quality of life. The incidence of rectal cancer in the world in 2020 was 3.8%[1]. The incidence of rectal cancer is affected by factors, including heredity, obesity, dietary habits, smoking and other factors. The illness is becoming more common, with a rise in both the number of cases and deaths each year[2]. With advances in medical technology and development of new treatment techniques, the combination of neoadjuvant therapy and surgery has become widely used for the treatment of the rectum cancer[3, 4].

Recent studies have shown that patients with locally advanced rectal cancer who received radiotherapy and chemotherapy before total mesorectal excision (TME) exhibited improved outcomes in terms of tumour response and survival[5, 6]. Initially postoperative or preoperative radiotherapy (RT) studies and recent studies of combinations of concurrent chemotherapy and radiotherapy have shown improvement in local control and a reduction in recurrences[7-9].

Neoadjuvant chemoradiotherapy (NCRT), particularly neoadjuvant radiotherapy and sphincter-sparing surgeries, has been criticized for causing complaints such as bowel discomfort, urgency, and fecal incontinence[10-12].These functional disorders have negative affect on the patient's quality of life[13, 14].

With the development of technology, the use of three dimensional conformal radiotherapy (3DCRT) has

become more advanced, intensity-modulated radiotherapy (IMRT) and image-guided radiotherapy (IGRT) have begun to be used routinely in cancer treatment techniques. The definition of this conformity also includes tomographic images necessary for treatment planning.

The utilisation of contrast agent in tomography is beneficial in the determination of the target volume and obtaining more accurate results in critical organ identification[15].It is recommended that computed tomography (CT) images with intravenous contrast (IV) be used for staging purposes in regions from the liver to the rectum[16].

The objective of this study was to assess the impact of contrast agent used for imaging purposes in the treatment of neoadjuvant rectal cancer patients on dose calculations in 3DCRT using four field box technique and helical therapy (HT) treatment techniques. HU changes in tomography images when contrast is used in the study will also be investigated.

2. Materials and Methods

2.1. Patient Selection

A total of eighteen patients with rectal cancer who had undergone neoadjuvant treatment at the Radiation Oncology Department of Necmettin Erbakan University Medicine Hospital (The ethics institutional review board of this retrospective study was approved by the ethics committee of Necmettin Erbakan University Medicine School with approval number 2024/4948) between January 2011 to December 2023 were randomly selected. All patients with appropriate renal function and creatine resistance underwent contrast and non-contrast imaging before planning. Especially elderly patients were hydrated after imaging. The study included eleven male and seven female patients, all of whom were over the 18 years of age. The mean age of the patients selected for the study was 64. All patients were diagnosed with T3 stage. None of the patients had metastatic disease. All patients received concurrent chemotherapy.

2.2. Simulation

All patients were subjected to CT scan (Siemens Emotion Duo, Germany) in the supine position. Before planning, all patients underwent tomography with and without contrast. The patients were initially scanned without contrast enhancement and followed by a second scan with contrast enhancement, both performed with the 5 mm slice thickness, same fixation position and same coordinates. A solution of 300 mg/100 ml non-ionic contrast agent (Omnipaqe) was used as IV contrast. Oral contrast was administrated in the form of 20 to 40 millilitres of gastrografin in 1.5 litres of water. After the first non-contrast imaging was performed, the patients were given 1.5 litres of oral contrast. Then, the second shot was taken approximately 1 minute after IV contrast was administered via an automated injector.

2.3. Treatment Planning

The data obtained from CT scan was transferred via the Digital Imaging and Communication in Medicine (DICOM) protocol to Eclipse™ treatment planning system (TPS), (version 8.9.08, Eclipse, Varian Medical Systems, Palo Alto, CA, USA).The transferred CT images used to delineate critical organs (small bowel, bladder, right femur, and left femur) and planning target volume (PTV) by a radiation oncologist in accordance with the framework of RTOG (Radiation Therapy Oncology Group) protocol and clinical approaches. The contours were delineated on a non-contrast CT images (CT Set-1) with the help of image fusion with contrast CT images (CT Set-2). Then, the contours drawn on the CT Set-1 were copied to the contrast-enhanced CT with the help of fusion to be used in CT Set-2 plans for our retrospective study. Subsequently, all plans were generated by a medical physicist utilising the Pencil Beam Algorithm and 18 MV photon energy in Eclipse TPS, where the Siemens Primus Plus therapy device defined.

Four field box techniques were used in the planning process (anterior, posterior, right, and left). The prescribed dose for patient was 50 Gy in 25 fraction with a dose of 2 Gy/daily. During the planning, it was ensured that the PTV would receive at least 95% of the prescribed dose, while maximum dose allowed in the plan was set to 110%. Additionally, plans were also created using contrast-enhanced CT images under the same conditions. Then, the contours delineated in Eclipse TPS were transferred via DICOM to Accuray Precision version 2.0.1.1 (Accuray Incorporated, Madison, Wisconsin, USA) TPS, which employs the superposition/convolution planning algorithm of the Tomotherapy device. In this helical planning, a dose of 50 Gy was delivered with a field opening of 2.5 cm, a pitch of 0.287, and a modulator factor of 3.0. During the planning process, the same medical physicist made sure that the volume of the PTV received at least 95% of the prescribed dose, while the critical organ doses were kept as low as possible. These helical tomotherapy plans were repeated on contrast-enhanced CT under the identical conditions.

3. Results

A total of 18 patients who had undergone radiotherapy for rectal cancer were included in the study. The radiotherapy plans were calculated using two different algorithms; the pencil beam algorithm in 3DCRT with Eclipse TPS and the superposition/convolution algorithm with Accuray Precision TPS for tomotherapy plans. Figure 1 and Figure 2 shows the 95% of the prescribed dose distribution for 3DCRT and Tomotherapy plans respectively. Table 1 presents Hounsfield Units (HU) at

the same coordinates in both non-contrast and contrast-enhanced tomography images. We measured the changes in HU values with and without contrast in Eclipse TPS from ten points, trying to have the same coordinates for both images. We made HU readings by creating circular regions in TPS in sections that contain mostly vessels of PTV and where contrast changes in the bladder are more visible. While the minimum HU value before contrast was 14, this value reached 33 after contrast, and the maximum HU value before contrast was 62, but it reached 173 after contrast for PTV. With the addition of contrast resulted in average increase in HU in the PTV and bladder. The average increase in HU in the PTV was found to be statistically significant (p = 0.028).

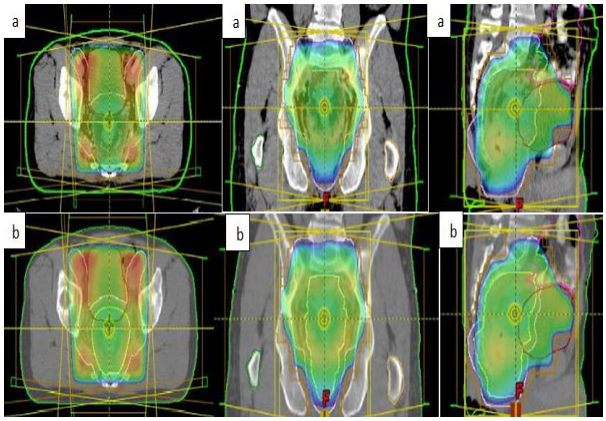

Figure 1. The 95% dose distribution of a patient for 3DCRT plans in axial, coronal, and sagittal planes; a) for contrast plan, b) for non-contrast plan.

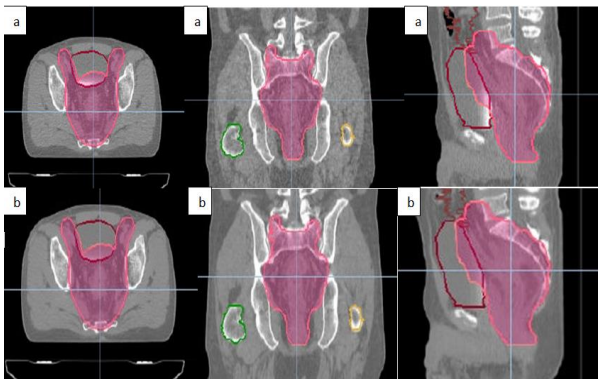

Figure 2. The 95% dose distribution of a patient for tomotherapy plans in axial, coronal, and sagittal planes; a) for contrast plan, b) for non-contrast plan.

The mean doses and standard deviations obtained for PTV and critical organs from TPS calculations made with 3DCRT and HT plans before and after contrast are compared in Tables 2 and 3 respectively. A comparison of the pre-contrast and post-contrast dose calculations was conducted using the SPSS independent t-test. When 3DCRT plans were compared for contrast and non-contrast images, no significant differences were observed in either the target tissue-PTV or the maximum and mean values of critical organs. It was observed that the average post-contrast doses increased significantly for small bowel only in helical therapy (p = 0.019).
Conversely, while the average maximum doses for PTV, small bowel, and bladder in helical planes increased after contrast (p values: 0.208; 0.083 and 0.560, respectively), these values decreased for the right femur and left femur (p values: 0.705 and 0.168, respectively). In HT plans, while the average post-contrast PTV, small bowel, right femur and, left femur doses increased (p values: 0.218; 0.019; 0.137 and 0.166, respectively), the bladder average dose value decreased (p = 0.812). For 3DCRT plans, while the average maximum doses decreased for the post-contrast PTV, bladder right femur and, left femur (p values: 0.646; 0.241; 0.481 and 0.577, respectively), they increased for the small bowel (p=0.241). While the average dose values decreased only for the target PTV after contrast (p = 0.270); It is high for the bladder, small bowel, right femur and, left femur (p values: 0.367; 0.089; 0.175 and 0.079, respectively). With regard to MU required for treatment, no difference was found before and after contrast for both planning techniques.

Table 1. Hounsfield Units (HU) differences due to contrast agent

Site	Min./Max. Range, Mean values (SD) in Hounsfield Units						
	CT Set-1 Min. Range	**CT Set-1 Max. Range**	**CT Set-2 Min. Range**	**CT Set-2 Max. Range**	**CT Set-1 Mean±SD**	**CT Set-2 Mean±SD**	**p-value**
PTV	14	62	33	173	37.4±18.35	70.4±38.30	0.028*
Bladder	-39	35	-16	117	-1±22.34	21.4±46.50	0.144

PTV, planning target volume; SD, standart deviation; Mean, mean HU values of structure; * significant value at $p<0.05$

Table 2. Mean differences in PTV and organ at risk due to contrast agent in 3DCRT plans

	Dose (cGy) mean values ± SD		
	CT Set-1	**CT Set-2**	**p-Value**
PTV			
Dmax(cGy)	5298,00±42, 30	5294,90±54,32	0,646
Dmean(cGy)	5069,00±46,93	5066,20±49,96	0,270
Bladder			
Dmax(cGy)	5267,30±66,22	5265,10±76,29	0,708
Dmean(cGy)	5014,60±85,14	5106,70±322,54	0,367
Small bowel			
Dmax(cGy)	5235,20±77,18	5240,60±84,60	0,241
Dmean(cGy)	1114,60±543,83	1202,70±543,84	0,089
Right femur			
Dmax(cGy)	5109,50±90,79	5107,20±95,96	0,481
Dmean(cGy)	2474,20±314,81	2480,70±319,47	0,175
Left femur			
Dmax(cGy)	5030,70±124,04	5027,80±129,80	0,577
Dmean(cGy)	2276,40±276,78	2290,20±285,78	0,079
MU	222,60±2,95	224,40±2,50	0,555

PTV, planning target volume; SD, standart deviation; 3DCRT, 3 dimensional conformal radiation therapy; Dmax, maximum dose of plan; Dmean, mean dose of structure

Table 3. Mean differences in PTV and organ at risk due to contrast agent in Helical Tomotherapy plans

	Dose (cGy) mean values ± SD		
	CT Set-1	**CT Set-2**	**p-Value**
PTV			
Dmax(cGy)	5302,20±36,11	5312,20±48,38	0,208
Dmean(cGy)	5067,30±40,50	5074,90±12,23	0,218
Bladder			
Dmax(cGy)	5286,70±66,79	5290,40±77,90	0,560
Dmean(cGy)	5006,40±96,44	5005,10±101,35	0,812

Small bowel			
Dmax(cGy)	5250,00±80,92	5258,90±89,01	0,083
Dmean(cGy)	995,43±461,48	1137,30±520,55	0,019*
Right femur			
Dmax(cGy)	5107,50±101,77	5106,00±107,28	0,705
Dmean(cGy)	2495,90±291,42	2504,60±297,48	0,137
Left femur			
Dmax(cGy)	5030,00±140,50	5028,90±147,08	0,168
Dmean(cGy)	2313,00±276,12	2323,80±283,66	0,166
MU	5362,60±71,76	5358,20±74,34	0,771

PTV, planning target volume; SD, standart deviation; 3DCRT, three dimensional conformal radiation therapy; Dmax, maximum dose of plan; Dmean, mean dose of structure; * significant value at $p<0.05$

4. Discussion

In the simulation phase of radiotherapy for pelvic diseases such as the rectum, IV contrast agents are frequently used for the purpose of delineation PTV and oral contrast agents are used to calculate the dose received by the intestines. In this study, we investigated the effects of these contrast agent on the dose distributions for two commercial TPSs using different calculation algorithms and connected to different treatment devices. Our findings revealed that there was no significant difference before and after contrast planning in almost any dosimetric parameter. This inability to find a difference is also applicable when comparing the MU values obtained for both techniques. There may be uncertainties in our study due to the fusion of two different CT scans. In addition, since there is optimization in the helical treatment plan, the results may be affected, but when we look at the literature, the differences in the dosimetric parameters of the treatment plans made with CT Set-2 and CT Set-1 are generally not significant. This may be due to the contrast used not being at a level that will affect the calculations of the algorithms.

In a study conducted by Heydarheydari, Farshchian and Haghparast [17], analysed the plans with CT Set-2 and CT Set-1 images of 11 pelvic cancer patients. Treatment plans created using Collapsed Cone and Superposition algorithms in DosiSoft ISOgray TPS. The researchers found no significant difference in target tissue PTV and critical organs, with the exception of the bladder in both CT situations. Similarly, in our study, while we did not find any significant difference in the target tissue PTV or critical organ doses between contrast and non-contrast plans in the 3DCRT technique, we found that in the Helical Therapy technique, the average dose value increased significantly only for the small bowel. The reason why there was a significant difference only in the bladder may be due to the planning algorithm used and the fact that contrast agents affect the bladder more.

Manindra Bhushan and his colleagues produced a contrast phantom. By assigning different HUs to this phantom, they obtained a non-contrast phantom. IMRT and VMAT plans were created for these phantoms using Eclipse TPS, which is compatible with the True-Beam linear accelerator. The plans created with both phantoms demonstrated comparable dose coverage for the PTV prostate for all photon energies, with exception of the VMAT plan created with the original phantom. As a result, they found target overdose meaningless for the planning made with both techniques[15].In our study, no significant dosimetric differences were observed in the PTV as a result of 3DCRT plans. We only found that the average doses for the small bowel in helical plans increased significantly after contrast.

Jabbari Nasrollah and colleagues created 3DCRT plans with and without IV contrast for 12 rectal patients and compared the doses. As a consequences, no significant difference was identified between contrast-enhanced and non-contrast 3DCRT plans. It was concluded that contrast-enhanced and non-contrast treatment plans were within tolerance limits for the clinic[16]. The results of this study did not reveal any significant differences between the contrast-enhanced and non-contrast for 3DCRT plans similar to their study.

Nadia Montero-Oleas and colleagues performed CT with and without oral contrast on rectal patients. Subsequently, 3DCRT and IMRT plans were created Eclipse TPS using the Acuros XB calculation algorithm with contrast-enhanced CT. These plans were than recreated with contrast-enhanced CT under the same conditions. Ultimately, they found no clinical differences in the majority of dose measurements. The greatest discrepancy was observed in the volume of the small intestine receiving 45 Gy. They interpreted that this difference may be lower due to contrast-enhanced CT. As a result, authors concluded that the use of oral contrast did not significantly impact dose calculations and may not affect the acceptance of plans, provided that the aforementioned limitations are taken into

account[18].According to the results we obtained from contrast-enhanced and non-contrast plans in our study, there were no differences that would affect clinical plan acceptance.

Yuta Shibamoto and his colleagues create two contrast-enhanced and non-contrast plans using Eclipse TPS for 5 pelvic cancer patients. They first made the plans on contrast-enhanced CT scans and then copied the plans to non-contrast images and recalculated. They found the average difference in MUs to be below 1% for both conditions. Consequently, they reported that there was no significant difference in dose calculations between contrast and non-contrast in treatment planning[19]. In our study, parallel to this study, the increase in MUs in 3DCRT contrast-enhanced plans was below 1%.

5. Conclusion

In our study, we compared 3DCRT and helical therapy plans using CT Set-2 and CT Set-1s to be used for the definition of PTV and critical organs in rectum cancer treatments. As a result, no significant difference was observed in terms of PTV and critical organs in the comparison of 3DCRT plans. In the comparison of helical plans, there was only a significant difference in the bladder. Based on these results, we suggest that planning can be done with a single CT Set-2 for 3DCRT treatments, both to avoid further discomfort for the patient and to prevent additional tomography doses. On the other hand, for helical therapy, we believe that it can be clinically evaluated whether the treatment will be performed with CT Set-2 depending on the patient's condition.

Acknowledgement

There are no financial declarations. This work is not grant funded.

Author's Contributions

Hikmettin Demir: Drafted and wrote the manuscript, supervised the experiment's progress, performed the experiment and result analysis.

Gül Kanyılmaz: Assisted in analytical analysis on the structure, supervised the experiment's progress, result interpretation and helped in manuscript preparation.

Osman Vefa Gül: Assisted in analytical analysis on the structure, supervised the experiment's progress, result interpretation and helped in manuscript preparation.

Ethics

There are no ethical issues after the publication of this manuscript.

References

[1]. H. Sung, J. Ferlay, R.L. Siegel, M. Laversanne, I. Soerjomataram, A. Jemal, F. Bray, Global cancer statistics 2020: GLOBOCAN estimates of incidence and mortality worldwide for 36 cancers in 185 countries, CA: a cancer journal for clinicians 71(3) (2021) 209-249.

[2]. Z. Yu, Y. Hao, Y. Huang, L. Ling, X. Hu, S. Qiao, Radiotherapy in the preoperative neoadjuvant treatment of locally advanced rectal cancer, Frontiers in Oncology 13 (2023).

[3]. R. Glynne-Jones, L. Wyrwicz, E. Tiret, G. Brown, C.d. Rödel, A. Cervantes, D. Arnold, Rectal cancer: ESMO Clinical Practice Guidelines for diagnosis, treatment and follow-up, Annals of Oncology 28 (2017) iv22-iv40.

[4]. A.B. Benson, A.P. Venook, M.M. Al-Hawary, L. Cederquist, Y.-J. Chen, K.K. Ciombor, S. Cohen, H.S. Cooper, D. Deming, P.F. Engstrom, Rectal cancer, version 2.2018, NCCN clinical practice guidelines in oncology, Journal of the National Comprehensive Cancer Network 16(7) (2018) 874-901.

[5]. M.J. van der Valk, C.A. Marijnen, B. van Etten, E.A. Dijkstra, D.E. Hilling, E.M.-K. Kranenbarg, H. Putter, A.G. Roodvoets, R.R. Bahadoer, T. Fokstuen, Compliance and tolerability of short-course radiotherapy followed by preoperative chemotherapy and surgery for high-risk rectal cancer–Results of the international randomized RAPIDO-trial, Radiotherapy and Oncology 147 (2020) 75-83.

[6]. T. Conroy, N. Lamfichekh, P.-L. Etienne, E. Rio, E. Francois, N. Mesgouez-Nebout, V. Vendrely, X. Artignan, O. Bouché, D. Gargot, Total neoadjuvant therapy with mFOLFIRINOX versus preoperative chemoradiation in patients with locally advanced rectal cancer: final results of PRODIGE 23 phase III trial, a UNICANCER GI trial, American Society of Clinical Oncology, 2020.

[7]. K.C. Peeters, C.A. Marijnen, I.D. Nagtegaal, E.K. Kranenbarg, H. Putter, T. Wiggers, H. Rutten, L. Pahlman, B. Glimelius, J.W. Leer, The TME trial after a median follow-up of 6 years: increased local control but no survival benefit in irradiated patients with resectable rectal carcinoma, Annals of surgery 246(5) (2007) 693-701.

[8]. M. Zoccali, A. Fichera, Role of radiation in intermediate-risk rectal cancer, Annals of surgical oncology 19 (2012) 126-130.

[9]. J.-P. Gérard, T. Conroy, F. Bonnetain, O. Bouché, O. Chapet, M.-T. Closon-Dejardin, M. Untereiner, B. Leduc, É. Francois, J. Maurel, Preoperative radiotherapy with or without concurrent fluorouracil and leucovorin in T3-4 rectal cancers: results of FFCD 9203, Journal of clinical oncology 24(28) (2006) 4620-4625.

[10]. A. Sipaviciute, E. Sileika, A. Burneckis, A. Dulskas, Late gastrointestinal toxicity after radiotherapy for rectal cancer: a systematic review, International Journal of Colorectal Disease 35 (2020) 977-983.

[11]. A. Dulskas, P. Kavaliauskas, L. Pilipavicius, M. Jodinskas, M. Mikalonis, N.E. Samalavicius, Long-term bowel dysfunction following low anterior resection, Scientific reports 10(1) (2020) 11882.

[12]. N.P. McKenna, K.A. Bews, K.J. Yost, R.R. Cima, E.B. Habermann, Bowel dysfunction after low anterior resection for colorectal cancer: a frequent late effect of surgery infrequently treated, Journal of the American College of Surgeons 234(4) (2022) 529-537.

[13]. E. Pape, P. Pattyn, A. Van Hecke, N. Somers, D. Van De Putte, W. Ceelen, E. van Daele, W. Willaert, Y. Van Nieuwenhove, Rectal cancer survivorship: the struggle of the low anterior resection syndrome (LARS), Annals of Oncology 29 (2018) viii698.

[14]. B. Celerier, Q. Denost, B. Van Geluwe, A. Pontallier, E. Rullier, The risk of definitive stoma formation at 10 years after low and ultralow anterior resection for rectal cancer, Colorectal disease 18(1) (2016) 59-66.

[15]. M. Bhushan, D. Tripathi, G. Yadav, L. Kumar, A. Dewan, S. Tandon, G. Kumar, I.K. Wahi, M. Gairola, Effect of contrast medium on treatment modalities planned with different photon beam energies: a planning study, reports of practical Oncology and radiotherapy 26(5) (2021) 688-711.

[16]. J. Nasrollah, M. Mikaeil, E. Omid, S.S. Mojtaba, Z. Ahad, Influence of the intravenous contrast media on treatment planning dose calculations of lower esophageal and rectal cancers, Journal of cancer research and therapeutics 10(1) (2014) 147-152.

[17]. S. Heydarheydari, N. Farshchian, A. Haghparast, Influence of the contrast agents on treatment planning dose calculations of prostate and rectal cancers, Reports of Practical Oncology & Radiotherapy 21(5) (2016) 441-446.

[18]. N. Montero-Oleas, A. Imbaquingo-Cabrera, A. Coloma-Espin, V. Collantes-Cruz, C. Molineros, C. Núñez-Silva, Dosimetric effects of oral contrast in the planning of conventional radiotherapy and IMRT, for rectal cancer treatment, Journal of Radiotherapy in Practice 22 (2023) e54.

[19]. Y. Shibamoto, A. Naruse, H. Fukuma, S. Ayakawa, C. Sugie, N. Tomita, Influence of contrast materials on dose calculation in radiotherapy planning using computed tomography for tumors at various anatomical regions: a prospective study, Radiotherapy and oncology 84(1) (2007) 52-55.

Celal Bayar University Journal of Science

Fake News Detection with Machine Learning Algorithms

Batuhan Battal[1], Başar Yıldırım[2], Ömer Faruk Dinçaslan[3], Gülay Çiçek[4]*

[1,2,3] Department of Software Engineering, Istanbul Beykent University, Sariyer, Istanbul, Turkey
[4] Department of Biomedical Engineering, Istanbul Beykent University, Sariyer, Istanbul, Turkey

* gulaycicek@beykent.edu.tr
* Orcid No: 0000-0002-6607-1181

Received: 24 April 2024
Accepted: 7 September 2024
DOI: 10.18466/cbayarfbe.1472576

Abstract

Nowadays, with the advancement of technology, the use of news sources has also undergone a great evolution. News sources have constantly evolved from past to present, ranging from magazines to radios, from newspapers to televisions. The fact that it has become so easy to access news has caused society to pay more attention to fake news. Fake news has the ability to influence society through news sources such as social media, which can reach wider audiences with the development of technology. The difficulties of users in accessing accurate and reliable sources in this information flow that shapes their daily lives increases the potential for the spread of fake news, and it becomes increasingly difficult to distinguish between real and fake news. In this study, classification models for fake news detection were designed using machine learning algorithms. The dataset, which includes fake and real news examples, contains 42,000 examples. Each class, including fake and real samples, contains 22,000 sample data. In order to increase data quality, accuracy and usability, preprocessing methods were applied to the data set. The removal of numbers, stop words, and html tags was done in the pre-processing step to remove unnecessary information from the text. Models were created for fake news detection with singular and ensemble classification algorithms. Performance evaluation of the models was performed using 5-fold cross-validation. In the performance comparisons of the models, values such as accuracy, sensitivity, specificity, tp rate and fp rate were calculated. The highest performance results were observed in the random forest classification algorithm with an accuracy rate of 76%.

Keywords: Fake News Detection, News on Social Media, Classification.

1. Introduction

Throughout the entire historical process, humanity has needed various means of communication and communication, has constantly improved these tools and these developments have brought societies closer. Since the beginning of the modern era, people have witnessed a lot of development, in the past, these events were spread among the people through rumors and this situation has created the need to convey to the people in a more reliable and comprehensive way. As examples of these communication tools; although communication tools such as smoke communication and homing pigeons were sometimes used for various reasons such as war, these primitive communication tools have evolved into more modern technological devices such as correspondence, newspapers, magazines, as well as telegraph, radio and television. Especially in the modern times of technology, the parallel spread of information has led to the rapid spread of false and manipulated information. Therefore, these tools and requirements have also brought information pollution. Just as it is difficult to access accurate information in today's world, it has also been difficult to detect false information and turn it into correct information in the past [1]. But this challenge is more intense now than in the past. Because one-sided news sources are written from a certain point of view, people have been subjected to great manipulation from the moment they first received the news and imposed this dirty information on people. At times, this situation was consciously used by state officials or institutions to use the public for their evil purposes [2]. For example: Procopius, who lived in Byzantium in the 500s AD, was a historian. After he managed to attract the attention of Emperor Justinianus with his official history writings, he produced dubious information known as "anecdotes" in order to tarnish the reputation of the emperor and kept this secret until his death. Pietro Aretino wrote strange sonnets about the candidates to manipulate the papal elections in 1522. He started singing these sonnets to the public near the statue known as Pasquino in Navona Square in Rome.

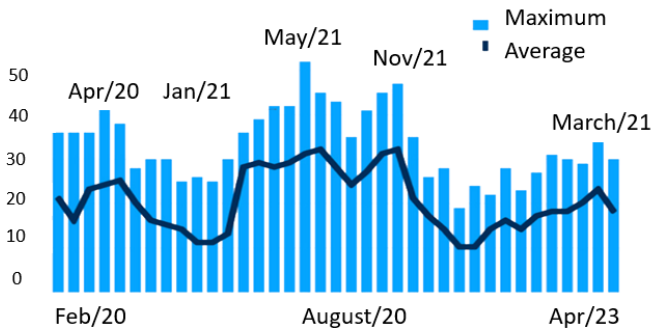

Figure 1. Effects of Fake Trends on the Agenda [3]

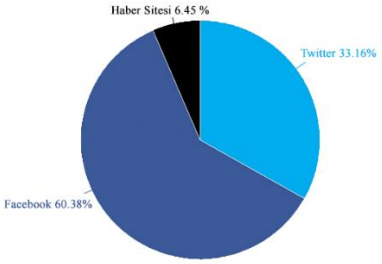

Figure 2. Fake News Distribution on Social Media [4]

The term “pasquinade” later evolved into a general usage for immoral and often false news about public figures [5]. Today, social media platforms play an important role in receiving and sharing news. However, fake trends appearing on these platforms can mislead users and have widespread effects. Twitter is a platform known for its rapid flow of information and provides a striking example of how fake trends form and spread on this network. In Figure 1, it is possible to see the ratios of the effects of fake trends on the agenda to the months. In light of these developments, not only the manipulative effect of misinformation has increased, but also the spread of correct information has increased rapidly. People's interests have expanded further and they have begun to have ideas about the world, not just the region they live in. Thus, as the interest and desire for science increases, over time technology does not stand still as it always does. With the increase in these areas of interest, technological developments have increased exponent tially. These events have begun to spread rapidly around the world. Especially after this interest in the technology sector, new inventions have naturally begun to enter people's lives. Of course, the most important of these inventions are the computer and the mobile phone. With the introduction of these tools into people's lives, of course, information has become more fluid than in the past. People now carry a news machine in their pockets and can access information whenever they want.

Today, a communication platform called digital media has emerged with mobile phones. Therefore, the number of users is also increasing. Access to information has become faster and more comprehensive than ever before. Among these wide-ranging resources, the easy and widespread use of the internet and social media platforms facilitates the sharing of information, but also allows misleading content to spread rapidly. This situation has created an environment that allows fake news to spread much more easily and thus, contrary to popular belief, it has become more difficult for the user to access reliable and accurate information.

Considering this emerging situation, users' difficulties in accessing accurate and reliable sources in this information flow that shapes their daily lives increases the potential for the spread of fake news and it becomes increasingly difficult to distinguish between real and fake news. At the core of this incident, the detection of these fake news is not only an information security issue, but also has a very critical importance for the healthy functioning of a democratic and moral society. Because fake news can influence the way societies think, undermine public trust and even shape political decisions. Following these, detecting fake news and distinguishing it from real information has become a major challenge today. As in the past, today there have been many manipulative movements and political tactics aimed at misleading the public. Although this is sometimes for the good of the public, it can sometimes

have bad consequences [6]. Regarding these manipulative events, the fake news post targeting the American president that took place in the USA in 2017 is given as an example. “In the long history of misinformation, recent developments in fake news hold a special place, especially when Kellyanne Conway, special advisor to US President Donald Trump, went to great lengths to invent the Kentucky massacre to defend the travel ban on Muslim countries. The fabrication of alternative facts is also quite rare historically, but the equivalent of today's poisonous, tasteful articles and tweets can be found in different historical periods, even in ancient times. ”

Fake News is gaining widespread popularity by spreading rapidly, especially through social media channels and online news sites. The influence of social media algorithms, the use of emotional content, people's tendency to confirm their own opinions, and the lack of scrutiny of news sources make it easier for fake news to spread. As seen in Figure 2, the distribution of fake news in social media channels is shown. As society uses social media more, it has been observed that the distribution of fake news has increased significantly on Facebook and Twitter. With the proliferation of information brought about by the digital revolution, the rise of social media and the increased availability of online news, the potential for the spread of fake news has naturally increased much more. This situation causes consciously produced misinformation to be shared, sometimes at almost the same speed and interaction as real news [7]. Therefore, detecting and combating fake news has become an important problem faced by modern societies in the information age. Therefore, users need to be more conscious and careful when using social media [8].

Due to the nature of social media platforms, the speed at which news and information shares reach large audiences has reached a considerable level. Since the number of users of these social media platforms has reached millions of people, the spread of fake news has reached lightning speed over time, especially on social media platforms such as Instagram, Twitter, YouTube, Facebook and TikTok. Therefore, these platforms, which everyone has access to, have also increased their user portfolio, and users now include not only adults but also children. According to research done; As people get younger, the time spent on using social platforms increases. As a result of this information, it is observed that social media use is inversely proportional to age. Getting news is the most frequently cited reason for using social media among all age groups except Generation Z [9].

Twitter has now become the new news source. Day by day, people lose their trust in news sources and get almost most of their news from Twitter. With journalists now active on social media, news circulation has become even more intense. This intensity has been abused by some people and institutions and has become manipulative, and over time it has turned into a disadvantageous situation. Fake news made by malicious users affects human activities in every aspect. In this context, identifying fake news is a critical issue in order to protect the individuals or institutions that are the main theme of the news and to ensure that readers obtain reliable information [10]. In addition to accessing information being special, detecting fake news is of great importance. One of the benefits of this is that the reader reaches a single truth and in addition, their trust in the news system increases. For this reason, it is essential to examine fake news in more detail before starting fake news detection studies [11].

In this study, for the modeling created for the detection of fake news, primarily data cleaning (getting rid of noisy and inconsistent data), data integration (bringing together different data sources), data selection (to turn the data sets used into a better categorized data set). It needs to be made suitable for data processing using data mining techniques such as identifying important data to be analyzed) and data transformation. Thus, thanks to these well-categorized data sets, it will be easier to detect fake news [12]. In addition to facilitating communication, social media platforms also face problems such as the spread and interaction of bot accounts. In particular, Twitter constantly takes various measures to distinguish between real and fake accounts [13]. Within the scope of these measures, the number of closed bot accounts is increasing day by day. As seen in Figure 3, the rates of bots closed on Twitter are given by month [14].

Figure 3. Closed Bots

In the study of Shu and other researchers, it can be seen that they examined the psychological and social aspects of fake news in traditional media and social media, as seen in Figure 4. When we look at the first category, there are fake accounts created for propaganda purposes, while the second category includes the "echo chamber" effect, which occurs as a result of users following people with similar thoughts and trusting the news shared by these accounts, where they tend to receive and share news that is close to their interests, even though it is fake news. It has been emphasized that fake news spread by fake accounts created for propaganda purposes on social media is spread through social bots, troll accounts and semi-robot accounts. News frequently shared by troll or bot accounts in similar time periods is perceived as true by real users and shared by many real accounts in a short time. This increases the credibility of fake news shared through real accounts [15].

In the balanced dataset containing equal number of fake and real news samples, relevant preprocessing methods were applied to the dataset in order to improve data quality and increase accuracy and usability. Thus, the effect of unexpected results was minimized and the way was opened for the creation of a more robust model. Different classification models were created with single (Logistic regression, Decision Tree, Gradient Booster, Random Forest, K Nearest Neighbor, Naive Bayes and Support Vector classification) and ensemble classification (ensemble classification) algorithms. Cross-validation was used to objectively ensure the performance of the model. Accuracy, sensitivity, specificity, tp ratio, fp ratio values were calculated to compare the performance techniques of different classifiers. Fake news detection was detected with a higher success rate in the random forest classification algorithm compared to single classification algorithms. The following features were taken into account for an interesting model.

1.1 Features That Make a Pattern Interesting

In our study, an automatic pattern (model) was studied that detects the accuracy of the news in the tweets sent on Turkish texts shared on the Twitter network.

1.1.1 Easily Understandable by People

As in Section II, in the Literature study section, studies and analyzes related to the detection of fake news are given. In Section III, definitions and details of the classification algorithms used in the Method section are given. In Section IV, the results of the classification algorithms used in the previous section were obtained and compared and examined. This study focuses on the detection of fake news and the strategies and solutions used in this process. The comprehensibility factor plays a critical role in ensuring that the information in the article is understandable to a wide audience. This study addresses the issue of fake news detection in a way that everyone can understand, by focusing on methods such as avoiding complex terms, supporting with examples and using visual tools. In the fight against fake news, clear communication plays a vital role in raising public awareness and taking effective measures.

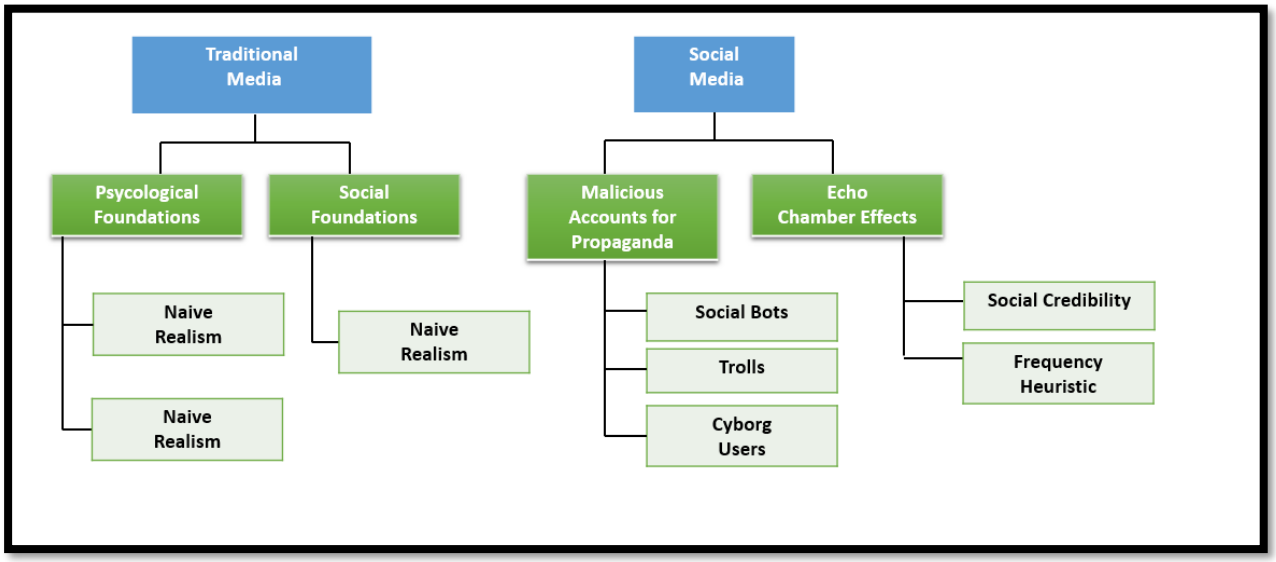

Figure 4. Types of Fake News [4]

1.1.2 Validity of the Pattern

This study focuses on detecting fake news on Twitter. We discuss new strategies for Twitter analysis and fake news detection to combat misleading information that spreads rapidly on social media platforms. The study offers a more reliable approach to combating fake news by addressing issues such as strengthening validation processes and using test data effectively to obtain highly accurate results. These strategies are an important step in increasing society's access to accurate information and reducing misleading content spread on social media.

1.1.3 Potentially Useful Pattern

This study discusses how potentially useful data can be used to detect fake news on Twitter, an important platform of social media. Detection of fake news is of critical importance in ensuring society's access to accurate information and combating misleading content. This study examines in detail the potentially useful features obtained by analyzing Twitter data and how this data can be used effectively in detecting fake news. In order to contribute to fake news detection processes, our study emphasizes the role of potentially useful data in fake news analysis.

1.1.4 Novality of the Pattern

In this study, a new perspective on the detection of fake news is presented and a model developed on Twitter data is discussed. On social media platforms, where fake news spreads rapidly, it is inevitable to adopt an approach beyond traditional methods. This study explains in detail how a new and innovative model was created and its success in detecting fake news effectively. This novel (innovative) model, developed using Twitter data, manages to stand out in fake news analysis. Additionally, experiences on real and fake test data are presented in detail in the article to concretely prove the features provided by the model.

As in Section II, in the Literature study section, studies and analyzes related to the detection of fake news are given. In Section III, definitions and details of the classification algorithms used in the Method section are given. In Section IV, the results of the classification algorithms used in the previous section were obtained and compared and examined.

2. Literature review

In the literature, it can be seen that many studies have been carried out to detect fake news on social media. For example, in the studies of Mehmet Kayakuş and Fatma Yiğit Acıkgöz (2023), as a first step, they tried to obtain research and information about fake news and in the light of this information, a draft was created and the study started. Then, the semi-supervised artificial intelligence algorithm was applied to the structured fake news dataset. The data is divided into two as training and test data according to the 70 percent - 30 percent random assignment method. When the study results are examined according to the f-measure, it is seen that the Naive Bayes classification algorithm is more successful than the Decision Trees classification algorithm [16].

Taşkın and his team (2021) used machine learning-based methods in their study to detect fake news that could mislead people. Pre-processing was applied to the data set used for this purpose and fake news was detected with machine learning processes. Unsupervised learning

algorithms, Non-Negative Matrix Multiplication and Linear Discriminant Analysis; Prediction was made with supervised learning algorithms, K Nearest Neighbor, Support Vector Machines and Random Forest algorithms. Successful results have been obtained in supervised learning algorithms with an f-measure value of 0.86 [17]. In their study on fake news detection with machine learning methods, Zeba and her team [18] achieved 96.8% accuracy with Naive Bayes and 99.6% accuracy with neural network and support vector machines [19]. Aswini and his team offer solutions to fake news detection with deep learning methods. The model outperforms existing architectures by 2.5% and achieves an accuracy of 94.21% on test data [20]. In the study of Fatima and his team on fake news detection, the frequency inverse document frequency (TF-IDF) term consisting of n-grams and the bagging method were used as feature extraction techniques for the dataset consisting of fake and real news. In the study, it was observed that the N gram method gave better results than the bag method and the most successful results (100% accuracy) were achieved with support vector machine algorithms [21]. Sathish and his colleagues used various machine learning algorithms to detect fake and real news. They achieved 99.7% accuracy with the decision tree [22]. In the age we live in today, fake news has become a serious problem. Identifying and stopping the spread of misinformation is of importance. In order to examine the current emotional environment, textual data must first be converted into numerical data. Using TF-IDF, textual data was converted into numerical data. Models for fake news detection were developed using decision trees, support vector machines and logistic regression classification algorithms. The study achieved a maximum accuracy of 98% with machine learning algorithms [23]. People prefer the internet to access news because it is easy and cheap. In this study, they developed models with machine learning methods using the publicly available LIAR dataset for fake news detection [24]. Fake news affects our social life in every field, especially politics and education. Various classification algorithms and machine learning models have been developed to detect fake news. Methods such as Term Frequency-Inverted Document Frequency were used for feature extraction and support vector, naive bayes, passive aggressive classifier were used as classification algorithms. The highest accuracy of 95.00% was obtained with support vector machines [26].

Fake news or unreal news that harms social integrity appears everywhere. The study enabled the detection of fake news using probabilistic latent semantic analysis. In order to detect fake and real news, different machine and deep learning techniques were compared using three different data sets. In the study, it was observed that deep learning techniques gave more successful results than machine learning techniques. In this encounter, it was observed that the Bi-LSTM algorithm gave the most successful results (95% accuracy) in detecting fake news [27]. Fake news has a huge negative impact on the majority of society. In order to detect these news, three different evaluation methods: Count Vectorizer, TF-IDF Vectorizer and N gram were used. Models for fake news detection were developed using Naive Bayes, SVM, Random Forest and Logistic Regression classification methods. The highest success rate was achieved with the SVM classifier (93% accuracy) [28]. Models have been developed with data mining methods to automate the authenticity of news received from various sources such as websites, blogs and e-content. Data mining techniques are applied to collect data, clean and visualize the data. The aim of the study is to develop models to understand misleading information. In order to detect fake news efficiently, models have been created using data mining methods to detect fake news by combining the title and text of the news [29]. In the study, it is classified using the ensemble model, which consists of three popular machine learning models, namely Decision Tree, Random Forest and Extra Tree classifier, for the detection of fake news, which achieves better accuracy compared to the current situation. While 100% accuracy was achieved for the ISOT dataset, 99.8% accuracy was achieved for the Liar dataset [30]. A classification model was developed with machine learning techniques to enable the detection and dissemination of facts. Features were extracted from the dataset using text representation models such as Bag of Words, Term Frequency-Inverse Document Frequency (TF-IDF) and bi-gram frequency. It has been observed that the TF-IDF model gives more successful results than the bag of words and TF-IDF method. Fake news has become quite common in digital media. For this purpose, Z and his colleagues developed models with machine and deep learning algorithms for the detection of fake news. Naive Bayes and Support Vector Machine were used as machine learning algorithms, and Long Short-Term Memory (LSTM), Neural Network with Keras and Neural Network with TensorFlow were used as deep learning algorithms. Accuracy, precision, recall and f-measure values were included in the performance comparison of the models. The results have shown that deep learning algorithms provide more successful results than machine learning algorithms. The highest accuracy rate was obtained with the LSTM model (92.99%) [31]. Khaled and his colleagues developed models using Machine and Deep Learning methods to detect fake news in the Arabic language. LSTM, bidirectional LSTM, CNN+LSTM, and CNN+BiLSTM methods were used as deep learning models. Experiments were carried out using three different data sets. It was observed that the BiLSTM model performed better than other models in terms of accuracy [32]. Fake and Misleading content always misleads people, causing turmoil in public life. In Bengali, models were created with machine learning algorithms to detect fake news. This algorithm uses TF-IDF method for feature extraction. Feature selection was made with Extra Tree Classifier.

Feature selection was made with Extra Tree Classifier. An 87% accuracy rate was achieved with the Gaussian Naive Bayes classification algorithm [33].

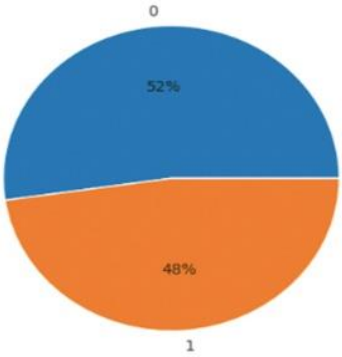

Figure 5. Ratio of Fake News to Real News [4]

In this study, we discuss a creative model developed on Twitter data by bringing a different perspective to this field regarding the detection of fake news. In today's social media platforms, where fake news spreads rapidly, it is very important to adopt an approach other than traditional methods. This study explains in detail how a new, understandable and innovative model was created and highlights the success of this model in effectively detecting fake news. This new model, developed with the use of Twitter data, manages to stand out in fake news analysis. In addition, the article presents in detail the experiences made on real and test data in order to concretely prove the features provided by the model.

3. Method

3.1 Data set

In this study, it is aimed to detect tweets containing real and fake news spread on Twitter on a certain subject with artificial intelligence. Within the scope of this research, a topic that was trending on Twitter and contained fake news was selected. The data set was divided into training and test data using the K Fold Cross Validation (K=2) method. The training data was used to define and learn the parameters of the model. Figure 5 shows the ratio of total fake and real news in this data set. Table 1 shows 5 examples of the first version of our data set.

3.1.1 Getting Data from Twitter and Topic Selection

The tweets sent regarding this issue were referenced from the Kaggle study called "fake news detection". After text pre-processing and analysis were carried out on the determined tweet messages, two categories were created: real and fake news. These categories are classified as real and fake. There are four attributes in the real category; these are "title", "text", "subject" and "date". Title has approximately 21,000 different values. Text has approximately 21,000 different values. 53% of the tags under the Subject heading are political news, and 47% are news from the rest of the world. Date includes the period from 13-01-2016 to 31-12-2017. In total, there are approximately 42,000 pieces of data in the real and fake.

Data Preprocessing Steps

In this study, KDD (Knowledge Discovery in Databases) steps were applied, KDD refers to the data mining process and consists of several stages [18].

The KDD stages are;

1. Data Cleansing: The data mining process usually starts with real-world data. This data may contain missing, inaccurate or inconsistent information. During the data cleaning phase, such problems are resolved and the data set is prepared.

2. Data Integration: Data from different sources should be integrated. Data integration involves combining, adapting, and bringing together data sets.

3. Data Selection: This is the stage of selecting relevant data features and subsets. This involves selecting data that suits the purpose of analysis.

4. Data Transformation: The data set is transformed through processes such as itemization and normalization. This can help the dataset be more effective in the modeling stages.

5. Data Mining: In the data mining phase, various itemization techniques are used to discover patterns, relationships or information. Algorithms such as decision trees, support vector machines and clustering can be used at this stage.

6. Pattern Evaluation: Where visualization and information presentation techniques are used to mine instant information for users

7. Presentation of Information: Where visualization and information representation techniques are used to present data mined information to users.

Table 1. Initial State of the Data Set

	Title	Text	Subject	Date
0	Donald Trump Sends..	Donald Trump Just…	News	Dec 31, 2014
1	Drunk Bragging	House Intelligence…	News	Dec 31, 2017
2	Sherif David…	On Friday, it was…	News	Dec 30, 2017
3	Trump Is So…	On Christmas day…	News	Dec 29, 2017
4	Pope Francis…	Pope Francis	News	Dec 29, 2017

In our study, the steps taken to detect a pattern (Fig. 6) are given below.

- Data Cleaning: The data in this study contains missing, incorrect or inconsistent information. During the data cleaning phase, such problems were resolved and the data set was prepared. For example, the missing values were checked with the msno.bar () function and the number with missing values was found with isnull ().sum(). This phase focused on missing data, meaningless characters, or other data integrity issues.

- Data Integration: Data from different sources should be integrated. Data integration involves combining, adapting and bringing together data sets. It accomplishes this stage by combining two separate data sets containing fake and real news (with pd. concat ()).

- Data Selection: This is the phase of selecting relevant data features and subsets. This involves selecting data that suits the purpose of analysis. For example, the columns "title", "text", "subject", "date" can be selected.

- Data Transformation: The data set is transformed through processes such as itemization and normalization. This will help the dataset be more effective in the modeling stages.

- Data Mining: In the data mining phase, various itemization techniques are used to discover patterns, relationships or information. In the data set in this study, various classification methods from data mining methods are applied to create a model for the purpose of distinguishing fake and real news with the "class" column.

- Pattern Evaluation: The results obtained for "pattern evaluation" or model evaluation can be evaluated by looking at the outputs of the models included in the code (Logistic Regression, Decision Tree, Gradient Booster, Random Forest, K-Nearest Neighbors, Naive Bayes, Support Vector Machine) [18]. Model evaluation is usually done using metrics such as accuracy, precision, recall and f-measure.

- Knowledge Presentation: This is the name given to the presentation stage. It is determined whether our data is ready for presentation, and the results of the modeling are shared with the necessary visuals and explanations.

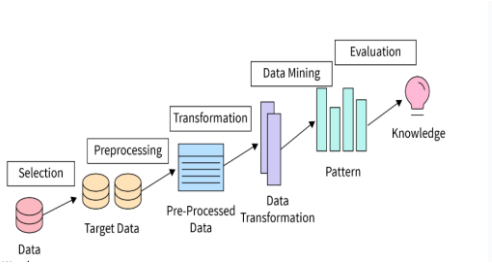

Figure 6. Fake News Detection Methodology

3.2.1 Text Preprocessing

Preprocessing method is a stage of great importance in text mining and application. In the text preprocessing step, crowded data, redundancies and useless data are cleared, thus the success of the study is expected to increase. The processes used for pre-processing are converting letters to lowercase characters, character cleaning, URL cleaning, cleaning HTML tags, cleaning new lines, cleaning numbers and digits [20]. These are different text preprocessing steps that can be done on texts in the preprocessing step. The data in the data set we use must have a common layout in a document where uppercase and lowercase letters are used. This may be caused by typos and possible errors. In text preprocessing, the uppercase or lowercase conversion process aims to change all the letters in a text so that they are all the same. Common words that do not add meaning to the relevant text, such as the use of punctuation marks, web programming codes, URLs, emoji's, frequently used and infrequently used words, are removed. Various stop word features should be extracted by analyzing stop words in the text data, that is, words that are commonly used and generally meaningless, using the list called Stopwords. Then the columns in the data frame are analyzed. cat cols: Lists containing categorical (string or category type) columns are printed one by one in our code. num cols: Lists containing numeric columns are printed as code. cat but car: Lists that are of category type but contain columns whose cardinality (number of unique values) is higher than a certain threshold value are printed as code.

3.2.2 Feature Extraction Methods

The "title", "subject" and "date" columns were extracted from the dataset, usually part of the data preprocessing step. Whether to remove or not use these attributes depends on the analysis purposes and the characteristics of the data set. We can explain the reasons for removing each of the title, title and date columns respectively as follows. The "title" usually contains text data and can contain many different words and characters. Therefore, they may need to be processed before being used directly. Title can be subjected to separate analysis, especially for use in text item modeling or natural language processing applications. However, it is possible to remove this column to focus on your original analysis. Topic titles usually refer to a specific topic or category. However, this information can already be found in the "class" column, which can be used as a target variable, especially if classification models are to be used. In this case, the "subject" column containing similar information may be unnecessary. Date can be important for time series analysis or analysis performed over specific date ranges. However, since this type of analysis is not performed and the "date" column does not affect the model, it may be preferable to remove this column. Removing columns simplifies the dataset and reduces unnecessary noise when training the model [21].

3.3 Classification

3.3.1 Supervised Machine Learning Algorithms

In this study, 7 classification algorithms were used to predict whether the news obtained from tweets on Twitter are fake or real. These; Logistic Regression Classification, Decision Tree Classification, Gradient Boosting Classification, Random Forest Classification, K Nearest Neighbor Classification, Naive Bayes [23].

3.3.2 Logistic Regression Classification (LR)

Logistic Regression is a model generally preferred for two-class (binary) classification problems. The general purpose of classification algorithms is to classify by determining the value of the dependent variable. The relationship between the sigmoid function and the coefficients in LR plays a critical role in the process of estimating the probability of the dependent variable. The results of the LR Classification algorithm's Principal Component Analysis (PCA) and K Fold approach without PCA are given in Table 2.

3.3.3 Decision Tree Classification (DT)

Decision trees are a widely used technique in the field of data mining and machine learning. This method can be applied to both classification and regression problems and is especially preferred because it is understandable and interpretable by humans. In this study, a model was created using decision tree classification and predictions were made on test data. The algorithm works by splitting the dataset and creating a custom classification model for each subset. The success of the model is strictly evaluated and the classification report reveals the results. The results obtained with the K-Fold Approach with PCA. The results of the DT classification algorithm with PCA and the K-Fold approach without PCA are given in Table 2.

3.3.4 Random Forest Classification (RF)

Random Forest Classification Method is an ensemble learning technique in which many decision trees are brought together. This methodology adopts an approach where each tree is trained independently and the overall model is obtained by taking the average or mode of the predictions of these trees. The main purpose of Random Forest is to obtain a more general and reliable model by reducing the tendency of a single decision tree to overfit. The exact success of the model is evaluated and the classification report is displayed as a result. The K Fold

approach results of the RF classification algorithm with PCA and without PCA are given in Table 2.

3.3.5 Gradient Boosting Classification (GBT)

Gradient Boosting is known as an ensemble learning technique and aims to create a strong model by combining weak decision trees. This method improves the success of the model by sequentially adding weak decision trees using an error reduction strategy. A frequently used application of Gradient Boosting is decision trees called Gradient Boosted Trees (GBT), which are especially preferred for classification and regression problems. The accuracy of the model is evaluated and presented as a classification report. The PCA and K Fold approach results of the GBT classification algorithm without PCA are given in Table 2.

3.3.6 K Nearest Neighbor Algorithm (KNN)

K-Nearest Neighbors (KNN) is a machine learning algorithm used for classification and regression problems. KNN is a simple and effective algorithm and performs especially well on small-sized datasets. The success of the model is evaluated with precision and the classification report is printed as a result. The PCA and K Fold approach results of the GBT classification algorithm without PCA are given in Table 2.

3.3.7 Naive Bayes Classification (NB)

Naive Bayes classifier is based on Bayes Theorem. Bayes' Theorem is a theorem that updates the probability of an event occurring with information from another context. Naive Bayes Lemma: The "naive" statement assumes independence between each feature of the model. That is, the presence or absence of one feature does not affect the presence or absence of other features. Text Data and Feature Extraction: While working on text data, it is first necessary to convert the text data into features. This is usually done using methods such as "TF-IDF" (Term Frequency-Inverse Document Frequency). Classification: Naive Bayes classifier creates a model using feature vectors and class labels. Feature vectors on text documents can be word frequencies or TF-IDF values. When a test data arrives, the Naive Bayes model calculates the probability that this data belongs to each class. Then, it classifies this data into the class with the highest probability. The success of the model is evaluated with precision and the classification report is printed as a result. The results of the NB classification algorithm's PCA and K Fold approach without PCA are given in Table 2.

3.3.8 Binary Classification Using Support Vector Machines (SVM)

Support Vector Machines (SVM) is a machine learning algorithm used especially for classification and regression problems. Essentially, it tries to create a hyperplane to separate classes in a given data set. The goal of SVM in the binary classification task is to find a hyperplane that best separates two classes in the dataset. A hyperplane is a plane in feature space that divides a subspace into two classes. The success of SVM in classifying data points belonging to a particular class depends on the distance of these points from the hyperplane. The success of the model is evaluated with precision and the classification report is printed as a result. The results of the NB classification algorithm's PCA and K Fold approach without PCA are given in Table 2.

3.4 Performance Metrics

The confusion matrix (Fig.7), also known as the error matrix, is a special tabular layout that allows visualizing the performance of a classification model. Various performance measures are used to determine the classification ability of machine learning algorithms. Statistical values such as accuracy, precision, sensitivity, recall and f-measure provide detailed information about prediction in classification performance measurements. The definitions and formulas of these statistical criteria are given below, respectively.

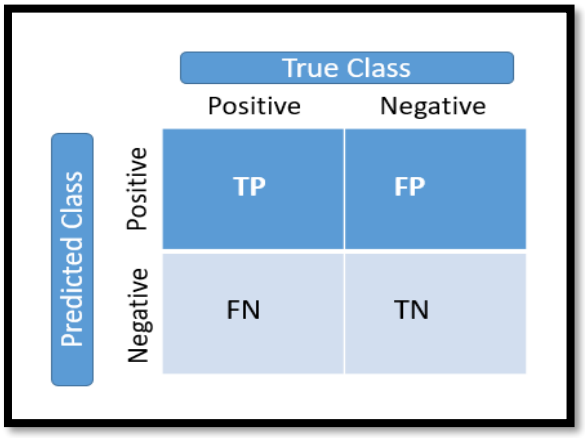

Figure 7. The Basic Structure of a Confusion Matrix

True Positive: A classification model correctly predicts the positive class.

True Negative: A classification model correctly predicts the negative class.

False Positive: This is when a classification model predicts a negative class as positive.

False Negative: This is when a classification model predicts a positive class as negative.

True Positive rate: The proportion of all negatives that yield positive test results.

$$Accuracy = \frac{\text{TP}}{TP + FN} \quad (1)$$

Accuracy: It refers to the rate at which a classification model correctly predicts a positive and negative class, in other words, the proportion of data that is correctly predicted among all data.

$$Accuracy = \frac{\text{TP} + \text{TN}}{TP + TN + FP + FN} \quad (2)$$

Sensitivity: It is the rate at which a classification model finds positive examples among all positive examples.

$$Sensitivity = \frac{\text{TP}}{TP + FN} \quad (3)$$

Specificity: It is the rate at which a classification model finds negative examples among all negative examples.

$$Specificty = \frac{\text{TN}}{TN + FP} \quad (4)$$

Recall: Total positive samples are the rate at which they are predicted as positive.

$$Recall = \frac{\text{TP}}{TP + FN} \quad (5)$$

Precision: The rate at which all predicted positive samples are actually positive.

$$Precision = \frac{\text{TP}}{TP + FP} \quad (6)$$

F- Measure: It is the harmonic mean of Precision and Recall values. Since it takes into account False Positive and False Negative results, it is an effective parameter in showing the classification performance of an unbalanced data set.

$$F - Measure = 2 * \frac{\text{Precision} * \text{Recall}}{Precision + Recall} \quad (7)$$

3.4.1 Validation Method

To best evaluate the model performance, the data is divided into two sections: training and testing. While the model is trained with training data, the performance of the model is measured with test data. In this study, k-fold cross-validation (Fig.8) was used to ensure accurate classification performance. This method divides the data into k parts. Each piece is taken as test data in turn and the other pieces are used as training data. After K stages, an average overall performance measure is obtained by taking into account the performances calculated at each stage.

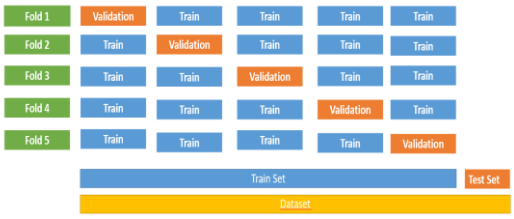

Figure 8. The Basic Structure of a Cross Validation

4. Experimental Results

In this study, the tweets sent on Twitter were recompiled with reference to the Kaggle study called fake news detection, re-examined with new codes and the results of the data set were examined by using classification methods from a different perspective. After the data pre-processing steps on the dataset were carried out on the determined tweet messages, two categories were created under the name of real and fake news. These are categorized as real and fake. There are 4 attributes in the real category, these are; title, text, subject, date. Title has approximately 21,000 unique values. Text has approximately 21,000 unique values. 53% of the tags under the Subject heading are political news and 47% are news from the rest of the world. Date includes the period from 13-01-2016 to 31-12-2017. In total, there are approximately 42,000 pieces of data in the real and fake categories. By applying KDD steps to these data, the data is made more compact, for example; After examining the data set, some preliminary processing was carried out on news headlines and text contents. Special characters, websites, HTML tags, etc. has been cleared. Then, TF-IDF vectorization was used to divide the data into training and test sets and convert the text data into numbers. Next, we train a Logistic Regression model with these vectors. This makes it easier to handle. Later, 7 different classification algorithms were used in this study. These classification algorithms used were Logistic Regression Classification, Random Forest Classification, Decision Tree Classification, Gradient Boosting Classification, K Nearest Neighbor Classification, Naive Bayes, Support Vector Classification algorithms. Training and test data are separated for machine learning, texts are converted into vectors and classification algorithm codes are written. Precision value expresses the proportion of predictions made by an algorithm that are actually correct. Especially in the fake and real news detection problem, it shows how much of the fake news in the data set is correctly identified. A high precision value indicates that the algorithm is successful in correctly classifying fake news.

Table 2. Performance Results of Classification Algorithms

	Accuracy	F-measure	Recall	Precision	Sensivity	Specificty	TP Rate	FP Rate
Logistic Regression Classification (PCA ON)								
Fold1	0.54	0.53	0.53	0.55	0.72	0.37	0.72	0.62
Fold2	0.54	0.52	0.52	0.56	0.74	0.36	0.74	0.63
Fold3	0.56	0.55	0.55	0.57	0.74	0.39	0.74	0.60
Fold4	0.55	0.54	0.54	0.55	0.69	0.41	0.69	0.58
Fold5	0.54	0.52	0.56	0.54	0.70	0.37	0.70	0.62
Average	0.55	0.55	0.56	0.56	0.72	0.38	0.72	0.62
Logistic Regression Classification (PCA OFF)								
	Accuracy	F-measure	Recall	Precision	Sensivity	Specificty	TP Rate	FP Rate
Fold1	0.62	0.62	0.62	0.64	0.75	0.75	0.75	0.79
Fold2	0.63	0.62	0.62	0.63	0.77	0.77	0.77	0.49
Fold3	0.61	0.61	0.61	0.61	0.74	0.74	0.74	0.51
Fold4	0.62	0.62	0.62	0.62	0.72	0.72	0.72	0.47
Fold5	0.63	0.62	0.62	0.63	0.73	0.73	0.73	0.47
Average	0.63	0.64	0.63	0.62	0.75	0.51	0.75	0.49
Decision Tree Classification (PCA OFF)								
	Accuracy	F-measure	Recall	Precision	Sensivity	Specificty	TP Rate	FP Rate
Fold1	0.69	0.69	0.69	0.69	0.65	0.65	0.65	0.26
Fold2	0.67	0.67	0.68	0.63	0.63	0.63	0.63	0.28
Fold3	0.68	0.68	0.68	0.67	0.67	0.67	0.67	0.30
Fold4	0.69	0.69	0.69	0.69	0.69	0.69	0.69	0.30
Fold5	0.67	0.67	0.67	0.67	0.67	0.67	0.67	0.32
Average	0.69	0.69	0.69	0.69	0.67	0.70	0.67	0.30
Decision Tree Classificatiob (PCA ON)								
	Accuracy	F-measure	Recall	Precision	Sensivity	Specificty	TP Rate	FP Rate
Fold1	0.71	0.71	0.71	0.71	0.70	0.73	0.70	0.26
Fold2	0.70	0.70	0.70	0.70	0.67	0.73	0.67	0.26
Fold3	0.69	0.69	0.69	0.69	0.68	0.71	0.68	0.28
Fold4	0.69	0.69	0.69	0.70	0.65	0.74	0.65	0.25
Fold5	0.69	0.69	0.69	0.69	0.65	0.72	0.65	0.27
Average	0.70	0.70	0.70	0.70	0.67	0.73	0.67	0.27
Random Forest Classification (PCA ON)								
	Accuracy	F-measure	Recall	Precision	Sensivity	Specificty	TP Rate	FP Rate
Fold1	**0.75**	**0.75**	**0.75**	**0.75**	**0.79**	**0.72**	**0.79**	**0.27**
Fold2	**0.72**	**0.71**	**0.72**	**0.72**	**0.72**	**0.71**	**0.72**	**0.28**
Fold3	**0.75**	**0.75**	**0.75**	**0.75**	**0.79**	**0.71**	**0.79**	**0.28**

Fold4	**0.74**	**0.74**	**0.74**	**0.74**	**0.78**	**0.70**	**0.78**	**0.29**
Fold5	**0.75**	**0.75**	**0.75**	**0.75**	**0.79**	**0.71**	**0.79**	**0.28**
Average	**0.75**	**0.75**	**0.75**	**0.75**	**0.78**	**0.71**	**0.78**	**0.29**
Random Forest Classification (PCA OFF)								
	Accuracy	F-measure	Recall	Precision	Sensivity	Specificty	TP Rate	FP Rate
Fold1	**0.75**	**0.75**	**0.75**	**0.75**	**0.79**	**0.72**	**0.79**	**0.27**
Fold2	**0.75**	**0.75**	**0.72**	**0.72**	**0.72**	**0.71**	**0.72**	**0.28**
Fold3	**0.76**	**0.76**	**0.75**	**0.75**	**0.79**	**0.71**	**0.79**	**0.28**
Fold4	**0.76**	**0.76**	**0.74**	**0.74**	**0.78**	**0.70**	**0.78**	**0.29**
Fold5	**0.74**	**0.74**	**0.75**	**0.75**	**0.79**	**0.71**	**0.79**	**0.28**
Average	**0.76**	**0.76**	**0.76**	**0.76**	**0.76**	**0.75**	**0.76**	**0.25**
Gradient Boosting Classification (PCA ON)								
	Accuracy	F-measure	Recall	Precision	Sensivity	Specificty	TP Rate	FP Rate
Fold1	0.73	0.72	0.73	0.73	0.82	0.63	0.82	0.36
Fold2	0.70	0.70	0.70	0.71	0.79	0.61	0.79	0.38
Fold3	0.72	0.71	0.72	0.73	0.84	0.60	0.84	0.39
Fold4	0.72	0.72	0.72	0.73	0.83	0.60	0.83	0.39
Fold5	0.73	0.73	0.73	0.75	0.85	0.62	0.85	0.37
Average	0.71	0.72	0.72	0.74	0.83	0.62	0.83	0.38
Gradient Boosting Classification (PCA OFF)								
	Accuracy	F-measure	Recall	Precision	Sensivity	Specificty	TP Rate	FP Rate
Fold1	0.71	0.71	0.71	0.72	0.81	0.81	0.81	0.38
Fold2	0.69	0.69	0.69	0.70	0.78	0.78	0.78	0.39
Fold3	0.71	0.71	0.71	0.73	0.84	0.84	0.84	0.39
Fold4	0.73	0.73	0.73	0.74	0.85	0.85	0.85	0.38
Fold5	0.73	0.72	0.73	0.74	0.85	0.85	0.85	0.39
Average	0.72	0.72	0.72	0.73	0.83	0.61	0.83	0.39
K Nearest Neighbor Classification (PCA ON)								
	Accuracy	F-measure	Recall	Precision	Sensivity	Specificty	TP Rate	FP Rate
Fold1	0.68	0.67	0.68	0.68	0.73	0.63	0.73	0.36
Fold2	0.65	0.65	0.50	0.65	0.70	0.60	0.70	0.39
Fold3	0.67	0.67	0.67	0.67	0.73	0.62	0.73	0.37
Fold4	0.65	0.65	0.65	0.65	0.70	0.60	0.70	0.39
Fold5	0.68	0.68	0.68	0.68	0.72	0.63	0.72	0.36
Average	0.67	0.67	0.67	0.67	0.72	0.62	0.72	0.38
K Nearest Neighbor Classification (PCA OFF)								
	Accuracy	F-measure	Recall	Precision	Sensivity	Specificty	TP Rate	FP Rate
Fold1	0.68	0.68	0.68	0.68	0.73	0.63	0.73	0.36

Fold2	0.65	0.65	0.50	0.65	0.70	0.60	0.70	0.39
Fold3	0.67	0.67	0.67	0.67	0.73	0.62	0.73	0.37
Fold4	0.65	0.65	0.65	0.65	0.70	0.60	0.70	0.39
Fold5	0.68	0.68	0.68	0.68	0.72	0.63	0.72	0.36
Average	0.67	0.67	0.67	0.67	0.72	0.62	0.72	0.38

Naive Bayes Classification (PCA ON)

	Accuracy	F-measure	Recall	Precision	Sensivity	Specificty	TP Rate	FP Rate
Fold1	0.58	0.53	0.58	0.65	0.91	0.25	0.91	0.74
Fold2	0.57	0.52	0.57	0.62	0.89	0.24	0.89	0.75
Fold3	0.56	0.51	0.56	0.62	0.90	0.24	0.90	0.75
Fold4	0.58	0.52	0.58	0.63	0.91	0.22	0.91	0.77
Fold5	0.58	0.54	0.58	0.64	0.90	0.27	0.90	0.72
Average	0.58	0.53	0.58	0.64	0.90	0.25	0.90	0.75

Naive Bayes Classification (PCA OFF)

	Accuracy	F-measure	Recall	Precision	Sensivity	Specificty	TP Rate	FP Rate
Fold1	0.57	0.49	0.57	0.68	0.96	0.18	0.96	0.81
Fold2	0.57	0.50	0.57	0.68	0.95	0.20	0.95	0.79
Fold3	0.56	0.48	0.56	0.67	0.95	0.18	0.95	0.81
Fold4	0.60	0.53	0.60	0.70	0.96	0.21	0.96	0.81
Fold5	0.58	0.51	0.58	0.70	0.96	0.20	0.96	0.78
Average	0.58	0.51	0.58	0.69	0.96	0.20	0.96	0.79

Support Vector Machines (PCA ON)

	Accuracy	F-measure	Recall	Precision	Sensivity	Specificty	TP Rate	FP Rate
Fold1	0.52	0.62	0.80	0.51	0.80	0.80	0.80	0.75
Fold2	0.52	0.62	0.81	0.50	0.81	0.81	0.81	0.74
Fold3	0.52	0.62	0.79	0.50	0.79	0.79	0.79	0.74
Fold4	0.55	0.63	0.74	0.55	0.74	0.74	0.74	0.66
Fold5	0.54	0.63	0.77	0.53	0.77	0.77	0.77	0.70
Average	0.53	0.63	0.79	0.52	0.79	0.28	0.79	0.72

Support Vector Machines (PCA OFF)

	Accuracy	F-measure	Recall	Precision	Sensivity	Specificty	TP Rate	FP Rate
Fold1	0.53	0.50	0.53	0.55	0.81	0.26	0.81	0.73
Fold2	0.54	0.50	0.54	0.55	0.80	0.27	0.80	0.72
Fold3	0.50	0.47	0.50	0.51	0.75	0.26	0.75	0.73
Fold4	0.56	0.53	0.56	0.57	0.82	0.28	0.82	0.71
Fold5	0.52	0.49	0.52	0.53	0.78	0.27	0.78	0.72
Average	0.54	0.50	0.54	0.55	0.80	0.27	0.80	0.73

Figure 9. Classication Algorithm Results (PCA-OFF)

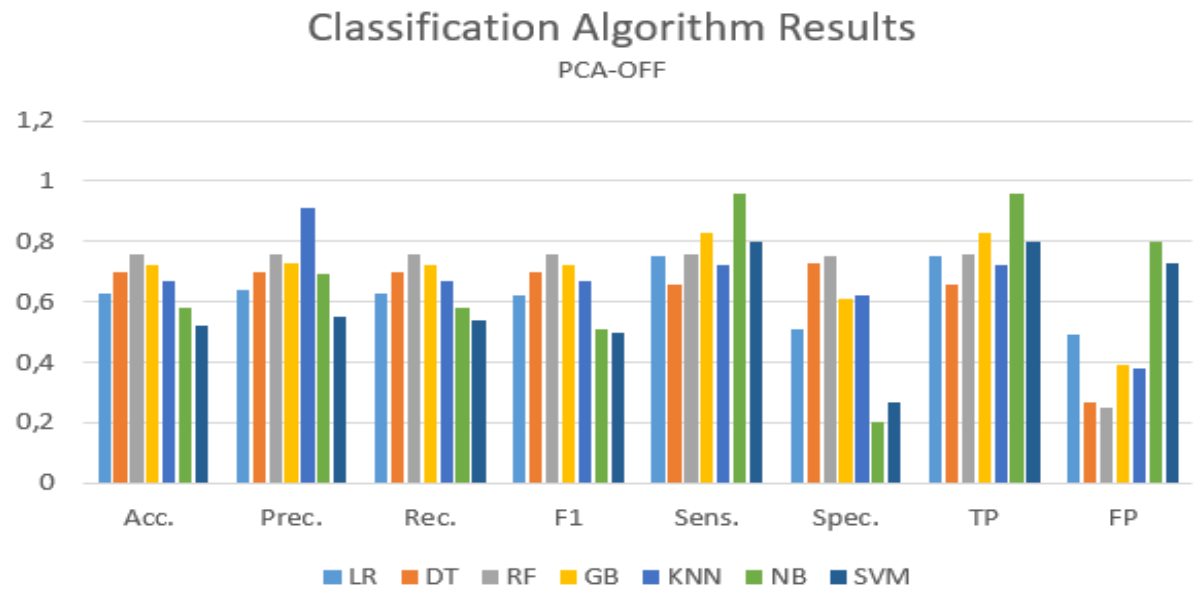

Classification Algorithm Results

Figure 10. Classification Algorithm Results (PCA-ON)

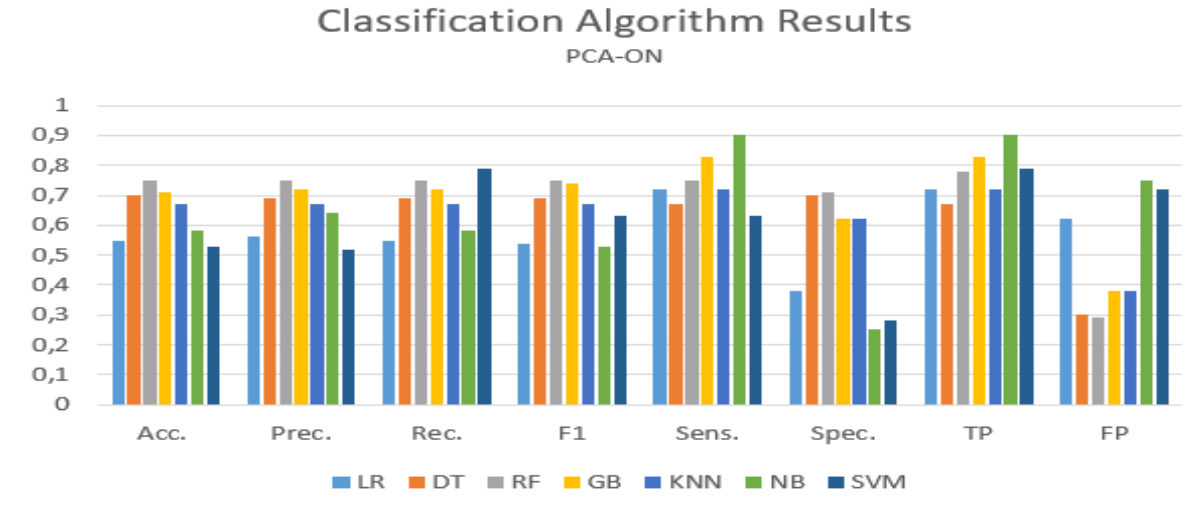

Classification Algorithm Results

The higher this metric is, the higher the success of the algorithm in correct labeling, and in our algorithm, the Random Forest Classifier gave the highest precision value. Its value is 0.76. In fact, in this study, a system that enables automatic detection of fake news was used. This system attracts attention with its ability to identify fake news in a short time. In this way, it is possible to quickly detect fake news and prevent its spread. While the accuracy score of the model obtained without using PCA of Random Forest Classification was 0.76, the accuracy rate after applying PCA was determined as 0.75. These results indicate higher precision values than the other six algorithms included in the study.

The purpose of PCA is to preserve the data and transform the data set into a subspace that can be expressed with fewer variables. For this purpose, observations were made to see whether there was a performance difference in the classification algorithms of PCA, one of the widely used dimension reduction methods. The classification performance results obtained without using PCA-OFF and using PCA-ON are given in the graphs. It has been observed that PCA classification algorithms do not have a performance-enhancing effect. The highest success results were observed with the random forest classification algorithm, which includes more than one classification algorithm.

As stated in Table 2, Figure 9 and Figure 10 and , the average performance results of the classification algorithms are as follows.

- By applying PCA of the Logistic Regression classification algorithm, the average performance results obtained are as follows, respectively. Accuracy is 55%, f-measure is 55%, recall is 56%, precision is 56%, sensitivity is 72%, True Positive is 72%, False Positive is 62%. Average performance without PCA the results are as follows. Accuracy 63%, f-measure 64%, recall 63%, precision 62%, sensitivity 75%, specificity 51%, True Positive 75%, False Positive 49%.

- The performance results of the Decision tree classification algorithm without applying PCA are as follows: Accuracy 69%, f-measure 69%, recall 69%, precision 69%, sensitivity is 67%, specificity is 70%, True Positive is 67%, False Positive is 30%. Average performance with PCA are results are as follows. Accuracy 70%, f-measure 70%, recall 70%, precision 70%, sensitivity 67%, specificity 73%, True Positive 67%, False Positive 27%.

- The average performance results obtained with applying the Random Forest classification algorithms are as follows, respectively. Accuracy 75%, f-measure 75%, recall 75%, precision 75%, sensitivity is 78%, specificity is 71%, True Positive is 78%, False Positive is 29%. Average performance without PCA are as follows, respectively. Accuracy 76%, f-measure 76%, recall 76%, precision 76%, sensitivity 76%, specificity 75%, True Positive 76%, False Positive 25%.

- Average performance results obtained applying the Random Forest classification algorithm principal component analysis are as follows, respectively. Accuracy 75%, f-measure 75%, recall 75%, precision 75%, sensitivity is 78%, specificity is 71%, True Positive is 78%, False Positive is 29%. Average performance obtained by applying principal component analysis The results are as follows. Accuracy 76%, f-measure 76%, recall 76%, precision 76%, sensitivity 76%, specificity 75%, True Positive 76%, False Positive 25%.

- The average performance results obtained with the Gradient Boosting classification algorithm with PCA are as follows, respectively. Accuracy 71%, f-measure 72%, recall 72%, precision 74%, sensitivity is 83%, specificity is 62%, True Positive is 83%, False Positive is 38%. The average results of gradient classification algorithm without PCA are as follows. Accuracy 72%, f-measure 72%, recall 72%, precision 73%, sensitivity 83%, specificity 61%, True Positive 83%, False Positive 39%.

- Average performance of KNN with PCA are as follows, repectively. Accuracy 67%, f-measure 67%, recall 67%, precision 67%, sensitivity is 72%, specificity is 62%, True Positive is 72%, False Positive is 38%. Average performance without PCA analysis are as follows. Accuracy 67%, f-measure 67%, recall 67%, precision 67%, sensitivity 72%, specificity 62%, True Positive 72%, False Positive 38%.

- The average performance results of Naive Bayes classification algorithm with PCA are as follows, respectively. Accuracy 58%, f-measure 53%, recall 58%, precision 64%, sensitivity is 90%, specificity is 25%, True Positive is 90%, False Positive is 75%. Average performance without PCA are as follows. Accuracy 58%, f-measure 51%, recall 58%, precision 69%, sensitivity 96%, specificity 20%, True Positive 96%, False Positive 79%.

- Average performance results of Support Vector Machine classification algorithm with PCA, obtained are as follows, respectively. Accuracy is 53%, f-measure is 63%, recall is 79%, precision is 52%, sensitivity is 79%, specificity is 28%, True Positive is 79%, False Positive is 72%. Average performance without PCA are as follows. Accuracy 54%, f-measure 50%, recall 54%, precision 55%, sensitivity 80%, specificity 27%, True Positive 80%, False Positive 73%.

5. Discussion

As seen in Table 3, many studies have been conducted to detect fake news. Although the performance results obtained are high, the models are not reliable and robust. The models are not robust due to reasons such as the unbalanced creation of data sets, not applying the cross-validation method and the inability to apply pre-processing methods throughout the study. In this study, the number of fake and real news data samples was selected equally, pre-processing methods were applied, and models were created with individual and ensemble classification algorithms. Cross-validation was used. Many performance metrics such as accuracy, sensitivity, specificity, tp rate, fp rate and f-measure were extracted and the models were compared. An original and reliable model has been created with follow-up steps to detect fake news.

Table 3. Classification Algorithm Results of Other Studies

Referans Study	**Classificiation Algorithms**	**Result**
Taşkın et al.	Non-Negative Matrix Multiplication, Linear Discriminant Analysis, K Nearest Neighbor Support Vector Machine Random Forest	f-measure 0.86
Zeba et al.	Naive Bayes Support Vector Machine	Accuracy 99.6%
Satish et al.	Decision Tree	Accuracy 99.7%
Nagaraji et al.	Support Vector Machine	Accuracy 95.00%
Asaad et al.	Bi-LSTM	Accuracy 95.00%
Alameri et al.	Naive Bayes, SVM, Random Forest, Losgistic Regression	Accuracy 93.00%
Akdeniz et al.	Naive Bayes, Support Vector Machine, LSTM, Neural Network,	Accuracy 92.99
Our method	Individual classifier (Logistic regression, decision tree, gradient boosting, random forest, k nearest neighbor, naïve bayes and support vector machine) and ensemble classification algorithm	Accuracy 76%

6. Conclusion

According to research, the rate of exposure of people in Türkiye and around the world to fake news is quite high. In addition, it has been observed that the ability to distinguish fake news is low. Additionally, considering that fake news spreads rapidly, especially within the first 2 hours after it is shared, it is of great importance to use automatic detection systems to detect fake news. Supervised learning algorithms perform clustering based on labeled data sets. In this study, the task of finding 2 clusters (real, fake) categorized in each subject was given to supervised learning algorithms. A method of 5-fold cross validation was adopted for conducting random sampling of the training and test data sets. Real and fake news clusters were determined by 7 different supervised learning algorithms using the training set. The resulting clusters were determined to be real or fake news by the clustering purity method. According to the model results obtained by classification methods without using PCA, Random Forest classification algorithm; It has a higher precision value than LR, DT, GB, KNN, NB and SVM algorithms and its value is 0.75. According to the model results obtained by classification methods using PCA, Support vector classification algorithm; According to classification results such as LR, DT, GB, KNN and NB, it has the lowest precision value and its value is 0.53. It is observed that the different supervised classification algorithms used in this study show superior performance compared to the referenced articles by separating the data from different numbers of test data. It is unique in terms of the methods applied in pattern formation. For example; Careful analyzes were made at every stage of the formation of the pattern and appropriate methods were determined. In summary, the use of labeled data in

this study appears to make supervised learning algorithms advantageous in terms of the ability to more effectively resolve similarities between data with the same labels. In order to optimize f-measure values, it may be necessary to examine in detail the people followed by users on social media platforms and the accounts followed by these people. During this review, it may be taken into consideration whether the accounts are bots, fake or accounts opened for propaganda purposes. For this reason, friendship graph will be used in future studies and this graph will be given as input to the automatic detection system, aiming to further increase the success of the algorithm.

Author's Contributions

Gülay ÇİÇEK: She served as article consultant. A road map was drawn to solve the problem. Revision has been carried out. Updates have been provided to the article.

Başar YILDIRIM: Participated in data preparation, coding and writing.

Batuhan BATTAL: Participated in data preparation, and writing.

Ömer Faruk DİNÇASLAN: Participated in data preparation and writing.

Ethics

There are no ethical issues after the publication of this manuscript.

References

[1]. Tugrulcan Elmas. T24, 2023

[2]. Mehmet Atakan Foça. Duvar gazatesi, 2018.

[3]. Selman Akyuz. ¨ SAHTE HABER. 02 2019.

[4]. Tugce Esin PINARBASI and Fatma Kübra ASTAM. Haberin Dönüşümü:Sosyal medya gazeteciliği pratikleri. İnönü Üniversitesi İletişim Fakültesi Elektronik Dergisi (İnif E-Dergi), 5(1):70-87,2020.

[5]. Kezban Karagöz. Post truth Çağında yayıncılışın geleceği, 2018.

[6]. Ersel Kiraz. Sosyal medyada shate haberin yayilmasinda kullanici Faktörü. İnönü Üniversitesi İletişim Fakültesi Elektronik Dergisi (İNİF E-Dergi), 5(1):9-24, 2020.

[7]. Barış Yetkin. Dijitalleşen siyasal iletişimde bilişimsel propaganda: Botlar. Pages 51-72, 05 2019.

[8]. Deniz Ergürel. Teknoloji ve İnternetle yeniden şekillenen medya. İletişim ve Diplomasi, (1):167-177, 2013.

[9]. Aygün ÖZSALİH. Yapay zeka yoluyla oluşturulan sahte haberlerin medya gündeminin belirlemesi. Turkish Online Journal of Design Art and Communication, 13(3):533-550, 2023.

[10]. Hiskmet Tosyali. Dijital çağda siyasal iletişim: Algoritmalar ve botlar. 04 2021.

[11]. Kai Shu, Amy Sliva, Suhang Wang, Jilian Tang, and Huan Liu, Fake news detection on social media: A data mining perspective. ACM SIGKDD Expolorarions Newsletter, 19, 08 2017.

[12]. Tirşe Erbaysal Filibel and Orhan Şener. Manipule edilmis enformasyonel bir vitring ve populist bir enformasyon Alani olarak twitter. Moment Dergi, 6(2):492-515, 2019.

[13]. Mesut Toğaçar, Kamil Eşidir, and Burhan Ergen. Yapay zeka tabanlı doğal dil işleme yaklaşımın kullanarak internet ortamında yayınlanmış sahte haverlerin tespiti. Journal of Intelligene Systems: Theory and Applications, 5:1-8, 2021.

[14]. Feyza Altunebey Özbay and Bilal Alataş. Çevirimiçi soyal medyada sahte haber tespiti. Dicle Üniversitesi Mühendislik Fakültesi Mühendislik Dergisi, 11(1):91-103, 2020.

[15]. Süleyman Gökahn Taşkın, Ecir Uğur Küçüksille, and Kamil Topla. Twitter üzerinde türkçe sahte haber tespiti, 2021.

[16]. Mehmet Kayakuş and Fatma Yiyği Açıkgöz. Twitter'da makine öğrenmesi yöntemiyle sahte haber tespiti. Abant Sosyal Bilimler Dergisi, 23 (2): 1011027, 2023.

[17]. Süleyman Gökhan Taşkın, Ecir Uğur Küçüksille and Kamil Topal. Twitter üzerinde türkçe sahte haber tespiti. Balıksesi Üniversitesi Fen Blimleri Enstitüsü Dergisi, 23:151-172, 2021.

[18]. Zeba Khanam, BN Alwasel, H Sirafi, and Mamoon Rashid. Fake news detection using machine learning approaches. In IOP conference series: materials science and engineering, volume 1099, page 012040. IOP Publishing, 2021.

[19]. Aswini Thota, Priyanka Tilak, Simrat Ahluwalia, and Nibrat Lohia. Fake news detection: a deep learning approach. SMU Data Science Review, 1(3):10, 2018.

[20]. Nihel Fatima Baarir and Abdelhamid Djeffal. Fake news detection using machine learning. In 2020 2nd International workshop on human-centric smart environments for health and well-being (IHSH), pages 125–130. IEEE, 2021

[21]. P Sathish Kumar, P Suthanthiradevi, C Arul Stephen, B Ebenezer Abishek, S Sivakumar, and M Mathiyarasu. Analysis and detection of fake news using machine learning. In 2024 3rd International Conference on Artificial Intelligence For Internet of Things (AIIoT), pages 1–6. IEEE, 2024.

[22]. Shreea Bose and Reek Roy. Enhancing fake news detection with sentiment analysis using machine learning. In 2023 7th International Conference on Electronics, Materials Engineering & Nano-Technology (IEMENTech), pages 1–5. IEEE, 2023.

[23]. Jasmine Shaikh and Rupali Patil. Fake news detection using machine learning. In 2020 IEEE international symposium on sustainable energy, signal processing and cyber security (iSSSC), pages 1–5. IEEE, 2020.

[24]. Shubha Mishra, Piyush Shukla, and Ratish Agarwal. Analyzing machine learning enabled fake news detection techniques for diversified datasets. Wireless Communications and Mobile Computing, 2022(1):1575365, 2022.

[25]. M Senthil Raja and L Arun Raj. Fake news detection on social networks using machine learning techniques. Materials Today: Proceedings, 62:4821– 4827, 2022.

[26]. Arun Nagaraja, Soumya KN, Anubhav Sinha, JAIN VINAY RAJENDRA KUMAR, and Prajwal Nayak. Fake news detection using machine learning methods. In International Conference on Data Science, E-learning and Information Systems 2021, pages 185–192, 2021.

[27]. Bashar Al Asaad and Madalina Erascu. A tool for fake news detection. In 2018 20th international symposium on symbolic and numeric algorithms for scientific computing (SYNASC), pages 379–386. IEEE, 2018.

[28]. Saeed Amer Alameri and Masnizah Mohd. Comparison of fake news detection using machine learning and deep learning techniques. In 2021 3rd international cyber resilience conference (CRC), pages 1–6. IEEE, 2021.

[29]. Khaled M Fouad, Sahar F Sabbeh, and Walaa Medhat. Arabic fake news detection using deep learning. Computers, Materials & Continua, 71(2), 2022.

[30]. Shafayat Bin Shabbir Mugdha, Sayeda Muntaha Ferdous, and Ahmed Fahmin. Evaluating machine learning algorithms for bengali fake news detection. In 2020 23rd International Conference on Computer and Information Technology (ICCIT), pages 1–6. IEEE, 2020.

[31]. Murat Emeç and Mehmet Ozcanhan. Veri Ön İşleme ve Öznitelik Mühendisliğinin Yapay Zeka Yöntemlerine Uygulanması, pages 33-54. 06 2023.

[32]. Emrah Gürlek, Fadime Akdeniz, Nada Misk, Reyhan Sahinbas, Uygar Aydin, Çiğdem Erol, and Burcu İlis. Makine Öğrenmesi Algoritmaları ile Covid-19 Test Sonuçlarının Tahmin Edilmesi, pages 353-369. 04 2023.

[**33].** Ensar Sağbaş, Osman Gökalp, and Aybars Ugur. Yüz İfadesi tanıma için mesafe oranlarına dayalı öznitelik çıkarımı ve genetic algoritmalar ile Seçimi. 2:19-29,07 2019.

[34]. Oğuz Kaynar, Halil Arslar, Yasin Görmez, and Yunus Emre Işık. Makine Öğrenmesi ve Öznitelik seçim yöntemleriyle saldırı tespiti. Bilişim Takonolojileri Dergisi, 11:1175-185, 2018.

[35]. Adem Korkmaz and Selma Bulut. Sahte web sitelerinin sınıflandırma algoritmaları ile tespit edilmesi. European Journal of Science and Technology, pages 826-833, 08 2019.

[36]. Feyyaz Koç and AbdulKerim Karabiber. Makine Öğrenmesi yöntemleri kullanılarak elektrikli cihazların sınıflandırılması. Türk Doğa ve Fen Dergisi, 10(1):159-165, 2021.

-

Celal Bayar University Journal of Science

All-optical NOT, OR, and XOR Logic Gates Using Silicon Slot Waveguides

Semih Korkmaz[1]*

[1] Department of Computer Engineering, Bandirma Onyedi Eylul University, Balikesir 10200, Türkiye

* semihkorkmaz@bandirma.edu.tr
* Orcid No: 0000-0001-5576-7653

Received: 9 June 2024
Accepted: 9 September 2024
DOI: 10.18466/cbayarfbe.1498313

Abstract

All-optical NOT, OR, and Exclusive OR(XOR) logic gates utilizing silicon slot waveguides are proposed and numerically analyzed in this work. The structure has a silicon slab with slot regions such as two input waveguides and square cavity resonators and one output waveguide. The optical spectra of the designed structures are attained with the method of finite difference time domain. The all-optical logic gate features of the design are achieved by applying optical signals with 0^0 or 180^0 phase differences from the input ports. Basic parameters such as transmission spectrum (T), modulation depth (MD), and contrast ratio (CR) are performed to show the optical features and ability of the proposed logic gates. The threshold transmission limit is 1.7% to define the status of the output ports as ON or OFF. At 689.5 nm, the maximum transmission, modulation depth, and contrast ratio are 149%, 97%, and 15.36 dB, respectively.

Keywords: Optical logic gates, Silicon slot waveguides, Transmission spectrum.

1. Introduction

All-optical devices have enabled new improvements in photonic devices to transmit information along the optical channels with high efficiency [1-4]. To achieve this, the waveguide-based device is more commonly used [5-7]. There are main waveguide types like metal-insulator-metal waveguides [8,9], insulator-metal-insulator waveguides [10,11], metal slot waveguides [12], and dielectric slot waveguides [13]. Among these structures, dielectric waveguides are preferred due to their low power consumption, low cost, and high transmission efficiency [14-17]. By using dielectric slot waveguides, there are many research fields to optimize performances of optical-based devices in the last decade such as power splitters [18,19], Mach-Zehnder interferometers [20], logic gates [21], modulators [22] and sensors [23]. Dielectric or metal slot waveguide-based systems are frequently used to carry out the all-optical logic gates. Silicon slot waveguides are chosen with their lower propagation losses, and ease of fabrication features compared to the metal slot waveguides [24,25]. All-optical devices which are OR, NOT, and Exclusive OR(XOR) logic gates with silicon slot waveguides are numerically designed and analyzed in this work. The spectrum of transmission and magnetic fields distributions for the suggested all-optical logic devices are reached via the method of finite-difference time-domain (FDTD) with perfectly matched layer boundary conditions that are performed along the x- and y axes. Only one structure is utilized during all analyses. The study includes two basic stages. In the first stage, the ideal dimensions of the structure have been obtained by geometric parameter sweep analyses. In the second stage, numerical analyses of all-optical OR, XOR, and NOT logic devices are carried out without changing the dimensions of the structure. To demonstrate the structure's OR, XOR, and NOT logic gate functionalities, optical signals with either the 0^0 phase difference or 180^0 phase differences are transmitted through the silicon slot waveguides. When the OR logic gate is analyzed, the applied signals have the same phase. On the other hand, when XOR and NOT logic gates are examined, there are 0^0 or 180^0 phase differences for the applied input signals.

2. Materials and Methods

Figure 1 presents the design for all-optical OR, NOT, and XOR logic devices. This structure includes etched regions like waveguides and square resonators on the 100 nm-thick silicon plate. The depth of the etched regions is 100 nm. The main purpose of using a resonator in such

Celal Bayar University Journal of Science
Volume 20, Issue 3, 2024, p 84-90
Doi: 10.18466/cbayarfbe.1498313

systems is to enhance light at certain wavelengths and to adjust the resonance wavelengths by varying the geometric parameters of the resonators. Furthermore, utilizing resonators enables narrower resonances for specific ranges [26,27]. In that design, there are two input ports, one output port, and two identical and symmetrical square resonators. Palik model is used for the optical constants of the silicon [28]. The refractive index of the air is 1. Transverse magnetic polarized Gaussian sources are applied from the input ports. The logic 0 (OFF) or logic 1 (ON) states of the output are determined by the lowest level in the transmission. This is called threshold transmission. When the value of transmission is bigger than the limit of threshold transmission, the output is defined as logic 1 (ON). When the value of transmission is lower than the threshold transmission, the output is defined as OFF [29]. Lumerical Solutions solver based on the method of FDTD is used to attain the optical spectrum results of the designed structure [30]. The transmission values are obtained with the formula (1) [31]. P_{out} and P_{in} represent the powers at the output port and input port, respectively.

$$T = P_{out}/P_{in} \qquad (1)$$

The contrast ratio (CR) is another fundamental parameter for optical logic gates. It is calculated using the formula (2) [32].

$$CR(dB) = 10log\left(\frac{P_h}{P_l}\right) \qquad (2)$$

In this formula, P_h represents the minimum power value while the state of output is a logic high level (ON). P_l denotes the maximum power value as the state of output is a logic low level (OFF).

The modulation depth (MD) is the other basic parameter that is formulated using the expression (3) [29].

$$MD = \left(\frac{T|ON_{max} - T|OFF_{min}}{T|ON_{max}}\right) \times 100\% \qquad (3)$$

In this expression, $T|ON_{max}$ represents the maximum transmission for logic level 1, while $T|OFF_{min}$ denotes the minimum transmission for logic level 0. Table 1 shows the lengths of the proposed structure. To attain the optimal values of the structures, parameter sweep analyses have been performed in the first stage. To do this, the optical signal is sent from only input 1. Figure 2 presents the transmission spectrum for the refractive index change of the transmission medium. When the refractive index of the medium is increased from 1 (air) to 1.9 with a 0.3 step size, the transmission values decrease from 55% to 45%. During this analysis, the lengths given in Table 1 are used. Figure 3(a) presents the transmission spectrum for the parameter sweep of w_1. w_1 is the critical parameter for transmitted signals due to the thickness of the waveguides. w_1 is changed from 20 nm to 50 nm. When the w_1 increases, the transmission values increase from 26% to 55%. Figure 3(b) presents the transmission spectrum obtained by the w_2 parameter sweep. The transmission values show different levels when w_2 is increased from 75 nm to 90 nm.

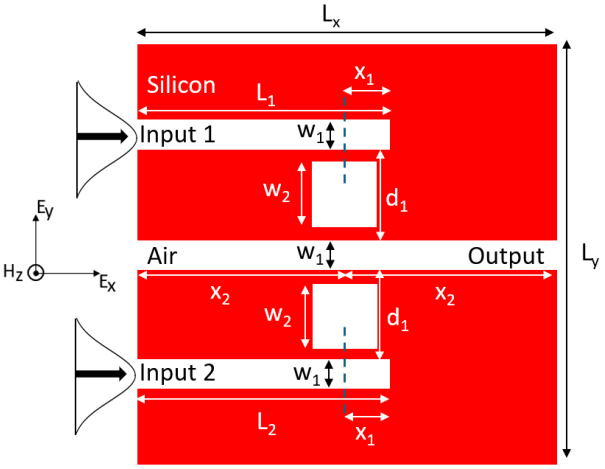

Figure 1. The illustration of the designed structure.

Table 1. The lengths of the proposed structure.

Parameter	Length (nm)
$L_X = L_Y$	400
$L_1 = L_2$	280
x_2	200
d_1	100
x_1	80
w_2	80
w_1	50

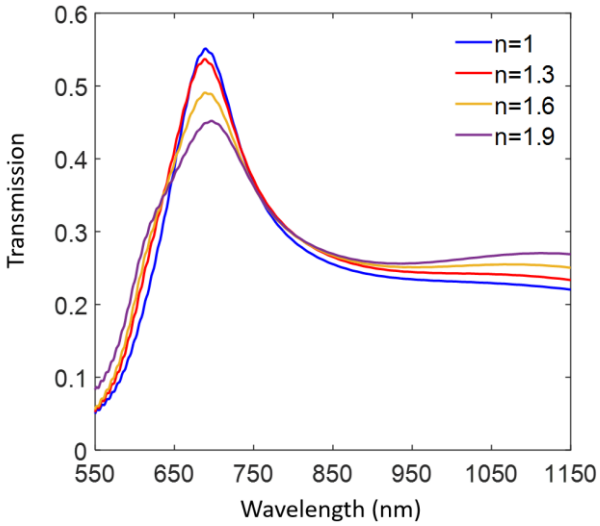

Figure 2. The transmission spectrum of the structure for different mediums.

The square design is obtained when w_2 is 80 nm, resulting in the highest transmission. Figure 3(c) visualizes the transmission spectrum from the variation of the x_1 parameter. x_1 is the important parameter for the transmitted signals due to the couplings between the

waveguides and resonators. x_1 is changed from 20 nm to 80 nm. When the x_1 is increased, the transmission values increase from 36% to 55% at 689.5 nm. Figure 3(d) illustrates the transmission spectrum obtained from varying the parameter of x_2. When x_2 is increased from 140 nm to 200 nm, the transmission values increase from 30% to 55% at 689.5 nm. During the parameter sweeps, the lengths are constant except for the changed parameter. According to these analyses, the optimal lengths for w_1, w_2, x_1, and x_2 are defined as 50 nm, 80 nm, 80 nm, and 200 nm, respectively. Due to the structure limit of 400 nm × 400 nm, maximum length increments are reached in the parameter analyses in Figure 3. The structure remains consistent for all-optical logic gates during analyses. By adjusting the phases of the applied signal, three different logic gates can be achieved. To obtain higher transmission values, the refractive index of the medium for etched regions is 1 for the suggested all-optical logic gates.

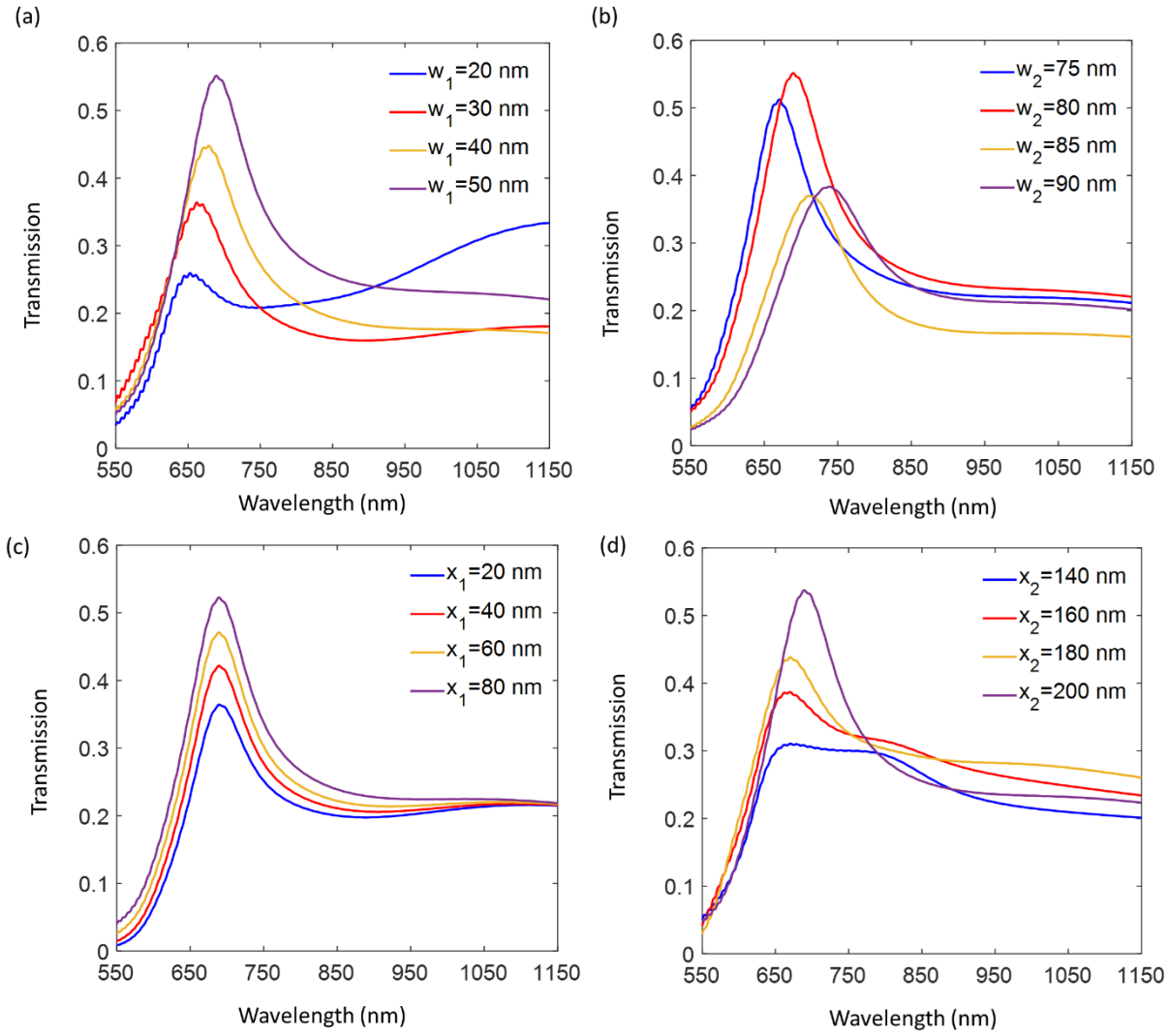

Figure 3. The transmission spectrum of the suggested structure for the sweep of (a) w_1, (b) w_2, (c) x_1, and (d) x_2.

3. Results and Discussion

3.1 Analysis of all-optical logic gates

3.1.1 Optical NOT gate

In the second stage, the first optical logic gate is a NOT gate. For that purpose, input 2 is used as a control port. During this analysis, logic 1 is applied from this port. When the signals are applied from the two ports, there are 180^0 phase differences between them. When the input 1 is logic 0 (OFF), the state of the output port is logic 1 (ON). As the input 1 is logic 1 (ON), the state of the output port is logic 0 (OFF) with a destructive interference effect. While all-optical logic gates are analyzed, constructive interference takes place if the signals are sent from the two ports in the same phase. The destructive interference occurs if the signals are applied in different phases [33,38]. Figure 4 visualizes the transmission spectrum of all-optical NOT gates. As given in Table 2, the values of transmission are 55% and 1.6% when input 1 is logic 0 and logic 1, respectively. Since

1.7% is threshold transmission, 55% and 1.6% present the status of the output ports as ON and OFF, respectively. According to the results obtained in this study, the threshold transmission value has been determined to be 1.7%, which is very low compared to values in the literature [34-38]. Transmission values higher than this threshold are considered logic 1, while values lower than it are considered logic 0. Figure 4 also presents the magnetic fields distributions at 689.5 nm when input 1 is logic 0 (blue line) and logic 1 (red dashed line). At 689.5 nm, the optical NOT gate demonstrates CR and MD values of 15.36 dB and 97%, respectively.

Table 2. The states of input 1 and input 2, the phase differences of the applied input signals, the transmission values, and the output states of all-optical NOT logic gate.

Input 1	Input 2 (Control port)	Phase Differences	Transmission (at 689.5 nm)	Output
Logic 0	Logic 1	0^0	55%	ON
Logic 1	Logic 1	180^0	1.6%	OFF

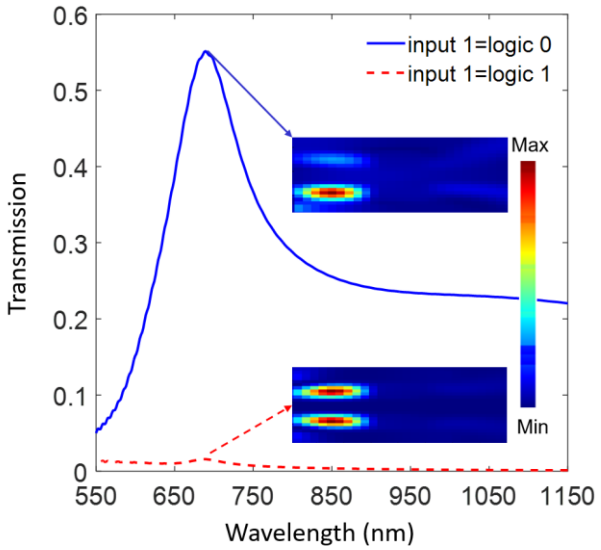

Figure 4. The spectrum of transmission and the magnetic fields distributions of suggested all-optical NOT gates for input 1=logic 0 and input 1=logic 1 at 689.5 nm.

3.1.2 Optical OR gate

The second logic gate is the all-optical OR gate. In this part, input 1 and input 2 are utilized to apply the input signals. During this analysis, the applied signals have the same phase. 01, 10, and 11 input signals are applied orderly from input 1 and input 2 as given in Table 3. Figure 5 visualizes the spectrum of transmission for the all-optical OR gate. When 01 and 10 are applied, the transmission value is 55%. When 11 is applied, the transmission value reaches its highest value of 149% with the constructive interference effect. In this analysis, all transmission values are higher than the threshold transmission value, resulting in ON output states. Figure 5 also illustrates the magnetic fields distributions for input 1=logic 0 and input 2=logic 1 (blue line), input 1=logic 1 and input 2=logic 0 (red dashed line), and input 1=logic 1 and input 2=logic 1 (brown dashed line) at 689.5 nm. When the transmission value increases, stronger modes are localized on the structure.

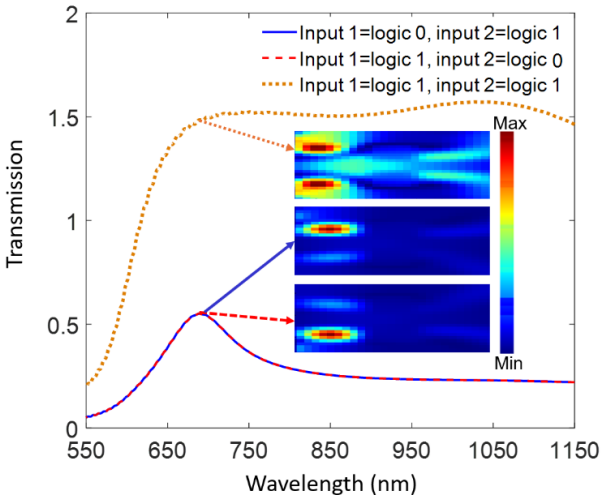

Figure 5. The spectrum of transmission and the magnetic fields distributions of suggested all-optical OR gates for input 1=logic 0 and input 2=logic 1, input 1=logic 1 and input 2=logic 0, and input 1=logic 1 and input 2=logic 1 at 689.5 nm.

Table 3. The states of input 1 and input 2, the phase differences of the applied input signals, the transmission values, and the output states of all-optical OR logic gate.

Input 1	Input 2	Phase Differences	Transmission (at 689.5 nm)	Output
Logic 0	Logic 1	0^0	55%	ON
Logic 1	Logic 0	0^0	55%	ON
Logic 1	Logic 1	0^0	149%	ON

3.1.3 Optical XOR gate

The third logic gate is the all-optical XOR gate. In this part, the input signals are applied from input 1 and input 2 as seen in Table 4. The signals have similar phases while the 01 and 10 input signals are sent. As the signals of 11 are applied, there is a 180° phase difference between the two input ports. Figure 6 illustrates the spectrum of transmission for the all-optical XOR gate. The values of transmission reach 55% when 01 and 10 are injected from the two input ports. The value of transmission is at the lowest level of 1.6% when 11 is applied with the effect of destructive interference. Since 1.7% is the threshold transmission value, output ports with 55% and 1.6% transmission represent the ON and OFF states, respectively. Figure 6 also visualizes the distributions of magnetic fields at 689.5 nm for input 1=logic 0 and input 2=logic 1 (blue line), input 1=logic 1 and input 2=logic 0 (red dashed line), and input 1=logic 1 and input 2=logic 1 (brown dashed line). When the transmission value is 55%, stronger modes are localized on the structure. Similar to the XOR gate, the optical NOT gate supports CR and MD values of 15.36 dB and 97%, respectively. This study generally demonstrates better results than previous studies in terms of the threshold transmission limit and transmission value, as shown in Table 5.

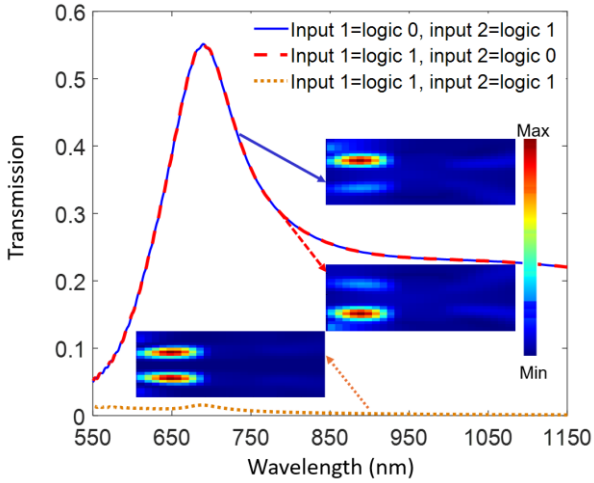

Figure 6. The spectrum of transmission and the magnetic fields distributions of all-optical XOR gates for input 1=logic 0 and input 2=logic 1, input 1=logic 1 and input 2=logic 0, and input 1=logic 1 and input 2=logic 1 at 689.5 nm.

Table 4. The states of input 1 and input 2, the phase differences of the applied input signals, the transmission values, and the output states of all-optical XOR logic gate.

Input 1	Input 2	Phase Differences	Transmission (at 689.5 nm)	Output
Logic 0	Logic 1	0^0	55%	ON
Logic 1	Logic 0	0^0	55%	ON
Logic 1	Logic 1	180^0	1.6%	OFF

Table 5. Comparison of the study with previously reported studies.

Reference	Number of designed optical logic gates	Transmission threshold value	The highest transmission	The highest contrast ratio (dB)
[34]	1	50%	73%	3.16
[35]	2	30%	69%	24.76
[36]	3	30%	78%	20.66
[37]	3	-	80%	25.86
[38]	4	20%	143%	28.75
This study	3	1.7%	149%	15.36

4. Conclusion

This work presents the results of all-optical OR, XOR, and NOT logic devices with silicon slot waveguides. The FDTD method is used to determine the spectra of transmission and distributions of magnetic fields for the structures. To reach the ideal geometrical lengths of the structure, parameter sweep analyses have been performed. The highest transmission value is 149% for optical OR logic gates. The maximum modulation depth and contrast ratio are 97% and 15.36 dB for optical NOT and XOR logic gates. The study presents valuable results in designing dielectric waveguide-based optical devices.

Author's Contributions

Semih Korkmaz: Designed the structure, performed the analysis, drafted and wrote the manuscript

Ethics

There are no ethical issues after the publication of this manuscript.

References

[1]. Chai, Z, Hu, X, Wang, F, Niu, X, Xie, J, Gong, Q. 2017. Ultrafast all-optical switching. *Advanced Optical Materials*; 5(7): 1600665.

[2]. Wang, X, Qi, H, Hu, X, Yu, Z, Ding, S, Du, Z, Gong, Q. 2021. Advances in photonic devices based on optical phase-change materials. *Molecules*; 26(9): 2813.

[3]. Wesemann, L, Davis, TJ, Roberts, A. 2021. Meta-optical and thin film devices for all-optical information processing. *Applied Physics Reviews;* 8(3): 031309.

[4]. Mohammadi, M, Habibi, F, Seifouri, M, Olyaee, S. 2022. Recent advances on all-optical photonic crystal analog-to-digital converter (ADC). *Optical and Quantum Electronics*; 54(3): 192.

[5]. Khonina, SN, Voronkov, GS, Grakhova, EP, Kazanskiy, NL, Kutluyarov, RV, Butt, MA. 2023. Polymer waveguide-based optical sensors—interest in bio, gas, temperature, and mechanical sensing applications. *Coatings*; 13(3): 549.

[6]. Wang, Z, Xu, X, Fan, D, Wang, Y, Subbaraman, H, Chen, RT. 2016. Geometrical tuning art for entirely subwavelength grating waveguide based integrated photonics circuits. *Scientific Reports*; 6(1): 24106.

[7]. Ferrando-Rocher, M, Herranz-Herruzo, JI, Valero-Nogueira, A, Baquero-Escudero, M. 2021. Half-mode waveguide based on gap waveguide technology for rapid prototyping. *IEEE Microwave and Wireless Components Letters*; 32(2): 117-120.

[8]. Singh, L, Zhu, G, Kumar, GM, Revathi, D, Pareek, P. 2021. Numerical simulation of all-optical logic functions at micrometer scale by using plasmonic metal-insulator-metal (MIM) waveguides. *Optics & Laser Technology*, 135: 106697.

[9]. Swarnakar, S, Reddy, SK, Harijan, R, Kumar, S. 2021. Design and modelling of all-optical NAND gate using metal–insulator–metal (MIM) waveguides-based Mach–Zehnder interferometers for high-speed information processing. *Optical and Quantum Electronics*; 53(9): 493.

[10]. Shnan, NS, Sadeghi, S, Farzaneh, M, Hamidi, SM, Belotelov, VI, Chernov, AI. 2022. Longitudinal magneto-optical Kerr effect in insulator/metal/insulator grating structure. *Journal of Superconductivity and Novel Magnetism;* 35(11): 3397-3401.

[11]. Jasim, WA, Ali, FM, Abdullah, AK, AbdulNabi, MA. 2021. Design and simulation of optical logic gates based on insulator-metal–insulator (IMI) plasmonic waveguides for optical communications. *International Journal of Nonlinear Analysis and Applications*; 12(2): 2483-2497.

[12]. Dionne, JA, Lezec, HJ, Atwater, HA. 2006. Highly confined photon transport in subwavelength metallic slot waveguides. *Nano Letters*; 6(9): 1928-1932.

[13]. Su, R, Tang, D, Ding, W, Chen, L, Zhou, Z. 2011. Efficient transmission of crossing dielectric slot waveguides. *Optics Express;* 19(5): 4756-4761.

[14]. Mashanovich, GZ, Gardes, FY, Thomson, DJ, Hu, Y, Li, K, Nedeljkovic, M., Penades JS, Khokhar, AZ, Mitchell, CJ, Stankovic S, Topley R, Reynolds, SA, Wang, Y, Troia, B, Passaro, VMN, Littlejohns, CG, Bucio, TD, Wilson PR, Reed, GT. 2014. Silicon photonic waveguides and devices for near-and mid-IR applications. *IEEE Journal of Selected Topics in Quantum Electronics*; 21(4): 407-418.

[15]. Dhingra, N, Dell'Olio, F. 2020. Ultralow loss and high extinction ratio TM-pass polarizer in silicon photonics. *IEEE Photonics Journal*; 12(6): 1-11.

[16]. Sun, L, Zhang, Y, He, Y, Wang, H, Su, Y. 2020. Subwavelength structured silicon waveguides and photonic devices. *Nanophotonics*; 9(6): 1321-1340.

[17]. Su, Y, Zhang, Y, Qiu, C, Guo, X, Sun, L. 2020. Silicon photonic platform for passive waveguide devices: materials, fabrication, and applications. *Advanced Materials Technologies*; 5(8): 1901153.

[18]. Malka, D, Danan, Y, Ramon, Y, Zalevsky, Z. 2016. A photonic 1×4 power splitter based on multimode interference in silicon–gallium-nitride slot waveguide structures. *Materials;* 9(7): 516.

[19]. Nikolaevsky, L, Shchori, T, Malka, D. 2018. Modeling 1×8 MMI Green Light Power Splitter Based on Gallium-Nitride Slot Waveguide Structure. *IEEE Photonics Technology Letters;* 30(8): 720-723.

[20]. Sarkar, D, Jamal, I, Mitra, SK. 2013. Analysis, design and fabrication of optical waveguides for Mach–Zehnder Interferometry. *Optics Communications*; 311: 338-345.

[21]. Yu, R, Zhang, J, Chen, W, Wang, P, Li, Y, Li, J, Qiang F, Tingge D, Hui Y, Yang, J. 2021. Optical reversible logic gates based on graphene-silicon slot waveguides. *Optik*; 228: 166182.

[22]. Rutirawut, T, Talataisong, W, Gardes, FY. 2021. Designs of silicon nitride slot waveguide modulators with electro-optic polymer and the effect of induced charges in Si-substrate on their performance. *IEEE Photonics Journal*; 13(2): 1-15.

[23]. Chiang, LY, Wang, CT, Lin, TS, Pappert, S, Yu, P. 2020. Highly sensitive silicon photonic temperature sensor based on liquid crystal filled slot waveguide directional coupler. *Optics Express*; 28(20): 29345-29356.

[24]. Lipson, M. 2005. Guiding, modulating, and emitting light on silicon-challenges and opportunities. *Journal of Lightwave Technology*; 23(12): 4222-4238.

[25]. Simili, DV, Cada, M. 2019. Low loss slow light propagation in silicon slot waveguide. *Optics Express;* 27(18): 26203-26217.

[26]. Qin, W, Liu, J, Yang, WW, Chen, JX, Li, Y, Xu, RL. 2021. Integrated-designs of filtering circuits based on adjustable dielectric waveguide resonators. *IEEE Transactions on Circuits and Systems II: Express Briefs*; 69(2): 284-288.

[27]. Korkmaz, S. 2024. Design and analysis of high performance 1×N optical wavelength demultiplexers based on MIM waveguide with polygon resonators. *Optical and Quantum Electronics*; 56(7): 1219.

[28]. Palik, ED. Handbook of optical constants of solids. Academic Press, 1998; pp 565-566.

[29]. Abdulwahid, SH, Wadday, AG, Abdulsatar, SM. 2023. Design of optical combinational circuits utilized with hybrid plasmonic waveguides. *Plasmonics*; 18(1): 9-28.

[30]. Lumerical FDTD Solutions, www.lumerical.com.

[31]. Korkmaz, S. 2024. Multiple ultra-narrow band-stop filters based on MIM plasmonic waveguide with nanoring cavities. *Physica Scripta*; 99(3): 035503.

[32]. Anagha, EG, Jeyachitra, RK. 2022. Optimized design of an all-optical XOR gate with high contrast ratio and ultra-compact dimensions. *Applied Physics B*; 128(2): 21.

[33]. Choi, D, Shin, CK, Yoon, D, Chung, DS, Jin, YW, Lee, LP. 2014. Plasmonic optical interference. *Nano Letters*; 14(6): 3374-3381.

[34]. Fakhruldeen, HF, Mansour, TS. 2020. Design of plasmonic NOT logic gate based on insulator–metal–insulator (IMI) waveguides. *Advanced Electromagnetics;* 9(1): 91-94.

[35]. Mainka, Sharma, S, Zafar, R, Mahdieh, MH, Singh, G, Salim, M. High contrast ratio based all-optical OR and NOR plasmonic logic gate operating at E band. In Optical and Wireless Technologies: Proceedings of OWT 2018, Singapore, 2020, pp 325-332.

[36]. Zafar, R, Nawaz, S, Salim, M. 2018. Fano resonance excited all-optical XOR, XNOR, and NOT gates with high contrast ratio. *Plasmonics*; 13(6): 1987-1994.

[37]. Dolatabady, A, Granpayeh, N. 2017. All-optical logic gates in plasmonic metal–insulator–metal nanowaveguide with slot cavity resonator. *Journal of Nanophotonics*, 11(2): 026001-026001.

[38]. El Haffar, R, Mahboub, O, Farkhsi, A, Figuigue, M. 2022. All-optical logic gates using a plasmonic MIM waveguide and elliptical ring resonator. *Plasmonics*; 17: 831–842.

Celal Bayar University Journal of Science

The Thermal Performance of The Plate-fin Heat Sink under Natural Convection at Different Power Levels and Ambient Temperatures

Mesut Abuşka[1*], Vahit Çorumlu[2]

[1]Manisa Celal Bayar University, Akhisar Vocational School, Dept. of Machine 45200, Manisa, Türkiye
[2]Manisa Celal Bayar University, Akhisar Vocational School, Dept. of Electrical and Energy 45200, Manisa, Türkiye

* mesut.abuska@cbu.edu.tr
* Orcid No: 0000-0003-2686-9786

Received: 13 August 2024
Accepted: 24 September 2024
DOI: 10.18466/cbayarfbe.1532575

Abstract

The thermal performance of a flat heat sink and a plate-fin heat sink was experimentally compared under natural convection conditions at thermal powers of 16.5 W and 33 W and ambient temperatures of 30°C and 40°C. For the same heating powers, surface and junction temperatures increased as the ambient temperature rose from 30°C to 40°C, but the increase was not as much as the ambient temperature change. For the flat heat sink, the increase in junction temperature was 5°C at 16.5 W and 6.68°C at 33 W. For the plate-fin heat sink, the increase in junction temperature was 3.55°C at 16.5 W and 4.47°C at 33 W. The increase in surface temperature for the flat heat sink was 5.35°C at 16.5 W and 5.91°C at 33 W, while for the plate-fin heat sink, the surface temperature increase was 4.76°C at 16.5 W and 2.22°C at 33 W. The thermal resistance of the flat heat sink was around 4 K/W, while for the plate-fin heat sink, it ranged between 2-2.5 K/W, providing approximately twice the advantage in thermal resistance for the plate-fin model compared to the flat model. Under all conditions, the Rayleigh number (Ra) significantly decreased with the increase in ambient temperature but increased with the applied thermal power. Thus, the increase in Rayleigh number with power was more pronounced in the plate-fin model, indicating a more significant effect. In the plate-fin model, the fin efficiency slightly decreased with the increase in ambient temperature, from 0.63 to 0.62 at 16.5 W and from 0.65 to 0.64 at 33 W.

Keywords: heat sink, plate-fin, natural convection, ambient temperature, power.

1. Introduction

Heat sinks are passive heat exchangers that transfer heat generated by electronic or mechanical devices to a fluid, thus maintaining the device temperature within the desired range. Heat sinks are commonly used in the thermal management of CPUs, GPUs, RAM modules, laser systems, power transistors such as light emitting diodes (LEDs), SSRs (Solid State Relays), and other high-power semiconductor devices such as optoelectronics. As the electrical and electronics industry rapidly evolves, the devices in use are experiencing increased electrical and thermal loads while their sizes are being reduced or there is a demand for miniaturization. The goal of size reduction is to decrease the overall volume and reduce the raw material inputs required for manufacturing. One of the most critical factors affecting the lifespan of electronic components is the operation of these components above the specified safe temperature ranges. The most common and effective method to ensure that devices operate within the appropriate temperature range is the use of heat sinks, which are both efficient and relatively economical. Approximately 55% of electronic equipment failures are attributed to systems operating at undesirably high temperatures [1]. Operating at elevated temperatures significantly shortens the lifespan of these devices, making thermal management in electronic systems increasingly crucial alongside technological advancements. Heat sinks are typically employed with natural convection in applications without space or volume constraints and with forced convection in constrained electronic applications. Key factors influencing the cooling performance of heat sinks include the material used in manufacturing, surface geometry, fin design, and the type of convection. In this context, the literature has focused on fin geometry, arrangement, size,

structure, and modifications to enhance cooling performance by increasing the heat transfer area and creating turbulence regions while maintaining acceptable pressure drop and flow blockage levels. Parameters such as flow rate and ambient temperature also play a significant role in performance. Design principles prioritize simplicity, reliability, and minimizing manufacturing and operational costs. Although extensive research on heat sinks is in the literature, this study reviews the most relevant works based on the specific geometry, convection type, and experimental test characteristics under investigation.

Doğan and Doğan [2] experimentally investigated the thermal performance of a plate-fin heat sink (PF_{hs}) under natural convection conditions with fin heights ranging from 15 to 40 mm, a base fin spacing of 12 mm, a fin thickness of 3 mm, and varying gap ratios between the fin tips and the base from 0.25 to 1. They found that the optimal gap ratio for fins providing the best thermal performance was between C=0.50 and C=0.75, with this optimal ratio being primarily dependent on fin height and the Rayleigh number. In the study by Haghighi et al. [3], the thermal performance of heat sinks with plate-type and cubic plate-type fins under natural convection was evaluated at Rayleigh numbers of 8-9.5x106, heating powers of 10-120 W, fin spacing of 5-12 mm, and fin counts of 5-9. A 10-41.6% increase in heat transfer was recorded in the cubic plate-type fin heat sink. As the fin spacing increased, thermal resistance decreased, but the increase in fin number did not positively contribute to heat transfer. The optimal configuration for the cubic plate-type heat sink was seven fins with an 8.5 mm fin spacing. Shen et al. [4] examined the effect of eight different orientations on the thermal performance of a PF_{hs} under natural convection. They concluded that the mismatch between the heat transfer area and flow blockage was a key factor affecting heat transfer under both natural and forced convection and that fin density played a significant role in orientation. Şevik and Özdilli [5] studied the effect of different fin geometries, such as trapezoidal and grooved, on the thermal performance of plate-type heat sinks. These geometries were designed with fin heights of 10-20 mm and analyzed numerically using SolidWorks Flow Simulation at thermal powers of 5W and 10W. The heat sinks were compared regarding temperature distribution, material weight, fin height, and surface area. The trapezoidal geometry performed best, followed closely by the trapezoidal-grooved geometry. At 5W, the maximum temperature difference between models was 3°C for a 20 mm fin height and 6°C for a 10 mm fin height. At 10W, the maximum temperature difference was 4°C for the 20 mm fins and 8°C for the 10 mm fins. The modeling results indicated that maximum temperature was more affected by fin height than fin geometry. Özdilli and Şevik [6] designed three types of heat sinks aimed at minimizing junction temperature: a trapezoidal plate-type finned model (Model-1), a chamfered trapezoidal finned model (Model-2), and a standard plate-type heat sink for comparison. Under natural convection, Models 1 and 2 achieved thermal resistance values that were 14-17% better than the standard model. Models 1 and 2 also provided a 5-15% advantage in junction temperature compared to the standard model. Yalçın [7] used Finite Element Modeling (FEM) to study the effects of fin geometry (straight and wavy), fin count (4-6-8), fin thickness, and material type (aluminum and copper) on the thermal performance of plate-type heat sinks exposed to temperatures of 50, 150, and 250°C. The study found that increasing the fin number while decreasing the fin thickness resulted in higher temperature differences in the heat sinks, thereby increasing the heat transfer rates. Feng et al. [8] examined the performance of standard and cross PF_{hs}s under natural convection, finding an 11% increase in total heat transfer coefficient for the cross model without changing material or cost. Banerjee et al. [9] conducted a numerical analysis of plate-type, cylindrical, and conical finned heat sinks with identical surface areas, identifying the conical model as the most efficient fin structure despite the lowest efficiency being observed in the cylindrical type. They determined the PF_{hs} as the most effective fin structure. Altun and Ziylan [10] experimentally studied heat transfer in vertical sinusoidal wavy fins under natural convection. Their results showed that wavy fins provided better heat transfer than plate fins; however, beyond a certain wave width, the increased blockage of fluid flow negatively impacted natural convection. They also noted that a significant portion of total heat transfer occurred through radiation and that this should be considered in the design of finned heat sinks for natural convection applications. Charles and Wang [11] compared the performance of plate, trapezoidal, and inverted trapezoidal fin heat sinks under natural convection at heating powers ranging from 3 to 20 W. While the heat transfer coefficient of the standard plate-fin model was higher than that of the trapezoidal model, the inverted trapezoidal model provided a 25% and 10% advantage over the trapezoidal and standard plate models, respectively. The advantage of the inverted trapezoidal model was attributed to a larger temperature difference and improved air passage. Do et al. [12] investigated the thermal resistance of plate-type heat sinks for cooling concentrated photovoltaic modules under natural convection, considering input power and tilt angle. They found that the optimal fin spacing depended on temperature difference and tilt angle.

In the literature, studies on forced convection are predominant, studies on natural convection are rare, and the effect of ambient temperature on performance is almost negligible. This study aims to experimentally determine the performance of PF_{hs} at different powers and ambient temperatures in natural convection. In addition, the performance comparison was made with a flat heat sink [13].

Celal Bayar University Journal of Science
Volume 20, Issue 3, 2024, p 91-99
Doi: 10.18466/cbayarfbe.1532575

2. Experimental Setup and Thermal Analysis

2.1. Experimental setup

In this study, a PF_{hs} was experimentally tested under natural convection conditions at different heating powers and ambient temperatures, and a flat heat sink (F_{hs}) was also used for comparison. In order to address the effect of ambient temperature and power difference on thermal performance in general rather than a specific fin geometry, a plate-fin heat sink, one of the most commonly used fin geometries, was designed and manufactured. While there is an outdoor design temperature standard for industrial coolers (ASHRAE, TSE, etc.), since there is no national or international standard for design ambient temperature standards for heat sinks, 30°C and 40°C were selected as the test ambient temperature. Here, it was assumed that these devices are generally around these temperatures. There is no standard for test powers, and many power values were taken into account in the literature, and in this study, they were randomly selected. Table 1 presents the technical specifications of the heat sinks tested, while Fig. 1 provides the technical drawings, photographs, and thermal images of the heat sinks.

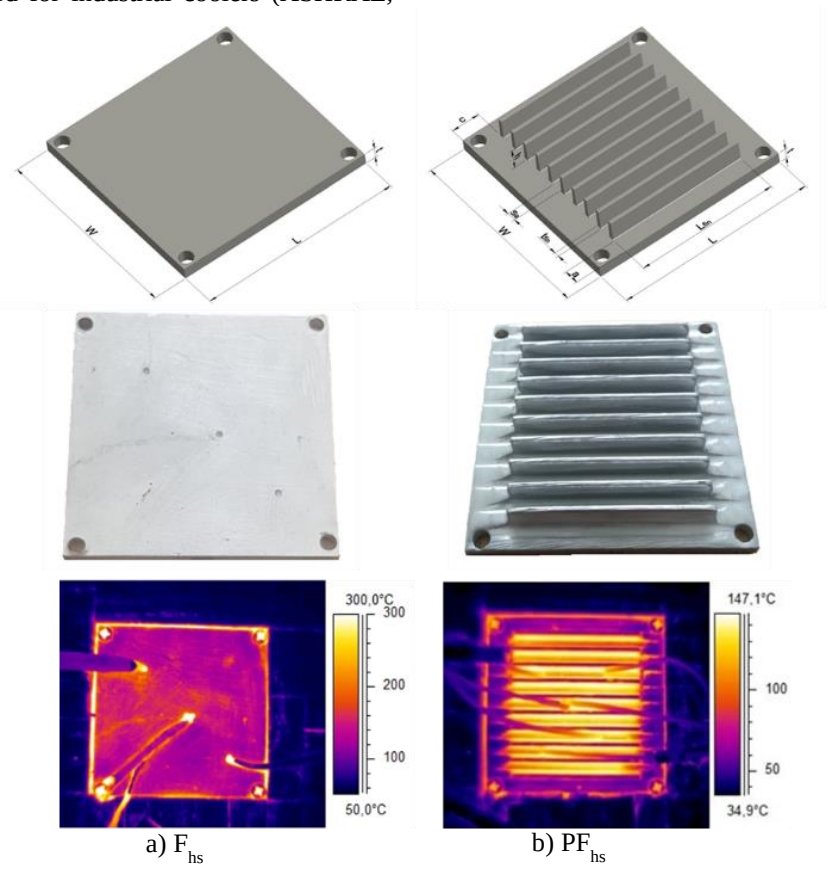

a) F_{hs} b) PF_{hs}

Figure 1. Technical drawing, photograph, and thermal image of F_{hs} and PF_{hs}

Table 1. Technical specifications of HSs.

Heat sink	Base				Fin						Area	Mass
	mm				mm						m^2	G
	W	L	t	no	h	L_{fin}	t_{fin}	s_a	a	c		
PF_{hs}	80	80	5	10	10	54	2.6	4.33	7.5	13	0.0177	114.3
F_{hs}	80	80	5	-	-	-	-	-	-	-	0.0064	83.8

The thermal performance tests of the heat sinks under natural convection conditions were conducted at ambient temperatures of 30°C and 40°C, with heating powers of 16.5 W and 33 W. The experimental setup for natural convection is shown in Fig. 2, which includes a photograph and a schematic diagram. The experimental setup consists of an ambient heater with a thermostat, a test platform, heating resistance, a power supply, a thermal camera, a data logger, and temperature sensors. During the tests, two thermostat-controlled electric heaters were used to maintain a constant ambient temperature. The experiment commenced once the

ambient temperature reached the predefined temperature. The ambient temperature was measured using two thermocouples and PT1000-type temperature sensors. A custom-made heating resistance (80x80x3 mm) was controlled by an adjustable DC power supply to deliver the specified heat loads to the heat sinks. A 150x150x30 mm firebrick was prepared with a slot at its geometric center to accommodate the heat sink and heating resistance, with the test models placed accordingly. The bottom and sides of the heat sink slot were insulated with felt insulation (k:0.0336 W/mK), and the surrounding area was further insulated with polyurethane foam. Three thermocouples were placed in a channel on the bottom surface of the heat sink to measure the junction temperature. For surface temperature measurements, three thermocouples were used for the flat model, while six were used for the finned model—three on the base plate and three on the fins. A thermal camera was positioned 200 mm away from the heat sinks for measurements. The technical specifications of the measurement devices used in the thermal performance tests of the heat sinks are provided in Table 2.

Table 2. Technical specifications of heat sink models.

Sensor/Device	Model	Range/specification	Accuracy
Thermocouple	Elimko	-35+250 °C, T-type	±0.5 °C
Temperature sensor	Comet SN234	-50+200 °C, PT1000 type	±0.15 °C
Thermal camera	FLIR SC325	-20-350 °C	±2 °C or ±2%
Thermostat		220V, 50Hz, 10A, -50+110 °C	±0.03 °C
Multimeter	CHY 21	Digital Multimeter	±(0.5%+1 digit) V ±(1.0%+1 digit) A
Heater	BYM Resistance	DC 0-24 V, max 190 W	
DC power supply	Sayntech 23003	0-30 V x 2 and 5 V, 0-5 A x 2 and 3 A	
Universal data logger	Comet MS6D	16 inputs	
Scales	Extent JCS-B	Maks. 3 kg	0.1 g

During the experiment, the ambient heater was first turned on to allow the environment to reach the specified temperature of 30°C, which took approximately one hour. Once the target temperature was achieved, the measurement devices in the experimental setup and the heating resistance of the heat sink were activated. The setup was operated at the initial test power of 16.5 W for 4 hours, followed by an increase to 33 W, where it was operated for an additional 4 hours. This procedure was repeated separately for an ambient temperature of 40°C. The system took about 3 hours to reach a steady state and was maintained in this regime for approximately 1 hour. The experimental setup and its schematic diagram are shown in Fig. 2.

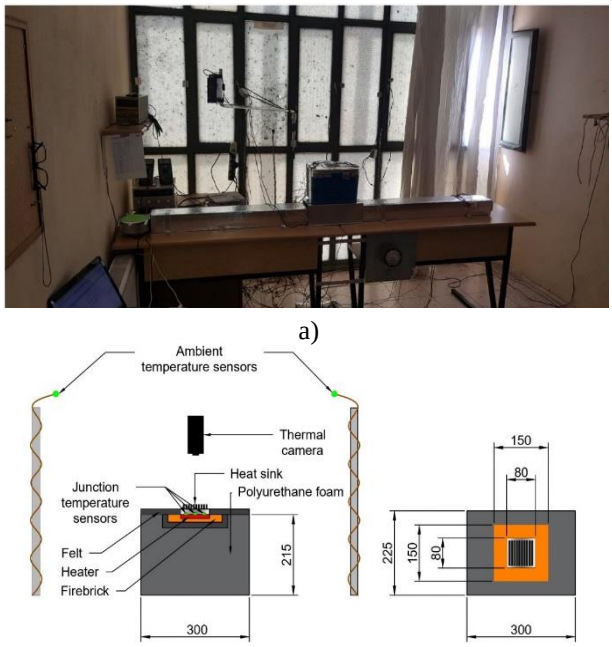

Figure 2. (a) Experimental setup, (b) Schematic view.

2.2. Thermal analyses

The thermal power applied to the heat sink, denoted as $\dot{Q}_{in}$, is equal to the electrical power of the heating resistor, $\dot{Q}_{EP}$. The electrical power can be expressed using the current (I) and voltage (V) values as follows:

$$\dot{Q}_{EP} = \dot{Q}_{in} = IV \quad (1)$$

The heat transfer from the surface of the heat sink to the surrounding environment occurs through convection and radiation. Heat loss due to conduction from the edges and base of the heat sink to the environment is neglected. Therefore, the heat transfer from the heat sink to the surroundings can be expressed as follows:

$$\dot{Q}_{in} = \dot{Q}_{con} + \dot{Q}_{rad} \quad (2)$$

Here, $\dot{Q}_{con}$ represents the convective heat transfer, and $\dot{Q}_{rad}$ represents the heat transfer through radiation, which can be expressed as:

$$\dot{Q}_{rad} = \frac{\sigma A_{hs}({T_{surf}}^4 - {T_{surw}}^4)\varepsilon_s}{(1-\varepsilon_s)+\frac{A_{hs}}{A_{surw}}} \quad (3)$$

In this equation, σ is the Stefan-Boltzmann constant, and A_{hs} is the total heat transfer surface area where both radiation and convection occur. A_{surw} represents the area of the surrounding air wall, T_{surf} is the average surface temperature, T_{surw} is the temperature of the surrounding environment, and ε_s is the emissivity of the surface. The convective heat transfer rate can be calculated as follows:

$$\dot{Q}_{con} = hA_{hs}\eta_o(T_{bp} - T_a) \quad (4)$$

In this equation, h denotes the average convective heat transfer coefficient, T_{bp} is the base plate temperature, T_a is the ambient temperature, and η_o represents the overall fin efficiency, which is calculated as:

$$\eta_o = 1 - \frac{A_{fin}}{A_{hs}}(1 - \eta_f) \quad (5)$$

The fin efficiency η_f is given by:

$$\eta_f = \frac{T_{fin}-T_a}{T_{bp}-T_a} \quad (6)$$

The Nusselt number Nu is defined as:

$$Nu = {hL}/{k} \quad (7)$$

where L is the characteristic length and k is the thermal conductivity of the air. The Rayleigh number Ra is the ratio of buoyancy-driven convection to viscous resistance and is calculated as:

$$Ra = \frac{g\beta(T_{surf}-T_a)L^3}{\nu\alpha} \quad (8)$$

Here, g is the acceleration due to gravity, β is the thermal expansion coefficient of the air, ν is the kinematic viscosity, and α is the thermal diffusivity of the air. The thermophysical properties of the air are considered at the film temperature, T_{film}, calculated as:

$$T_{film} = \frac{T_a+T_{surf}}{2} \quad (9)$$

The average surface temperature of the heat sink, T_{surf}, is calculated as:

$$T_{surf} = \frac{A_{bp}T_{bp}+A_{fin}T_{fin}}{A_{hs}} \quad (10)$$

where A_{bp} is the area of the base plate without fins, A_{fin} is the total fin area, and T_{fin} is the average fin temperature.

Thermal resistance R_{th}, defined as the ratio of the temperature difference between the heat sink surface and the ambient temperature to the input power, is a key thermal characteristic of the heat sink and can also be expressed as:

$$R_{th} = \frac{T_{surf}-T_a}{\dot{Q}_{in}} \quad (11)$$

The total heat transfer coefficient h_T is related to the thermal resistance and is calculated as follows:

$$\frac{1}{h_T A_{hs}} = R_{th} = \frac{T_{surf}-T_a}{\dot{Q}_{in}} \quad (12)$$

The total heat transfer coefficient h_T is expressed as:

$$h_T = \frac{1}{R_{th}A_{hs}} \quad (13)$$

The uncertainties in the experimentally determined thermal resistance, convective heat transfer coefficient, and overall fin efficiency are calculated using the following equation:

$$W_R = \left[\left(\frac{\partial R}{\partial x_1}w_1\right)^2 + \left(\frac{\partial R}{\partial x_2}w_2\right)^2 + \cdots + \left(\frac{\partial R}{\partial x_n}w_n\right)^2\right]^{1/2} \quad (14)$$

Based on the calculations, the maximum uncertainties for thermal resistance, convective heat transfer coefficient, and overall fin efficiency are 2.37%, 1.84%, and 1.05%, respectively.

3. Results and Discussion

This section presents the heat transfer characteristics of the heat sink under natural convection conditions. The experiments were conducted at ambient temperatures of 30°C and 40°C with heating powers of 16.5 W and 33 W. The time-dependent average surface temperature (T_{surf})

Celal Bayar University Journal of Science
Volume 20, Issue 3, 2024, p 91-99
Doi: 10.18466/cbayarfbe.1532575

and junction temperature (T_j) for the specified ambient temperature and heating power under natural convection are shown in Fig. 3. The experimental measurement data generally exhibited stable behavior. The temperature curves reached a steady state after approximately 180 minutes. Naturally, the highest temperature curve corresponds to the junction temperature, with the average surface temperature following a similar trend at a lower level.

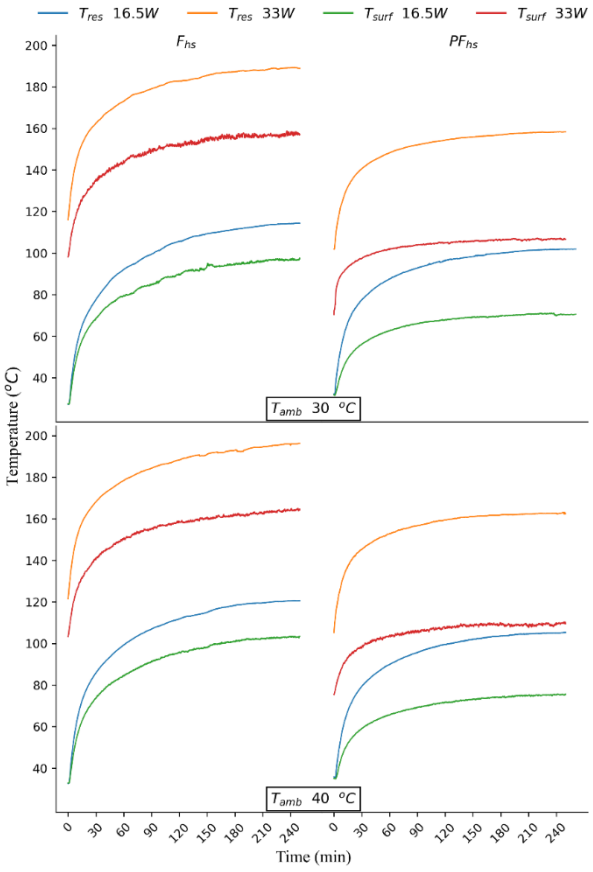

Figure 3. Time-dependent temperature measurement data.

To better understand the situation, Fig. 4 and Fig. 5 present the junction and surface temperatures data based on the average values during the steady-state period (last 60 minutes). For the same heating powers, both junction and surface temperatures increased with the rise in ambient temperature. In the 16.5 W experiment, the junction temperature in the F_{hs} increased from 115.68°C to 120.68°C as the ambient temperature rose from 30°C to 40°C, while at 33 W, it increased from 189.97°C to 196.65°C. In other words, the ambient temperature rise at the same power level also raised the junction temperature, which for the F_{hs} was 5°C at 16.5 W and 6.68°C at 33 W. For the PF_{hs}, the junction temperature increased from 101.6°C to 105.15°C in the 16.5 W experiment and from 157.75°C to 162.22°C at 33 W as the ambient temperature increased. This difference was 3.55°C at 16.5 W and 4.47°C at 33 W.

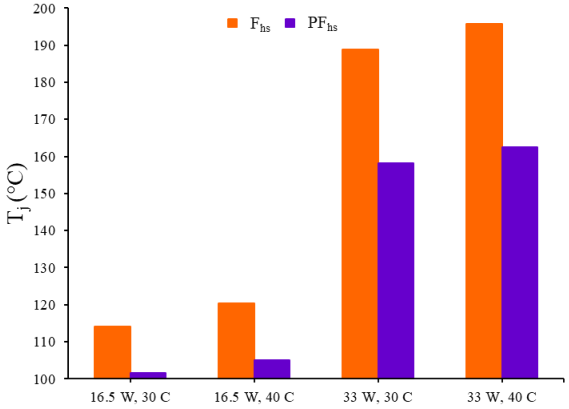

Figure 4. Variation of junction temperature depending on ambient temperature and thermal power.

For the surface temperature, in the case of the PF_{hs}, the temperature increased from 70.67°C to 75.43°C with an ambient temperature rise from 30°C to 40°C at 16.5W power, and from 106.87°C to 109.09°C at 33W power. The temperature rise difference for the PF_{hs} was 4.76°C at 16.5W and 2.22°C at 33W. For the F_{hs}, considering the surface temperature, the temperatures increased from 97.91°C to 103.26°C with an ambient temperature rise at 16.5W, and from 158.78°C to 164.69°C at 33W. The temperature rise difference for the F_{hs} was 5.35°C at 16.5W and 5.91°C at 33W. When considering the ambient temperature increase for the same heating powers, both the junction and surface temperatures of the PF_{hs} increased, but this increase was not as significant as in the F_{hs}. This indicates that the larger surface area of PF_{hs} positively affects the heat transfer performance, resulting in less increase in junction and surface temperatures with rising ambient temperatures compared to the flat type. Specifically, at 16.5W, the temperature difference between the two types with ambient temperatures of 30°C and 40°C is approximately 27°C, while at 33W, the temperature difference between them ranges from 45°C to 55°C.

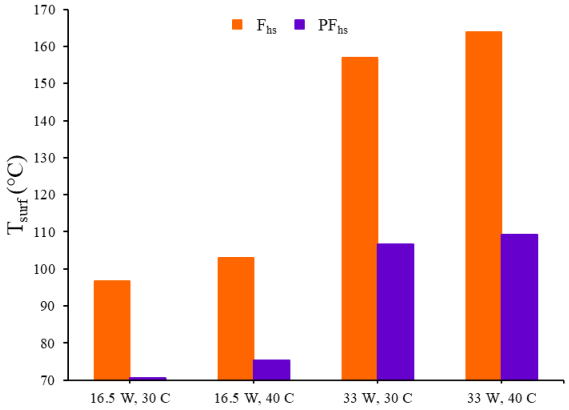

Figure 5. Variation of surface temperature depending on ambient temperature and thermal power.

Celal Bayar University Journal of Science
Volume 20, Issue 3, 2024, p 91-99
Doi: 10.18466/cbayarfbe.1532575

Fig. 6 shows the results of thermal resistance. Generally, the thermal resistance decreases slightly with increasing ambient temperature and thermal power. The thermal resistance of the F_{hs} typically hovers around 4 K/W, whereas for the PF_{hs}, it ranges between 2-2.5 K/W. For the F_{hs}, the thermal resistance decreases from 4.09 K/W to 3.93 K/W with an increase in ambient temperature from 30°C to 40°C at 16.5W and from 3.88 K/W to 3.83 K/W at 33W. For the PF_{hs}, the thermal resistance decreases from 2.38 K/W to 2.24 K/W with an increase in ambient temperature from 30°C to 40°C at 16.5W and from 2.31 K/W to 2.15 K/W at 33W. This indicates that the 10°C increase in ambient temperature results in an approximate 2-6°C increase in the heat sink surface temperatures.

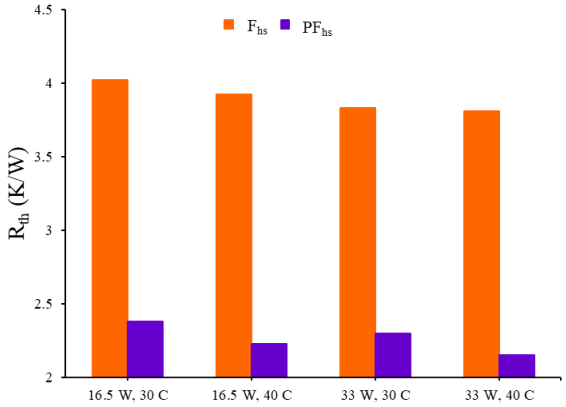

Figure 6. Variation of thermal resistance depending on ambient temperature and thermal power.

Fig. 7 presents the convective heat transfer coefficients. A slight increase in convective heat transfer coefficient values was observed for the same power levels with rising ambient temperature. The coefficients for the F_{hs} are around 30 W/m²K, whereas for the PF_{hs}, the coefficients are around 22 W/m²K. More specifically, for the F_{hs}, the coefficients increase from 28.97 W/m²K to 30.10 W/m²K with an ambient temperature rise from 30°C to 40°C at 16.5W, and slightly increase from 30.14 W/m²K to 30.47 W/m²K at 33W. For the PF_{hs}, the convective heat transfer coefficient rises from 21.44 W/m²K to 22.74 W/m²K with an ambient temperature increase from 30°C to 40°C at 16.5W and slightly increases from 21.87 W/m²K to 23.59 W/m²K at 33W. The coefficient increase difference for the F_{hs} with an ambient temperature rise from 30°C to 40°C is 1.13 and 0.33 W/m²K for the respective power levels. For PF_{hs}, the coefficient increase difference with an ambient temperature rise from 30°C to 40°C is 1.30 and 1.72 W/m²K for the respective power levels.

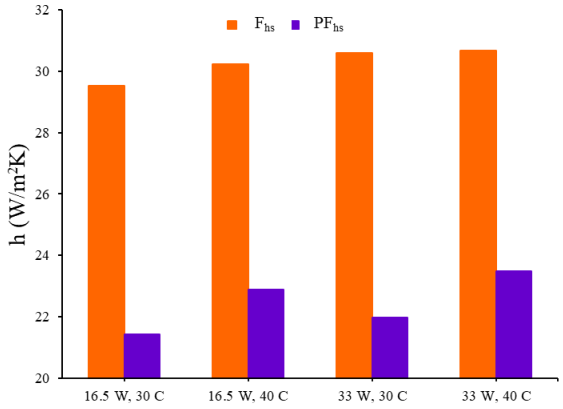

Figure 7. Variation of Convective heat transfer coefficient depending on ambient temperature and thermal power.

Fig. 8 shows the variation of the Nusselt number with thermal power and ambient temperature. The Nusselt number for the F_{hs} hovers around 20.5, while the PF_{hs} hovers around 16. For the F_{hs}, the Nusselt number slightly increases from 20.42 to 20.86 with an ambient temperature rise from 30°C to 40°C at 16.5W, while it slightly decreases from 19.72 to 19.62 at 33W. For the PF_{hs}, the Nusselt number increases slightly from 15.63 to 16.33 with an ambient temperature rise from 30°C to 40°C at 16.5W and from 15.23 to 16.23 at 33W.

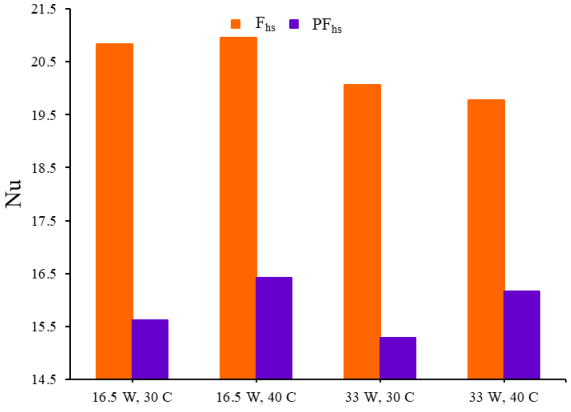

Figure 8. Variation of Nusselt number depending on ambient temperature and thermal power.

Table 3 summarizes the data calculated based on the experimental results. The Prandtl number, defined as the ratio of momentum diffusivity to thermal diffusivity or, in other words, the ratio of the thickness of the velocity boundary layer to the thermal boundary layer, is 0.72 for all experimental conditions with the PF_{hs}. For the F_{hs}, it is also 0.72 in the 16.5 W experiments, similar to the plate model, while it slightly decreases to 0.71 in the 33 W experiments.

The Grashof number, defined as the ratio of buoyancy to viscous forces, is crucial in natural convection studies for

indicating the flow characteristics (laminar or turbulent). Overall, a significant decrease in the Grashof number was observed in all experimental conditions with increasing ambient temperature. More specifically, for the PF_{hs}, the Grashof number decreases from 29076 to 25301 at 16.5 W when the ambient temperature increases from 30°C to 40°C and from 44497 to 38810 at 33 W. For the F_{hs}, the Grashof number decreases from 41948 to 36966 at 16.5 W and from 54025 to 49150 at 33 W. This suggests that the increase in ambient temperature significantly reduces the Grashof number. The difference in the Grashof number reduction due to the increase in ambient temperature is quite similar for both power levels in the flat model, being around 5000. In the plate model, the effect of ambient temperature increase on the Grashof number is approximately 3800 at 16.5 W, while it is 5700 at 33 W. Therefore, at 16.5 W, a lower Grashof number is observed in the plate model compared to the flat model, while at 33 W, a higher Grashof number is observed.

The Rayleigh number, a dimensionless number indicating the effectiveness of convection under natural conditions, can be described as the ratio of factors that accelerate convection to those that delay it. The Rayleigh number at which convection begins depends on the system's environmental conditions and geometry. According to the experimental results, the Rayleigh number significantly decreases with the rise in ambient temperature under all conditions but increases with the applied thermal power. For the PF_{hs}, the Rayleigh number decreases from 20990 to 18231 at 16.5 W and from 31949 to 27826 at 33 W when the ambient temperature increases from 30°C to 40°C. For the F_{hs}, it decreases from 30160 to 26526 at 16.5 W and from 38510 to 34975 at 33 W. The difference in the Rayleigh number reduction due to ambient temperature in the F_{hs} is 3634 at 16.5 W, slightly decreasing to 3535 at 33 W. The same applies to the PF_{hs}, where the reduction difference is 2759 at 16.5 W and 4123 at 33 W. This shows that the decrease in Rayleigh number becomes more pronounced and more affected in the plate model with increasing power.

One of the thermal characteristics of the heat sink, the fin efficiency, was slightly negatively impacted in the plate-fin model when the ambient temperature increased from 30°C to 40°C, dropping from 0.63 to 0.62 at 16.5 W and from 0.65 to 0.64 at 33 W. A very slight increase is observed when considering the effect of increased thermal power on fin efficiency.

Table 3. Calculated dimensionless parameters.

	Ambient temperature	**30 °C**		**40 °C**	
	Heat input	16.5 W	33 W	16.5 W	33 W
PF_{hs}	Prandtl	0.72	0.72	0.72	0.72
	Grashof	29099	44326	25188	38907
	Rayleigh	21007	31826	18150	27894
	η_o	0.76	0.77	0.75	0.77
	η_f	0.63	0.65	0.62	0.64
F_{hs}	Prandtl	0.72	0.71	0.72	0.71
	Grashof	41484	53856	36912	49095
	Rayleigh	29831	38399	26488	34939

4. Conclusion

The thermal performance of the PF_{hs}, compared to the F_{hs}, was experimentally tested under natural convection conditions at thermal power levels of 16.5 W and 33 W and ambient temperatures of 30°C and 40°C. The main findings from this study are summarized below:

- The heat sink's ability to transfer heat to the environment depends on the ambient temperature, which ideally represents the minimum temperature the heat sink can reach. When analyzing fin efficiency and overall fin efficiency at different power levels and ambient temperatures, the values appear close to each other. This result suggests that as the ambient temperature increases, the surface and junction temperatures will also rise.
- For the same heating powers, the surface and junction temperatures increased as the ambient temperature rose from 30°C to 40°C, but the increase was not as significant as the rise in ambient temperature. The increase in junction temperature for the F_{hs} was 5°C at 16.5 W and 6.68°C at 33 W. For the PF_{hs}, the increase in junction temperature was 3.55°C at 16.5 W and 4.47°C at 33 W. The increase in surface temperature for the F_{hs} was 5.35°C at 16.5 W and 5.91°C at 33 W, while for the PF_{hs}, it was 4.76°C at 16.5 W and 2.22°C at 33 W. From this, it can be concluded that the larger surface area of the PF_{hs} positively influenced heat transfer performance, resulting in less increase in junction

and surface temperatures compared to the flat type, and making it less affected by the ambient temperature rise. This was also a key factor in the noticeable difference in junction and surface temperature levels between the flat and PF_{hs}s.

- Regarding thermal resistance, a slight decrease was observed with increasing ambient temperature, parallel with the thermal power. The thermal resistance for the F_{hs} hovered around 4 K/W, whereas it ranged between 2-2.5 K/W for the PF_{hs}. Thus, the PF_{hs} provided an approximately two-fold advantage in thermal resistance compared to the flat type.
- The Nusselt number values for the F_{hs} were around 20.5, while for the PF_{hs}, they were around 16. This can be attributed to the fact that the heat transfer area of the flat type is noticeably smaller compared to the plate model.
- The Rayleigh number significantly decreased with increasing ambient temperature under all conditions but increased with the applied thermal power. This indicates that the increase in the Rayleigh number due to the increase in power was more pronounced in the plate model, showing that it was more affected.
- The fin efficiency in the plate-fin model was slightly negatively affected by the ambient temperature increase, decreasing from 0.63 to 0.62 at 16.5 W and 0.65 to 0.64 at 33 W.

Based on the perspective gained from this experimental study, future research could focus on the effects of fin height, fin spacing, and modifications on the fins.

Acknowledgement

The authors declare that they have no known competing financial interests or personal relationships that could have appeared to influence the work reported in this paper.

Author's Contributions

Mesut Abuşka: Conceptualization, Formal analysis, Investigation, Methodology, Project administration, Resources, Software, Visualization, Writing - original draft, Writing - review & editing.
Vahit Çorumlu: Conceptualization, Formal analysis, Investigation, Methodology, Resources, Software, Visualization, Writing - original draft, Writing - review & editing.

Ethics

There are no ethical issues after the publication of this manuscript.

References

[1]. Khattak, Z., Ali, H. M. 2019. Air cooled heat sink geometries subjected to forced flow: A critical review. *International Journal of Heat and Mass Transfer*, 130: 141-161.

[2]. Doğan, M., Doğan, D. 2017. Experimental investigation of natural convection heat transfer from fin arrays for different tip-to-base fin spacing ratios. *Isı Bilimi ve Tekniği Dergisi*, 37(1): 147-157.

[3]. Haghighi, S. S., Goshayeshi, H. R., Safaei, M. R. 2018. Natural convection heat transfer enhancement in new designs of plate-fin based heat sinks. *International Journal of Heat and Mass Transfer*, 125: 640-647.

[4]. Shen, Q., Sun, D., Xu, Y., Jin, T., Zhao, X. 2014. Orientation effects on natural convection heat dissipation of rectangular fin heat sinks mounted on LEDs. *International Journal of heat and mass transfer*, 75: 462-469.

[5]. Şevik, S., Özdilli, Ö. Study of the effect of fin geometry on the performance of a plate-fin heat sink, In 2nd International African Conference on Current Studies of Science, Technology Social Sciences, Abuja, Nigeria, 2020 pp 315-328.

[6]. Özdilli, Ö., Şevik, S. 2021. Effect of channel and fin geometries on a trapeze plate-fin heat sink performance. *Proceedings of the Institution of Mechanical Engineers, Part E: Journal of Process Mechanical Engineering*, 235(5): 1326-1336.

[7]. Yalçın, B. 2015. Soğutucu Plakalarda Yüzey Geometrisinin ve Kanatçık Sayısının Isı İletimine Etkisinin Sonlu Eleman Analizi İle Araştırılması. *Uluslararası Teknolojik Bilimler Dergisi*, 7(3): 27-39.

[8]. Feng, S., Shi, M., Yan, H., Sun, S., Li, F., Lu, T. J. 2018. Natural convection in a cross-fin heat sink. *Applied Thermal Engineering*, 132: 30-37.

[9]. Banerjee, B., Chattrejee, S., Das, S., Datta, J. 2022. Steady State Free Convection through some Variable Fin Geometries. *YMER* 21(7): 952-959.

[10]. Altun, A. H., Ziylan, O. (2019). Experimental investigation of the effects of horizontally oriented vertical sinusoidal wavy fins on heat transfer performance in case of natural convection. *International Journal of Heat and Mass Transfer*, 139: 425-431.

[11]. Charles, R., Wang, C. C. (2014). A novel heat dissipation fin design applicable for natural convection augmentation. *International Communications in Heat and Mass Transfer*, 59: 24-29.

[12]. Do, K. H., Kim, T. H., Han, Y. S., Choi, B. I., Kim, M. B. (2012). General correlation of a natural convective heat sink with plate-fins for high concentrating photovoltaic module cooling. *Solar Energy*, 86(9): 2725-2734.

[13]. Çorumlu, V. (2024). The effects of input power and ambient temperature on the thermal performance of conical pin fin heat sink in natural convection. *International Journal of Thermal Sciences*, 197, 108855.

Celal Bayar University Journal of Science

Triphenylamine-Based Solid-State Emissive Fluorene Derivative with Aggregation-Induced Emission Enhancement Characteristics

Seda Cetindere[1]*, Musa Erdoğan[2]

[1] Gebze Technical University, Department of Chemistry, Gebze, Kocaeli, Türkiye
[2] Kafkas University, Faculty of Engineering and Architecture, Department of Food Engineering, Kars, Türkiye

* sdemirer@gtu.edu.tr
* Orcid No: 0000-0001-7599-8491

Received: 16 July 2024
Accepted: 26 September 2024
DOI: 10.18466/cbayarfbe.1516889

Abstract

Aggregation-induced emission (AIE) has garnered considerable attention in recent years. Understanding the mechanisms underlying AIE phenomena is crucial. Here, we present the design and synthesis of a novel fluorene derivative (**4**) based on triphenylamine, which exhibits typical AIE properties. The structure of it was totally characterized using FT-IR, MALDI-TOF mass analysis, elemental analysis, ^{1}H, and ^{13}C NMR spectroscopy. It displayed strong solid-state emission with diverse fluorescence characteristics. The AIE property of the compound was systematically studied using photoluminescence spectroscopy, revealing a distinct yellow light-emitting phenomenon. The solid-state luminescence showed a red shift of 148 nm compared to its luminescence in dilute dimethylformamide (DMF) solutions. Moreover, photophysical characteristics, including absorption and emission spectra, as well as fluorescence lifetime, were examined using UV–vis absorption and fluorescence emission spectroscopy. Compound (**4**) exhibited superior photosensitization abilities in both solid and solution states, with a notably enhanced effect observed in the solid state compared to the solution state.

Keywords: AIE, Fluorene, Photophysical property, Solid-state emission, Triphenylamine.

1. Introduction

Organic luminescent materials have garnered significant attention in recent decades due to their potential applications in organic electronics [1], optoelectronics [2], bio/chemosensors [3-4], and bioimaging [5-6]. Typically, these compounds are required to function effectively in solid-states [7-8]. This preference arises because once they aggregate in the solid-state, their fluorescence often diminishes rapidly or even fully quenches due to aggregation-caused quenching (ACQ) [9-10]. Various compounds, such as silole, triphenylethene, and triarylamine derivatives, have been synthesized and studied extensively for their ACQ behavior [11-12]. However, the notorious ACQ phenomenon severely limits the emission efficiency of aggregates, posing a significant challenge in the practical application of luminescent materials [13-14]. Luckily, Tang and colleagues discovered an AIE phenomenon in 2001, which stands in direct contrast to ACQ [15]. Materials exhibiting AIE emit efficiently in aggregated or solid states. This discovery has revolutionized the field by enabling the effective application of fluorescent materials. Leveraging the beneficial AIE effect, researchers have explored and developed optoelectronic devices [16], fluorescence sensor systems [17], and optical waveguides [18-21], all capable of efficient solid-state emission. The discovery and understanding of AIE have thus opened new avenues for creating more effective luminescent materials that perform better in real-world applications.

Fluorene, also known as 9*H*-fluorene (1), is a chemical compound represented by the formula $(C_6H_4)_2CH_2$ (Figure 1). This organic substance forms white crystals that emit a purple fluorescence, hence its name derived from this characteristic [22]. Fluorene-based dyes have become integral in various technologies due to their unique properties. These compounds feature a flat biphenyl structure with an extensive π-conjugated system, offering advantages such as solubility, distinct photophysical characteristics, and ease of modification [23-25]. As a result, fluorene derivatives have been extensively studied and developed into probes for applications in molecular dynamics and bioimaging,

spanning monomers, polymers, and dendrimers. The synthesis and potential applications of fluorene derivatives have garnered significant attention, establishing fluorene-based research as a prominent field in recent years [22]. These derivatives play crucial roles in materials science, finding widespread use in optical and 3D data storage [26], organic light-emitting devices [27], dye-sensitized solar cells [28], and nonlinear optical devices for telecommunications [22]. Similarly, the triphenylamine (TPA) nucleus holds considerable importance in materials science due to its advantageous thermal, electrochemical, photoelectric, and photophysical properties [29]. Organic systems incorporating the TPA donor structure are known for their notable photophysical and optical attributes, such as redox activity, efficient hole-conduction, high electron mobility, stability, solubility, two-photon absorption capability, high photoluminescent efficiency, and excellent optoelectronic characteristics [30]. Hence, the TPA scaffold is frequently favored as the electron-donor unit in organic-based materials.

In this study, a novel fluorene derivative incorporating a TPA moiety (**4**) was intentionally designed and synthesized, as illustrated in Scheme 1. The synthesis process and the detailed characterization of this luminescent compound are extensively documented. Furthermore, the photophysical properties of the compound have been thoroughly investigated. Notably, it demonstrates outstanding characteristics associated with AIE. Moreover, the solid-state form of compound (**4**) exhibits significantly enhanced fluorescence compared to its solution state.

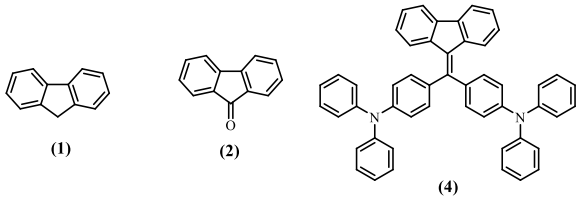

Figure 1. Molecular structures of 9*H*-fluorene (**1**), 9*H*-fluoren-9-one (**2**), and 4,4'-((9*H*-fluoren-9-ylidene) methylene)bis(*N*,*N*-diphenylaniline) (**4**)

2. Experimental

2.1. Materials and equipment

The chemicals used for synthesis were employed without further purification unless otherwise specified. We used chemical substances bought from commercial sources and deuterated solvent $CDCl_3$ for conducting NMR spectroscopy. All reactions were conducted under an argon atmosphere. The progress of the reactions was monitored using thin-layer chromatography (TLC) plates coated with silica gel. Purification of compounds were done by using column chromatography with powdered silica gel. The IR spectrum was acquired using a Perkin Elmer Spectrum 100 FT-IR spectrophotometer. Mass spectra were acquired on a Bruker Daltonics Microflex mass spectrometer. NMR spectra were recorded in $CDCl_3$ solutions using a Varian 500 MHz spectrometer. Absorption spectra were measured on a Shimadzu 2101 UV spectrophotometer in the UV–Visible region. Emission and excitation spectra were obtained using a Varian Eclipse spectrofluorometer. Fluorescence lifetimes were measured with a Horiba- Jobin-Yvon-SPEX Fluorolog 3-2iHR instrument.

2.2. Synthesis of 4,4'-((9*H*-fluoren-9-ylidene) methylene)bis(*N*,*N*-diphenylaniline), Compound (4)

The compound 9-(dibromomethylene)-9*H*-fluorene (**3**) was synthesized from 9*H*-fluoren-9-one (**2**) according to the literature [31]. To prepare compound (**4**), 500 mg (1.49 mmol) of compound (**3**) was reacted with $Pd(PPh_3)_4$ (47 mg, 0.044 mmol) and dissolved in 30 mL of DME (dimethoxyethane) in a 100 mL flask. A solution containing 4-(diphenylamino)phenylboronic acid (903 mg, 3.12 mmol) and Na_2CO_3 (473 mg, 4.46 mmol) in degassed water (15 mL) was then added to the flask. The mixture was heated under reflux for 24 hours. Once the reaction finished, the mixture was treated tree times with 50 mL ethyl acetate. The organic layers were combined and filtered on Na_2SO_4, and then concentrated under low pressure. Crude product underwent purification via column chromatography on silica gel using a solvent mixture consisting of 10% ethyl acetate and n-hexane. The resulting solid was recrystallized from a mixture of CH_2Cl_2/n-hexane (9:1), yielding compound (**4**) as yellow solid, with a yield of 970 mg (98%). It exhibited a melting point of 220°C. Elemental analysis showed the following composition in wt.-% for $C_{50}H_{36}N_2$ (calculated): C 90.33%, H 5.46%, N 4.21%. The experimental values were found to be C 90.26%, H 5.33%, N 4.15%, indicating good agreement with the calculated values. Spectral data for compound (4) included: FT-IR peaks at vmax (cm^{-1}): 3055, 3036, 1586, 1492, 1441, 1315, 1273, 751, 695. Mass spectrometry (MALDI-TOF) showed an m/z value of 664.206 [M+]. ^1H NMR spectrum (in $CDCl_3$) displayed peaks at δ ppm: 7.74 (d, J = 7.5 Hz, 2H), 7.34-7.19 (m, 32H), 6.95 (m, 2H). ^{13}C NMR spectrum (in $CDCl_3$) showed peaks at δ ppm: 148.08, 147.41, 131.56, 129.38, 124.94, 124.63, 123.40, 122.48, 119.22. These data collectively characterize the synthesized compound (**4**), confirming its structure and purity.

2.3. Photopyhsical measurements

UV-vis and fluorescence spectroscopy were employed to study the photophysical properties of compound (**4**). The absorption and emission profiles were investigated in $1x10^{-6}$ M solutions of various solvents including tetrahydrofuran (THF), ethyl acetate (EA), dichloromethane (DCM), acetone (Ace), dimethylformamide (DMF), dimethyl sulfoxide (DMSO), acetonitrile (MeCN), ethanol (EtOH),

Celal Bayar University Journal of Science
Volume 20, Issue 3, 2024, p 100-105
Doi: 10.18466/cbayarfbe.1516889

methanol (MeOH), and n-hexane (n-Hex) (see Figure S7). Among these solvents, DMF was identified as the optimal choice due to its effective solubility for compound (**4**). Further investigation focused on DMF solutions, where absorption, emission and excitation spectra of compound (**4**) were recorded at a concentration of $1x10^{-6}$ M (see Figure 2). Additionally, solid-state absorption and emission spectra of compound (**4**) were examined (see Figure 3). The fluorescence quantum yield (Φ_F) of compound (**4**) was determined using the comparative method with a standard reference, 9,10-Diphenylanthracene (Φ_F = 0.95 in EtOH), according to Eq. (1) [32].

$$\Phi_F = \Phi_F(Std)\frac{F \cdot A_{Std} \cdot \eta^2}{F_{Std} \cdot A \cdot \eta^2_{Std}} \quad (1)$$

In this equation, Φ_F(Std) represents Φ_F of the reference molecule. F and F_{Std} denote the integrated areas under the fluorescence emission curves of compound (**4**) and the reference molecule, respectively. A and A_{Std} indicate the absorbances of compound (**4**) and the reference molecule at their respective excitation wavelengths. η^2 and η^2_{Std} are the squares of the refractive indices of the solvents for compound (**4**) and the reference molecule, respectively. The solutions of both compound (**4**) and the reference molecule were fixed at a concentration of $1x10^{-6}$ M for this measurement. Additionally, the fluorescence lifetime (τF) of compound (**4**) was directly measured and analyzed using a mono exponential calculation method.

3. Results and Discussion

3.1. Synthesis and Characterization

The fluorene derivative (**4**) was synthesized through a two-step reaction process outlined in Scheme 1. Initially, the dibromine derivative (**3**) was synthesized by reacting commercially available 9*H*-fluoren-9-one (**2**) with CBr_4 and PPh_3, following a procedure described in the literature (Fig. S5-S6) [31]. Subsequently, fluorene derivative (**4**) was obtained in high yield via a Suzuki coupling reaction between dibromide derivative (**3**) and 2.1 equivalents of (4-(diphenylamino)phenyl) boronic acid. The purity of compound (**4**) was confirmed through various analytical techniques including FT-IR, matrix-assisted MALDI-MS, ^{1}H NMR, ^{13}C NMR spectroscopy, and elemental analysis. Spectral data for compound (**4**) are provided in the Supplementary Information (Fig. S1-S4). All spectroscopic data corroborated the structure of compound (**4**). The FT-IR spectrum of compound (**4**) showed characteristic peaks indicative of its structure: aromatic =C-H stretches at 3055 and 3036 cm^{-1}, aromatic -C=C- stretch at 1586 cm^{-1}, and -C-N-C- stretch at 1273 cm^{-1} (Fig. S1). The molecular ion peak observed in the matrix-assisted MALDI-MS spectrum was 664.206 m/z, which closely matched the calculated value for compound (**4**) of 664.29 m/z (Fig. S2). In the ^{1}H NMR spectrum of compound (**4**), all expected aromatic proton signals appeared between 7.5-6.9 ppm (Fig. S3). Similarly, the ^{13}C NMR spectrum displayed aromatic carbon and quaternary carbon signals within the range of 150-115 ppm (Fig. S4). These spectroscopic analyses collectively confirmed the successful synthesis and structural integrity of compound (**4**).

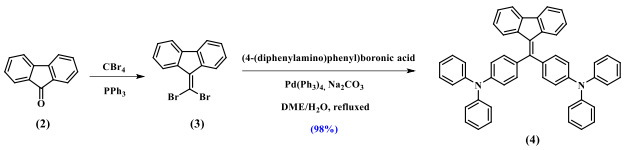

Scheme 1. Synthetic pathway of compound **(4)**.

3.2. Optical properties

Photophysical properties of compound (**4**) were thoroughly investigated in various solvents at a concentration of $1x10^{-6}$ M using UV-vis absorption and emission spectroscopy (Fig. S5). In DMF, the absorption spectrum of compound (**4**) displayed its maximum absorption band at 302 nm. Upon excitation at 340 nm, the emission spectrum showed a maximum emission band at 402 nm (Fig. 2). In the solid-state, compound (**4**) exhibited different absorption and emission characteristics compared to its DMF solution state (Fig. 3). Specifically, the emission wavelength shifted to 550 nm in the solid-state, indicating a red shift in emission compared to the 402 nm observed in DMF solution (Fig. 3b). This shift often indicates differences in molecular packing and environment between solution and solid phases. Φ_F of compound (**4**) was determined to be 0.78 in EtOH, using a comparative method with a standard reference (Fig. 4). Additionally, the τF of compound (**4**) was directly measured (Fig. 4). The τF value was determined through mono exponential calculations to be 1.7 ± 0.005 ns, representing the characteristic time scale of the fluorescence emission decay for the compound. These results provide a comprehensive understanding of the optical properties of compound (**4**), highlighting its behavior in different solvent environments and in solid-state conditions.

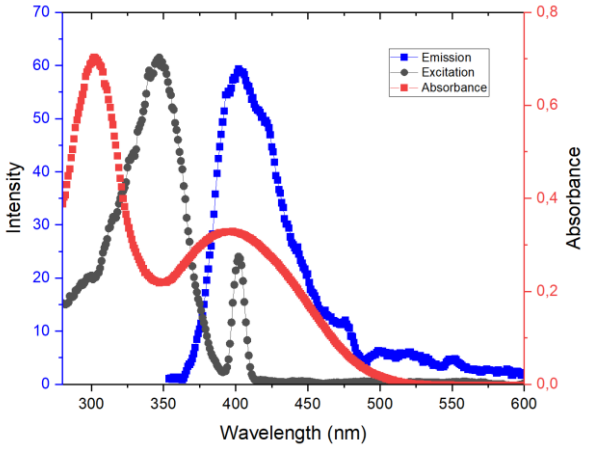

Figure 2. Absorption, emission and excitation spectra of compound (**4**) in DMF (λ_{exc}:340 nm).

Celal Bayar University Journal of Science
Volume 20, Issue 3, 2024, p 100-105
Doi: 10.18466/cbayarfbe.1516889

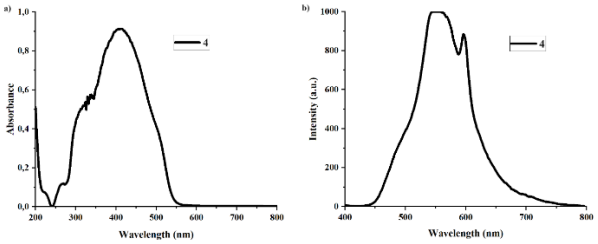

Figure 3. Solid-state **a)** absorption **b)** emission spectra of compound (**4**) (λ_{exc}:340 nm).

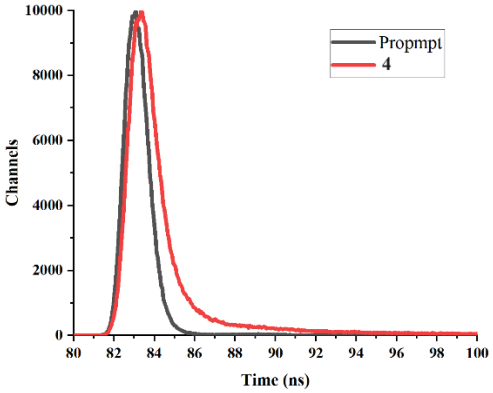

Figure 4. Fluorescence lifetime spectrum of compound (**4**).

3.3. Aggregation induced emission

Indeed, compound (**4**) demonstrates interesting photophysical properties, especially in mixed DMF-water solvent systems where the polarity and aggregation state can be tuned. Here's a breakdown of the observations: UV-vis Absorption Spectra (Figure 5a): In dilute DMF solution (1×10^{-6} M), compound (**4**) exhibits an absorption peak at 402 nm. As the fraction of water in the DMF-water mixture increases, the absorbance intensity gradually decreases. There is also a slight red shift observed in the absorption peak, particularly noticeable in the 50% DMF-water mixture. Fluorescence Emission Spectra (Figure 5b): The emission intensity of compound (**4**) remains weak when the water fraction is between 0% to 40% in the DMF-water mixture. Interestingly, at 50% water content, deteriorations in the emission profile start to appear, indicating possible aggregation effects. Additionally, an increase in the water fraction from 10% to 40% leads to a red shift in the emission wavelength by approximately 16 nm. These observations suggest that compound (**4**) exhibits significant AIE characteristics. The AIE effect is commonly observed in organic fluorophores where their emission intensity increases as they aggregate in the solid-state or in highly viscous environments, contrary to their behavior in dilute solutions where emissions are typically weaker due to non-radiative decay processes. In the case of compound (**4**), the presence of water in the DMF mixture seems to promote aggregation, leading to enhanced emission intensity and a shift in emission wavelength. These findings are crucial for understanding and potentially utilizing compound (**4**) in applications where controlled emission properties are desired, such as in sensing or imaging technologies.

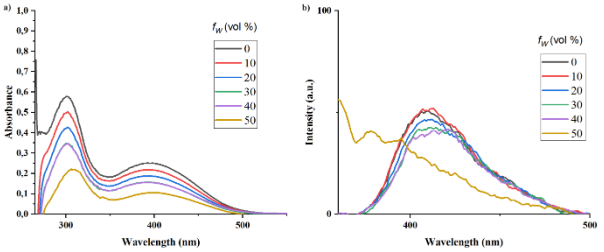

Figure 5. (a) Absorbance and b) emission spectra of dilute solutions of compound (**4**) ($1x10^{-6}$ M) in DMF-water mixtures with different water contents (0–50%). (λ_{exc}= 340 nm).

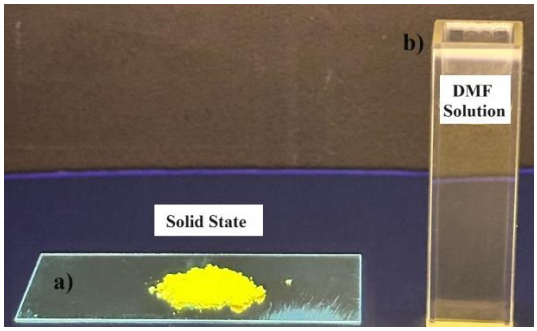

Figure 6. Photograph of a) solid-state sample and b) DMF solution of (**4**) under 365 nm UV illumination.

4. Conclusion

A novel electron-rich π-conjugated organic compound (**4**) featuring bis-TPA donor groups, and a fluorene core was successfully designed and synthesized in high yield through a two-step reaction process. The structural characterization of compound (**4**) was rigorously confirmed using FT-IR, MALDI-MS, ^{1}H NMR, ^{13}C NMR spectroscopy, and elemental analysis, all of which confirmed its structure accurately. We conducted a thorough investigation of photophysical features such as absorption, emission, excitation, and fluorescence lifetime using UV-vis and fluorescence spectroscopy instruments. Compound (**4**) exhibited bright yellow fluorescence in its solid-state form, indicating promising optical properties. Moreover, through studies of its AIE characteristics, it showed typical behavior where its emission intensity increased significantly in aggregated or solid-state environments compared to solution states. The strong solid-state emission characteristics of compound (**4**) suggest its potential for practical applications where intense and stable fluorescence is advantageous. Future studies will explore its mechano-chromic properties, further expanding its potential utility in responsive materials.

Author's Contributions

Seda Cetindere and Musa Erdoğan equally contributed to this manuscript, study conception, design, and synthesis. All authors read and approved the final manuscript.

Ethics

There are no ethical issues after the publication of this manuscript.

References

[1]. Zhao, Z, Lam, JWY, Tang, BZ. 2012. Tetraphenylethene: a versatile AIE building block for the construction of efficient luminescent materials for organic light emitting diodes. *J Mater Chem*; 22:23726-40.

[2]. Huang, J, Yang, X, Li, X, Chen, P, Tang, R, Li, F, Lu, P, Ma, Y, Wang, L, Qin, J, Li, Q, Li, Z. 2012. Bipolar AIE-active luminogens comprised of an oxadiazole core and terminal TPE moieties as a new type of host for doped electroluminescence. *Chem Commun;* 48: 9586-8.

[3]. Martinez-Manez, R, Sancenon, F. 2003. Fluorogenic and chromogenic chemosensors and reagents for anions. *Chem. Rev*; 103(11): 4419-4476.

[4]. Wang, M, Zhang, G, Zhang, D, Zhu, D, Tang, BZ. 2010. Fluorescent bio/chemosensors based on silole and tetraphenylethene luminogens with aggregation-induced emission feature. *J. Mater. Chem*; 20: 1858.

[5]. Yang, Y, Zhao, Q, Feng, W, Li, F. 2013. Luminescent chemodosimeters for bioimaging. *Chem. Rev*; 113: 192.

[6]. Zhang, Q, Yu, P, Fan, Y, Sun, C, He, H, Liu, X, Lu, L, Zhao, M, Zhang, H, Zhang, F. 2020. Bright and stable NIR-II J-aggregated AIE dibodipy-based fluorescent probe for dynamic in vivo bioimaging. *Angew. Chem., Int. Ed.;* 60: 3967.

[7]. Shimizu, M, Takeda, Y, Higashi, M, Hiyama, T. 2009. 1,4-Bis(alkenyl)-2,5-dipiperidinobenzenes: minimal fluorophores exhibiting highly efficient emission in the solid state. *Angew Chem Int Ed*; 48: 3653-6.

[8] Xue, P, Sun, J, Chen, P, Gong, P, Yao, B, Zhang, Z, Qian, C, Lu, R. 2015. Strong solid emission and mechanofluorochromism of carbazole-based terephthalate derivatives adjusted by alkyl chains. *J Mater Chem C*; 3: 4086-92.

[9]. Yuan, WZ, Lu, P, Chen, S, Lam, JW, Wang, Z, Liu, Y, Kwok, HS, Ma, Y, Tang, BZ. 2010. Changing the behavior of chromophores from aggregation-caused quenching to aggregation-induced emission: development of highly efficient light emitters in the solid state. *Adv Mater*; 22: 2159-63.

[10]. Domaille, DW, Que, EL, Chang, CJ. 2008. Synthetic fluorescent sensors for studying the cell biology of metals. *Nature Chemical Biology*; 4: 168–175.

[11]. Hong, YN, Lam, JWY, Tang, BZ. 2011. Aggregation-induced emission. *Chem. Soc. Rev*; 40: 5361–5388.

[12]. Hong, YN, Lam, JWY, Tang, BZ. 2009. Aggregation-induced emission: phenomenon, mechanism and applications. *Chem. Commun;* 4332-4353.

[13]. Kwok, RTK, Leung, CWT, Lam, JWY, Tang, BZ. 2015. *Chem. Soc. Rev*; 44: 4228–4238.

[14]. Mei, J, Hong, Y, Lam, JWY, Qin, A, Tang, Y, Tang, BZ. 2014. Aggregation-Induced Emission: The Whole Is More Brilliant than the Parts. *Adv. Mater*; 26: 5429–5479.

[15]. Luo, J, Xie, Z, Lam, JWY, Cheng, L, Chen, H, Qiu, C, Kwok, HS, Zhan, X, Liu, Y, Zhu, D, Tang, BZ. 2001. Aggregation-induced emission of 1-methyl-1,2,3,4,5-pentaphenylsilole. *Chem. Commun*; 1740–1741.

[16]. Kumbhar, HS, Shankarling, GS. 2015. Aggregation induced emission (AIE) active β-ketoiminate boron complexes: synthesis, photophysical and electrochemical properties. *Dyes Pigments*; 122: 85-93.

[17]. Kumar, M, Vij, V, Bhalla, V. 2012. Vapor-phase detection of trinitrotoluene by AIEE active hetero-oligophenylene-based carbazole derivatives. *Langmuir*; 28: 12417-21.

[18]. Shi, C, Guo, Z, Yan, Y, Zhu, S, Xie, Y, Zhao, YS, Zhu, W, Tian, H. 2013. Self-assembly solid-state enhanced red emission of quinolinemalononitrile: optical waveguides and stimuli response. *ACS Appl. Mater. Interfaces*; 5(1): 192-8.

[19]. Gu, X, Yao, J, Zhang, G, Zhang, C, Yan, Y, Zhao, Y, Zhang, D. 2013. New electron-donor/acceptor-substituted tetraphenylethylenes: aggregation-induced emission with tunable emission color and optical-waveguide behavior. *Chem Asian J*; 8(10): 2362-9.

[20]. Xu, F, Wang, H, Du, X, Wang, W, Wang, DE, Chen, S, Han, X, Li, N, Yuan, MS, Wang, J. 2016. Structure, property and mechanism study of fluorenone-based AIE dyes. *Dyes and Pigments;* 129: 121-128.

[21]. Du, X, Su, H, Zhao, L, Xing, X, Wang, B, Qiu, D, Wang, J, Yuan, MS. 2021. AIE-based donor–acceptor–donor fluorenone compound as multi-functional luminescence materials. *Mater. Chem. Front*; 5: 7508-7517.

[22]. Shaya, J, Corridon, PR, Al-Omari, B, Aoudi, A, Shunnar, A, Mohideen, MIH, Qurashi, A, Michel, BY, Burger, A. 2022. Design, photophysical properties, and applications of fluorene-based fluorophores in two-photon fluorescence bioimaging: A review. *Journal of Photochemistry and Photobiology C: Photochemistry Reviews*; 52, 100529.

[23]. Abbel, R, Schenning, APHJ, Meijer, EW. 2009. Fluorene-based materials and their supramolecular properties. *J. Polym. Sci. Part A: Polym. Chem*; 47: 4215–4233.

[24]. Moura, GLC, Simas, AM. 2010. Two-photon absorption by fluorene derivatives: systematic molecular design. *J. Phys. Chem. C*; 114(13): 6106–6116.

[25]. Kurdyukova, IV, Ishchenko AA. 2012. Organic dyes based on fluorene and its derivatives. *Russ. Chem. Rev;* 81: 258–290.

[26]. Ogawa, K. 2014. Two-photon absorbing molecules as potential materials for 3D optical memory. *Appl. Sci*; 4 (1): 1–18.

[27]. Lin, Y, Chen, Y, Ye, TL, Chen, ZK, Dai, YF, Ma, DG. 2012. Oligofluorene-based push–pull type functional materials for blue light-emitting diodes, *J. Photochem. Photobiol. A: Chem;* 230(1): 55-64.

[28]. Lim, K, Kim, C, Song, J, Yu, T, Lim, W, Song, K, Wang, P, Zu, N, Ko, J. 2011. Enhancing the performance of organic dye-sensitized solar cells via a slight structure modification. *J. Phys. Chem. C;* 115: 22640–22646.

[29]. Erdoğan, M, Horoz, S. 2021. Synthesis and characterization of a triphenylamine-dibenzosuberenone-based conjugated organic material and an investigation of its photovoltaic properties. *Journal of Chemical Research*; 45(1-2): 207-212.

[30]. Erdoğan, M, Orhan, Z, Daş, E. 2022. Synthesis of electron-rich thiophene triphenylamine based organic material for photodiode applications. *Optical Materials*; 128:12446.

[31]. Chen, ZQ, Chen, T, Liu, JX, Zhang, GF, Li, C, Gong, WL, Xiong ZJ, Xie, NH, Tang, BZ, Zhu, MQ. 2015. Geminal cross-coupling of 1, 1-dibromoolefins facilitating multiple topological π-conjugated tetraarylethenes. *Macromolecules*; 48(21): 7823-7835.

[32]. Yildirim-Sarikaya, S, Ardic-Alidagi, H, Cetindere, S. 2023. Novel BODIPY-Fluorene-Fullerene and BODIPY-Fluorene-BODIPY Conjugates: Synthesis, Characterization, Photophysical and Photochemical Properties. *Journal of Fluorescence*; 33: 297–304.

[33]. Tan, S, Yin, Y, Chen, W, Chen, Z, Tian, W, Pu, S. 2020. Carbazole-based highly solid-state emissive fluorene derivatives with various mechanochromic fluorescence characteristics. *Dyes and Pigments*; 177: 108302.

[34]. Chen, Z, Liang, J, Han, X, Yin, J, Yu, GA, Liu, SH. 2015. Fluorene-based novel highly emissive fluorescent molecules with aggregate fluorescence change or aggregation-induced emission enhancement characteristics. *Dyes and Pigments*; 112: 59-66.

[35]. Gouthaman, S, Jayaraj, A, Sugunalakshmi, M, Sivaraman, G, Swamy, PCA. 2022. Supramolecular self-assembly mediated aggregation-induced emission of fluorene-derived cyanostilbenes: multifunctional probes for live cell-imaging. *J. Mater. Chem. B*; 10: 2238.

[36]. Zhou, X, Li, H, Chi, Z, Zhang, X, Zhang, J, Xu, B, Zhang, Y, Liu, S, Xu, J. 2012. Piezofluorochromism and morphology of a new aggregation-inducedemission compound derived from tetraphenylethylene and carbazole. *New. J. Chem*; 36: 685–693.

[37]. Dong, YQ, Lam, JWY, Qin, AJ, Sun, JX, Liu, JZ, Li, Z, Sun, JZ, Sung, HHY, Williams, ID, Kwok, HS, Tang, BZ. 2007. Aggregation-induced andcrystallization-enhanced emissions of 1,2-diphenyl-3,4-bis(diphenylmethylene)-1-cyclobutene. *Chem. Commun*; 3255–3257.

[38]. Duraimurugan, K, Balasaravanan, R, Siva, A. 2016. Electron rich triphenylamine derivatives (D-π-D) for selective sensing of picric acid in aqueous media. *Sensors and Actuators B*; 231: 302–312.